UNIVERSITY OF SOUTHAMPTON

FACULTY OF ENGINEERING SCIENCE AND MATHEMATICS

Optoelectronics Research Centre

Liquid Crystal Adaptive Planar Optical Devices

Benjamin D. Snow

Submitted for the degree of Doctor of Philosophy

December 2010

UNIVERSITY OF SOUTHAMPTON

ABSTRACT

Optoelectronics Research Centre

Doctor of Philosophy

Liquid Crystal Adaptive Planar Optical Devices

Benjamin D. Snow

This thesis presents a series of experimental studies based on using liquid crystals (LC) with planar optical lightwave components. Adaptive optical devices have been fabricated by combining LCs with direct UV written buried channel waveguide and Bragg grating structures.

It has been discovered that the hysteresis seen in previous LC tunable Bragg grating devices is due to a process known as the pincement transition. Pincement involves the transition from a splay-bend wall in the nematic LC to a pair of oppositely charged half-integer disclination lines. The voltage-based transient behaviour of the pincement transition correlated with the tuning curve response seen in voltage controlled LC tunable gratings.

In order to reduce the hysteresis effect a new grooved substrate geometry was introduced. Rather than accessing the Bragg grating vertically via a wet etch process, the substrates are precision machined using a dicing saw to allow side-access. The result is significantly reduced hysteresis, with a maximum tuning range of over 1nm with the application of under 30V(pp).

Tunable chirped Bragg gratings based on standard PCB technology using arrays of resistors as heating elements were designed and tested. The group delay slope of the chirped gratings was tuned by 4ps/nm using a combination of heating elements and thermoelectric cooling.

Finally, LC compounds were then tested for suitability as waveguiding media. It was found that both hollow fiber and planar substrate systems using an LC as the core guiding medium successfully guided both visible and IR light at telecomms wavelengths.

Contents

List of Figures

List of Tables

Declaration of Authorship

I, **Benjamin D. Snow**, declare that the thesis entitled

Liquid Crystal Adaptive Planar Optical Devices

and the work presented in the thesis are both my own, and have been generated by me as the result of my own original research. I confirm that:

- this work was done wholly or mainly while in candidature for a research degree at this University;
- where any part of this thesis has previously been submitted for a degree or any other qualification at this University or any other institution, this has been clearly stated;
- where I have consulted the published work of others, this is always clearly attributed;
- where I have quoted from the work of others, the source is always given. With the exception of such quotations, this thesis is entirely my own work;
- I have acknowledged all main sources of help;
- where the thesis is based on work done by myself jointly with others, I have made clear exactly what was done by others and what I have contributed myself;
- parts of this work have been published as in Publications, Appendix B.

Signed:

Date: 28th November, 2010.

Acknowledgements

I am incredibly grateful to my supervisors Prof. Malgosia Kaczmarek and Prof. Peter Smith for their fantastic support, knowledge and advice, and for simply the amount of time they have spent helping me throughout my PhD. I am also extremely grateful to Dr. James Gates for all the help he has given me throughout my time at the ORC, not least his knowledge and expertise in the lab.

I would like to thank all of the members of the group, both past and present, for their support: Dr. Corin Gawith, Dr. Huw Major, Dr. Dmytro Kundys, Dr. Rafiq Adikan, Mario Garcia-Ramirez, Chaotan Simo, Sumiaty Ambran, Dominic Wales, Dr. Chris Holmes, Richard Parker, Lewis Carpenter and Helen Rogers. Special thanks go to Richard, Lewis and Helen, for without them my time finishing my PhD would have been far less enjoyable.

Thank you also to everyone in the ORC who has helped and supported me during my time here: Dr. Andriy Dyadyusha, Dr. Eleanor Tarbox, Eve Smith, Dr. Peter Lanchester, Dr. Hazel Hung-Batemen, Dr. James Bateman, Dr. Dave Banks, Dr. Mark Darby, Dr. Trina Ng, Angela Camerlingo, Ed Weatherby, Mark Lessey, Simon Butler, Chris Nash, Kevin Sumner, Neil Sessions, Dave Sager, Dr. Timothy May-Smith, Hamish Hunt and many others who I have shared time with at the ORC.

Thank you to my friends and family for their continual support and understanding. Thank you to my parents, Anne and Ralph Snow, for helping me throughout the entirety of my PhD, and to my brother, Jonathan Snow, for his apparent sense of humour. Thanks also to my friends who decided not to ask ”Haven’t you finished yet?” whenever they saw me!

Finally, thanks go to EPSRC for supporting me for the duration of my PhD and for giving me the opportunity to work at the ORC.

Benjamin D. Snow

Abbreviations

5CB	4n′-pentyl-cyanobiphenyl
AOM	Acousto-Optic Modulator
ASE	Amplified Spontaneous Emission
AWG	Arrayed Waveguide Gratings
BBO	β-barium-borate
CNC	Computer Numerical Control
CVD	Chemical Vapour Deposition
DCF	Dispersion Compensating Fibre
DGW	Direct Grating Writing
DUW	Direct UV Writing
EDC	Electronic Dispersion Compensation
EOM	Electro-Optic Modulator
FBG	Fiber Bragg Grating
FHD	Flame Hydrolysis Deposition
FMM	Film Mode Matching
GDR	Group Delay Ripple
HPDLC	Holographic Polymer Dispersed Liquid Crystals
IO	Integrated Optics
IR	Infrared
LC	Liquid crystal
LCD	Liquid Crystal Display
LED	Light Emitting Diode
MBE	Molecular Beam Expitaxy
MEMS	Micro-Electro-Mechanical System
MPS	Modulation Phase-Shift
MVA	Multi-domain Vertical Alignment
NRZ	Non-Return-to-Zero
ODE	Ordinary Differential Equation

OPD	Optical Path-length Difference
OSA	Optical Spectrum Analyzer
PDLC	Polymer Dispersed Liquid Crystals
PECVD	Plasma Enhanced Chemical Vapour Deposition
PIC	Photonic Integrated Circuit
PM	Polarization Maintaining
POLICRYPS	Polymer-LC-Polymer Slices
PSO	Position Synchronized Output
RIE	Reactive Ion Etching
ROADM	Reconfigurable Optical Add-Drop Multiplexer
RTA	Rapid Thermal Annealing
SPM	Self-Phase Modulation
TE	Transverse Electric
TM	Transverse Magnetic
TIR	Total Internal Reflection
VA-LCD	Vertical Alignment LCD
VNA	Vector Network Analyzer
VOA	Variable Optical Attenuators
WDM	Wavelength Division Multiplexing

“I’m sciencing as fast as I can.”

Chapter 1

Introduction

1.1 The world's biggest city

In the space of barely twenty years, this city has been irreversibly transformed from a basic medium for data transfer to a vast, seemingly infinite metropolis of information, commerce, media, arts, shopping, socializing, and countless other facets. This ever expanding city is, of course, the Internet. Arguably the most revolutionary technological invention of the recent past, the Internet in its current form owes almost its entire existence to one area of engineering: optics.

The physical enabler of the Internet is undoubtedly the optical fibre, and even those without a scientific bent will be aware of its importance. However, its comparatively unsung counterpart, integrated optics, still requires special attention for its increasingly apparent uses, and also as the basis of this thesis. The Internets motorways, the optical fibres, have been built, but they are getting busier. The dense data throughput now needs to be controlled even more rigorously to keep it running efficiently, and this is where integrated optics becomes increasingly important.

Integrated optics is the name given to combining several optical or electro-optical components onto a common substrate. Various substrate materials have been used including silica-based materials (silica-on-silicon), other glasses such as tantalum pentoxide or alumina, and semiconductors. The work presented in this thesis involves only silica-based substrates. Components possible in silica can

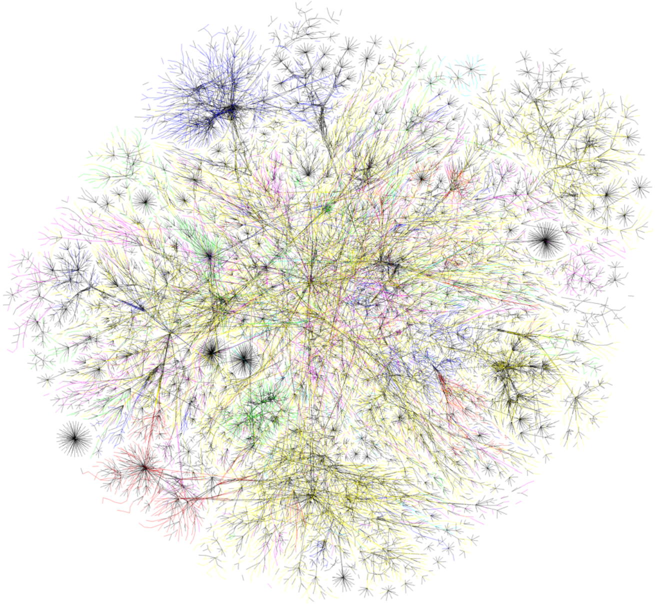

Figure 1.1: A conceptual map of a portion of the Internet, 2005

range from splitters, filters, and couplers, to lasers, switches, and modulators [1].

Integrated optics has found uses not only in a telecommunications capacity, but also in areas such as optical data storage, medicine, security, sensing, laser fusion and Intel's new Light Peak™ technology. This diversification of applications was in no small part due to the rapid economic decline of the Internet sector at the turn of the century. This forced the optics industry into finding new applications for new markets. But perhaps the most interesting challenge is to provide products for a more economically pressured telecommunications industry that still requires new and improved technologies.

1.2 Motivation

The motivation behind integrated optics is to create higher performance and lower cost devices. Many of the aforementioned optical components can be fabricated on the same substrate. This has the advantages of fast fabrication time, low loss between components, reduced production costs and small resultant package size. Substrate manufacture can employ well established fabrication techniques used in the semiconductor industry, thus aiding production of high quality, low cost and robust devices.

The motivation behind this work has been to develop and explore advanced planar Bragg grating structures and devices. From an application perspective, this involves designing and fabricating devices that could be used for filtering, multiplexing/demultiplexing, and dispersion management. From a more fundamental scientific perspective, this work involves understanding the physics behind the operation of these devices. Much work has been performed in order to understand the physics of liquid crystal (LC) tunable Bragg grating devices, as LCs themselves pose an interesting set of both problems and benefits.

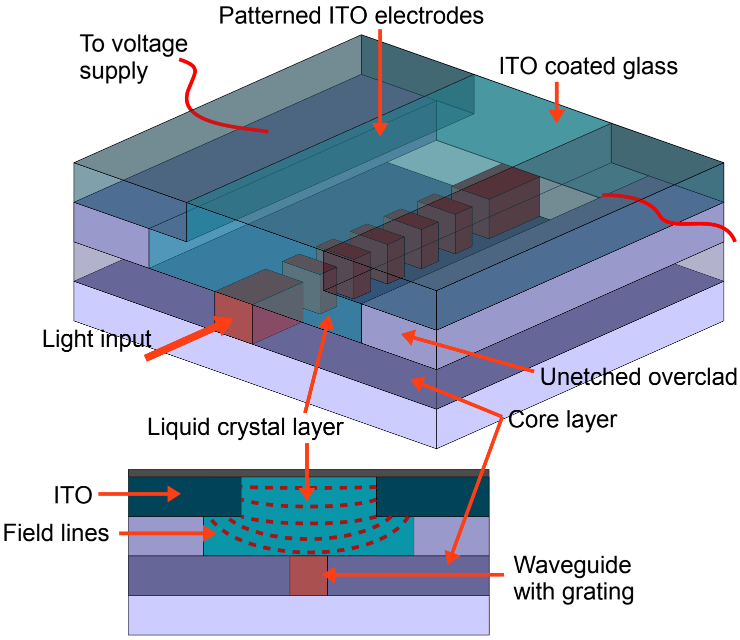

Figure 1.2: Diagram of an electrically tunable LC Bragg grating device

A large part of this thesis has been devoted to furthering the understanding of LC-based tunable planar Bragg grating devices. The concept of such devices was first introduced by Sirleto et al [2], and a working device has been fabricated and tested by Adikan et al [3]. A schametic of this device is shown in Fig. 1.2. This device involved using a nematic LC as an adaptive overclad on a planar buried channel waveguide and Bragg grating structure. LCs are particularly interesting because they exhibit both optical and dielectric anisotropy. This can be exploited by applying external fields to the LC in specially fabricated cells to reorient its constituent molecules. This causes the effective refractive index seen by a linearly polarized propagating mode in the waveguide and Bragg grating to vary. The result is a tuning in the Bragg reflection wavelength and hence a voltage-controlled optical filter. However, it was found experimentally in the first devices that there is not a simple relationship between applied voltage and Bragg wavelength shift.

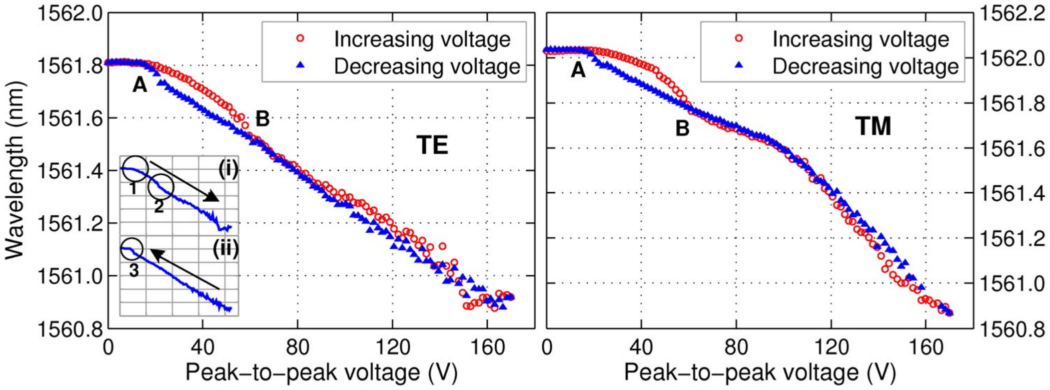

Figure 1.3: Absolute device tuning curves for both TE and TM polarised light showing hysteresis between points A and B [3]. The insets show the same curves for increasing (arrow pointing downwards) and decreasing (arrow pointing upwards) voltages. In inset (i), the circles numbered 1 and 2 show the two threshold points at ~22V and ~57V respectively. In inset (ii), the low voltage threshold at ~17V is circled and numbered 3.

In the original devices it was found that the tuning curves exhibited hysteresis, as shown in Fig. 1.3. One of the primary aims of the work presented in this thesis has been to discover the causes of this hysteresis and, if possible, methods to improve the tuning response. This involves understanding the behaviour of LC's in general and also how they behave when bounded by treated surfaces. Surface treatments are important as they will ultimately govern the alignment of the LC in a confined geometry such as an LC cell or a tunable grating device. Once the alignment has been controlled in a cell or confined device, it is then important to understand the LC reorientation mechanisms occuring when applying an external field to the cell. Therefore a large portion of the work undertaken in this thesis aims to analyze the behaviour of LC's in electrically tunable devices, in geometries appropriate for tunable Bragg gratings.

1.3 Thesis Structure

Further to the discussion above, a broader background of integrated optics will be given in Chapter 2. This will aim to develop an understanding of how the specific optical structures fabricated and tested in this thesis fit in to the broader topic of integrated optics. Most notably these include the buried channel waveguide and Bragg grating structures, and how the application of LC's can provide tunable devices. This chapter also provides a historical overview of integrated optics and highlights the motivation behind its development. Qualitative descriptions of some common integrated optical components used throughout this thesis are presented briefly. A more theoretically rigorous analysis will be provided in following chapters.

Chapter 3 provides the theoretical overview of slab and channel waveguide structures including analytical solutions to the slab waveguide geometry. Starting with Maxwell's equations, electric field distributions in dielectric and anisotropic media are obtained. When confined to waveguiding structures, such as the slab and channel waveguides, it is shown that these field distributions take the form of optical modes. These modes, if eigenmodes of the system, will propagate unperturbed through the waveguide. However, by using a periodic refractive index structure, the modes can be converted into backward propagating modes. This is the principle of a Bragg reflector, and Chapter 3 finishes with a theoretical treatment of Bragg gratings which were utilized in work presented in Chapters 7, 8, and 9. Some adaptations of Bragg gratings, namely apodization and chirp, are also described.

Chapter 4 presents an overview of the LC physics relevant to this work. The concept of a nematic LC is introduced along with some of their general physical attributes. This is followed by an explanation of how LC's behave in externally applied fields, which for this work involves exclusively electric fields. Moving towards LC's in confined geometries, a description of LC alignment effects associated with surface treatments is presented. An explanation of the concept of LC topological defects is also given. These have great importance in the analysis of the tuning devices as explained in Chapter 7. Chapter 4 concludes with a description of how LC cells can be used in polarized microscopy to interrogate LC molecular dynamics and associated physical processes. Their analogy with waveplates is provided which is a manifestation of their optical birefringence in confined cells.

Chapter 5 provides an overview of fabrication methods for the integrated optical components used in this work. Starting from a standard microelectronics industry silicon wafer, the process of fabricating a three-layer silica-on-silicon wafer used extensively throughout this thesis is described. This includes deposition techniques and the concept and use of photosensitivity in doped silica glasses. Subsequently, descriptions of fabrication processes utilized in producing channel waveguides are given. This includes the unique in-house Direct UV Writing (DUW) system capable of fabricating the aforementioned buried channel waveguides and Bragg gratings simultaneously.

Chapter 6 further develops the concept of DUW and introduces the advanced fabrication techniques such as simultaneous buried channel and Bragg grating inscription, known as Direct Grating Writing (DGW). This includes an explanation of the UV writing system and how various parameters of this system can be used to affect the resultant waveguides and gratings. Examples are given of how gratings can be engineered to produce a variety of spectral responses. This chapter also presents some work undertaken in order to optimize the fabrication of LC cells and LC-based tunable planar Bragg gratings. A description is given of the photolithographic process used to fabricate the transparent electrodes used in electrically tunable devices.

Chapter 7 describes the causes of the hysteresis seen in the tuning curves of the LC planar Bragg gratings. The hysteresis was found to be caused by a transition called *pincement*. Pincement is the transformation of a wall into a pair of disclination lines, both of which are explained in Chapter 4. It is a consequence of specific combination of cell geometry, alignment caused by surface treatment and the direction of the applied field. Further analysis of the disclinations formed during this process revealed an interesting structure under interrogation with high resolution microscopy. There was inherent periodicity in the disclinations which is referred to as the "zigzag" configuration. Zigzag disclinations were also found to have point defects with alternating topological charge at each vertex. This is shown to be analogous to the standard "escaped" geometry in a homeotropically aligned capillary.

Chapter 8 presents results on a new geometry for LC-tunable Bragg grating devices. This is a grooved geometry formed via precision machining of the substrates prior to UV writing. Instead of vertical access tuning cells where the LC is applied above a grating, these cells provided alternative side-access of the grating. The groove is filled with LC and the realignment occurs beside, rather than above, the grating. The aim of these modified devices was to remove the hysteresis effect caused by the disclination dynamics. This was achieved by relocating the disclination such that it was no longer in close proximity to the waveguide and grating. The chapter concludes with examples of tuning curves that exhibit no hystereis.

Chapter 9 introduces an alternative method of tuning a planar Bragg grating's wavelength by way of thermal tuning. This work utilizes a different type of Bragg grating, known as a chirped grating, for the purpose of residual dispersion management. The key property of a chirped grating in this context is its linear group delay response. Careful control of the group delay of the reflected light as a function of wavelength allows for compensation of chromatic dispersion in optical fibre links. This chapter presents proof-of-concept results on the thermal tuning of the group delay slope. Thermal tuning is achieved using simple printed circuit board technology combined with the UV-written planar Bragg grating structures. The tunability in the group delay slope was over 4ps/nm, with power consumption below 0.5W when using one heating element.

Chapter 10 extends the concept of LC's in integrated optical components. Instead of using the LC as an adaptive overlayer, the LC can be used as the guiding medium itself. Presented here are initial results of LC's being successfully used as the core in a silica-clad waveguide. Combining machined substrates with controlled surface alignment allowed light transmission in 12.5mm long LC waveguides with losses of 30dB/cm. The losses are typical of LC's in the nematic phase. This chapter demonstrates LC waveguides operating in both the visible and near-IR spectral regions.

Chapter 11 will summarise the work undertaken and the results obtained in this thesis. There will also be a brief discussion on extensions to this work, suggesting possible routes for further research.

References

[1] R. G. Hunsperger. *Integrated Optics*. Springer New York, New York, NY, 2009.

[2] L. Sirleto, G. Coppola, G. Breglio, G. Abbate, G. C. Righini, and J. M. Oton. "Electro-optical Switch and Continuously Tunable Filter based on a Bragg Grating in a Planar Waveguide with a Liquid Crystal Overlayer". *Optical Engineering*, 41(11):2890, 2002.

[3] F. R. Mahamd Adikan, J. C. Gates, A. Dyadyusha, H. E. Major, C. B. E. Gawith, I. J. G. Sparrow, G. D. Emmerson, M. Kaczmarek, and P. G. R. Smith. "Demonstration of 100 GHz electrically tunable liquid-crystal Bragg gratings for application in dynamic optical networks". *Optics Letters*, 32(11):1542–1544, 2007.

Chapter 2

Introduction to Integrated Optics

2.1 Integrated Optics

The concept of integrated optics emerged in the late 1960's when Stewart E. Miller proposed the idea of 'a miniature form of laser beam circuitry' [1]. An excellent, and extensive, overview of the early progression of integrated optics can be found in [2]. The premise was to replace discrete free-space optical apparatus with miniature optical components on a common substrate, otherwise known as a photonic integrated circuit (PIC) [3,4].

Several factors were motivating the drive towards integrated optics. Existing free-space optical setups utilizing lasers, modulators, mirrors, detectors and so on were susceptible to environmental changes such as temperature variations and vibrations. Isolating optical circuit assemblies from thermal, mechanical and acoustic ambient changes is achievable through small device size. The result is a more stable, efficient, and rugged package that also will not suffer alignment issues. Small devices also become more economical as they can be mass produced, and will also require less material. Low cost fabrication techniques derived from those in the well-established micro-electronics industry could be use to create future PICs.

However, despite continual enthusiasm towards integrated optics, the field has not advanced as fast as first anticipated. For example, reference [3] provides an artists impression of a monolithic GaAs integrated optical transmitter, including a laser source, electro-optic modulators and switches, a directional coupler and the outputs coupled to single mode fibers. Devices of this nature were proposed over 30 years ago, but such a level of integration has yet to be realised.

One of the main issues hindering the progression of integrated optics is the lack of a common substrate in which to define integrated circuits. The rapid growth of IC's for electronics can be attributed to the availability of ideal compatible materials: the silicon wafer, silica insulator, and aluminium or copper wiring. However, there is no universal substrate on which to craft integrated optical circuits, unlike silicon wafers. As such, many different dielectric, semiconductor and polymer materials must be used to provide various functions.

For example, light sources in the form of laser diodes can be made with GaAlAs or GaInAsP, detectors can use InGaAs, modulators $LiNbO_3$, and passive components SiO_2 or Si. Polymeric devices have be shown to provide several of these functions such as switches, filters and attenuators [5], but full integration has yet to be achieved. Integration of several different materials to provide the level of functionality required for devices comes at a price. Increased complexity of design inevitably leads to increased manufacturing costs. However, this is unavoidable, particularly in hybrid designs where different substrates are bonded together to create a complete device. The alternative is the monolithic approach whereby a single substrate is used to house all the required components. Added functionality is achieved by modifying parts of the substrate, for example rare-earth doping a section of SiO_2 to create active optical regions [6].

Additional complexity arises from the requirement to use different substrate materials as each material will inevitably require different manufacturing processes. Several fabrication methods have been used to produce integrated optical components and waveguides. Crystalline materials such as semiconductors often make use of epitaxial deposition methods such as Molecular Beam Expitaxy (MBE). $LiNbO_3$ waveguides can use fabrication methods such as in-diffusion of metals, ion exchange or proton exchange, ion implantation, and even radiation damage [7, 8]. Polymers often employ spin coating or dip coating techniques which are relatively inexpensive and uncomplicated, but can have problems with poor purity and uniformity. Dielectrics can use sputtering, thermal oxidation, Chemical Vapour Deposition (CVD) or Flame Hydrolysis Deposition (FHD).

For integrated optics to evolve past bespoke systems and enter mass production there needs to exist a dominant material and associated manufacturing process. There also, perhaps more importantly, needs to exist a demand for devices that require large-scale optical integration and high component volume. Few applications currently possess these requirements, unlike the electronic equivalent where billions of transistors are required for advanced computational processes. The comparisons with integrated electronics and the problems faced by PIC's are discussed in [9].

However, integrated optics has found applications in telecommunications, such as Arrayed Waveguide Gratings (AWG) [9] and splitters, but currently devices are not at the level of integration that was first predicted. From a telecommunications viewpoint, one of the most attractive features of integrated optics is its bandwidth, which is comparable to that of standard optical fiber, both spectrally and in terms of data transfer. As the signal is carried by optical pulses rather than electrical currents, the bandwidth limiting effects caused by capacitance and inductance can be negated. Metallic conductors are plagued by frequency dependent attenuation arising from the skin depth reduction at high frequencies. Conversely, optical connections have no such problems at high frequencies. However, they are not perfect. Signal transmission is limited by dispersion, especially in high bit-rate systems, but there are methods available to overcome this problem. Attenuation is also present in optical waveguides, in the form of scattering, absorption and radiative losses.

The work in this thesis will focus on the use of silica-on-silicon substrates and integrated components. These are predominantly passive components that include waveguides and Bragg grating structures. They can be made active by the addition of an electro-optic material, such as a liquid crystal, or by exploiting the thermo-optic effect in the substrate itself. Both of these methods to create active integrated optical components will be discussed later.

Whether a substrate is providing passive or active components, its core property is its ability to guide light. The optical fiber is the most widespread optical waveguide. However, for integrated optics purposes a circular waveguide is impractical from a fabrication viewpoint. It is therefore common to use planar waveguides, which often have rectangular cross-section, as they provide better coupling between other integrated optics devices. There are a variety of different planar waveguides and fabrication techniques, and these will be discussed in the following chapters.

2.1.1 Planar Waveguides

A waveguide is an optical element that provides confinement of light via total internal reflection. To allow this, the guiding medium must have a higher refractive index than the surrounding medium. Thus, as in an optical fiber, the core must possess a higher index than the cladding. In planar geometries, the three standard waveguide structures are the rib, ridge and buried channel waveguides. Some of these waveguides can be further categorized into either symmetric or asymmetric waveguides.

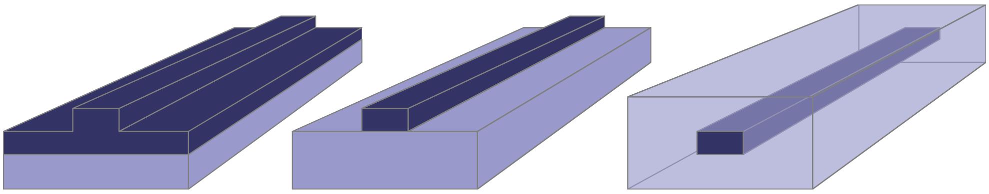

Figure 2.1: Illustration of three common channel waveguide structures: rib, ridge and buried channel.

Noted in each example waveguide in Fig. 2.1 is the higher index core which carries the optical signal. This allows light to be transported between different integrated optics components, and even into and out of an integrated optical circuit. These elements are often called optical interconnects, but are referred to in this work as channel waveguides (specifically buried channel waveguides). There are several other passive components that can constitute an integrated optics device such as splitters, couplers and filters [10]. However, for the purposes of this thesis, only the aforementioned channel waveguides, filters, and a modified channel structure known as an s-bend will be considered.

A complete, fully operational device would consist of a combination of these, and other, elements. Routing and multiplexing devices would use complex arrays of waveguides and filters on a single chip. Lasing and amplification components would need optically active regions, and also waveguides to transfer the signal. Optical integration requires both optically passive and active devices and this poses a challenge, particularly in monolithic design. Even so, the SiO_2-on-Si substrate has the potential to house lasers, amplifiers, modulators, couplers, splitters and filters [11–13], and so provides a promising avenue of integrated optics research.

These devices have found applications not only in telecommunications and data transfer, but also in sensing applications. This includes microfluidic circuits and lab-on-a-chip applications, military applications, and chemical sensing. Another market for integrated optics is the consumer electronics industry where optical data storage and media are becoming ever more prevalent.

2.1.2 Bragg Gratings

In the context of integrated optics, filtering can be achieved by components called planar Bragg grating structures [14], which are a particular type of dielectric mirror. Bragg gratings allow a particular wavelength, or wavelength band, to be reflected and sent back down the waveguide. This is achieved by coupling the incident or forward-propagating optical mode to other modes. Backward propagating modes are obtained from reflection or short-period gratings, whereas forward propagating modes are obtained from transmission or long-period gratings. The modes can be guided core modes, cladding modes, or non-guided radiative modes, depending on the waveguide and grating parameters. Any light not coupled into another mode will be transmitted through the grating unperturbed.

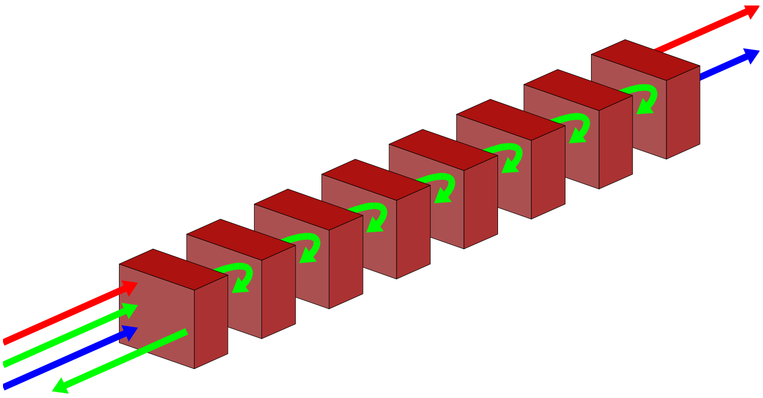

Figure 2.2: Principle of Bragg grating reflection. The grating filters and reflects one wavelength, while the others are transmitted.

In order to change the spectral response of a Bragg grating, several parameters can be modified during and after fabrication. During fabrication, the following typical parameters may be adjusted:

- the period of the grating planes
- the refractive index difference between successive grating planes
- the length of the grating
- apodization
- chirp
- tilting or blazing of grating planes

After fabrication, several of these parameters can be further modified to allow for spectral adjustments. The filtered wavelength, or wavelengths, can be spectrally tuned for adaptive filtering. Also, the apodization and chirp profiles can be modified to produce different reflection and phase responses.

Aside from the filtering and add/drop functions that Bragg gratings can provide, they can also be used in many other applications using optical fiber [15, 16]. Gratings can be used in distributed feedback lasers and distributed Bragg reflector lasers as mirror components [17, 18]. Bragg gratings are also used for gain flattening in optical amplifiers [19]. They can also be used for dispersion and residual dispersion compensation in long-haul telecomms networks [20–22]. Their other main application is sensing, where they have been used to measure stress/strain, pressure, temperature, and have also been employed as chemical sensors [23, 24].

2.1.3 Liquid Crystals in Integrated Optics

Liquid crystals (LC) were first combined with integrated optics in the early 1970's. Pioneers of this hybrid technology were Hu and Whinnery [25, 26]. The great potential of LC's as adaptive elements in many applications is due to their unique electro-optical properties. They typically have large electro-optic (EO) coefficients and so can be easily modified with low power electronics. Without question the most common adaptation of LC's into integrated optics has been the Liquid Crystal Display (LCD). This multi-billion pound industry has become so dominant it is easy to forget that the versatility of LC's lends them to many other applications. However, it is perhaps fitting to provide examples of two such LC display devices as they contain many parallels with the devices used extensively throughout this thesis.

One particular variation of the LCD, known as the Vertical Alignment LCD (VA-LCD), has similarities to the cells fabricated in this thesis. The principle of VA-LCD is shown in Fig.2.3. In a VA-LCD, the LC is confined between two ITO-coated substrates, which are treated to provide perpendicular alignment at the surfaces. The cell is contained between two crossed polarizers which provide extinction of the light in the ’off’ state. As a field is applied to the LC, the molecules reorient such that they become parallel to the substrate. The angle the molecules make to the polarization axis, and the thickness of the LC, govern the degree of rotation of the input light such that the cell becomes transmissive. This is known as the ’on’ state.

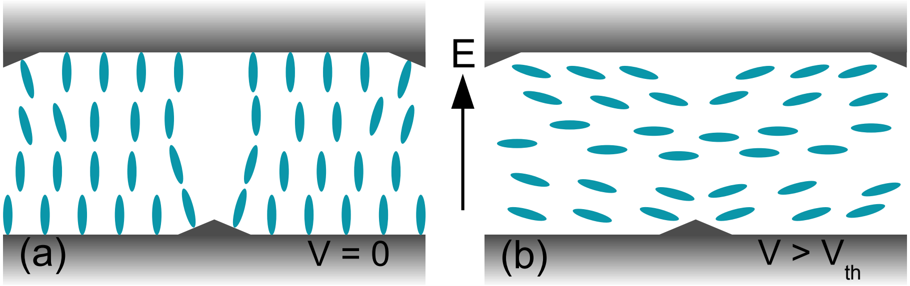

Figure 2.3: Diagram of a VA-LCD cell in (a) the ’off’ state, and (b) the ’on’ state

In the ’off’ state, the LC molecules are everywhere normal to the surface of both polarizers, hence no rotation of the polarization is possible. When in the ’on’ state, the LC molecules are aligned at 45° to both polarizers. By careful control of the cell thickness, and by utilizing the birefringence of the LC, 90° rotation of the polarization can be achieved. Hence the LC cell becomes transmissive and the associated pixel is illuminated. The triangular protrusions added to the substrate create domains which provides a symmetric viewing angle. Hence this LCD mode is often called Multi-domain Vertical Alignment (MVA).

In-Plane Switching (IPS) is another display mode that uses an electrode switching mechanism similar to that used in the cells in this thesis. IPS uses planar aligned surfaces such that the LC director is parallel to the polarizer, and the analyzer is crossed. In the ’off’ state, the LC produces no phase retardation, and the analyzer absorbs the linearly polarized light. In the 'on' state, the field reorients the director and causes phase retardation, thus modulating the transmittance through the analyzer. This IPS principle is shown in Fig.2.4. Some devices in this thesis used what is essentially a combination of the VA field realignment from homeotropic to planar, and the in-plane electrode geometry in the IPS mode.

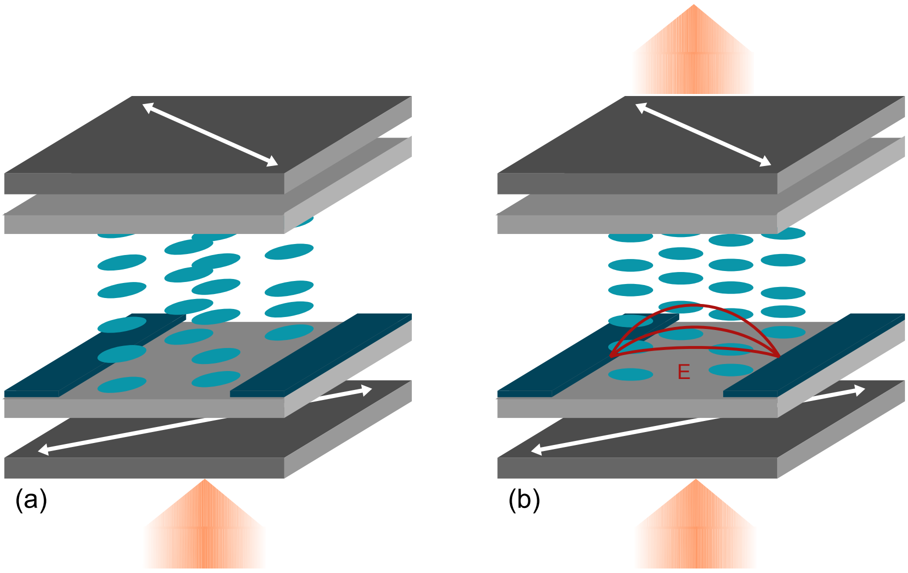

Figure 2.4: Diagram of an IPS cell in (a) the 'off' state, and (b) the 'on' state

LC's are applicable to integrated optics for a multitude of reasons. They are easily fabricated in thin-film forms and thus are compatible with integrated optics substrates. Aside from using an LC in its pure form, Polymer Dispersed Liquid Crystals (PDLC) provide a more stable compound while still retaining much of the EO ability. The holographic PDLC system (HPDLC) has been used to fabricate electrically switchable Bragg gratings [27, 28]. Another possible fabrication route is the Polymer-LC-Polymer Slices material (POLICRYPS) which consists of alternating layers of LC and polymer [29]. This choice of LC materials allows for versatility not only in fabrication method but also in the range of devices obtainable.

Beneficial physical properties of LC's include: low absorption in both the visible and near-infrared regions, high birefringence, and large EO effects with low driving voltages. As they have refractive indices from 1.4-1.6, they are suitable for integration with a variety of silica fibers, SiO_2-on-Si substrates, and polymers. Very small amounts of LC are required, hence it is a potentially cost-effective option for a multitude of devices.

LC’s have been used to develop such integrated optical devices as Variable Optical Attenuators (VOA) [30]. VOA’s are used for power equalization in wavelength-division-multiplexed (WDM) transmission systems, where the gain of fiber amplifiers is wavelength dependent. LC’s have also found uses in telecommunications systems that include tunable Fabry-Perot interferometric filters, switches, and spatial light modulators [31–34]. Recently there has been interest in developing distributed feedback lasers using LC’s, in particular cholesteric (chiral) fluorescent dye-doped LC’s [35,36]. In this instance the chiral LC host provides the feedback due to its periodic twisted structure, and the laser dye provides the gain. LC’s have also been used for switchable optical phase modulators, diffraction gratings, and diffractive waveplates utilizing the POLICRYPS structure [37–39].

2.1.4 Combining Liquid Crystals and Bragg Gratings

The key optical integration step in this thesis is the combination of the Bragg grating and LC to produce the tunable gratings described in Chapter 1. This was first demonstrated in the planar geometry by Sparrow [40]. By exposing the buried grating, through etching of the cladding or precision machining, to allow access to the evanescent field of the propagating mode means the grating is now susceptible to changes in the surrounding external medium. In this case the medium is an LC which exhibits electro-optic properties due to its dielectric and optical anisotropy. The changes in the surrounding medium, the LC, are created through application of an external electric field. The optical anisotropy in the LC results in light polarized along the molecular long axes experiencing a higher refractive index than light polarized normal to the molecules. The dielectric anisotropy is such that the long axes will align parallel with an applied field.

Fig. 2.5 demonstrates the concept of a voltage-controlled Bragg grating. In the field-off state (a), the light is polarized normal to the LC molecular orientation. Hence the evanescent field component of the propagating mode experiences the ordinary refractive index of the LC, which is lower than the extraordinary index.

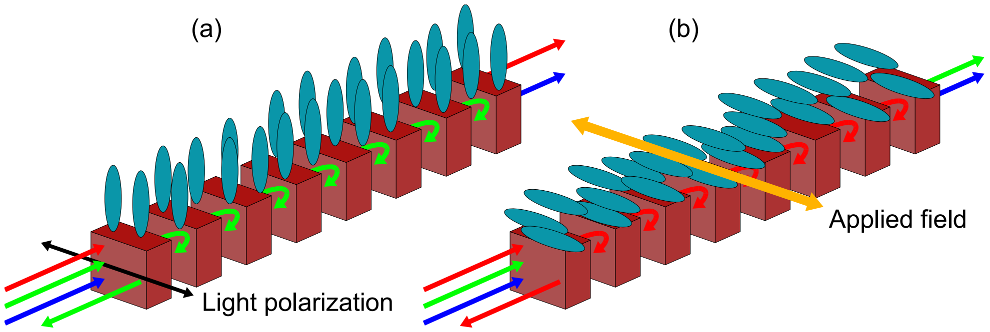

Figure 2.5: Principle of an LC-tunable planar Bragg grating. (a) With no applied field, and light polarized normal to the LC molecular axes, the reflection wavelength is short compared to the field-on state. (b) With an applied field, the LC molecules rotate and align parallel with the field. The reflection wavelength increases.

The resultant Bragg reflection wavelength, given by:

$$\lambda_B = 2n_{eff}\Lambda \tag{2.1}$$

is at its shortest wavelength. In the field-on state, the molecules align parallel with the field. The propagating mode is polarized parallel to the LC molecular axes. Therefore the evanescent field component experiences the higher extraordinary index. From Eqn.(2.1), it can be seen that if n_{eff} increases, as would be the case for (b), the Bragg reflection wavelength increases accordingly. Molecular rotation, and therefore n_{eff}, is a function of the applied field, and the result is a voltage-tunable optical filter.

2.2 Summary

This chapter has given an overview of the motivations and challenges faced by designers of integrated optics components. Some examples of components vital for the work in this thesis have been given, including the planar waveguide structure and the Bragg grating. A historical perspective has been presented while also describing some of the many applications of Bragg gratings. Also described were liquid crystals, which provide a versatile addition to the area of integrated optics. They have the potential to produce devices for modern telecommunications and adaptive optics markets. LC's are used extensively throughout this thesis and provide bountiful opportunities and challenges for optical integration.

The following chapters will provide the theoretical overview required to understand those devices used in this thesis, starting with basic planar waveguide structures and moving on to planar Bragg gratings. The second theoretical overview will explain the physics of LC's, how they behave in applied fields, and explain the defect mechanics in confined LC devices.

References

[1] S. E. Miller. "Integrated Optics: An Introduction". *Bell System Technical Journal*, 48(7):2059–2069, September 1969.

[2] P. K. Tien. "Integrated optics and new wave phenomena in optical waveguides". *Reviews of Modern Physics*, 49(2):361–420, April 1977.

[3] E. M. Conwell. "Integrated optics". *Physics Today*, 29(5):48, May 1976.

[4] R. G. Hunsperger. *Integrated Optics*. Springer New York, New York, NY, 2009.

[5] L. Eldada. "Polymer Integrated Optics: Promise versus Practicality". *Proceedings of SPIE*, 4642:11–22, 2002.

[6] S. T. Kow, Y. Yap, C. H. Pua, W. Y. Chong, A. W. P. Law, F. R. Mahamd Adikan, A. S. M. A. Haseeb, and H. Ahmad. "Selective area rare-earth doping of planar glass samples for monolithic integration of optically passive and active waveguides". *Optik - International Journal for Light and Electron Optics*, 121(8):722–725, April 2010.

[7] M. N. Armenise. "Fabrication techniques of lithium niobate waveguides". *IEE Proceedings J Optoelectronics*, 135(2):85, 1988.

[8] K. Peithmann, M.-R. Zamani-Meymian, M. Haaks, K. Maier, B. Andreas, K. Buse, and H. Modrow. "Fabrication of embedded waveguides in lithium-niobate crystals by radiation damage". *Applied Physics B*, 82(3):419–422, December 2005.

[9] I. P. Kaminow. “Optical Integrated Circuits: A Personal Perspective”. *Journal of Lightwave Technology*, 26(9):994–1004, May 2008.

[10] G. Lifante. *Integrated Photonics: Fundamentals*. Wiley, 2003.

[11] M. R. Poulsen, P. I. Borel, J. Fage-Pedersen, J. Hubner, M. Kristensen, J. H. Povlsen, K. Rottwitt, M. Svalgaard, and W. Svendsen. “Advances in silica-based integrated optics”. *Optical Engineering*, 42(10):2821, 2003.

[12] J. Li and D. Jia. “Novel electro-optical modulator utilizing GeO2-doped silica waveguide”. *Transactions of Tianjin University*, 15(3):222–224, July 2009.

[13] C. Dragone. “Low-loss wavelength routers for WDM optical networks and high-capacity IP routers”. *Journal of Lightwave Technology*, 23(1):66–79, January 2005.

[14] G. D. Emmerson. *Novel Direct UV Written Devices*. PhD thesis, University Of Southampton, 2003.

[15] T. Suhara and H. Nishihara. “Integrated Optics Components and Devices using Periodic Structures”. *IEEE Journal of Quantum Electronics*, 22(6):845–867, June 1986.

[16] C. R. Giles. “Lightwave Applications of Fiber Bragg Gratings”. *Journal of Lightwave Technology*, 15(8):1391–1404, 1997.

[17] S. Wang. “Principles of Distributed Feedback and Distributed Bragg-reflector Lasers”. *IEEE Journal of Quantum Electronics*, 10(4):413–427, April 1974.

[18] A. Yariv and M. Nakamura. “Periodic Structures for Integrated Optics”. *IEEE Journal of Quantum Electronics*, 13(4):233–253, April 1977.

[19] M. Rochette, M. Guy, S. LaRochelle, J. Lauzon, and F. Trepanier. “Gain Equalization of EDFA’s with Bragg Gratings”. *IEEE Photonics Technology Letters*, 11(5):536–538, May 1999.

[20] J. A. R. Williams, I. Bennion, K. Sugden, and N. J. Doran. “Fibre Dispersion Compensation using a Chirped in-fibre Bragg Grating”. *Electronics Letters*, 30(12):985, 1994.

[21] J. Kwon, S. Kim, S. Roh, and B. Lee. "Tunable Dispersion Slope Compensator Using a Chirped Fiber Bragg Grating Tuned by a Fan-Shaped Thin Metallic Heat Channel". *IEEE Photonics Technology Letters*, 18(1):118–120, January 2006.

[22] S. Doucet and S. LaRochelle. "Inter-Channel Residual Dispersion Compensator for 40 Gbit/s WDM Optical Systems". *Optical Society of America*, pages 8–10, 2007.

[23] A. D. Kersey, M. A. Davis, H. J. Patrick, M. LeBlanc, K. P. Koo, C. G. Askins, M. A. Putnam, and E. J. Friebele. "Fiber Grating Sensors". *Journal of Lightwave Technology*, 15(8):1442–1463, 1997.

[24] Y. Rao. "Recent Progress in Applications of In-Fibre Bragg Grating Sensors". *Optics and Lasers in Engineering*, 31(4):297–324, April 1999.

[25] C. Hu and J. R. Whinnery. "Field-realigned nematic-liquid-crystal optical waveguides". *IEEE Journal of Quantum Electronics*, 10(7):556–562, 1974.

[26] J. R. Whinnery, C. Hu, and Y. S. Kwon. "Liquid-crystal waveguides for integrated optics". *IEEE Journal of Quantum Electronics*, QE-13(4):262–267, 1977.

[27] R. L. Sutherland, V. P. Tondiglia, and L. V. Natarajan. "Electrically Switchable Volume Gratings in Polymer-Dispersed Liquid Crystals". *Scanning Electron Microscopy*, 64(9):1074–1076, 1994.

[28] G. P. Crawford. "Electrically Switchable Bragg Gratings". *Optics and Photonics News*, 14(4):54, 2003.

[29] R. Caputo, A. De Luca, L. De Sio, L. Pezzi, G. Strangi, C. Umeton, A. Veltri, R. Asquini, A. DAlessandro, D. Donisi, R. Beccherelli, A. V. Sukhov, and N. V. Tabiryan. "POLICRYPS: A Liquid Crystal Composed Nano/microstructure With a Wide Range of Optical and Electro-optical Applications". *Journal of Optics A: Pure and Applied Optics*, 11(2):024017, February 2009.

[30] K. Hirabayashi, M. Wada, and C. Amano. "Liquid crystal variable optical attenuators integrated on planar lightwave circuits". *IEEE Photonics Technology Letters*, 13(6):609–611, June 2001.

[31] W. A. Crossland, T. V. Clapp, T. D. Wilkinson, I. G. Manolis, A. G. Georgiou, and B. Robertson. "Liquid Crystals in Telecommunications Systems". *Molecular Crystals and Liquid Crystals*, 413(908420906):363–383, 2004.

[32] K. Hirabayashi and T. Kurokawa. "Liquid Crystal Devices for Optical Communication and Information Processing Systems". *Liquid Crystals*, 14(2):307–317, 1993.

[33] D. Donisi, B. Bellini, R. Beccherelli, R. Asquini, G. Gilardi, M. Trotta, and A. D'Alessandro. "A Switchable Liquid-Crystal Optical Channel Waveguide on Silicon". *IEEE Journal of Quantum Electronics*, 46(5):762–768, May 2010.

[34] A. D'Alessandro and R. Asquini. "Liquid Crystal Devices for Photonic Switching Applications: State of the Art and Future Developments". *Molecular Crystals and Liquid Crystals*, 398(1):207–221, June 2003.

[35] P. Palffy-Muhoray, W. Cao, M. Moreira, B. Taheri, and A. Munoz. "Photonics and lasing in liquid crystal materials". *Philosophical transactions. Series A, Mathematical, physical, and engineering sciences*, 364(1847):2747–61, October 2006.

[36] A. Ford, S. Morris, and H. Coles. "Photonics and Lasing in Liquid Crystals". *Materials Today*, 9(7-8):36–42, July 2006.

[37] L. De Sio, N. Tabiryan, R. Caputo, A. Veltri, and C. Umeton. "POLICRYPS Structures as Switchable Optical Phase Modulators". *Optics Express*, 16(11):7619–24, May 2008.

[38] D. Donisi, A. D'Alessandro, R. Asquini, R. Beccherelli, L. Sio, R. Caputo, and C. Umeton. "Realization of an Optical Filter Using POLICRYPS Holographic Gratings on Glass Waveguides". *Molecular Crystals and Liquid Crystals*, 486:31–37, 2008.

[39] R. Asquini, A. D'Alessandro, C. Gizzi, P. Maltese, R. Caputo, C. Umeton, A. Veltri, and A. V. Sukhov. "Optical Characterization at Wavelengths of 632.8nm and 1549nm of Policryps Switchable Diffraction Gratings". *Molecular Crystals and Liquid Crystals*, 398(1):223–233, June 2003.

[40] I. J. G. Sparrow, D. A. Sager, C. B. E. Gawith, P. G. R. Smith, G. D. Emmerson, M. Kaczmarek, and A. Dyadyusha. "25GHz tunability of planar

bragg grating using liquid crystal cladding and electric field". In *Quantum Electronics and Laser Science Conference*, volume 2, pages 963–965, 2005.

Chapter 3

Background

The focus of this project is the fabrication and analysis of integrated optical devices, specifically slab and channel waveguides, and Bragg grating structures. To understand the propagation of light in the optical waveguide structures and birefringent media used in this project, the basic concepts and equations of electrodynamic theory are presented in section 3.1. These equations can be utilized to analyze light confinement and formation of optical modes in waveguides, and also to analyze propagation of light through birefringent media.

Bragg gratings are periodic (or aperiodic) modulations in refractive index. They have several spectral attributes that can be controlled and these will be described in section 3.2. One key property is the peak reflection wavelength, which is governed by the effective refractive index of light propagating in the waveguiding structure. The effective modal index is, in turn, governed by the refractive indices of the surrounding dielectric media, or cladding regions.

If the cladding of a waveguide is removed, such that the channel waveguide containing a Bragg grating is exposed, other materials can be placed in contact with the grating. In this work, for example, a liquid crystal (LC) is applied to the exposed region. The LC can undergo field-induced realignment, and this allows for electrical tuning of the LC birefringence. Changing the orientation of the LC molecules will change the effective refractive index in the direction of propagation and will therefore modify the waveguide effective index. This allows for tuning of the peak Bragg reflection wavelength.

The reorientation mechanisms occuring in LC tunable Bragg grating devices are non-trivial and tuning of these devices is dependent upon achieving appropriate realignment. Exploring the realignment processes can give better insight into the tuning response of these devices and may allow new methods to allow control of tuning response. Chapter 4 discusses LC properties and how these govern their optical properties.

3.1 Maxwell's Equations

Before analyzing specific optical structures such as planar and channel waveguides and Bragg grating structures, a basic description of light propagation in optical media will be given. This analysis begins with Maxwell's equations, which are then adapted for each individual case. Maxwell's equations are the set of four fundamental equations governing electromagnetism. The differential form of these equations is:

$$\begin{aligned} &\text{(i)} \quad \nabla \cdot \mathbf{D} = \rho_f, \quad &&\text{(iii)} \quad \nabla \times \mathbf{E} = -\frac{\partial \mathbf{B}}{\partial t} \\ &\text{(ii)} \quad \nabla \cdot \mathbf{B} = 0, \quad &&\text{(iv)} \quad \nabla \times \mathbf{H} = \mathbf{j}_f + \frac{\partial \mathbf{D}}{\partial t} \end{aligned} \tag{3.1}$$

These equations interrelate the four vector quantities: **E**, the electric field, **D**, the electric displacement field, **B**, the magnetic flux density and **H**, the magnetic field. They also include ρ_f, the free charge density and $\mathbf{j}_f$, the free current density. However, the waveguides used in this work are assumed to have no free charge ($\rho_f = 0$), and no free current ($\mathbf{j}_f = 0$) which reduces Eqn.(3.1) to:

$$\begin{aligned} &\text{(i)} \quad \nabla \cdot \mathbf{D} = 0, \quad &&\text{(iii)} \quad \nabla \times \mathbf{E} = -\frac{\partial \mathbf{B}}{\partial t} \\ &\text{(ii)} \quad \nabla \cdot \mathbf{B} = 0, \quad &&\text{(iv)} \quad \nabla \times \mathbf{H} = \frac{\partial \mathbf{D}}{\partial t} \end{aligned} \tag{3.2}$$

Using the relations $\mathbf{D} = \epsilon \mathbf{E}$, and $\mathbf{B} = \mu \mathbf{H}$ converts Eqn. 3.2 into:

$$\begin{aligned} &\text{(i)} \quad \nabla \cdot \mathbf{E} = 0, \quad &&\text{(iii)} \quad \nabla \times \mathbf{E} = -\frac{\partial \mathbf{B}}{\partial t} \\ &\text{(ii)} \quad \nabla \cdot \mathbf{B} = 0, \quad &&\text{(iv)} \quad \nabla \times \mathbf{B} = \mu\epsilon \frac{\partial \mathbf{E}}{\partial t} \end{aligned} \tag{3.3}$$

The two vector quantities, **E** and **B**, can be decoupled by applying the curl to both sides:

$$\nabla \times (\nabla \times \mathbf{E}) = -\frac{\partial}{\partial t}(\nabla \times \mathbf{B}) = -\mu\epsilon\frac{\partial^2 \mathbf{E}}{\partial t^2}$$
$$\nabla \times (\nabla \times \mathbf{B}) = \mu\epsilon\frac{\partial}{\partial t}(\nabla \times \mathbf{E}) = -\mu\epsilon\frac{\partial^2 \mathbf{B}}{\partial t^2}$$

Using the vector identity $\nabla \times (\nabla \times \mathbf{V}) = \nabla(\nabla \cdot \mathbf{V}) - \nabla^2\mathbf{V}$ results in:

$$\nabla^2\mathbf{E} = \frac{1}{c^2}\frac{\partial^2 \mathbf{E}}{\partial^2 t}, \quad \nabla^2\mathbf{B} = \frac{1}{c^2}\frac{\partial^2 \mathbf{B}}{\partial^2 t} \tag{3.4}$$

since $\nabla \cdot \mathbf{E} = 0$ and $\nabla \cdot \mathbf{B} = 0$. These are the three dimensional wave equations governing the propagation of electromagnetic radiation in matter.

The solutions to Maxwell's equations for monochromatic light take the form of sinusoidal waves. An infinite plane wave propagating in the z-direction has solutions of the form:

$$f(z,t) = \mathrm{A}\cos(kz - \omega t + \phi) \tag{3.5}$$

where A is the amplitude, k is the wavenumber, and ω is the angular frequency. The argument of the cosine is the phase and ϕ, an arbitrary phase constant. Written in complex exponential notation, Eqn.(3.5) can be written as:

$$f(z,t) = \Re e[\mathrm{A}\,\mathrm{e}^{i(kz-\omega t+\phi)}] \tag{3.6}$$

where the real part of the complex function has been extracted.

3.1.1 Polarization

The general solution of Maxwell's equations (3.4) posed in Eqn.(3.6) can be specified in terms of the electric field vector:

$$\mathbf{E} = Ae^{i(\mathbf{k}.\mathbf{r}-\omega t+\phi)} \tag{3.7}$$

where **E** is the electric field vector, and A is the amplitude. By suitable use of the Cartesian coordinate system, the propagation direction can be defined as parallel to the z-axis. It then follows that the electric field can be written in terms of two components orthogonal to the z-axis:

$$E_x = A_x e^{i(kz-\omega t+\phi_x)} \tag{3.8}$$

$$E_y = A_y e^{i(kz-\omega t+\phi_y)} \tag{3.9}$$

Now only two parameters are needed to specify the polarization state of the light beam: the relative amplitude A_y/A_x and the relative phase difference $\phi = \phi_y - \phi_x$. For the special case where $\phi = 0$ or π, the electric field oscillates in a fixed direction perpendicular to the z-axis, otherwise known as linearly polarized light. Here, the relative amplitudes of A_x and A_y give the angle of the polarization. The second special case is where $\phi = \pi/2$ and $A_x = A_y$, resulting in circularly polarized light. For all other cases, the polarization state is elliptical. As will be seen in later chapters, ϕ can be a function of position.

3.1.2 Anisotropic Media

If the permittivity is direction dependent, the material is said to be anisotropic. As such, **D** also becomes direction dependent. The electric displacement field can be written in terms of vacuum and relative permittivities as $\epsilon = \epsilon_0\epsilon_r$. This implies:

$$\mathbf{D} = \epsilon_0\epsilon_r\mathbf{E} \tag{3.10}$$

In anisotropic materials, the permittivity is a function of direction and becomes a tensor:

$$\bar{\bar{\epsilon}}_r = \begin{bmatrix} \epsilon_{xx} & \epsilon_{xy} & \epsilon_{xz} \\ \epsilon_{yx} & \epsilon_{yy} & \epsilon_{yz} \\ \epsilon_{zx} & \epsilon_{zy} & \epsilon_{zz} \end{bmatrix} \tag{3.11}$$

Assuming a non-absorbing and non-optically active material, $\epsilon_{ij} = \epsilon_{ji}$. Now, as the tensor is symmetric, it can be diagonalized by choosing suitable axes. If the x, y, z axes are the principal axes, only diagonal components of the tensor are non-zero, thus:

$$\bar{\bar{\epsilon}}_r = \begin{bmatrix} \epsilon_{xx} & 0 & 0 \\ 0 & \epsilon_{yy} & 0 \\ 0 & 0 & \epsilon_{zz} \end{bmatrix} \tag{3.12}$$

In the case of uniaxial crystals the tensor in Eqn.(3.12) can be simplified further. If the crystal's principal axis is parallel to the z-direction, then $\epsilon_{xx} = \epsilon_{yy}$, and Eqn.(3.12) reduces to:

$$\bar{\bar{\epsilon}}_r = \begin{bmatrix} \epsilon_{x} & 0 & 0 \\ 0 & \epsilon_{x} & 0 \\ 0 & 0 & \epsilon_{z} \end{bmatrix} \tag{3.13}$$

Eqn.(3.13) can be expressed in terms of refractive indices if $n = \sqrt{\epsilon_r}$ such that:

$$\bar{\bar{\epsilon}}_r = \begin{bmatrix} {n_o}^2 & 0 & 0 \\ 0 & {n_o}^2 & 0 \\ 0 & 0 & {n_e}^2 \end{bmatrix} \tag{3.14}$$

In this scenario, n_e is the refractive index experienced by the component of light polarized along the z-axis, otherwise known as the *extraordinary* axis. All linear polarizations orthogonal to the z-axis will experience refractive index n_o, thus the *ordinary* axes can be defined as the x,y axes. Thus linearly polarized light can be decomposed into two components parallel to the ordinary and extraordinary axes.

3.1.3 Waveplates

Uniaxial crystalline materials produce phase delay between orthogonal polarization states for light propagating perpendicular to the optical axis. Attributes such as birefringence and material thickness can be chosen such that the phase delay takes specific values. In these cases, the crystal can act as a waveplate whose effect is to modify the output polarization by a fixed amount. Uniaxial liquid crystalline materials such as nematic phase LC's can be used as waveplates. With suitable device parameters, nematic LC's can act as variable waveplates with electrically controllable birefringence. As such, the principles of waveplates will be discussed and subsequently their relevance to the nematic LC cells used in this project.

The two orthogonal polarization components parallel to the ordinary and extraordinary axes will travel through the uniaxial birefringent material with differing phase velocities. These two components are in phase as they approach the crystal, but their relative phase varies during propagation through the medium. The phase delay between the two orthogonal polarization components is utilized in devices such as waveplates. A birefrigent material of specific thickness and orientation can create differing optical path lengths for the orthogonal polarization states. The relative optical path length difference (OPD) through a uniaxial crystal for light propagating perpendicular to the optical axis is given by:

$$\Omega = d(|n_e - n_o|) \tag{3.15}$$

and the relative phase delay by:

$$\Delta\phi = \frac{2\pi}{\lambda}d(|n_e - n_o|) = \frac{2\pi}{\lambda}\Omega \tag{3.16}$$

The relative phase delay is dependent upon both the OPD and the wavelength of light, and the OPD is a function of the birefringence. The recombination of the two polarization components upon leaving the birefringent medium with a relative phase difference governs the resultant polarization state.

Waveplates can be described using vector analysis. Starting with the principal axes x,y,z, the incident electric field vector of the polarized light can be resolved into components parallel and perpendicular to the optical axis. For input light propagating along the z axis and polarized at an angle ϕ with respect to the x-axis, the orthogonal components of the electric field $\mathbf{E}_{in}$ that determine the state of polarization can be represented as:

$$\mathbf{E}(z) = \hat{\mathbf{i}}E_x e^{i(k_x z - \omega t)} + \hat{\mathbf{j}}E_y e^{i(k_y z - \omega t)} \tag{3.17}$$

where $k_x = 2\pi n_e/\lambda$, $k_y = 2\pi n_o/\lambda$, $E_x = E_0\cos\phi$ and $E_y = E_0\sin\phi$. Eqn.(3.17) can be written as:

$$\mathbf{E}(z) = \left[\hat{\mathbf{i}}E_x + \left(\hat{\mathbf{j}}E_y e^{i(k_y z - \omega t)} e^{-i(k_x z - \omega t)}\right)\right] e^{i(k_x z - \omega t)} \tag{3.18}$$

and so:

$$\mathbf{E}(z) = \left[\hat{\mathbf{i}}E_x + \hat{\mathbf{j}}E_y e^{i(k_y - k_x)z}\right] e^{i(k_x z - \omega t)} \tag{3.19}$$

Substituting for k_x and k_y gives:

$$\mathbf{E}(z) = \left[\hat{\mathbf{i}}E_x + \hat{\mathbf{j}}E_y e^{i2\pi(n_o - n_e)z/\lambda}\right] e^{i(k_x z - \omega t)} \tag{3.20}$$

Now if $\phi = 45°$, $E_x = E_y$ and so:

$$\mathbf{E}(z) = \frac{E_0}{\sqrt{2}}\left[\hat{\mathbf{i}} + \hat{\mathbf{j}}e^{i2\pi(n_o - n_e)z/\lambda}\right] e^{i(k_x z - \omega t)} \tag{3.21}$$

Eqn.(3.21) describes the resultant polarization state of light that has propagated through a uniaxial crystal with birefringence $|n_e - n_o|$ and thickness z. Taking $\alpha = e^{i2\pi(n_o - n_e)z/\lambda}$ produces:

$$\mathbf{E}(z) = \frac{E_0}{\sqrt{2}}\left[\hat{\mathbf{i}} + \hat{\mathbf{j}}\alpha\right] e^{i(k_x z - \omega t)} \tag{3.22}$$

So if α = 1, the polarization state remains the same. However, if α = -1, the birefringent material acts as a half wave plate, rotating the plane of polarization by 2ϕ. In this instance:

$$\begin{aligned} \tfrac{2\pi}{\lambda}z|n_o - n_e| &= \pi, 3\pi, 5\pi, ... \\ \tfrac{2z}{\lambda}|n_o - n_e| &= 2m + 1 \end{aligned} \tag{3.23}$$

where m is an integer, and λ is the wavelength. If α = $+i$ or $-i$ the birefringent crystal acts as a quarter wave plate and the resultant polarization state is right circular and left circular polarized respectively. Therefore:

$$RCP \Rightarrow \frac{2\pi}{\lambda}z|n_o - n_e| = \pi/2, 5\pi/2, 9\pi/2, ... \tag{3.24}$$

$$\Rightarrow \frac{2z}{\lambda}|n_o - n_e| = 2m + \frac{1}{2} \tag{3.25}$$

$$LCP \Rightarrow \frac{2\pi}{\lambda}z|n_o - n_e| = 3\pi/2, 7\pi/2, 11\pi/2, ... \tag{3.26}$$

$$\Rightarrow \frac{2z}{\lambda}|n_o - n_e| = 2m + \frac{3}{2} \tag{3.27}$$

where RCP and LCP indicate right circularly polarized and left circularly polarized light respectively.

It has been shown that a waveplate can be used to transform polarization states. The discussion in Chapter 4 will focus on the properties of liquid crystal cells and will show how they are locally equivalent to waveplates when viewed through crossed polarizers in transmission microscopy experiments.

3.2 Waveguides and Bragg Gratings

The field of integrated optics relies on the principle of controlling or guiding the path of light through optical circuitry. The most important component is the optical waveguide. An optical waveguide is a structure that confines and directs wave propagation. In this project, electromagnetic waves in the short wavelength infrared region will be guided by a suitable dielectric medium, namely doped silica. Bragg gratings are periodic structures integrated into optical waveguides and are an invaluable tool in the fields of telecommunications systems and sensing. They provide functions such as reflecting or filtering certain wavelengths, mode coupling, and dispersion compensation depending on the design parameters.

This chapter provides a description of the properties of waveguides and Bragg gratings, starting with the simple planar slab waveguide and then moves on to the more complex channel waveguides. Before describing guided waves using modal analysis, it is helpful to include a ray-optic description of the phenomena that permit guided waves. The principle of Bragg gratings will then be described.

3.2.1 Planar Optical Interfaces

Light incident upon a planar boundary, such as those in waveguides, will experience the phenomena of reflection and refraction. The interaction of light with a planar boundary can be succinctly described by Snell's law, which states that the angle of reflection and refraction of incident light are related by:

$$n_1 \sin\theta_1 = n_2 \sin\theta_2 \tag{3.28}$$

where θ_1 and θ_2 are the angles of incidence and refraction respectively, n_1 and n_2 are the refractive indices of the two media either side of the planar interface as shown in Fig. 3.1. If $n_1 > n_2$, and the angle of refraction is set to be $\pi/2$, the angle of incidence is given by $\theta_1 = \sin^{-1}(n_2/n_1)$ and at this angle the refracted wave travels along the interface between the two media. The value of θ_1 at which this occurs is known as the critical angle. Any incident angle greater than this results in no refraction, therefore no transmission and all the light is reflected from the surface by the phenomena known as total internal reflection (TIR). Conversely, if

$n_1 < n_2$ then θ_r can never equal $\pi/2$ and TIR is not possible.

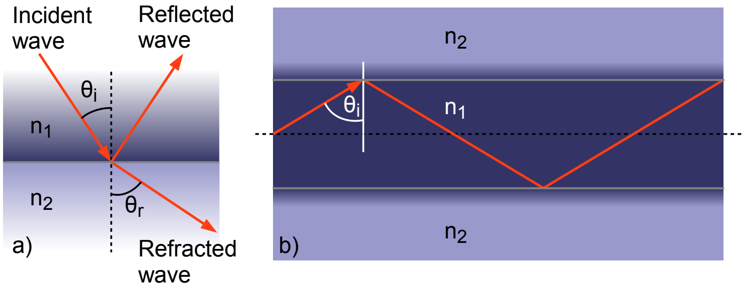

Figure 3.1: a) Reflection and refraction at a planar interface, b) Light guided by TIR in a planar slab waveguide

Although the ray path of light is confined within the core region, there is some component of the optical power that resides outside the core. This is known as the evanescent field and it is part of the guided light. In this situation the ray optic description of guided light becomes unsuitable and therefore propagation must be analysed in terms of optical modes.

3.2.2 The Planar Slab Waveguide

The structure shown in Fig. 3.1 was a planar slab waveguide. In this situation, the principle of guided waves was explained with a ray-optic description. A more mathematically rigorous description uses modal analysis beginning from Maxwell's equations. The derivation of the wave equations from Maxwell's equations was given earlier in section 3.1. However, this derivation assumed an isotropic medium with $\epsilon_r = 1$. Maxwell's equations will now be revisited in terms of an inhomogenous medium. The treatment of the planar slab waveguide in this section is based on the presentation by Ghatak and Thyagarajan [1].

Maxwell's equations for an isotropic, linear, nonconducting and nonmagnetic medium take the form:

$$\nabla \times \mathbf{E} = -\mu_0 \frac{\partial \mathbf{H}}{\partial t} \tag{3.29}$$

$$\nabla \times \mathbf{H} = \epsilon_0 n^2 \frac{\partial \mathbf{E}}{\partial t} \tag{3.30}$$

$$\nabla \cdot \mathbf{D} = \epsilon_0 \nabla \cdot (n^2 \mathbf{E}) = 0 \tag{3.31}$$

$$\nabla \cdot \mathbf{H} = 0 \tag{3.32}$$

where **D** is the electric displacement vector, **E** is the electric field vector and **H** is the magnetic field vector. μ_0 is the permeability of free space, ϵ_0 the permittivity of free space, and n the refractive index of the guiding medium. To decouple equations (3.29) and (3.30), first take the curl of (3.29):

$$\nabla \times (\nabla \times \mathbf{E}) = -\mu_0 \frac{\partial}{\partial t}(\nabla \times \mathbf{H}) \tag{3.33}$$

Now using the vector identity $\nabla \times (\nabla \times \mathbf{V}) = \nabla(\nabla \cdot \mathbf{V}) - \nabla^2 \mathbf{V}$ and Eqn.(3.30) gives:

$$\nabla(\nabla \cdot \mathbf{E}) - \nabla^2 \mathbf{E} = -\epsilon_0 \mu_0 n^2 \frac{\partial^2 \mathbf{E}}{\partial t^2} \tag{3.34}$$

Eqn.(3.31) can be written as:

$$\epsilon_0 \nabla \cdot (n^2 \mathbf{E}) = \epsilon_0 [\nabla n^2 \cdot \mathbf{E} + n^2 \nabla \cdot \mathbf{E}] \tag{3.35}$$

therefore

$$\nabla \cdot \mathbf{E} = -\frac{1}{n^2} \nabla n^2 \cdot \mathbf{E} \tag{3.36}$$

which can be inserted into Eqn.(3.34) to obtain:

$$\nabla^2 \mathbf{E} + \nabla \left(\frac{1}{n^2} \nabla n^2 \cdot \mathbf{E} \right) - \epsilon_0 \mu_0 n^2 \frac{\partial^2 \mathbf{E}}{\partial t^2} = 0 \tag{3.37}$$

This is the wave equation for the electric field component of light propagating through a medium with refractive index n. In a slab waveguide, each layer is uniform. Therefore, for light propagating in either the core or the cladding, the second term of Eqn.(3.37) vanishes leaving:

$$\nabla^2 \mathbf{E} - \epsilon_0 \mu_0 n^2 \frac{\partial^2 \mathbf{E}}{\partial t^2} = 0 \tag{3.38}$$

which is identical to Eqn.(3.4) except for the inclusion of the refractive index term. Similarly, taking the curl of Eqn.(3.30) and employing equations (3.29) and (3.30) results in the equivalent wave equation for magnetic fields:

$$\nabla^2 \mathbf{H} - \epsilon_0 \mu_0 n^2 \frac{\partial^2 \mathbf{H}}{\partial t^2} = 0 \tag{3.39}$$

If the slab waveguide has a refractive index that is invariant in two directions y,z and only varies in the x direction, as depicted in Fig. 3.2, the solutions to the wave equations (3.38) and (3.39) take the form:

$$\mathrm{E}_j = \mathcal{E}_j(x) e^{i(\beta z - \omega t)} \tag{3.40}$$

$$\mathrm{H}_j = \mathcal{H}_j(x) e^{i(\beta z - \omega t)} \tag{3.41}$$

for $j = x, y, z$. The symbol β represents the propagation constant of the mode and ω the angular frequency. Applying these solutions to equations (3.29) and (3.30) results in two independent sets of equations. These produce two similar solutions for electric and magnetic fields that can propagate through the high index layer of Fig. 3.2. The solutions for the propagating radiation are known as eigenmodes (or modes) of the system as they are transverse field distibutions $\mathcal{E}_j, \mathcal{H}_j$, that are supported by the system which remain invariant during propagation.

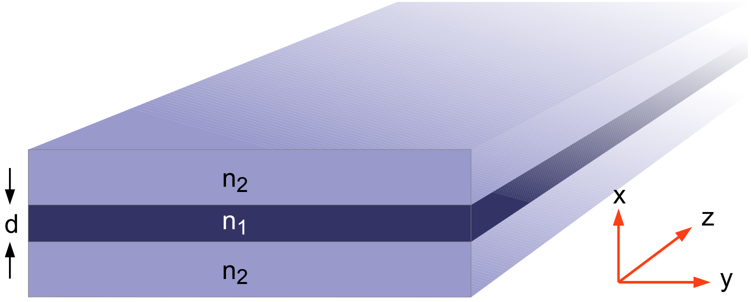

Figure 3.2: A planar slab waveguide with $n_1 > n_2$

Substituting the solutions (3.40) and (3.41) back into equations (3.29) and (3.30) and separating the x,y,z components results in two sets of equations. The first set contains only non-vanishing values of $\mathcal{E}_y, \mathcal{H}_x$ and $\mathcal{H}_z$. The second set contains only non-vanishing values of $\mathcal{E}_x, \mathcal{E}_z$ and $\mathcal{H}_y$. These are known as TE (transverse electric) and TM (transverse magnetic) modes respectively. It can be seen that TE modes have their electric field component oscillating exclusively in the y-plane, and TM modes have their magnetic field oscillating exclusively in the y-plane.

By considering the first set of equations for the TE mode, the electric field is described by:

$$\frac{d^2\mathcal{E}_y}{dx^2} + [k_0^2 n^2(x) - \beta^2]\mathcal{E}_y = 0 \tag{3.42}$$

where k_0 is the free space wavenumber given by $\omega(\mu_0\epsilon_0)^{1/2} = 2\pi/\lambda$. As n is a function of x, Eqn.(3.42) can be split into two equations for the specific case shown in Fig. 3.2. In this scenario, the index profile is given by:

$$n(x) = \begin{cases} n_1; & |x| < d/2 \\ n_2; & |x| > d/2 \end{cases} \tag{3.43}$$

where $n_1 > n_2$. By applying appropriate boundary conditions which state both tangential field components $\mathcal{E}_y$ and $\mathcal{H}_z$ are continuous at the interfaces $x = \pm d/2$

(see Fig. 3.2), Eqn.(3.42) can be defined for the two regions in Eqn.(3.43). This produces:

$$\frac{d^2\mathcal{E}_y}{dx^2} + [k_0^2n_1^2 - \beta^2]\mathcal{E}_y = 0 \tag{3.44}$$

for the core layer, and:

$$\frac{d^2\mathcal{E}_y}{dx^2} + [k_0^2n_2^2 - \beta^2]\mathcal{E}_y = 0 \tag{3.45}$$

for the cladding layers. The guided modes of the system are those that are mostly confined to the core region of the slab waveguide, and their fields decay in the cladding. This implies:

$$\beta^2 > k_0^2n_2^2 \tag{3.46}$$

and also:

$$\beta^2 < k_0^2n_1^2 \tag{3.47}$$

to satisfy the boundary conditions that the field cannot be discontinuous at the interfaces $x = \pm d/2$. Therefore, for guided modes

$$n_2^2 < \frac{\beta^2}{k_0^2} < n_1^2 \tag{3.48}$$

showing that for guided modes the refractive index of the core layer must be higher than that of the cladding layers. This analogous to the condition required for TIR as in the ray optic description given earlier. If $k_0^2 < \beta^2 < k_0^2n_2^2$, the modes are supported in the cladding rather than the core and are known as cladding modes. For $\beta^2 < k_0^2$ the solutions are oscillatory for $|x| > d/2$ and they are known as radiation modes, the power leaks away from the core and is not guided. The three different modes are shown in Fig. 3.3.

Equations (3.44) and (3.45) can be written in the form:

$$\frac{d^2\mathcal{E}_y}{dx^2} + \kappa^2\mathcal{E}_y = 0; \quad |x| < d/2 \tag{3.49}$$

$$\frac{d^2\mathcal{E}_y}{dx^2} - \gamma^2\mathcal{E}_y = 0; \quad |x| > d/2 \tag{3.50}$$

where $\kappa^2 = k_0^2n_1^2 - \beta^2$ and $\gamma^2 = k_0^2n_2^2 - \beta^2$. Now, by applying suitable boundary conditions such that $\mathcal{E}_y$ and $d\mathcal{E}_y/dx$ are continuous at $x = \pm d/2$, and remembering that the slab waveguide under consideration is symmetrical about $x = 0$ implies

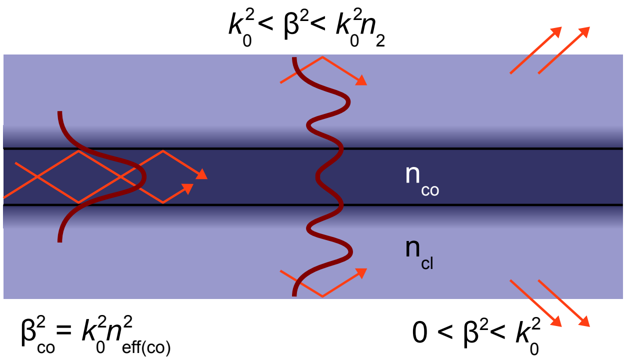

Figure 3.3: The three types of mode supported by a channel waveguide or fiber: (*left*) the fundamental mode guided in core, (*middle*) a cladding mode, (*right*) a non-guided radiation mode

the field is either symmetric or antisymmetric about $x = 0$. The symmetric solutions are given by:

$$\mathcal{E}_y(x) = \begin{cases} Acos(\kappa x); & |x| < -d/2 \\ Ce^{-\gamma x}; & |x| > d/2 \end{cases} \tag{3.51}$$

and the antisymmetric solutions by:

$$\mathcal{E}_y(x) = \begin{cases} Bsin(\kappa x); & |x| < -d/2 \\ \dfrac{x}{|x|}De^{-\gamma|x|}; & |x| > d/2 \end{cases} \tag{3.52}$$

where A, B, C and D are constants. Continuity of the fields at the boundaries implies:

$$Acos\left(\frac{\kappa d}{2}\right) = Ce^{-\gamma d/2} \tag{3.53}$$

and

$$-\kappa Asin\left(\frac{\kappa d}{2}\right) = -\gamma Ce^{-\gamma d/2} \tag{3.54}$$

Dividing Eqn.(3.54) by Eqn.(3.53) gives:

$$\xi tan\xi = \frac{\gamma d}{2} \tag{3.55}$$

where

$$\xi = \frac{\kappa d}{2} = \sqrt{(k_0^2 n_1^2 - \beta^2)}\frac{d}{2} \tag{3.56}$$

Also:

$$\frac{\gamma d}{2} = \sqrt{\left(\frac{1}{4}V^2 - \xi^2\right)} \tag{3.57}$$

where

$$V = k_0 d\sqrt{n_1^2 - n_2^2} \tag{3.58}$$

which is the dimensionless waveguide parameter. The V number determines the guidance behaviour of the waveguide. Eqn.(3.55) can now be written as:

$$\xi tan\xi = \sqrt{\left(\frac{1}{4}V^2 - \xi^2\right)}; \quad \textbf{symmetric modes} \tag{3.59}$$

and similarly:

$$-\xi cot\xi = \sqrt{\left(\frac{1}{4}V^2 - \xi^2\right)}; \quad \textbf{antisymmetric modes} \tag{3.60}$$

By inspection it can be seen that:

$$\left(\frac{V}{2}\right)^2 = \eta^2 + \xi^2 \tag{3.61}$$

where $\eta = \xi tan\xi$ or $-\xi cot\xi$. Equations (3.59), (3.60) and (3.61) can be plotted together to produce a graphical representation of the propagation constants and allowed modes of the system. In Fig. 3.4 are plots of the left hand side of both Eqn.(3.59) and (3.60), with the right hand side plotted in red and purple for two different values of V. It can be concluded that the points where these circular lines intersect with the tan and cot functions are guided modes of the waveguide. Given as examples are curves for $V = 4$ (red) and $V = 10$ (purple), which

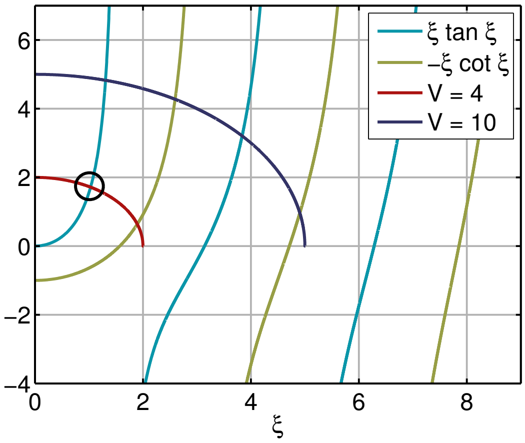

Figure 3.4: Graphical solutions of the mode equations for a symmetric planar slab waveguide. Blue lines represent symmetric modes, olive lines represent antisymmetric modes. Two solutions of Eqn.(3.61) for positive values of ξ are also shown.

are shown to support two (one symmetric, one antisymmetric) and four modes respectively. Shown in Fig. 3.5 are examples of radial intensity distributions of some low-order modes in a step-index waveguide for V = 8. It can be seen that for higher order modes, there is a greater fraction of power in the cladding.

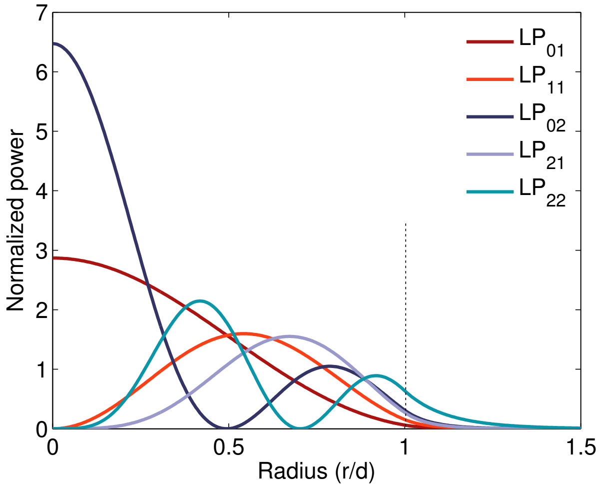

Figure 3.5: Radial intensity distributions for a step-index waveguide for V = 8. The plots are normalized to the same total modal power.

Generally, the larger the V number, the more mores are supported in the waveguide. V depends on wavelength, core thickness, and relative refractive index difference. Therefore, a thicker core or a larger index difference will permit more guided modes in a planar slab waveguide. Single mode operation occurs for $0 < V < \pi$, where the core will only support the first symmetric mode as circled in Fig. 3.4. The waveguides used in this project are designed for single-mode use.

3.2.3 Channel Waveguides

The planar slab waveguide described in section 3.2.2 only had confinement in the x-direction. Therefore the y and z directions were equivalent. By adding an extra degree of confinement so that the waveguide is invariant only along z, the structure becomes a channel waveguide, as displayed in Fig. 3.6 where the guiding channel is the darkened region with index n_1. As before, guided modes must have an effective index below that of the core. This implies that the surrounding dielectric medium must have $n_{clad} < n_1$ but otherwise the cladding can have any index structure.

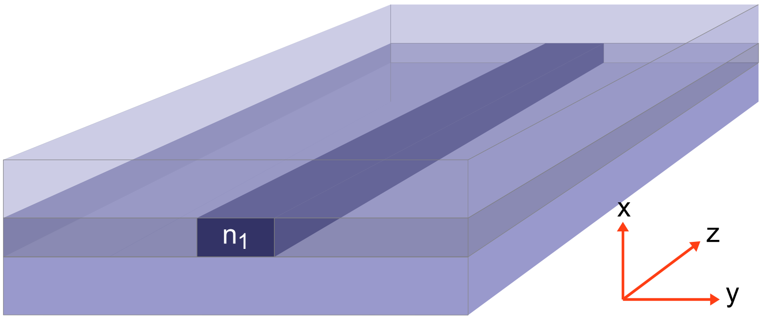

Figure 3.6: A rectangular channel waveguide

The system is a generalized case and simplifying assumptions must be made to allow analytical solutions to be formed. The boundary conditions for channel waveguides are non-trivial and as such solving the wave equation in such a geometry becomes extremely complicated. Hence the problem is often simplified by using approximations or numerical analysis. For example, taking a cross-section of the waveguide in the $x-y$ plane, the index structure can be defined as in Fig. 3.7. This system is used in the Marcatili approach [2] for finding the effective index of guided modes in the core. The main assumption in this method is that, for a well guided mode, the electric field is mostly confined to the core and the field decays exponentially in regions 2,3,4,5. The field extends even less into the shaded regions and these can therefore be neglected. As such, this method only requires the field to be continuous over each of the four boundaries bordering the core region. The index profile can be approximated as a combination of two slab waveguides, one along the x-direction (2-1-4), and another along the y-direction (5-1-3). Subsequently, propagation constants can be determined for the different regions to find the waveguide effective index.

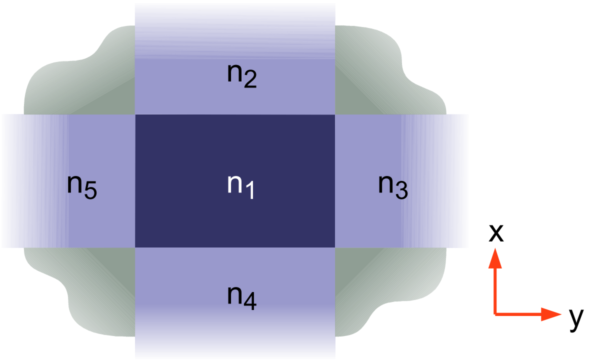

Figure 3.7: The Marcatili approach to channel waveguide refractive index structure

The modes in a channel waveguide are not pure TE or TM modes, as these are not supported. The modes that are supported are often called *hybrid modes* which are equivalent to TEM modes polarized along the x and y directions. They can therefore be classified in two groups: E^x_{pq} and E^y_{pq}, with p and q indicating the number of nodes in the field distributions in the x and y directions respectively. E^x_{pq} modes have transverse field components E_x and H_y, resembling TM modes in a slab waveguide. E^y_{pq} modes have transverse field components E_y and H_x, and resemble TE modes in a slab waveguide.

The limitations of this simplified model are more apparent with small V numbers. The field distribution of the guided modes will extend further into the cladding regions and as such the previously ignored shaded areas of Fig. 3.7 become more influential. The effect of V number on modal power distribution is shown in Fig. 3.8 where the percentage of power in the core is 99, 98, 95 and 74$\%$ for V = 8,6,4 and 2 respectively. Also, the model uses a step-index profile which is not an accurate representation of the index profile produced in UV-written waveguide structures. Nevertheless, it provides a useful insight into the behaviour of channel waveguide structures.

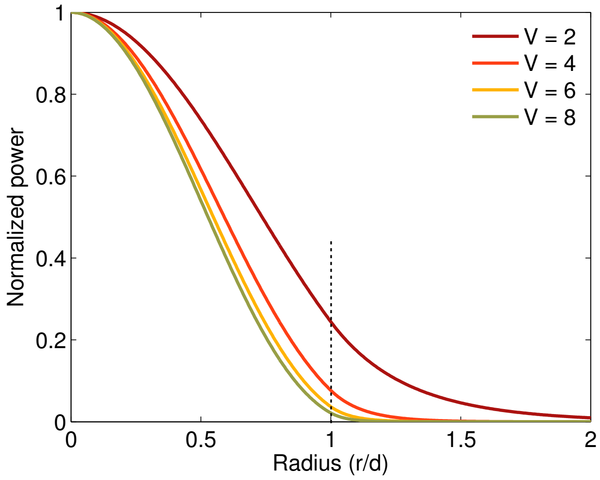

Figure 3.8: The effect of V number on modal power distribution.

3.2.3.1 Computational Analysis

Occasionally for complex channel waveguide structures it is helpful to utilize computational methods to analyze a waveguide's parameters. Computational analysis is a convenient method to obtain transverse modal patterns and effective refractive index values. Therefore some of the waveguides fabricated in this thesis are analyzed with the waveguide mode solver FIMMWAVE™. This is a fully vectorial solver based on the Film Mode Matching (FMM) technique [3].

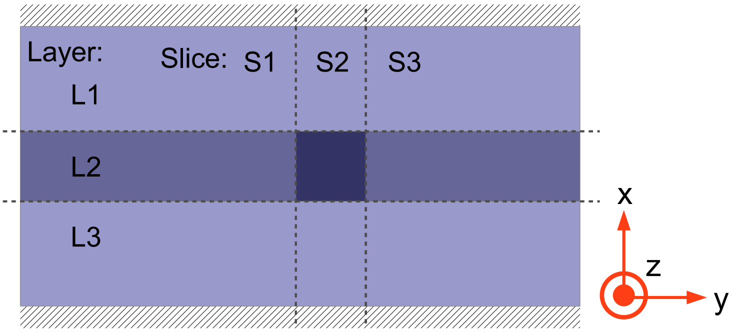

Figure 3.9: Film Mode Matching for a buried channel waveguide with a high index central layer, two cladding layers, and a guiding core

FMM involves dividing the waveguide cross-section into "slices" denoted S1, S2, S3 as shown in Fig. 3.9. Within each slice there is no refractive index variation in the y-direction. Each slice is formed by a stack of layers denoted L1, L2, L3. The waveguide can be bound by perfectly conducting electric or magnetic "walls" placed sufficiently far from the waveguide core that the field components are negligible. The walls (hatched regions in Fig. 3.9) absorb any remaining modal power in the modes of the slices, avoiding problems with power reflecting from boundaries. FMM matches the field distributions at the slice interfaces for TE and TM modes by adjusting the modal amplitudes in each slice. Every 1-dimensional mode in each slice must produce a field profile that everywhere obeys Maxwell's equations.

The FIMMWAVE FMM solver takes the boundary conditions at the vertical sides of the waveguide analysis area and propagates a trial solution towards the centre. The propagation constant (β) is also scanned over a range of values until a solution is found which satisfies all boundary conditions. The two trial solutions are propagated towards the centre and meet at a line called the "mode matching interface". The field distributions must be continuous over this interface for a solution to be accepted.

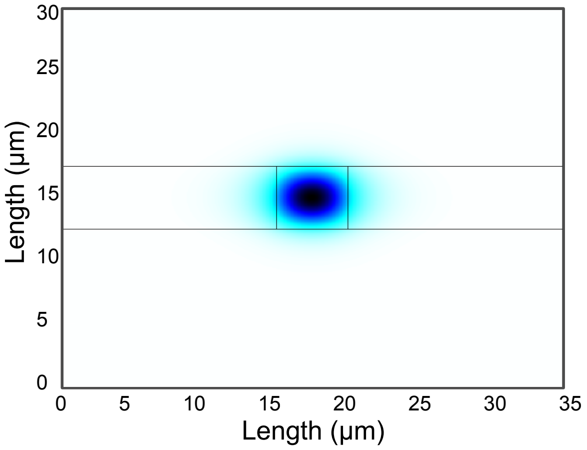

Figure 3.10: An example of FIMMWAVE calculating a modal field distribution. Shown is the fundamental TE mode for a substrate with refractive index profile similar to Fig. 3.9

3.3 Bragg Gratings

Planar Bragg gratings are periodic perturbations of the effective refractive index of an optical waveguide structure. This effective index modulation can be produced by variation of the physical dimensions of the waveguide, or by varying the refractive index. In locations where the refractive index changes, a percentage of the propagating light is reflected. If a waveguiding structure has many such interfaces, forward propagating light will be periodically reflected from each interface. The relative phase of all such reflections will be dependent on the period of refractive index modulation and the wavelength of the propagating light. For one particular wavelength, known as the Bragg wavelength, all of these reflections will be in phase and constructively interfere to create a counterpropagating light wave, whose wavelength is centered about the Bragg wavelength. Reflections at other wavelengths do not add constructively as they do not reflect in phase, and therefore these wavelengths are transmitted by the grating structure.

Much of the literature available in this area involves fiber Bragg gratings (FBG) and their properties. Thorough reviews of Bragg grating properties are available in [4, 5] and [6]. However, aside from the obvious difference in geometry, planar Bragg gratings have many similarities to FBG's and can be analyzed as such. FBG's written into optical fiber are often imposed on top of a waveguiding structure, whereas the UV writing techniques employed in this project allow channel waveguides and planar Bragg gratings to be defined simultaneously, starting effectively from a slab waveguide substrate. As fiber gratings are defined into a pre-existing waveguide, the resultant refractive index modifications are additive only. Direct Grating Writing (DGW) has no such limitation.

Bragg gratings have various attributes that can be modified to tailor the response. Such attributes include induced index change, length, apodization, period chirp and fringe tilt. These can allow effects such as fine spectral filtering, dispersion compensation, and mode coupling in core and cladding regions. The two main types of Bragg gratings are reflection or short-period gratings, with mode coupling occurring between counter-propagating modes, and transmission or long-period gratings, in which the coupling is between co-propagating modes. This project uses exclusively short-period gratings and the following discussion involves only this grating type.

3.3.1 Bragg Grating Response

When light propagates through a waveguide structure and encounters a grating, under certain conditions the propagating mode can be strongly coupled to the same, but counterpropagating, mode. This occurs for a guided mode that satisfies the *Bragg condition*. The Bragg condition uses the principles of energy and momentum conservation. Energy conservation implies that the total energy for incident, transmitted and reflected waves is conserved, assuming a lossless waveguide. Therefore the frequency of the incident and reflected radiation must be equal. Conservation of momentum implies the sum of the incident wavevector k_i and the grating wavevector K must equal the wavevector of the reflected wave k_r:

$$k_r = k_i + K \tag{3.62}$$

where $K = 2\pi/\Lambda$ and Λ is the grating period. This is demonstrated pictorially in Fig. 3.11. When the Bragg condition is satisfied $k_r = -k_i$, therefore Eqn.(3.62) becomes:

$$\frac{2\pi}{\lambda}n_{eff} + \frac{2\pi}{\Lambda} = -\frac{2\pi}{\lambda}n_{eff} \tag{3.63}$$

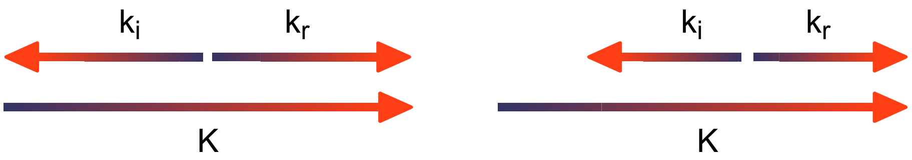

a) Coupling occurs between co- and counter-propagating modes when their wavevectors are equal and opposite

b) If there is a mismatch in the wavevectors, there is minimal power transferred into the backward propagating mode and hence no reflection.

Figure 3.11: Illustration of wavevector addition for a) the Bragg condition, producing reflected power and b) a wavevector mismatch, producing no reflected power

where n_{eff} is the effective modal index. This simplifies to the Bragg grating condition:

$$\lambda_B = 2n_{eff}\Lambda \tag{3.64}$$

where λ_B is the Bragg wavelength.

The Bragg reflection condition can be visualized with the ray-optic description. Consider a mode with bounce angle θ_1 reflecting into a mode propagating in the opposite direction with bounce angle $\theta_2 = -\theta_1$. As the mode propagation constant $\beta = (2\pi/\lambda)n_{eff}$ where $n_{eff} = n_{core}\sin\theta$, Eqn.(3.62) can be written as:

$$\beta_2 = \beta_1 + m\frac{2\pi}{\Lambda} \tag{3.65}$$

where m is the diffraction order. For Bragg gratings first order diffraction dominates so $m = -1$ and $\beta_2 = -\beta_1$ for identical modes which gives the same result as Eqn.(3.64). This situation is displayed in Fig. 3.12.

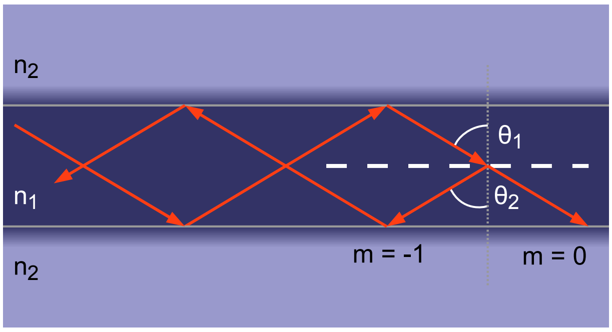

Figure 3.12: Ray-optic illustration of core-mode Bragg reflection by a Bragg grating

Additional spectral information, other than the central reflection wavelength, can be extracted by using coupled mode theory. Rigorous coupled mode analysis for Bragg gratings in waveguides can be found in several sources (e.g. [7]). However, for this work only a simplified analysis is required along with the results of applying coupled mode theory.

For propagation along the +z direction, the refractive index profile $n(z)$ along the Bragg grating is given by:

$$\delta n_{eff}(z) = \overline{\delta n_{eff}}(z)\left[1 + \gamma \cos\left(\frac{2\pi}{\Lambda}z + \phi(z)\right)\right] \tag{3.66}$$

where $\overline{\delta n_{eff}}$ is the refractive index perturbation averaged over a grating period, γ is the fringe visibility of the index change, and $\phi(z)$ describes the grating chirp. For $\gamma = 1$, and assuming no chirp $\phi(z) = 0$, Eqn.(3.66) can be written as:

$$\delta n_{eff}(z) = \overline{\delta n_{eff}}(z)\left[1 + \cos\left(Kz\right)\right] \tag{3.67}$$

Now the grating has been defined, it is left to examine the coupling that occurs between identical forward and backward propagating modes. Firstly, the propagation in the unperturbed waveguide region can be described by:

$$E_a = Ae^{i(\omega t - \beta_1 z)} \tag{3.68}$$

$$E_b = Be^{i(\omega t + \beta_2 z)} \tag{3.69}$$

where A and B are the constant amplitudes of the two modes. Mode E_a is a forward propagating mode (+z) and E_b a backward propagating mode. Now, a periodic perturbation can cause power exchange between the two modes. The coupled mode equations in this case are:

$$\frac{dA}{dz} = \kappa B e^{i\Gamma z} \tag{3.70}$$

$$\frac{dB}{dz} = \kappa A e^{-i\Gamma z} \tag{3.71}$$

where $\Gamma = \beta_1 + \beta_2 - K$ and κ is a coupling coefficient given by:

$$\kappa = \frac{\pi \overline{\delta n_{eff}}(z)}{\lambda_0} \tag{3.72}$$

The phase-matching condition requires $\Gamma = 0$ so that $\beta_1 + \beta_2 = K$ where $K = 2\pi/\Lambda$. Therefore differentiating Eqn.(3.71) with respect to z, and using Eqn.(3.70), results in:

$$\frac{d^2B}{dz^2} = \kappa^2 B \tag{3.73}$$

with the solution:

$$B(z) = b_1 e^{\kappa z} + b_2 e^{-\kappa z} \tag{3.74}$$

Substituting in Eqn.(3.71) gives:

$$A(z) = b_1 e^{\kappa z} - b_2 e^{-\kappa z} \tag{3.75}$$

Assume the power incident at the left hand side of a grating of length L is unity, $A(z = 0) = 1$, as depicted in Fig. 3.13. As there is no perturbation beyond $z = L$, there will be no power transferred into the backward propagating mode, therefore:

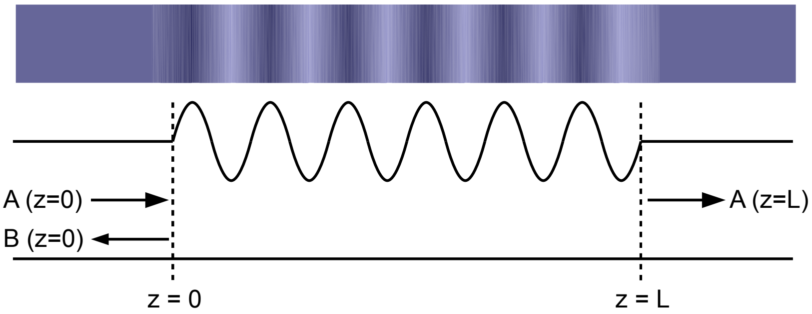

Figure 3.13: A periodic perturbation in a waveguide, under the phase-matching condition, acts as a reflector

$$B(z = 0) = 0 \tag{3.76}$$

Therefore:

$$b_1 e^{\kappa z} + b_2 e^{-\kappa z} = 0 \tag{3.77}$$

As $z = 0$ and $b_1 e^{\kappa z} - b_2 e^{-\kappa z} = 1$ implies that $b_1 - b_2 = 1$, and by using the algebraic expression $cosh(x) = \frac{1}{2}(e^x + e^{-x})$ gives:

$$b_1 = \frac{e^{-\kappa L}}{2cosh(\kappa L)}; \quad b_2 = \frac{-e^{\kappa L}}{2cosh(\kappa L)} \tag{3.78}$$

Also, as $sinh(x) = \frac{1}{2}(e^x - e^{-x})$ this leads to expressions for the amplitudes $A(z)$ and $B(z)$:

$$B(z) = \frac{sinh(\kappa(z - L))}{cosh(\kappa L)} \tag{3.79}$$

$$A(z) = \frac{cosh(\kappa(z - L))}{cosh(\kappa L)} \tag{3.80}$$

As $B(z)$ corresponds to the backward propagating mode, the reflection coefficient for the periodic structure can be defined as:

$$R = \frac{B(z=0)}{A(z=0)} = -tanh(\kappa L) \tag{3.81}$$

Thus the peak reflectivity is given by:

$$r = |R|^2 = tanh^2(\kappa L) \tag{3.82}$$

Eqn.(3.82) only describes the peak reflectivity of the grating. The shape of the grating response around the reflection peak must take into account detuning around the centre wavelength. The derivation of the grating reflectivity can be found in [6]. In this situation the reflection spectrum of the grating is given by [5]:

$$r = \frac{\sinh^2\left(\sqrt{\kappa^2 - \hat{\sigma}^2}L\right)}{\cosh^2\left(\sqrt{\kappa^2 - \hat{\sigma}^2}L\right) - \dfrac{\hat{\sigma}^2}{\kappa^2}} \tag{3.83}$$

in which L is the grating length and κ and $\hat{\sigma}$ are a.c. and d.c. coupling coefficients respectively.

The grating reflectivity described in Eqn.(3.83) typically produces spectra such as those shown in Fig. 3.14. The grating length was kept constant while the refractive index modulation depth was increased. It can be seen that both the reflectivity and the bandwidth of the grating are dependent on these parameters.

The bandwidth of a grating can be defined as the spectral width between the first minima either side of the reflection peak. This can be expressed as [5]:

$$\frac{\Delta\lambda_0}{\lambda} = \frac{\overline{\delta n_{eff}}}{n_{eff}}\sqrt{1 + \left(\frac{\lambda_D}{\overline{\delta n_{eff}}L}\right)^2} \tag{3.84}$$

It can be seen that the bandwidth is dependent upon the refractive index modulation and the length of the grating. The bandwidth as a function of refractive index perturbation is shown in Fig. 3.15. When the index modulation is small, the bandwidth has very little dependence on the modulation. As such, when $\overline{\delta n_{eff}} \ll \lambda_D/L$, the *weak grating limit*, Eqn.(3.84) becomes:

$$\frac{\Delta\lambda_0}{\lambda} \approx \frac{\lambda_D}{n_{eff}L} \tag{3.85}$$

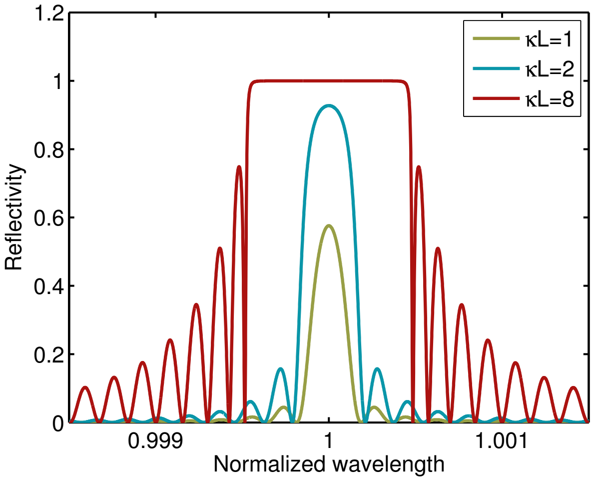

Figure 3.14: Reflection spectra as a function of normalized wavelength for uniform gratings with constant length and κL values of 1,2 and 8, calculated using Eqn.(3.83)

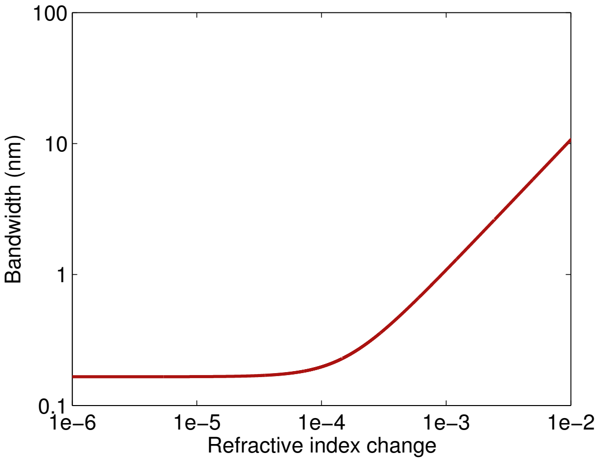

Figure 3.15: Bandwidth of a uniform, 1cm long Bragg grating with varying refractive index modulation

The bandwidth of weak gratings is said to be “length limited”. Conversely, in the *strong grating limit* where $\overline{\delta n_{eff}} \gg \lambda_D/L$, Eqn.(3.84) reduces to:

$$\frac{\Delta\lambda_0}{\lambda} \approx \frac{\overline{\delta n_{eff}}}{n_{eff}} \tag{3.86}$$

Therefore, for strong gratings where light at the reflection wavelength does not propagate the full length of the grating, the bandwidth is independent of length and directly related to the index modulation depth.

3.3.1.1 Apodization

The grating spectra shown at the end of the previous chapter have a central reflection peak surrounded by sidelobes. These sidelobes become large even for moderate grating strengths. For filtering and sensing applications these sidelobes become problematic. Hence in order to remove the sidelobes a process known as *apodization* is used. This involves modifying the gratings coupling strength as a function of position. As a uniform grating can be approximated to a sinusoidal perturbation convoluted with a top-hat function, the resultant frequency spectrum (from Fourier theory) would produce a sinc function. Sinc functions have characteristic ripples around their centre, which correspond to the sidelobes seen in Fig. 3.14.

By applying a suitable apodization or windowing function these sidelobes can be reduced to tolerable levels. The gratings fabricated in this thesis often employ Gaussian apodization with a function of the form:

$$\mathbb{A} = e^{-x^2/L^2} \tag{3.87}$$

where x is the position along the grating and L is the length of the grating. Shown in Fig. 3.16 is the effect of Gaussian apodization on a uniform Bragg grating. The plots are made with the authors own computational grating model. This uses an ordinary differential equation (ODE) solver and implements adaptive step-size 4th order Runge-Kutta numerical integration to solve the coupled mode equations (3.70) and (3.71). The program is written in Matlab™ and is provided as reference in Appendix A.

3.3.1.2 Chirp

Chirp is the term often used to describe a signal whose frequency increases or decreases as a function of time. In the case of Bragg gratings, chirp describes the increase or decrease in the grating period as a function of position. The most common chirped gratings are linearly chirped gratings, which are used in this thesis. Linear chirping is achieved by monotonically varying the period of the grating along its length. The equation for the Bragg reflection wavelength

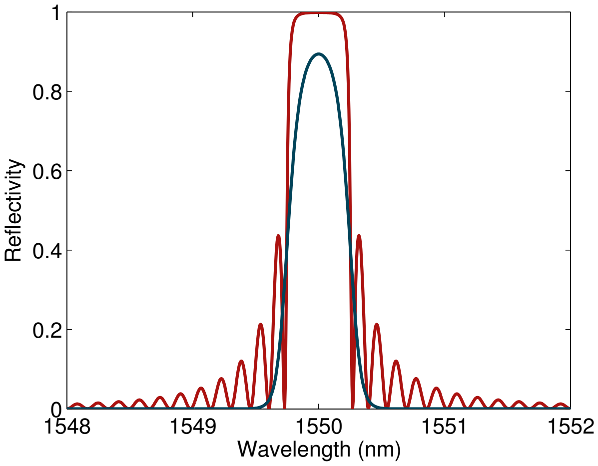

Figure 3.16: Unapodized (red) and apodized (blue) spectra for a 5mm long grating with $\kappa L = 4$

becomes:

$$\lambda_B(z) = 2N_{eff}\Lambda(z) \tag{3.88}$$

where $\lambda_B(z)$ is the position dependent reflection wavelength, N_{eff} is the effective refractive index of the propagating mode, and $\Lambda(z)$ is the position dependent grating period. Linear chirp can be defined as:

$$\Lambda(z) = \Lambda_0 + \Lambda_1(z) \tag{3.89}$$

where Λ_0 is the starting period and Λ_1 is the linear change in the period along the grating. Chirp is often stated in nm/cm, which describes the spectral change in Bragg reflection wavelength per cm of grating.

Fig. 3.17 demonstrates the effect of chirping a 5mm long grating with a κL value of 4. As would be expected from Eqn.3.88 the reflection band is broadened compared to the uniform grating, while the peak reflectivity is reduced. As the reflected light is now distributed over a broad reflected band rather than at a specific wavelength, the peak reflected power diminishes.

3.4 Summary

Starting from Maxwell's equations, light propagation in anisotropic media has been discussed. This has followed into waveguides and Bragg grating structures,

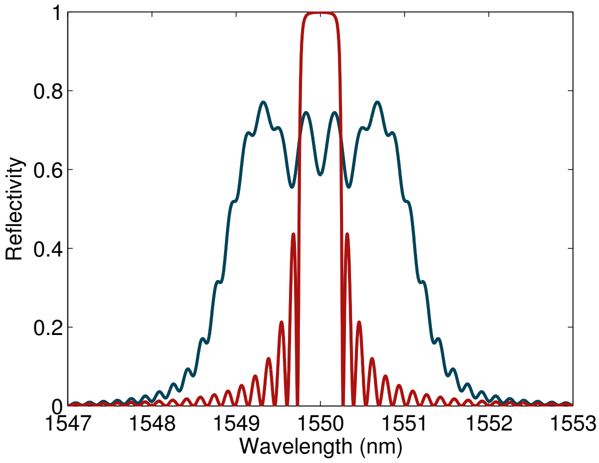

Figure 3.17: Unchirped (red) and chirped (blue) spectra for a 5mm long grating with $\kappa L = 4$

many of which have been fabricated during this thesis. Analytical solutions for simple waveguide geometries have been developed from Maxwell's equations to explain the concept of light guidance and modal confinement. However, more complex geometries require computational analysis and this is provided by the mode solver FIMMWAVE using a fully vectorial FMM algorithm. Important properties of Bragg gratings have been described mathematically, and spectra have been computed using the author's own program. Finally, the concepts of apodized and chirped gratings have been introduced with an explanation of how they change a grating's spectral profile.

References

[1] A. Ghatak and K. Thyagarajan. *Introduction to Fiber Optics*. Cambridge, UK, 1998.

[2] K. Okamoto. *Fundamentals of Optical Waveguides*. Academic Press, USA, 2006.

[3] A. Sudbo. "Film mode matching: a versatile numerical method for vector mode field calculations in dielectric waveguides". *Journal of Pure and Applied Optics*, 2:211–233, 1993.

[4] A. Othonos and K. Kalli. *Fiber Bragg gratings: fundamentals and applications in telecommunications and sensing*. Artech house, 1999.

[5] T. Erdogan. “Fiber grating spectra”. *Journal of Lightwave Technology*, 15(8):1277–1294, 1997.

[6] R. Kashyap. *Fiber Bragg Gratings*. Academic Press, USA, 1999.

[7] A. Yariv. “Coupled-mode theory for guided-wave optics”. *IEEE Journal of Quantum Electronics*, 9(9):919–933, 1973.

Chapter 4

Liquid Crystals

Liquid crystals (LC), as the name suggests, exhibit properties reminiscent of both liquids and crystalline solids. That is, they flow like liquids, but are not isotropic. The constituent molecules have either positional or orientational order, or both. This is because compounds that exhibit liquid crystalline phases tend to consist of anisotropic molecules. LC's can be broadly classified into two main variants: nematics and smectics, while cholesteric LC's are 'twisted' nematics, in which the molecules rotate with a constant pitch along an axis. Cholesteric LC's (chiral nematic) can be formed from chiral molecules or by doping a nematic with a chiral dopant. Smectics are LC phases where the molecules are present in layers. There is positional order, as well as orientational order, in smectics as the centres of mass are arranged in layers. This project requires only the use of nematic LC's, chosen because of their easily exploitable birefringence and electrooptic response. Further information regarding the various phases can be found in [1] or [2].

4.1 Nematic Liquid Crystals

The nematic LC phase is the most basic liquid crystalline phase as it possesses long-range orientational order but no long-range positional order. The orientational order, or crystallinity, arises from the shape of the constituent molecules. Nematics can be formed from a variety of "mesogens" with basic shapes. The most common of which is the rod-like, uniaxial mesogen. Other shapes have also been fabricated, including disk-shaped mesogens that produce discotic or columnar phases, and banana-shaped mesogens [3,4]. LC's can also be thermotropic or lyotropic. Thermotropic LC's exhibit temperature-dependent phase behaviour, whereas lyotropic LC's exhibit concentration-dependent phases. This thesis uses exclusively rod-like, thermotropic nematics.

Thermotropic LC's have specific temperatures at which their phase changes. For the case of an LC which only exhibits the nematic phase, its phase transitions are:

$$C \overset{22}{\longleftrightarrow} N \overset{35}{\longleftrightarrow} I$$

where C indicates crystallinity, N the nematic phase, and I the purely isotropic phase. Transition temperatures, defined above the arrows, indicate the temperature window over which liquid crystallinity occurs. In this case phase transition temperatures (in degrees Celsius) of 5CB (4-n-pentyl-4′-cyanobiphenyl), a common nematic LC, have been used. All LC's in this thesis are nematic at room temperature.

Nematic long-range orientational order can be induced by applied fields, order imposed by physical boundaries, or more commonly a combination of both. Boundary imposed order, which is governed by the surface itself, is due to steric interactions between mesogens. The surface can be treated to impose different alignment states, such as parallel (planar) or homeotropic (perpendicular) alignment shown in Fig. 4.1. Such surface treatments are explained in Chapter 6. For LC molecules with permanent electric dipoles, dipole-dipole (van der Waals) interactions will also contribute to the molecular alignment. Field-induced realignment is caused by either permanent or induced electric dipoles (or both) aligning themselves with the applied field.

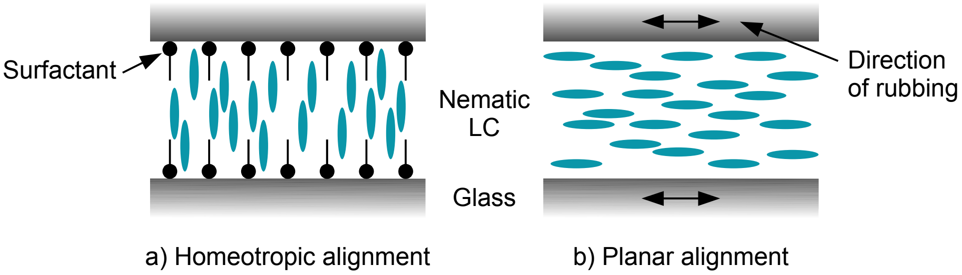

Figure 4.1: Two common alignments for a confined LC: (a) homeotropic, (b) planar.

Long-range order can be classified by an "order parameter", S, which describes the degree to which LC mesogens align with each other over a whole ensemble. However, this does not describe realignment processes occuring in the LC bulk. Indeed, for closed systems that are not heated or taken through phase transitions, as with devices in this thesis, the order parameter does not change significantly. It is therefore more convenient to use a parameter known as the "director", **n**. The director is the statistical average of the orientation of the LC molecules in a small volume. As it is a vector which often varies spatially, **n**(x,y,z), the concept of a "director field" is often used. This describes the spatial change in orientation of **n**, and therefore the molecules, over µm length scales.

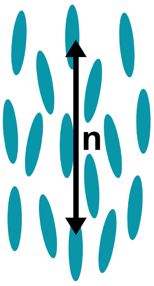

Figure 4.2: Defining the director in a local region of LC

Perturbations in the director field are known as deformations. For deformations that occur over distances much larger than the molecular length (i.e. smooth or continuous deformations), the aforementioned order parameter will not change. Deformations can be described mathematically by an elastic continuum theory pioneered by Frank [5]. This treats the LC as an anisotropic liquid with elastic distortion and restoring forces. There are three possible deformation modes for a nematic LC: splay, twist, and bend.

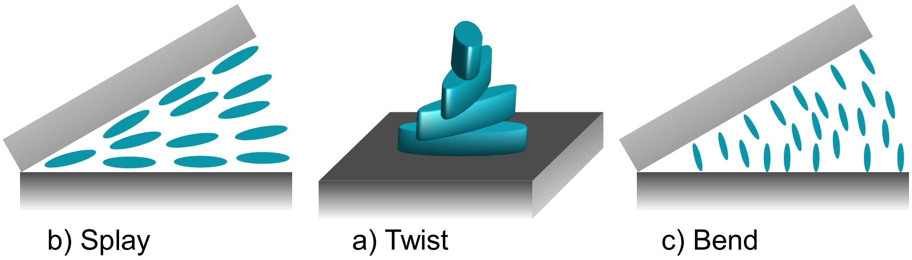

Figure 4.3: The three types of deformation that can occur in nematics, a) twist, b) splay and c) bend.

An aligned nematic LC is in essence a uniaxial crystal. Hence the crystal axes are defined perpendicular and parallel to **n**. These directions exhibit differing refractive indices due to the molecular structure of the LC, similar to uniaxial crystals (Eqn.3.14). The effective refractive index can therefore be given by:

$$n^2 = \begin{bmatrix} {n_\perp}^2 & 0 & 0 \\ 0 & {n_\perp}^2 & 0 \\ 0 & 0 & {n_\parallel}^2 \end{bmatrix} \tag{4.1}$$

Linearly polarized light can be decomposed into two components, one parallel to **n** and one perpendicular. These two components will inherit a relative phase delay while propagating through the LC. For LC's with positive birefringence where $\Delta n = n_\parallel - n_\perp > 0$, as with those used in this thesis, light polarized along **n** experiences a higher refractive index then light polarized normal to **n**.

4.2 Liquid Crystals in an Applied Field

Perhaps the main reason LC's are so prevalent in display and optical applications is their response to externally applied electric fields. Field-induced realignment is vital because it allows for exploitation of LC birefringence. The response of an LC to an applied field arises from the electrical polarization of the molecules. This includes electronic polarization which arises from displacement of electrons by the action of the external electric field, and orientation polarization which is associated with the orientation of the permanent molecular dipoles in the applied field.

In nematics, the polarizability anisotropy is positive due to their rod-like shape. This implies the polarizability is larger along the molecular axis than perpendicular to it. Therefore, the contribution of the electronic polarization to the dielectric anisotropy is also positive. The result is non-polar nematic compounds will exhibit positive dielectric anisotropy. Additionally, polar compounds that have a relatively small angle between the polarization axis and the molecular axis, such as n-cyanobyphenyls, have relatively large axial values of the dipole moment. Therefore they too have positive anisotropy. In general the contribution of the orientation polarization depends on the magnitude of the dipole moment and the angle between the dipole and the molecular long axis. The sign of the total dielectric anisotropy is determined by the relative magnitude of the electronic and orientation polarizations. Given that the relaxation time for a confined LC is [2]:

$$\tau = \frac{\gamma}{K}\left(\frac{d}{\pi}\right)^2 \tag{4.2}$$

a 7μm thick cell containing 5CB would have a relaxation time of ~50ms[1], where γ is the viscosity coefficient, K is the elastic constant and d is the cell width. Typically an a.c. electric field of 1kHz is used to reorient the LC, and as such the permanent dipole has little effect on field-induced realignment as the orientation polarization cannot follow the variation of the field. This implies field-induced realignment from kHz electric fields is dominated by the induced electronic polarization.

The combined dipole moment, or the induced polarization of the material, is related to the electric field by:

$$\mathbf{P} = \epsilon_0 \chi_e \mathbf{E} \tag{4.3}$$

where ϵ_0 is the permittivity of free space and χ_e is the electric susceptibility. For an anisotropic medium χ_e will be direction-dependent and can therefore be defined with respect to the LC director, hence:

$$\chi_e = \begin{bmatrix} \chi_\perp & 0 & 0 \\ 0 & \chi_\perp & 0 \\ 0 & 0 & \chi_\parallel \end{bmatrix} \tag{4.4}$$

It can be assumed that there is rotational symmetry about the director axis. Thus there are two values for χ_e, $\chi_\parallel$ for an electric field applied parallel to **n** (z-direction) and $\chi_\perp$ for a field applied perpendicular to **n** (x and y directions). For the case where $\chi_\parallel$ is greater than $\chi_\perp$ the anisotropy of the dielectric susceptibility, $\Delta\chi$, is said to be positive. For a nematic LC the induced polarization is therefore given by [7]:

$$\begin{aligned} \mathbf{P} &= \epsilon_0 \chi_\parallel (\mathbf{E}\cdot\mathbf{n}) + \epsilon_0 \chi_\perp \left[\mathbf{E} - (\mathbf{E}\cdot\mathbf{n})\mathbf{n}\right] \\ &= \epsilon_0 \left[\chi_\perp \mathbf{E} + \Delta\chi(\mathbf{E}\cdot\mathbf{n})\mathbf{n}\right] \end{aligned} \tag{4.5}$$

The dielectric anisotropy provides a method of alignment by electric fields as it causes rotation of the LC molecules under the action of the dielectric torque. The

---

[1] Relaxation time is the time taken for the orientation polarization to fall to 1/e of its original value [6]. $\gamma = 0.1$Pa.s, $K \approx 1 \times 10^{-11}$N, and $d = 7 \times 10^{-6}$μm

electric energy density in a nematic LC is approximately given by [2]:

$$\begin{aligned} f_e = -\frac{1}{2}\mathbf{P}\cdot\mathbf{E} &= -\frac{1}{2}\epsilon_0\left[\chi_\perp\mathbf{E} + \Delta\chi(\mathbf{E}\cdot\mathbf{n})\mathbf{n}\right]\cdot\mathbf{E} \\ &= -\frac{1}{2}\epsilon_0\chi_\perp E^2 - \frac{1}{2}\epsilon_0\Delta\epsilon(\mathbf{E}\cdot\mathbf{n})^2 \end{aligned} \tag{4.6}$$

noting that $\epsilon_\parallel = 1+\chi_\parallel$ and $\epsilon_\perp = 1+\chi_\perp$. Therefore $\Delta\chi = \chi_\parallel - \chi_\perp = \epsilon_\parallel - \epsilon_\perp = \Delta\epsilon$. The first term in Eqn.4.6 is independent of the orientation of the director with respect to the applied field, and so does not contribute to LC molecular reorientation in applied fields. The second term does depend on the orientation of **n** with respect to the applied field due to **E.n**. If **n** is perpendicular to **E**, $(\mathbf{E}\cdot\mathbf{n})^2 = 0$, and if **n** is parallel or anti-parallel to **E**, $(\mathbf{E}\cdot\mathbf{n})^2 = E^2$. So for an LC with positive dielectric anisotropy ($\Delta\epsilon > 0$), the electric energy is minimized when **n** is parallel or anti-parallel to the applied field. This is why LC's tend to align parallel or anti-parallel to an applied field. Conversely, for LC's with negative dielectric anisotropy ($\Delta\epsilon < 0$), the electric energy is minimized for **n** aligned perpendicular to the field and thus these LC's tend to align perpendicular to the field.

The dielectric anisotropy is not constant, it is dispersive and hence a function of frequency. At low frequencies all contributions to the overall polarization have an effect. However, for higher frequencies, the dielectric permittivity decreases and the dipolar reorientation eventually becomes negligible. This is because there is insufficient time for molecular reorientation before the field is again reversed [8]. Other contributions can dominate the overall polarization and the result can even be negative dielectric anisotropy in some frequency ranges. This is why cells fabricated in this thesis are always addressed with 1kHz electric fields. It also avoids problems with conduction due to contaminants. Shown in Fig. 4.4 is the highest frequency at which the molecules in a standard LC cell begin to reorient with the field as a function of applied voltage. It can be concluded that the dielectric response of the cell diminishes with increasing frequency. Higher voltages are needed to induce a response as the frequency of the applied field is increased. The cell exhibits no response below 15V at any frequency. This is due to the effect described in Section 4.2.1.

The data for the frequency characterization was obtained from a homeotropically aligned transmissive cell, as shown in Fig. 4.5. The cell was coated with homeotropic surfactant and filled with the LC 5CB under vacuum. The electrode width was 50μm and the cell gap was 12μm. An a.c. voltage was applied to

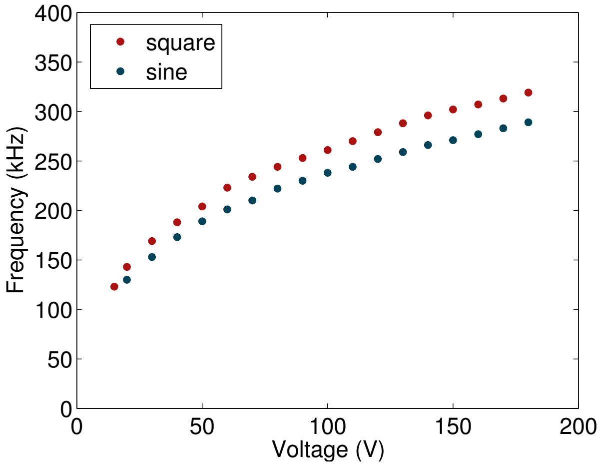

Figure 4.4: Frequency at which response of an LC cell vanishes as a function of voltage for two different waveforms. Data taken from captured images by analyzing the RGB value in a vertical slice of the image. If the slice has no value above background noise (5-10), the response is deemed to have vanished.

the ITO electrodes and the images captured with a cross polarized microscopy system using a PixeLINK™ PL-B958U USB camera.

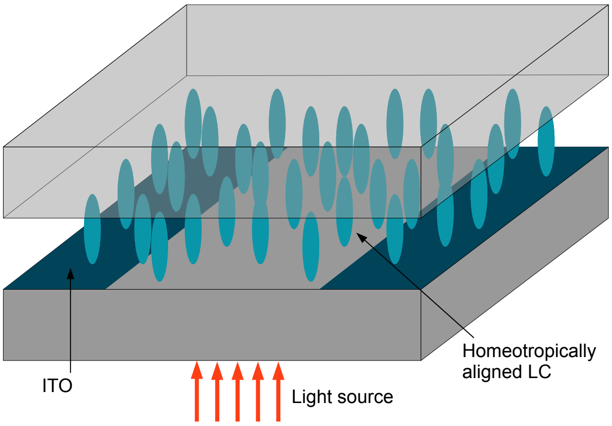

Figure 4.5: Cell used for frequency response measurements.

4.2.1 The Fréedericksz Transition

An important field-dependent effect to note is the phenomenon known as the Fréedericksz transition. For a nematic LC in an applied field and confined geometry, such as in Fig. 4.1 b) with the field applied between the glass plates, there will be no effect on the director configuration if $\mathbf{E} < \mathbf{E}_F$, where $\mathbf{E}_F$ is the critical value for the field. Above this value, a transition occurs between an unperturbed director conformation and a distorted one. The applied field is sufficient to overcome elastic and anchoring forces opposing reorientation and the LC can begin to align with the field. The local equilibrium configuration with an applied field greater than $\mathbf{E}_F$ depends on the magnitude and direction of the field with respect to the director axis, and also the dielectric anisotropy.

There is a competition between the orientation imposed by the field and the orientation imposed by the cell boundaries. The director near the boundary is dictated by the surface alignment effect and, further from the boundary, by the external field [9]. In the case of an LC with positive dielectric anisotropy, the equilibrium director configuration will tend towards an alignment parallel to the field. Complete rotation in a homeotropic cell often requires fields of magnitude several times $\mathbf{E}_F$, with the field applied normal to the initial director orientation. $\mathbf{E}_F$ is inversely proportional to the sample thickness, hence samples are typically 10µm thick or less. The threshold voltage for the Fréedericksz transition of a planar aligned LC is given by [2]:

$$V_{th} = E_F d = \pi\sqrt{\frac{K}{\epsilon_0 \Delta\epsilon}} \tag{4.7}$$

where d is the cell thickness, K is an elastic constant, and $\Delta\epsilon$ is the permittivity anisotropy. However, for a cell with in-plane electrodes where the interelectrode distance is not equal to the cell thickness, the threshold voltage is given by [10]:

$$V_{th} = \pi\frac{p}{d}\sqrt{\frac{K}{\epsilon_0 \Delta\epsilon}} \tag{4.8}$$

where p is the interelectrode distance.

All reorientation effects involve competition between the elastic and viscous torques opposing motion, and the torque from the applied field promoting reorientation. Elastic deformations, whether twist, splay or bend, cost energy. The dynamic behaviour in a LC always tends towards an equilibrium state which is determined by the minimization of free energy in the system. However, a discussion of the hydrodynamics of LC's is beyond the scope of this work.

4.3 Topological Defects

Variations in the director, such as deformations, have been described previously and they involved continuous variations of the director **n(r)** (splay, twist, or bend). However, there are instances where **n(r)** is no longer a smooth function of **r** at all locations. Hence defects in LC's are classified as either positions where **n** is undefined, or where the director field becomes discontinuous [11]. Defect regions have no orientational order and can be treated as the LC in isotropic phase. Dark filaments are often seen in nematic samples, and it is this feature which bore the name nematic, from the Greek νημα (*nema*) meaning thread. These features were named 'disinclinations' by F. C. Frank [5] and are now commonly known as disclinations to indicate that there are discontinuities in the "inclination" of the molecules. Disclinations are the most common type of line defect. Defects, in general, can arise from topological, energetic or dynamic properties of the system.

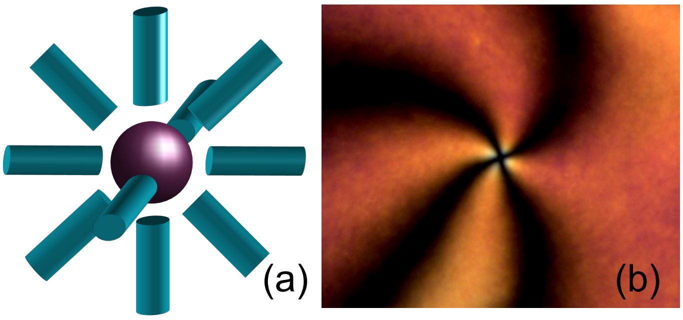

Figure 4.6: (a) Radial hedgehog defect (b) Defect imaged through crossed polarizers observed in a cell fabricated for this thesis.

Topological defects can be either one, two or three dimensional. One-dimensional defects, or singularities, are known as *hedgehogs* [12, 13]. Shown in Fig. 4.6(a) is a radial hedgehog point defect where **n(r)** points towards a singularity from all directions. If such a defect is viewed through crossed polarizers, there are four directions in which **n(r)** is parallel to either polarizer. Hence these defects are easily distinguished by four dark brushes emanating from the core, as shown in Fig. 4.6(b).

One-dimensional defects are not always stable; there may be a more favourable director configuration that leads to a hedgehog forming a two-dimensional defect, such as a disclination loop [12, 14]. A defect line is traced out by rotating a radial defect, as shown in Fig. 4.7(a). As the radius of the loop tends to zero, it will appear as a point defect, but loops of small but finite size can be seen in some cells (Fig. 4.7(b)). Loops that become broken or anchored at boundaries result in line defects or disclinations.

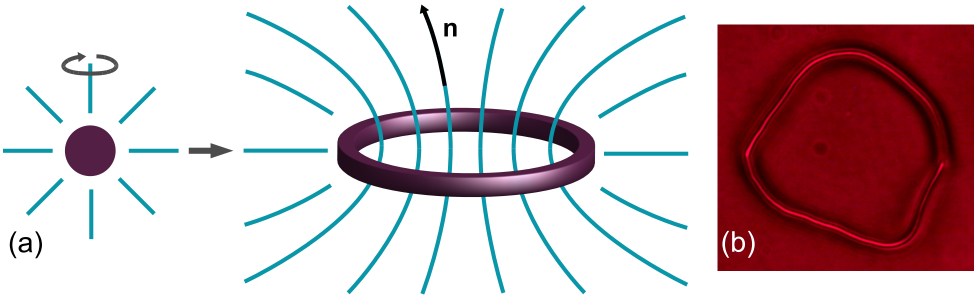

Figure 4.7: (a) A point defect rotated can form a disclination loop (b) Disclination loop observed in an LC cell fabricated for this thesis.

Disclinations are two-dimensional defects as they are lines where **n** is undefined. They propagate through the LC causing distortions of the director field that can be observed using polarized microscopy, which will be discussed later. Disclinations often terminate with either a point defect, usually at a boundary, or a three-dimensional "wall" defect which is in fact continuous. The disclinations applicable to this work are known as wedge disclinations.

It is useful to decribe such defects quantitatively by using a value known as the strength or winding number, k [15]. This indicates how many times **n** rotates through 2π when tracing a clockwise route around a defect. Point defects possess positive or negative integer values, i.e. $k = \pm1, \pm2, \pm3$. Line defects may also have half-integer values due to the translational invariance of the director, **n** ⇔ -**n**. Defects of opposite winding number may annihilate each other, removing discontinuities in the director field.

Wedge disclinations have winding number $\pm\frac{1}{2}$ and are topologically stable. There is no continuous deformation of a $\pm\frac{1}{2}$ disclination that can produce a smoother director field. The two forms of wedge disclination are shown in Fig. 4.8. As these two defects have opposite strength, they may annihilate each other to form a continuous director field.

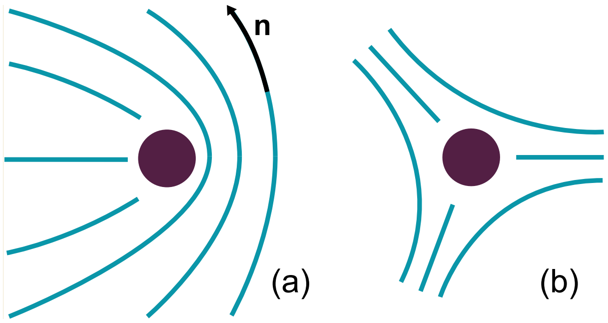

Figure 4.8: (a) Wedge disclination of strength +$\frac{1}{2}$, (b) Wedge disclination of strength -$\frac{1}{2}$

4.3.1 Walls

Although not strictly a defect, walls in nematic LC's are the closest topological state to a three-dimensional defect [16]. The difference is that walls are a continuous (non-singular) deformation of **n** rather than discontinuities, even though the director field can vary rapidly. Walls are often associated with the Fréedericksz transition in an applied field, as they separate field-aligned domains of opposite but equivalent director orientations. Inside the wall, the director configuration is unperturbed. This is shown in Fig. 4.9 where the central yellow region retains its homeotropic alignment. These walls are often termed Fréedericksz walls, inversion walls, or splay-bend walls. Perhaps the most fitting terminology is the splay-bend wall, as it is a combination of these deformations that permits the wall structure whilst retaining a continuous director field.

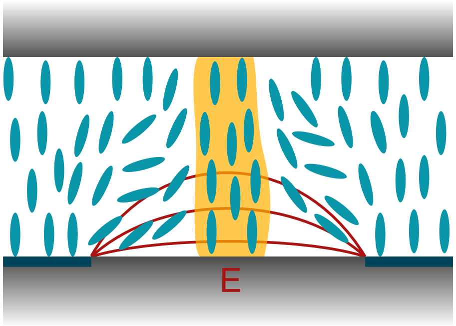

Figure 4.9: A Fréedericksz or splay-bend wall shown in the yellow area between two regions aligning with the applied field

Walls arise due to there being two symmetric, equivalent configurations of **n** as shown on the left and right sides of the cell in Fig. 4.9. These configurations appear when an external field is applied under certain boundary conditions, and are possible again due to the translational invariance of the director ($\mathbf{n} \Leftrightarrow$ -$\mathbf{n}$). As these walls are produced by applying a field perpendicular to the initial orientation, the field strength must be above a critical value $\mathbf{E}_F$. Fréedericksz walls are highly field-dependent and can produce unique behaviour in certain systems [17,18].

4.4 Liquid Crystals as Waveplates

An LC cell, whose thickness and birefringence can be controlled, will locally act as a waveplate of variable optical path length. The relative optical path length difference (OPD) through a section of LC is given by [10]:

$$\Omega = d(|n_{\parallel} - n_{\perp}|) \tag{4.9}$$

and the relative phase delay by:

$$\Delta\phi = \frac{2\pi}{\lambda} d(|n_{\parallel} - n_{\perp}|) \tag{4.10}$$

In this project, LC cells with uniform cell depth are used. Therefore d is constant and the phase delay is dependent on the wavelength of light used for illumination and the relative birefringence, Δn_r. Here, the relative birefringence is a term used to describe the apparent refractive index difference seen by polarized light resolved parallel and perpendicular to the electrode axes. This quantity, that will be explored later, is dependent upon applied fields and the geometry of the system.

4.5 Polarization Microscopy

Anisotropic materials, such as LC's, have optical properties that vary with the orientation of incident polarized light. Polarization microscopy is therefore the most common tool to analyze LC behaviour and topology. This technique uses a transmission microscope with the sample placed between crossed polarizers. The transmitted light intensity gives an indication of the alignment or realignment processes occurring in a LC cell. The transmitted light intensity is given by [10]:

$$I = I_0 \sin^2(2\varphi) \sin^2\left(\frac{\pi(n_{\parallel} - n_{\perp})d}{\lambda}\right) \tag{4.11}$$

The angle φ is the angle between the electrode axis and the analyzer orientation. If φ is set to 45°, the transmitted intensity depends only on the relative birefringence and the wavelength of light used:

$$T(\lambda) = \sin^2\left(\frac{\pi\Delta n(\lambda)d}{\lambda}\right) \tag{4.12}$$

If a homeotropic LC cell is illuminated by light through crossed polarizers, its optical anisotropy will cause transmission of light through the analyzer if a field is applied to the cell. Referring to Fig. 4.10, the voltage is applied between the two ITO electrodes, normal to the initial director orientation. The transmission gives an indication of Δn_r in that part of the cell, and therefore the amount of director rotation from the applied field. If no light is transmitted in a region between the electrodes, this implies there is no relative phase retardation between orthogonal polarization components. This can be caused by either a complete lack of director rotation from the homeotropic order, or from a seemingly isotropic region in the LC. Unperturbed regions can be the aforementioned splay-bend walls. Isotropic regions are often defects in the LC, whereby **n** is undefined which cause optical perturbations at the boundary between ordered and disordered LC states.

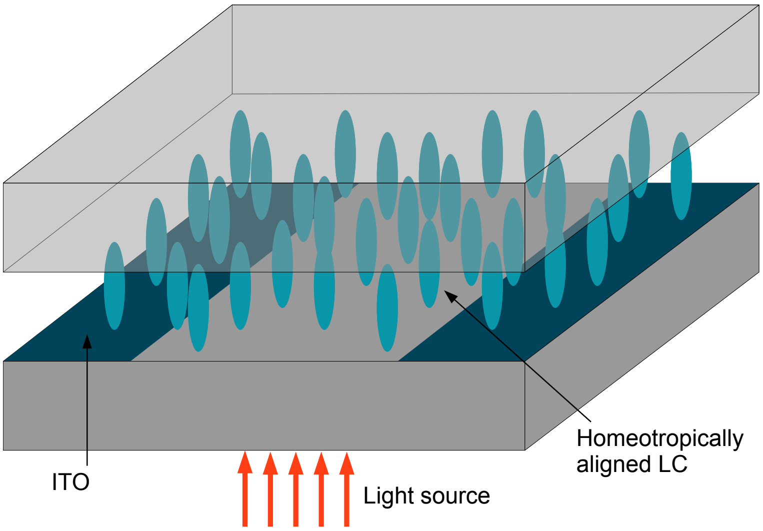

Figure 4.10: Molecular order in a homeotropically aligned LC cell with no applied voltage.

The homeotropically aligned nematic LC cells fabricated in this project, as depicted in Fig. 4.10, are used to explore the realignment processes occuring in previous electrically tunable planar Bragg grating devices. The previous devices were made from three-layer silica-on-silicon samples and were opaque due to the silicon being non-transmissive at visible wavelengths. Consequently new LC cells were fabricated from ITO coated glass to allow for transmission microscopy analysis and to permit the application of voltages across the cells.

In areas where **n** can realign with the field, light can be transmitted. The degree of realignment will determine which transmission colours will be visible in polychromatic experiments, and will govern the transmitted intensity in monochromatic experiments. If the director's plane of rotation is not along a polarizer axis, any reorientation of the bulk director orientation will permit transmission through the analyzer. Therefore, light is transmitted in the region between the electrodes where **n** is orienting along the field lines.

If walls are present they should permit no transmission of light. As shown in Fig. 4.11, in the wall region there will be no relative phase delay between orthogonal polarization components. Hence these regions will appear dark in transmission. It can also be seen that, in areas of field-induced reorientation, **n** is no longer normal to the surfaces. In these regions light will be transmitted.

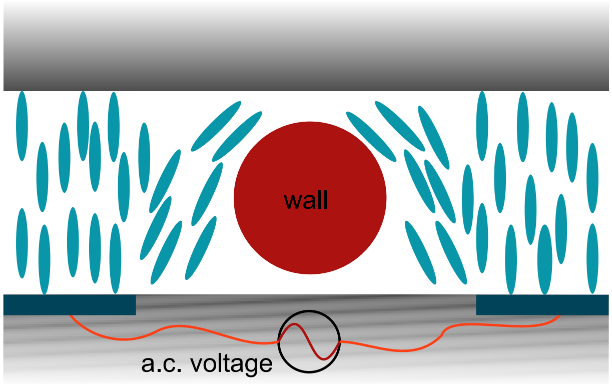

Figure 4.11: Section through a wall in a homeotropically aligned cell with applied voltage

4.6 Liquid Crystal Texture

One of the most revealing properties of LC alignment is the appearance in polarized microscopy. Such images can exhibit stark differences between well aligned and poorly aligned LC. They can display where the LC is aligning with an applied field, or where no realigment is occuring. Polarized microscopy images can also probe defects and defect dynamics where sufficient resolution is available. Presented now is the analysis of a generalised case of a homeotropic LC cell.

In a homeotropically aligned LC cell with illumination perpendicular to the cell, the plane of polarization is everywhere normal to the director axis. Thus there is no birefringence in this scenario, as depicted in Fig. 4.10. However, if an electric field is applied normal to the director axis across ITO electrodes, the molecules will experience field-induced reorientation. Due to the LC's in this project all having positive dielectric anisotropy, the long molecular axes, and therefore **n**, will tend to align parallel to the applied field. As the molecules reorient, the refractive index is no longer uniform in all positions. Displayed in Fig. 4.12 is the effect of an electric field applied normal to the director alignment. This is a stable director state that neglects transient effects and director discontinuities, both of which will be analyzed later. Hence **n** in the centre of the cell is portrayed as parallel to the applied field. It can be seen that, unlike in Fig. 4.10, the director alignment is now a function of position in the x-y plane. Thus the birefringence, and therefore the OPD, increases towards the centre of the electrode structure for light polarized in the x-y plane.

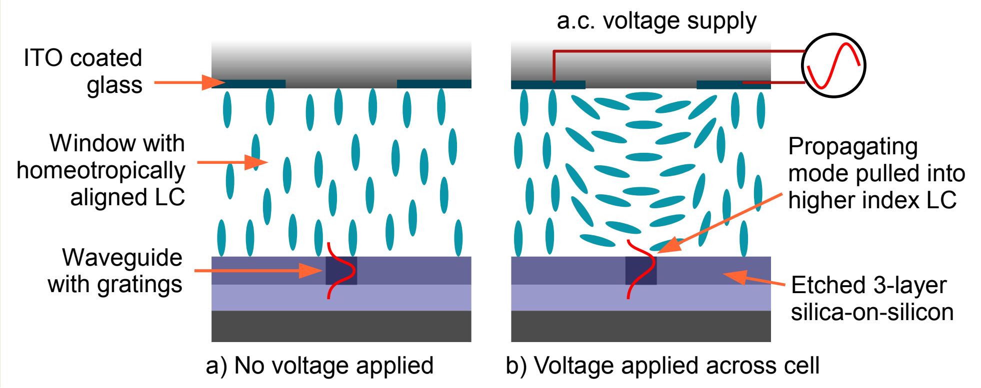

a) No voltage applied b) Voltage applied across cell

Figure 4.12: Topologically stable state in a homeotropic cell with applied voltage

This preliminary model is beginning to depict an inhomogeneous and dynamic wave retarder. This allows properties such as the relative birefringence and defects to be probed using polarization microscopy. The relative birefringence is more complicated than that implied in Fig. 4.12. The director is not at a constant angle $\theta(z)$ with respect to the z axis. Therefore, the relative birefringence is an integral over the LC thickness in the cell, effectively creating an average of the angle $\theta(z)$ over the thickness d. Thus Eqn.(4.11) can be revised such that [10,13]:

$$I = I_0 \sin^2(2\varphi) \sin^2 \int_0^d \left[\frac{\pi}{\lambda} \left(\frac{n_{\|} n_{\perp}}{\sqrt{n_{\|}^2 \cos^2\theta + n_{\perp}^2 \sin^2\theta}} - n_{\perp} \right) \right] dz \tag{4.13}$$

It is convenient to define the angle dependent refractive index term as:

$$n_\theta = \frac{n_{\|} n_{\perp}}{\sqrt{n_{\|}^2 \cos^2\theta + n_{\perp}^2 \sin^2\theta}} \tag{4.14}$$

Therefore Eqn.(4.13) becomes:

$$I = I_0 \sin^2(2\varphi) \sin^2 \int_0^d \left[\frac{\pi}{\lambda} \left(n_\theta - n_{\perp} \right) \right] dz \tag{4.15}$$

noting also that the relative birefringence can now be defined as $\Delta n_r = |n_\perp - n_\theta|$.

It can be seen that, for the homeotropic case where $\theta(z) = 0$ always, the integrand becomes 0. Therefore, with light propagating along the z axis, there is no transmitted light for any wavelength, as would be expected. Also, if the directors plane of rotation is along a polarizer axis, $\varphi = 0, \pm\pi/2$, and the same situation occurs. As this technique integrates a section of LC parallel to the direction of light propagation, 3-dimensional information is lost. As such, polarizing microscopy can only provide a generalization of the director alignment, and cannot probe the director orientation as a function of z. However, it still provides a useful tool for 2-dimensional mapping of director orientation. Fig. 4.13 shows how different director configurations, that are affected by boundary conditions and applied field, result in differing transmission characteristics.

4.6.1 Birefringence in Liquid Crystals

Using Fig. 4.13 as a reference, it can be seen that Δn_r as a function of x varies considerably. The unperturbed region in Fig. 4.13a will allow no transmission for any wavelength. However, in regions where **n** has a component in the x-y plane, transmission will be governed by the variation of $\theta(z)$ along x. Now, assuming $\theta(z)$ can be averaged to a single value θ through any line perpendicular to the x-y plane (analogous to a planar texture with pretilt), the expected transmission

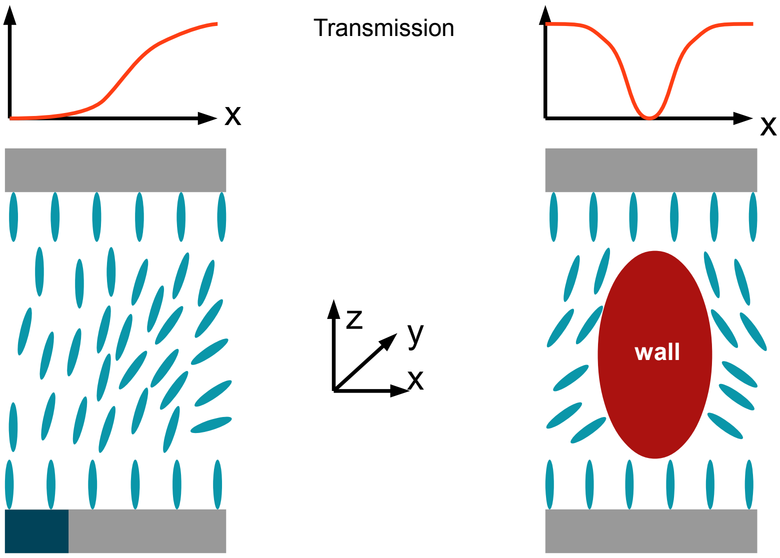

a) Inner electrode region. Director rotates such that long axes tend to align parallel with field lines. Birefringence becomes a function of x and z.

b) Wall region in centre of electrodes. LC molecules are homeotropically aligned. No relative birefringence in centre.

Figure 4.13: Diagram of various director configurations across the cell while applying a voltage, showing transmission across the electrodes

wavelengths can be calculated. In this case Eqn.(4.13) reduces to:

$$T = \sin^2\left[\frac{\pi d}{\lambda}\left(\frac{n_\parallel n_\perp}{\sqrt{n_\parallel^2\sin^2\theta + n_\perp^2\cos^2\theta}} - n_\perp\right)\right] \tag{4.16}$$

where T is the relative transmission, and the plane of director rotation is set at $45°$ to the polarizer axis. Using Eqn.(4.14), Eqn.(4.16) becomes:

$$T = \sin^2\left(\frac{\pi d}{\lambda}(n_\theta - n_\perp)\right) = \sin^2\left(\frac{\pi d}{\lambda}\Delta n_r\right) \tag{4.17}$$

Taking the principal axes as the x,y,z axes, the incident electric field vector of the polarized light can be resolved into components parallel and perpendicular to the plane of director rotation. In Fig. 4.14 the plane of rotation is set at $45°$ to maximize the relative transmission. Components of the incident E-field vector, which is aligned along the x-axis, are displayed.

The birefringence is a function of director alignment and thus a function of the average tilt angle away from normal alignment. So, proceeding in a similar fashion to that used for the waveplate analysis, the relative phase retardation between orthogonal polarization components is now given by:

$$\alpha = e^{i(\frac{2\pi}{\lambda}z|n_\perp - n_\theta|)} \tag{4.18}$$

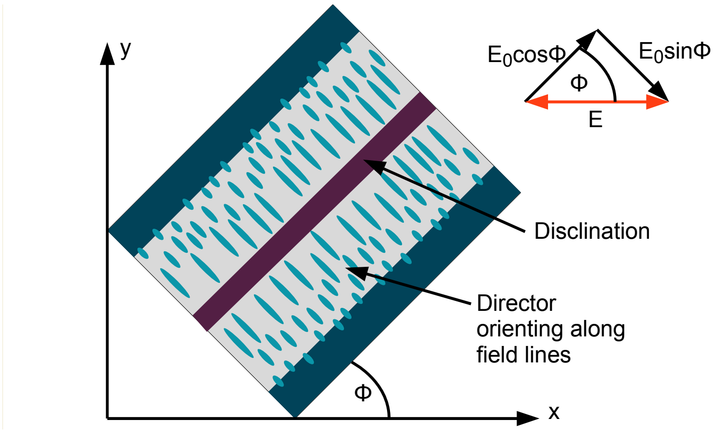

Figure 4.14: Resolving relative birefringence as a function of principal axes x,y

As before, if Eqn.(4.18) = 1, then the polarization state remains the same and no light is transmitted through the analyzer. However, if Eqn.(4.18) = -1, the LC acts as a half wave plate, rotating the plane of polarization by 2φ. In this instance:

$$\begin{aligned} \frac{2\pi}{\lambda} z|n_\perp - n_\theta| &= \pi, 3\pi, 5\pi, \ldots \\ \frac{2z}{\lambda}|n_\perp - n_\theta| &= 2m + 1 \\ \Delta n_r &= \frac{(2m+1)\lambda}{2z} \qquad (4.19) \end{aligned}$$

where m is an integer, λ is the wavelength of incident light, z is the thickness of the birefringent slab.

4.6.2 Monochromatic Analysis

Several factors make obtaining quantitative data from white light polarization microscopy difficult. Firstly, transmitted colours are affected by the perception of colour by the eye, light transmission of the birefringent medium, and the spectrum of illumination. It is therefore beneficial to perform analysis of phenomena in LC cells using monochromatic light.

To understand better the director reorientation occuring in cells under applied field, linearly polarized monochromatic light can be used to illuminate the cells. In this case the phase delay between orthogonal polarizations is governed only by Δn_r, as both z and λ are constant. Therefore the extent of the director rotation into the x-y plane can be mapped.

As **n** rotates into the x-y plane, light will be transmitted through the analyzer.

In regions where Eqn.(4.19) is satisfied, maximum transmission will be seen. However, as Δn_r is a quantity that varies with applied voltage, the same regions will allow no transmission as the voltage varies. For certain voltages, Δn_r is such that the cell produces no relative phase delay between polarization components, and there is no transmission. Therefore, as the voltage applied to the cell increases, there will be cycles of transmissive and non-transmissive output.

These cycles may only continue until the LC has reached maximum field-induced realignment. At this point, $n_\theta \rightarrow n_e$ and as such Δn_r is maximized. This realignment is not uniform across the electrode region of the cell, and will be affected by boundary conditions.

The initial anchoring produces homeotropic alignment at the boundaries. However, this anchoring is weak and does not govern the director alignment away from the surfaces above the Fréedericksz transition. Indeed, as the field increases, **n** will orient increasingly along the field lines. As both clockwise and anti-clockwise director rotations are equally probable, domain walls appear bounding different director orientations. This can result in a discontinuity in **n** known as a line defect or disclination. The director is undefined in this region and the disclination core can be approximated to the isotropic phase of the LC. It therefore causes scattering and appears dark. Walls also appear dark because these regions cause no relative phase delay between orthogonal polarization states incident upon the cell. Similarly, for point defects with finite size, a dark core will be seen.

The monochromatic polarized microscopy technique will be used extensively throughout this thesis. Data acquired from this method allows analysis of the director rotation in the LC cells designed to probe the physical effects seen in tunable devices. It will also provide insight into the properties of walls and defects and the role they play in defining the response of the associated integrated optical devices.

For example, data taken from a homeotropically aligned LC cell containing 5CB is shown in Fig. 4.16. An example image is given in Fig. 4.15. A narrow-band 639nm LED light source illuminates the cell, and the transmitted light is captured by a high-resolution colour camera. The figure illustrates the transmission across a slice transverse to the electrode axes. 50 vertical columns of pixels are averaged

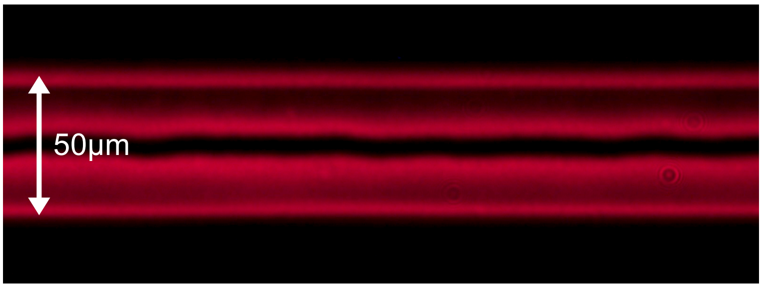

Figure 4.15: Example of a homeotropically aligned LC cell, viewed using cross-polarized microscopy, filled with 5CB under the application of 19V$_{pp}$ a.c. voltage. The voltage is applied to the ITO electrodes (which are at the top and bottom of the image).

to provide a transmission cross-section.

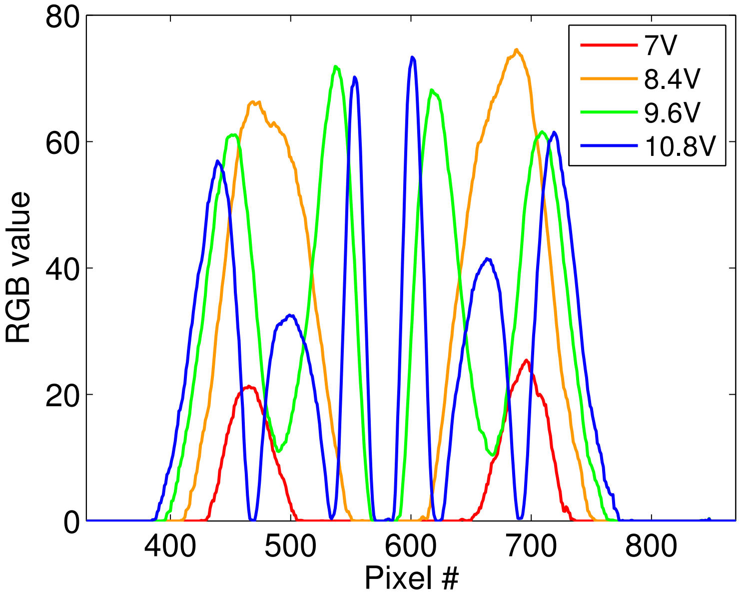

Figure 4.16: Transmission of a homeotropically aligned LC cell using a narrow-band LED light source with increasing applied voltage.

Using data from these images can aid analysis of LC molecular reorientation processes, and a summary of the analysis technique used in this work will now be given. For example, it can be seen that for all voltages (in the increasing voltage regime) the central region does not transmit. This is due to a wall structure being present between the electrodes which causes no rotation of the polarization as the wall maintains the original homeotropic alignment. The two regions either side of the wall become more transmissive as the LC rotates into the plane of the cell. Further rotation causes reduced transmission as seen in the 9.6V trace, this is because the polarization rotation at that position reaches 2π and causes extinction at the analyzer. Increasing the voltage further causes more rotation and additional transmission windows are seen (blue trace). It can also be seen that the wall in the centre becomes thinner with increasing voltage as its transverse distribution is restricted by the applied field. Hence monochromatic polarized microscopy is a powerful tool for analyzing the physical processes occuring in the cells fabricated during this thesis.

4.7 Summary

This chapter introduced the concept of nematic liquid crystals and how their dielectric anisotropy and birefringence is an invaluable tool in electro-optic devices. The effects of applying an electric field to liquid crystals has been described, including the Fréedericksz transition. An overview of liquid crystalline topological defects has also been provided, including disclination lines and inversion walls. Finally a description of how physical processes inside LC devices can be probed using polarized microscopy has been provided. Transmission cycling effects and extinction conditions have been described for a thin LC cell filled with a homeotropically aligned nematic LC.

References

[1] I.-C. Khoo. *Liquid Crystals*. Wiley, 2007.

[2] P. G. de Gennes. *The Physics of Liquid Crystals*. Oxford University Press, 1995.

[3] S. Chandrasekhar and G. S. Ranganath. “Discotic liquid crystals”. *Reports on Progress in Physics*, 53(1):57–84, January 1990.

[4] M. B. Ros, J. L. Serrano, M. R. de La Fuente, and C. L. Folcia. “Banana-shaped liquid crystals: a new field to explore”. *Journal of Materials Chemistry*, 15(48):5093, 2005.

[5] F. C. Frank. “I. Liquid crystals. On the theory of liquid crystals”. *Discussions of the Faraday Society*, 25:19, 1958.

[6] H. Stegemeyer. *Liquid Crystals*. Springer, New York, 1994.

[7] S.-T. Wu and D.-K. Yang. *Fundamentals of Liquid Crystal Devices*. Wiley, 2006.

[8] P. Yeh and C. Gu. *Optics of Liquid Crystal Displays*. Wiley, 2010.

[9] C. Hu and J. R. Whinnery. "Field-realigned nematic-liquid-crystal optical waveguides". *IEEE Journal of Quantum Electronics*, 10(7):556–562, 1974.

[10] T. Scharf. *Polarized Light in Liquid Crystals and Polymers*. Wiley, 2007.

[11] M. Kléman. *Defects in liquid crystals*, volume 52. Institute of Physics Publishing, 1989.

[12] M. Kléman and O. D. Lavrentovich. "Topological point defects in nematic liquid crystals". *Philosophical Magazine*, 86(25-26):4117–4137, 2006.

[13] O. D. Lavrentovich. "Defects in liquid crystals: surface and interfacial anchoring effects". *Patterns of Symmetry Breaking*, pages 161–195, 2003.

[14] H. Mori and H. Nakanishi. "On the Stability of Topologically Non-Trivial Point Defects", April 1988.

[15] R. Repnik, L. Mathelitsch, M. Svetec, and S. Kralj. "Physics of defects in nematic liquid crystals". *European Journal of Physics*, 24(4):481–492, July 2003.

[16] A. Rey. "Defect controlled dynamics of nematic liquids". *Liquid Crystals*, 7(3):315–334, 1990.

[17] S. Garg, E. Bramley, and U. D. Kini. "Electric Field Induced Walls in the Bend Geometry of a Nematic Liquid Crystal", December 1998.

[18] C. Chevallard, M. Clerc, P. Coullet, and J. M. Gilli. "Interface dynamics in liquid crystals". *The European Physical Journal E*, 1(2-3):179–188, 2000.

Chapter 5

Fabrication

This chapter will give an introduction to the various methods used for fabricating planar substrates, and the optical layers used to house waveguides and grating structures. A description of the process, from substrate manufacture through to finished waveguides with integrated Bragg gratings, will be presented. The techniques used to fabricate the devices in this thesis include Flame Hydrolysis Deposition (FHD), Direct UV Writing (DUW) and Direct Grating Writing (DGW). Other techniques will also be described briefly and compared.

Chapter 3 described common choices of substrate material for integrated optical components. The material used in this work is the silica-on-silicon platform or SiO_2:Si. There are several reasons for this choice of substrate. Firstly, it uses well-established technology derived from the silicon electronics industry and so production costs can be kept low [1]. Silicon wafers that would normally be used to accommodate billions of transistors can also be used for integrated optical (IO) substrates with silica layers, hence SiO_2:Si. There is inherent compatibility between these substrates and optical fibers as both use silica as the guiding medium. SiO_2:Si platforms also have the potential to accommodate optic and electronic functions on the same integrated optical device.

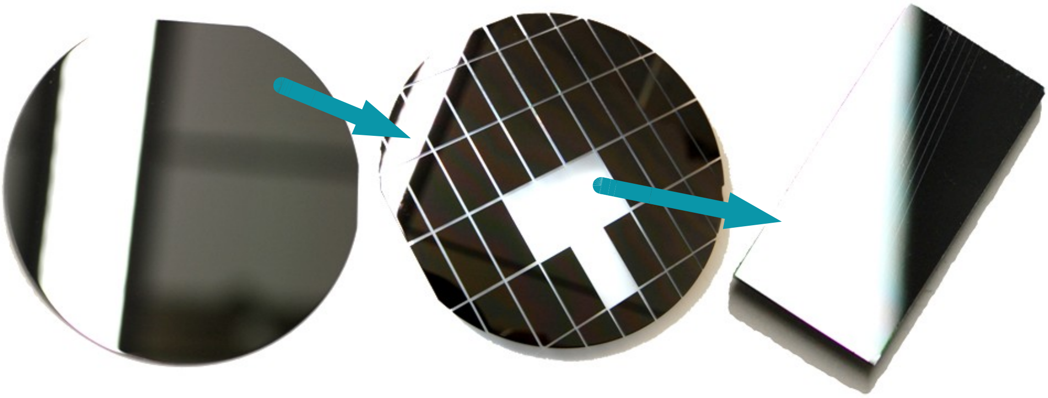

Figure 5.1: A 4-inch silicon wafer, a diced wafer forming 20x10mm samples, and a single substrate with UV-written waveguides

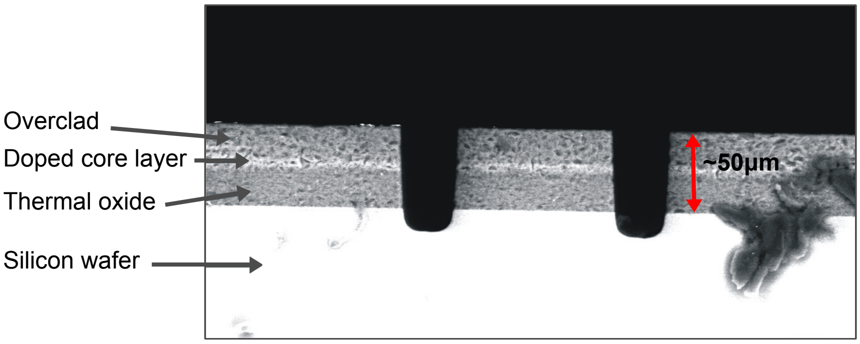

Figure 5.2: A Scanning Electron Microscope image of a standard three-layer silica-on-silicon sample. The sample contains two grooves from a machining process, as will be described in Chapter 8.

5.1 Silica-on-Silicon Substrates

The SiO_2:Si platform, as the name suggests, consists of silica-based layers atop a standard silicon wafer. Before applying the required silica layers, the wafer must be treated. Wafer treatment begins with a standard microelectronics process whereby a thin thermal oxide layer of silica is grown on the surface of the wafer. This is achieved by placing the wafers in a furnace in an ambient environment of either O_2 (dry oxidation) or H_2O (wet oxidation), and baking at a temperature of ~1100°C.

$$\begin{aligned} Si + O_2 &\rightarrow SiO_2 \\ Si + 2H_2O &\rightarrow SiO_2 + 2H_2 \end{aligned}$$

Elevated temperatures aid diffusion of the oxidant through the formed oxide layer to the silica-silicon interface. Even so, the oxidation rate is slow, roughly

85 hours for 1μm of oxide for dry oxidation at 1000°C [2]. Wet oxidation provides higher growth rates at the expense of poorer film quality. However, as this is not the guiding layer in our substrates and the planarity is not compromised, this does not pose a problem for the substrates used in this work. At the silica-silicon interface more oxide is formed, both growing up from the wafer and down into the silicon. The result is a silica layer over twice the thickness of the eaten silicon (1μm silica for every 0.44μm silicon consumed [2]). This causes a molecular volume mismatch and also thermal expansion variations, leading to compressive stress at the Si:SiO_2 boundary. Compressive stress is not necessarily detrimental to the layer quality as it can prevent formation and propagation of cracks in the layers.

The silica buffer layer in effect acts as a mediator to reduce stress in the post-deposited glassy layers. Adding this layer reduces the effects of thermal expansion mismatch, as silicon has a coefficient of thermal expansion over five times greater than that of silica. This not only reduces the potential for stress-induced birefringence, it also makes the core and cladding layers less susceptible to stress-based damage. Thermal oxide layers also extend the underclad, helping to simulate a semi-infinite cladding and preventing propagating modes leaking into the silicon. The oxide thickness for samples used in this work is typically ~15μm.

Now the base substrate for the IO devices has been formed, additional glass layers must be deposited on top to act as the core and cladding layers for planar waveguides. Simple oxidation is not suited to adding dopants to specific layers as diffusion of dopant molecules becomes a problem. Hence a layer-by-layer deposition technique is used to add the core and cladding layers to the oxidized silicon wafer.

5.2 Alternative Method for Silica Fabrication

Before discussing the FHD process used in this work it is useful to discuss the alternative approach. Plasma Enhanced Chemical Vapour Deposition (PECVD) is, as the name suggests, a derivative of Chemical Vapour Deposition (CVD) [3]. PECVD is a standard process in the microelectronics industry and a schematic of a typical chamber is shown in Fig. 5.3. With CVD, target substrates are placed into a vacuum chamber which is then fed volatile precursors, typically SiH_4, N_2O and a carrier gas, for example N_2, Ar or He. The gases decompose and react to deposit a film on the substrate. PECVD differs from CVD by utilizing r.f. electrical fields to ionize the gases, forming a plasma. This allows decomposition and reaction at lower temperatures than attainable with regular CVD.

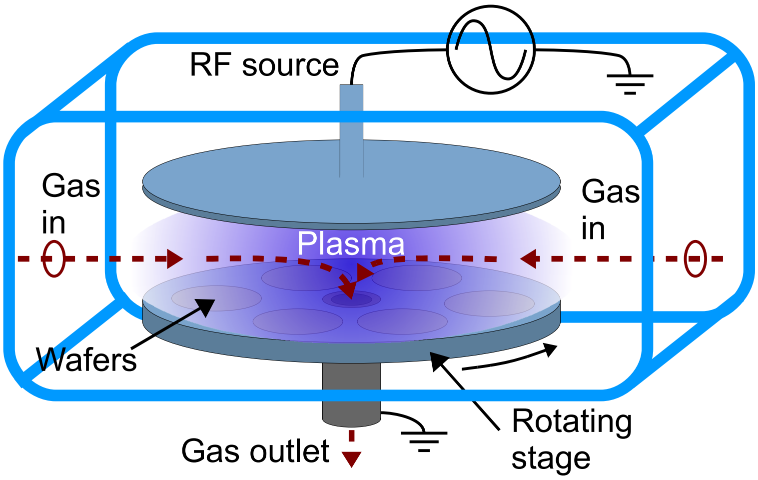

Figure 5.3: Plasma Enhanced Chemical Vapour Deposition

Glass layers formed by PECVD often contain significant amounts of hydrogen and nitrogen. Their associated bonds in the glass network cause absorption in the near-IR which is problematic for telecommunications devices. N-H, Si-H and O-H bonds all contribute to absorption losses which can be broad enough spectrally to interfere with the C-band (1525-1565nm) [4]. PECVD layers can also produce layers with defects and voids that cause scattering losses, while also making the material susceptible to water ingress. These problems can be reduced by annealing at high temperatures [5], however this negates the benefit of being able to deposit layers at 300°C or less. More recently, the use of nitrogen-based oxidants has been removed, reducing the losses of PECVD formed layers and making them suitable substrates for waveguiding applications [6]. Removing the nitrogen-based oxidants also removes the need for post-annealing.

As PECVD does not require a halide precursor, a wider variety of dopants can be used. However, PECVD is limited by the deposition thickness possible. Typically only a few µm can be deposited in any one step, whereas FHD can deposit the required 15µm in a single step. More than a few µm in a single deposition step can cause blistering and delamination [7]. This can be caused by hydrogen being hindered in its escape from the glass layer as it is being consolidated. Thus the PECVD technique can become more expensive and time consuming than FHD.

5.3 Flame Hydrolysis Deposition

An alternative to PECVD is the Flame Hydrolysis Deposition (FHD) process noted above [8], which is the method used to fabricate the substrates in this thesis. It is a common process used to deposit glass layers onto planar substrates. This is because it has the potential for high deposition rates, low loss layers and forms layers with low stresses.

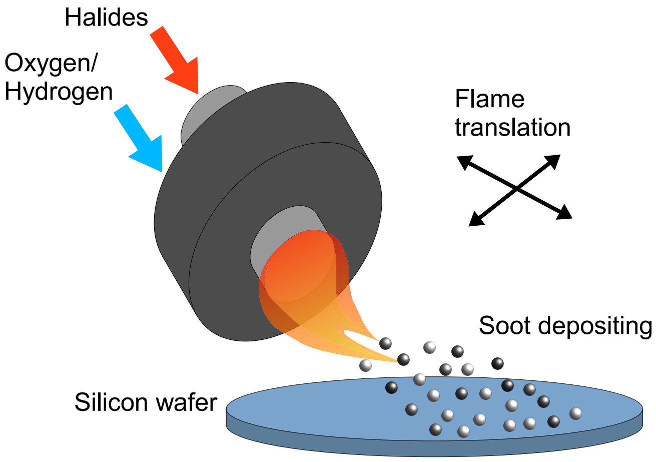

Figure 5.4: Flame Hydrolysis Deposition

An oxygen-hydrogen flame directed at the surface of the thermally oxidized silicon is fed halide precursors of the desired materials. These halides react via flame hydrolysis or oxidation to produce silica-based soot particles that are deposited onto the wafer. Using a flame above 1200°C favours direct oxidation, whereas with a lower temperature hydrolysis dominates [9]. Often a flame of > 2000°C is used, ensuring direct oxidation. For example, silicon tetrachloride, $SiCl_4$, can be oxidized or hydrolysed to produce silica:

$$\begin{aligned} SiCl_4 + O_2 &\rightarrow SiO_2 + 2Cl_2 \\ SiCl_4 + 2H_2O &\rightarrow SiO_2 + 4HCl \end{aligned}$$

Each deposited layer can also have dopants added with controlled concentrations by using the relevant halide. Germanium, phosphorus and boron are often used as additives and their respective oxides are also formed by either hydrolysis or oxidation. Doped or undoped layers are deposited successively onto the wafer and are treated individually. For these porous sooty deposited layers to act as glassy waveguiding layers, they must be consolidated by sintering or annealing. After each layer is deposited, the wafer is transferred to a furnace at ~1300°C to anneal it. The melting point of each layer is controlled such that the next deposited layer has a lower consolidation temperature than the previous layer. This reduces the effects of diffusion into previous layers.

Dopants affect particular properties of each layer, notably refractive index, thermal expansion coefficient and melting point. These effects are summarized in Table 5.1. From a post-processing perspective the important parameters are refractive index and photosensitivity. The refractive index profile determines the waveguiding characteristics of devices fabricated in the substrate, while the photosensitivity determines the ability to define buried channel waveguides and Bragg gratings using DUW and DGW respectively. Germanium is often used to enhance the photosensitivity of the silica layer, and boron exhibits a similar (but lesser) effect [10]. The role of phosphorus in photosensitivity is somewhat less clear, and seems to depend on factors such as the wavelength of the UV light and the prior treatment of the sample [11,12].

Substrates for DGW are typically either three layer or four layer silica-on-silicon. The underclad or second layer can be omitted and the oxide layer grown thicker to create a three layer sample. The core layer will contain the most germanium to increase the photosensitivity to UV radiation. The importance of this will be explained later in section 5.6. In this work the core layer is typically 5-7μm thick such that UV written channels support only single mode operation, whereas the cladding layers are typically 15μm thick so that the fundamental mode effectively sees an infinite cladding and therefore no modal power is lost.

To create these channel waveguides and Bragg gratings, an extra fabrication step is required. This involves the use of the DUW and DGW techniques noted earlier. They are powerful fabrication tools which allow for simultaneous definition of both the waveguides and gratings in a single process. This process will be explained in Chapter 6.

Dopant	**Refractive index**	**Melting point**	**Thermal expansion**
Germanium	Increases	Decreases	Increases
Phophorus	Increases	Decreases	Increases
Boron	Decreases	Decreases	Increases

Table 5.1: Effects of common dopants on silica substrate layer properties [10, 13]

The FHD facility at the University of Southampton was destroyed in the fire of 2005. Hence all the substrates used in this work were purchased from CIP Ltd..

5.4 Photosensitivity

Photosensitivity is the process whereby a material undergoes a change upon exposure to radiation. In relation to this work, it is the light-induced permanent refractive index change observed in silica-based glasses. This phenomenon requires particular attention, for it is this phenomenon that allows these planar layers with one-dimensional confinement to be transformed into waveguides with two-dimensional confinement.

At the wavelengths of interest silica itself is not sufficiently photosensitive. However, by doping silica with germanium, as noted earlier, the resultant glass mixture is sensitive to light. This phenomenon was first observed by Hill and co-workers in 1978 [14, 15]. They saw a permanent, and gradually increasing reflection in a 1 metre long section of germanium-doped low-mode-number silica fiber while exposing it to 488nm radiation from an Ar-ion laser.

The germanium-doped core of the fiber contained a longitudinal standing-wave pattern caused by Fresnel reflection from the far end. This standing-wave pattern increased the refractive index in areas of high intensity field, whilst leaving the remainder unchanged. The refractive index modulation proved to be self-enhancing. Over time this produced a Bragg reflection grating at the correct pitch to reflect the input light, thus reducing the transmitted power and creating a Bragg reflector.

The process of using germanium-doped materials to fabricate Bragg gratings has found applications in the telecommunications industry [16]. However, gratings written for telecommunications will obviously require different attributes, most notably the ability to reflect in the infra-red (IR) as opposed to the visible. As Hill's grating was a self-enhancing structure, it naturally reflected at the exposure wavelength. Silica-based telecom fibers are not sufficiently photosensitive at IR wavelengths to produce self-forming gratings and so they must be irradiated at a suitable absorbing wavelength.

Experiments by Lam and Garside [17] showed that the magnitude of the photoinduced refractive index change is proportional to the square of the illumination intensity at Ar-ion wavelengths (488 and 514.5nm). This suggested the absorption and resultant index change was caused by a two-photon process. Accordingly, the photosensitivity mechanism should be a one-photon process in the UV at 244nm and hence more efficient. This means that the photoinduced index change would need to be achieved by an external writing process, as opposed to Hill *et al*'s internal writing mechanism.

Bragg grating devices for telecommunications applications can be fabricated using the side-writing technique. This was first introduced by Meltz *et al* [18] to define in-fiber gratings in Ge-doped silica fiber. The process linking the UV absorption to the IR refractive index change is governed by the Kramers-Kronig dispersion relationship [19]. Kramers-Kronig relations link the real and imaginary parts of a complex function. In this case, the important property is the complex refractive index where the real part is the refractive index and the imaginary part is the absorption.

When the absorption band at 244nm is bleached by UV light, the absorption spectra of the material changes. Other absorption bands are created because different bonds between constituent compounds are formed. The change in absorption results in a refractive index change through the Kramers-Kronig relationship. This index change has a non-negligible effect in the visible and near IR wavelengths, hence this effect provides a means of inscribing integrated optical waveguides and Bragg gratings using UV exposure techniques.

There are other proposed mechanisms for photosensitivity and these include the densification or compaction model [20] and the stress relief model [21].

The compaction model is based on density changes within the germanosilicates caused by laser irradiation. This in turn leads to refractive index changes. The stress relief model is based on refractive index changes caused by alleviation of intrinsic thermoelastic stresses caused during fabrication. Deposited layers have different thermal expansion coefficients and upon cooling shrink by differing amounts causing stress between layers. UV irradiation is thought to relax this stress by breaking the aforementioned defect bonds and thus through the stress-optic effect changes the refractive index.

Although the photosensitivity of germanosilicates is sufficient to allow UV inscribed gratings, it can be further enhanced without adding yet more germanium. The process used to enhance photosensitivity in this thesis is that of hydrogen loading.

5.4.1 Hydrogen Loading

Adding more germanium seems like the obvious choice to increase photosensitivity. However, this creates problems such as degrading the glass-forming properties of the layer and also increasing optical loss. Therefore to increase the photosensitivity without increasing dopant levels, the process of hydrogen loading was developed. This was first reported by Lemaire in 1993 [22] whereby germanium doped silica fibers were exposed to a high pressure hydrogen environment. This increased the refractive index change, upon UV writing, of the samples by an order of magnitude to $\sim 6\times10^{-3}$.

The proposed mechanism for hydrogen enhanced photosensitivity in Ge-doped glasses is that upon UV exposure H_2 molecules react at Si–O–Ge sites, creating Si–OH and oxygen deficient Ge defects [21]. These germanium oxygen deficient centres (GODCs) have peak absorption resonances at ~240nm, and thus are sensitive to UV radiation. However, hydroxyl groups are known to cause losses at telecomms wavelengths from an absorption peak at 1.4μm [23]. For the purpose of the devices in this thesis, which are only tens of millimetres long at most, this additional attenuation is not too detrimental to the device performance.

The hydroxyl groups, and their associated losses, can be overcome by substituting hydrogen with deuterium, which has a similar photosensitivity enhancing property. As deuterium is heavier than hydrogen it has a lower resonant frequency for the OD or 'deuteroxyl' bond. Therefore its peak absorption is shifted beyond 1.6μm and so does not affect the telecomms transmission bands. Hydrogen was used for all samples in this work as the aim was to produce prototype devices and so the use of deuterium was deemed unnecessary and too costly.

5.5 Photolithography and Etching

So far the discussion has introduced planar layer deposition techniques, however a planar waveguide alone does not provide sufficient functionality to realise many of the components needed for an IO device. Planar layers, by definition, provide one-dimensional confinement of propagating light. Waveguides and grating structures in this work require two-dimensional confinement.

The conventional technique for fabricating planar waveguides involves standard photolithographic processes [24] and wafer processing steps described earlier. A silicon wafer is oxidized at 1100°C in a water steam atmosphere and a layer of silica is grown on top of the wafer. A core layer with elevated refractive index is deposited on top of the buffer layer. Common deposition processes are the aforementioned PECVD and FHD techniques. The core layer can be coated with a thin layer of e.g., nickel, chromium or polysilicon and subsequently patterned by lithography, using a plasma or wet etch to form the etch mask. The core layer etch is typically achieved by Reactive Ion Etching (RIE), which removes the unwanted core layer areas and leaves ridge waveguide structures. The etch mask can then be removed either in the etch chamber by changing the process gas/gases, or stripped with a solvent wash. Waveguides are then covered by a cladding layer which can be deposited by CVD, resulting in buried channel waveguide structures.

Photolithographic techniques are suitable for batch fabrication resulting in low device costs. They also do not require photosensitive layers for waveguide definition. However, masks, mask aligners and associated clean room facilities become costly, especially when making prototypes and small batches. Photolithography also is more susceptible to roughness at the sides of the waveguide, and waviness or inconsistent waveguide thickness. Sidewall roughness can be a result of the etching process which can induce scattering loss. This can have negative consequences, especially in sensitive grating structures where a controlled coupling coefficient is critical.

5.6 Direct UV Writing

The technique used to define buried channel waveguides in this work is known as Direct UV Writing (DUW). DUW exploits the UV photosensitivity of the hydrogen loaded FHD samples decribed previously. The technique was developed by Svalgaard in the 1990's [25], and has similarities to the UV writing techniques used for fiber Bragg grating inscription.

Direct UV writing (DUW) uses a frequency doubled argon-ion (Ar^+) laser operating at 488nm, in this case a Lexel™ 95-SHG laser. This produces a 244nm output which overlaps the absorption resonance of the photosensitive core in the three-layer silica-on-silicon, as discussed previously. An Ar^+ laser is used as it has good spatial coherence, with a coherence length suitable for writing Bragg gratings with an interferometric technique (discussed later). They also have good beam pointing stability such that devices requiring extended exposure times are possible. Frequency doubling is obtained from an intra-cavity β-barium-borate (BBO) crystal. The crystal is cut at such an angle to provide phase matching between the fundamental and doubled wavelengths.

Focussing the laser beam into the Ge-doped core of the three-layer substrate causes a local refractive index change. If the sample is translated underneath the static, focussed laser writing spot a structure with two-dimensional confinement can be produced. For a typical three-layer substrate, this technique produces a buried channel waveguide whose height is governed by the thickness of the photosensitive core layer and width by the diameter of the writing spot. The sample is translated using high precision stages under computer control.

The refractive index contrast between written and unwritten substrate is typically of the order 10^{-3}. Refractive index contrast is dependent on the UV illumination intensity at a given point on the substrate. The refractive index change is proportional to the intensity and duration of the UV exposure, until the index change saturates. These UV exposure parameters are summarised succinctly by the concept of fluence [7], which quantifies the energy illuminating the sample. It is dependent on the laser intensity and also the translation speed of the sample. Fluence is defined as:

$$F = \frac{I_{\mathrm{UV}} \times a}{v_{\mathrm{trans}}} \tag{5.1}$$

where I_{UV} is the average power density of the focussed laser spot, a is the spot diameter and v_{trans} is the sample translation speed. Fluence is typically measured in units of $\mathrm{kJcm^{-2}}$.

DUW has several advantages over photolithography-based waveguide definition. DUW does not require any additional processing steps, aside from the hydrogen loading for increased UV sensitization. Devices are ready to use once the writing process is complete meaning fabrication times for small numbers of devices are very small. As DUW does not require masks there is far more flexibility in waveguide design. Consecutive samples can have completely different UV written patterns, with little or no extra setup time or cost. Also, as the waveguide roughness is defined by the FHD deposition and not by post-processing, the waveguides are intrinsically optically smooth.

5.7 Direct Grating Writing

Direct Grating Writing (DGW) is an extension of the DUW writing technique discussed above. It is a technique that allows for simultaneous definition of both channel waveguides and Bragg grating structures. DGW uses a similar setup to that used by DUW, with additional components to transform it into an interferometric system. These components comprise an Acousto-Optic modulator (AOM) to allow modulation of beam intensity, and a beam splitter and additional optics to create an interference pattern. The precision air-bearing stage system is used to translate the sample underneath the beams, producing channel waveguides as before if no modulation is used, or Bragg gratings if the beam power is modulated. The DGW setup is shown in Fig. 5.5.

As with DUW, an $\mathrm{Ar^+}$ laser 488nm output line is frequency doubled to produce

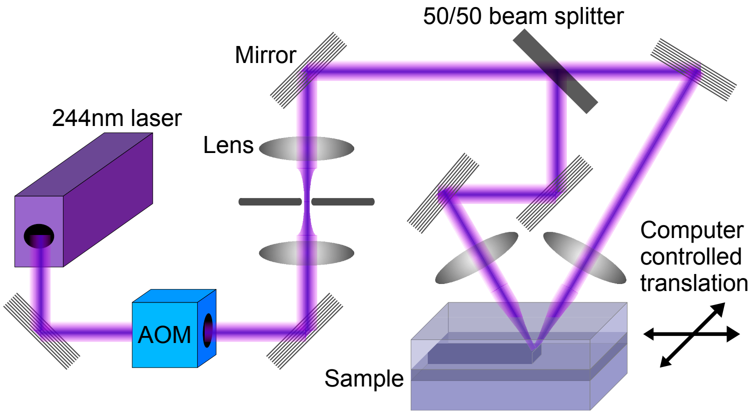

Figure 5.5: The Direct Grating Writing system

244nm light. The laser beam then travels into the AOM to provide modulation of the beam intensity. It is then focussed into a spatial filter to remove unwanted beam structure added by the BBO crystal. The result is a fundamental mode with approximately Gaussian cross-section. The beam is then split by a 50:50 beam splitter and the resulting beams are focussed such that they overlap in the photosensitive layer of the substrate. This produces an interference pattern in the sample whose period is determined by the wavelength of light and the angle between the beams:

$$\Lambda = \frac{\lambda_{UV}}{2\sin(\theta/2)} \tag{5.2}$$

With a writing wavelength of 244nm, and an angle between the beams of ~26°, the resultant spot has interference fringes with Λ_{spot} = 542nm. Therefore a focussed spot diameter of order ~5μm would contain less than 10 periods. The angle is chosen to allow fabrication of gratings that reflect in the telecommunications C-band (1525-1565nm). Comparatively, side writing techniques used in fiber Bragg grating fabrication typically use a ~100μm spot. Thus the DGW technique provides greater scope for modifying grating parameters, such as period, when engineering a grating structure.

As the angle between the crossed beams is fixed by the interferometer, the written grating wavelength must be tuned by other means. Using the equation for Bragg reflection [10]

$$\lambda_{Bragg} = 2n_{eff}\Lambda_{grating} \tag{5.3}$$

it can be seen that the peak reflection wavelength can be modified by two means.

Firstly, Λ_{grating} can be changed, not by angular tuning, but by detuning the imprint of the interference pattern.

The second method of changing the Bragg wavelength is by modifying n_{eff}. The effective refractive index of the written waveguide is modified by the fluence. As the laser power is kept constant during writing, the fluence is controlled by adjusting the translation speed. In practise both AOM firing frequency and translation speed are used to tailor the response of the Bragg gratings.

So far the discussion of DGW has involved only uniform Bragg gratings. However, with minor alterations to system parameters, Bragg gratings with different responses can be fabricated. In this thesis there are demonstrations of uniform, apodized, chirped and chirp-apodized gratings, all made with the same DGW system. To produce more complex gratings with precise spectral features, several other writing concepts must be introduced. These are explained in Chapter 6.

5.7.1 Grating Engineering

One of the fundamental properties governing a grating's response is the effective refractive index, not only of the grating but also of the channel waveguides leading to the grating. Gratings will often have channel waveguides attached to either end to provide coupling. Ideally there should be no abrupt transition between the two components to avoid unwanted Fresnel reflections. As explained by Fourier theory, the spatial components of a waveguide structure can be converted into their corresponding frequency components. Bragg gratings are defined by their spectral response which is determined by the spatial properties of the grating planes.

An abrupt change in coupling coefficient between waveguide and grating will produce a refractive index mismatch such that the index profile will resemble a top-hat function. Transformed into the frequency domain, this results in a function with a sinc^2 profile. This is not ideal for a Bragg grating in either a telecomms or sensing system as the required bandwidth increases and fitting algorithms become more complex. Therefore to avoid these unwanted spectral features the Bragg grating and channel waveguide can be 'fluence matched'.

When the laser power is pulsed to produce gratings, the effective fluence reduces because the substrate is not continuously exposed. Therefore if all other parameters are identical for both waveguides and gratings, there would be a fluence mismatch causing unwanted spectral features, as discussed above. The gratings are therefore fluence matched to the waveguides such that both components have the same effective refractive index. This can be achieved by several methods, as will be explained in Chapter 6.

5.7.2 Grating Response

By varying fluence, duty cycle, pitch, and translation speed during UV writing, various different types of grating can be fabricated. By altering these parameters along the length of a grating during writing, tailored spectral responses can be achieved. Uniform Bragg gratings, even without a fluence mismatch, have a characteristic sinc^2 spectral shape. Following from the discussion of grating response in Chapter 3 this can be approximated by Fourier theory as the convolution of a top-hat function with a sinusoid formed from the grating planes. The result is a sinc^2 function centered around the frequency of the sinusoid. Squaring the sinc function provides the intensity distribution associated with uniform Bragg gratings, as shown in Fig. 5.6.

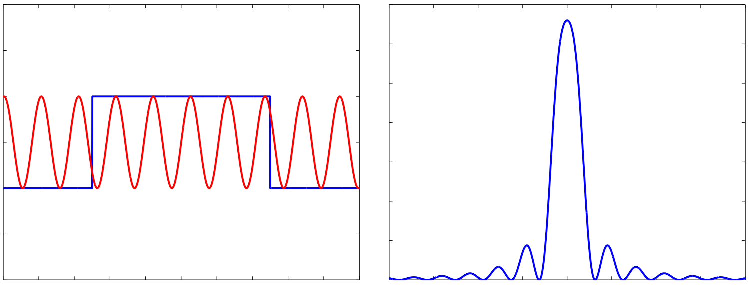

Figure 5.6: A top-hat and sinusoid (left), and a sinc^2 function (right)

Around the central peak of the sinc function are side lobes. These can be problematic, for example if gratings are spectrally close the side lobes can overlap which distorts the grating's spectral shape. In reality uniform Bragg gratings are rarely used due to the side lobes. To suppress the side lobes a process known as apodization is used. Apodization is a windowing or envelope function used to change the shape of another function. In the context of Bragg gratings, apodization is used to taper the coupling strength of a grating as a function of position. This reduces the abrupt interface between waveguide and grating such that the discontinuous top-hat profile is replaced with a smoothly varying, continuous function. Common apodization profiles are Gaussian, cosine and raised-cosine. The work in this thesis generally employed a Gaussian apodization profile during grating writing.

Uniform Bragg gratings have a predefined bandwidth, which is governed either by the length of the grating or the refractive index modulation depth, as discussed in Chapter 3. However, certain devices require Bragg gratings with larger bandwidths, such as in pulse compression or dispersion management. This can be achieved by a process known as 'chirping'. Whereas apodized gratings have a position dependent grating strength, chirped gratings have a position dependent grating period. The result is a grating whose reflection wavelength is position dependent, which has the effect of broadening the reflection bandwidth.

Chirp is achieved by changing the grating period as the sample is being written. Linear chirp is used in this thesis which is defined as a linear increase (positive chirp) or decrease (negative chirp) in grating period as a function of position. Because this causes different wavelengths of light to be reflected from different positions, chirp also has the effect of changing the group delay of the reflected light as a function of wavelength. For a grating with positive chirp, longer wavelengths have to travel further into the grating before they are reflected. This has the effect of increasing the delay for longer wavelengths. In the case of linear chirp, the group delay is a linear function of wavelength in the reflection band.

5.8 Summary

A review of the fabrication process for planar integrated optical devices has been presented, starting from a standard silicon wafer and ending with a fully integrated LC-based adaptive optical device. To fabricate the standard three-layer silica-on-silicon substrates, the silicon wafers are oxidized to grow a silica surface layer. Additional layers are deposited using the FHD process which creates sooty layers that are consolidated to form dense glassy layers. The core layer is doped with germanium to provide photosensitivity in the UV. This photosensitivity is further enhanced with a hydrogen loading process.

The photosensitivity is exploited by both the DUW and DGW techniques to define buried channel waveguide and Bragg grating structures. Using focussed UV laser light, single-mode channel waveguides operating in the near-IR can be written. The writing system can be customized such that advanced grating structures, including apodized and chirped gratings, can be fabricated.

Further explanation of the specific fabrication processes used in this thesis will be given in Chapter 6.

References

[1] Y. P. Li and C. H. Henry. "Silica-based optical integrated circuits". *IEE Proceedings - Optoelectronics*, 143(5):263–280, 1996.

[2] P. Rai-Choudhury. *MEMS and MOEMS technology and applications*. SPIE Publications, Bellingham, Washington, 2000.

[3] R. F. Bunshah. "Critical Issues in Plasma-Assisted Vapor Deposition Processes". *IEEE Transactions on Plasma Science*, 18(6):846–854, 1990.

[4] L. Pavesi and D. J. Lockwood. *Silicon Photonics*. Springer, 2004.

[5] G. Grand, J. P. Jadot, H. Denis, S. Valette, A. Fournier, and A. M. Grouillet. "Low-Loss PECVD Silica Channel Waveguides for Optical Communications". *Electronics Letters*, 26(25):2135, 1990.

[6] M. V. Bazylenko, M. Gross, P. M. Allen, and P. L. Chu. "Fabrication of Low-Temperature PECVD Channel Waveguides with Significantly Improved Loss in the 1.50-1.55-μm Wavelength Range". *IEEE Photonics Technology Letters*, 7(7):774–776, July 1995.

[7] I. J. G. Sparrow. *Development and Applications of UV Written Waveguides*. PhD thesis, University Of Southampton, 2005.

[8] P. Tandon and H. Boek. "Experimental and theoretical studies of flame hydrolysis deposition process for making glasses for optical planar devices". *Journal of Non-Crystalline Solids*, 317(3):275–289, March 2003.

[9] J. Bautista and R. Atkins. "The Formation and Deposition of SiO2 Aerosols in Optical Fiber Manufacturing Torches". *Journal of Aerosol Science*, 22(5):667–675, 1991.

[10] A. Othonos and K. Kalli. *Fiber Bragg gratings: fundamentals and applications in telecommunications and sensing*. Artech house, 1999.

[11] B. Malo, J. Albert, F. Bilodeau, T. Kitagawa, D. C. Johnson, K. O. Hill, K. Hattori, Y. Hibino, and S. Gujrathi. "Photosensitivity in phosphorus-doped silica glass and optical waveguides". *Applied Physics Letters*, 65(4):394, 1994.

[12] G. Pacchioni, L. Skuja, and D. L. Griscom. *Defects in SiO2 and Related Dielectrics: Science and Technology*. Springer, 2000.

[13] S. P. Watts. *Flame hydrolysis deposition of photosensitive silicate layers suitable for the definition of waveguiding structures through direct ultraviolet writing*. PhD thesis, University Of Southampton, 2002.

[14] K. O. Hill, Y. Fujii, D. C. Johnson, and B. S. Kawasaki. "Photosensitivity in optical fiber waveguides: Application to reflection filter fabrication". *Applied Physics Letters*, 32(10):647, 1978.

[15] K. O. Hill, B. Malo, F. Bilodeau, and D. C. Johnson. "Photosensitivity in Optical Fibers". *Annual Review of Materials Science*, 23(1):125–157, 1993.

[16] A. Othonos. "Fiber Bragg gratings". *Review of Scientific Instruments*, 68(12):4309–4341, 1997.

[17] D. K. W. Lam and B. K. Garside. "Characterization of single-mode optical fiber filters". *Applied Optics*, 20(3):440, February 1981.

[18] G. Meltz, W. W. Morey, and W. H. Glenn. "Formation of Bragg gratings in optical fibers by a transverse holographic method.". *Optics letters*, 14(15):823–5, August 1989.

[19] D. P. Hand and P. S. Russell. "Photoinduced refractive-index changes in germanosilicate fibers.". *Optics letters*, 15(2):102, January 1990.

[20] M. Douay, W. X. Xie, T. Taunay, P. Bernage, P. Niay, P. Cordier, B. Poumellec, L. Dong, J. F. Bayon, H. Poignant, and E. Delevaque. "Densification Involved

in the UV-Based Photosensitivity of Silica Glasses and Optical Fibers". *Journal of Lightwave Technology*, 15(8):1329–1342, 1997.

[21] M. G. Sceats, G. R. Atkins, and S. B. Poole. "Photolytic Index Changes in Optical Fibers". *Annual Review of Materials Science*, 23(1):381–410, August 1993.

[22] P. J. Lemaire, R. M. Atkins, V. Mizrahi, and W. A. Reed. "High Pressure H2 Loading as a Technique for Achieving Ultrahigh UV Photosensitivity and Thermal Sensitivity in GeO2 Doped Optical Fibres". *Electronics Letters*, 29(13):1191–1193, 1993.

[23] A. Ghatak and K. Thyagarajan. *Introduction to Fiber Optics*. Cambridge, UK, 1998.

[24] M. R. Poulsen, P. I. Borel, J. Fage-Pedersen, J. Hubner, M. Kristensen, J. H. Povlsen, K. Rottwitt, M. Svalgaard, and W. Svendsen. "Advances in silica-based integrated optics". *Optical Engineering*, 42(10):2821, 2003.

[25] M. Svalgaard, C. V. Poulsen, A. Bjarklev, and O. Poulsen. "Direct UV writing of buried singlemode channel waveguides in Ge-doped silica films". *Electronics Letters*, 30(17):1401, 1994.

Chapter 6

Advanced Fabrication Techniques

This chapter will further explain the fabrication techniques introduced in Chapter 5. Explained in detail is the Direct Grating Writing (DGW) system which is an integral part of the work in this thesis. The interaction between control software, laser modulation and substrate translation is described along with how each section operates.

Further detail will be given of the fabrication techniques used for LC cells and, in particular, LC tunable Bragg grating devices. Critical parameters are the surface treatment, either surfactant-based or polymer-based, and surface quality of the substrates and electrodes. The chapter will conclude with a description of the measurement techniques used throughout this work.

6.1 Direct Grating Writing

In order to expand on the Direct Grating Writing (DGW) process it is helpful to review the specific details of the writing system. The DGW setup is shown in Fig. 6.1. Firstly, the system is controlled by a computer using a FireWire™ interface. The computer contains software that uses a set of functions called G-code, which is part of the CNC (Computer Numerical Control) machine tool language. G-code controls both the Acousto-Optic Modulator (AOM) and the movement of the stages holding the sample. These must be linked in order to define Bragg grating structures.

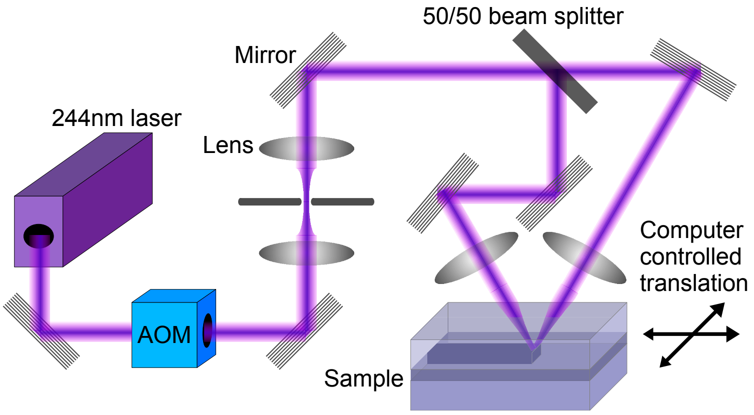

Figure 6.1: The Direct Grating Writing system

The computer program contains commands for both the movement of the stages and the firing positions for the AOM. These positions are uploaded as an array to an Aerotech A3200-npaq multi-axis machine controller prior to writing. Firing positions are where the Position Synchronized Output (PSO) from the A3200 changes state. In order to correlate the firing positions with the movement of the stages, as is needed for grating inscription, the A3200 acquires the position of the stage from a linear glass encoder on the Aerotech ABL9000 series air-bearing stage system. It then compares the current position to the positions defined in the array that was uploaded prior to writing. Once the positions correlate, the PSO output from the stage controller changes state. The PSO output is linked to the AOM and thus the AOM changes state.

This allows the AOM to modulate the beam intensity as a function of stage position whilst the stages are being translated. The AOM diffracts the beam when switched on and leaves it unaltered when switched off. In this setup the first order diffraction as used. Although the first order diffraction will only diffract a maximum of ~80% of the incoming beam power, it allows complete extinction of the beam when the diffraction is switched off. This is preferable to using the zeroth order which provides the maximum transmitted power but provides reduced contrast as it cannot fully extinguish the beam. The laser power is pulsed by the AOM which determines when the sample is illuminated with the interference pattern. The interference pattern is created by recombining the two beams after being split by an equally weighted beam splitter. One arm of the interferometer contains two mirrors in order to invert the beam's pattern in that arm. This ensures that when the beams are recombined the interference patterns overlap such that the spatial distributions of both patterns correlate.

For the purpose of Bragg grating inscription, the AOM is pulsed at the correct period that produces an aligned overlap of successive interference fringes. However, as discussed earlier, if the angle between the beams is fixed and only perfectly aligned overlap is used, there will be only one possible writing wavelength. Therefore the interference pattern is slightly detuned such that the grating period is not fixed according to $\Lambda_{spot} = \lambda_{UV}/2\sin(\theta/2)$ but is dependent on the degree of detuning. Detuning is achieved by slightly altering the AOM firing frequency with respect to the sample translation speed. Detuning of interference fringes will cause weakened grating planes, but not sufficiently so as to cause significant degradation of the grating response [1]. This is because the beam diameter and therefore the number of fringes in the beam is small (~10).

The system has demonstrated the ability to write both buried channel waveguides and Bragg gratings simultaneously. However, as the grating uses pulsed illumination for the grating and continuous illumination for the waveguide the two sections will be exposed to different average light intensities. Due to the photosensitivity of the germanium doped sample this leads to different average refractive index changes. This is the issue of fluence mismatch as described in Chapter 5.

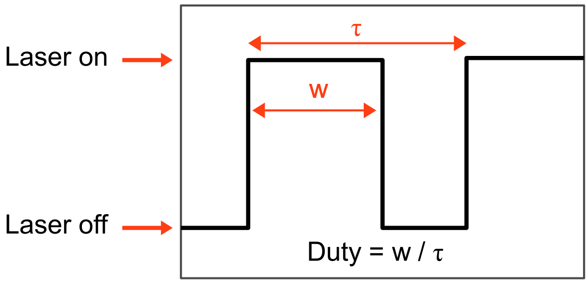

Figure 6.2: The concept of duty cycle. Duty cycle is the time the laser spends in the on state, w, as a percentage of a complete cycle, τ.

Another important parameter in grating fabrication is what is known as 'duty cycle', which is analogous to pulse width and is shown in Fig. 6.2. Duty cycle represents the ratio of laser on time to laser off time for a single grating period. A duty cycle equal to 1 implies the laser is fully on, thus the interference pattern is washed out and only a channel waveguide is written. A duty cycle of 0 implies no laser power, and thus no modification of refractive index structure. It would be expected that the lower the duty cycle the higher the index contrast [1]. However, the grating must still be fluence matched to the waveguide, and so the index contrast must increase. This requires an increase in fluence and therefore a reduction in translation speed. Low translation speeds pose problems as it implies a longer writing time. Increased writing times have the issue of hydrogen diffusing out from the samples, reducing photosensitivity, and also require a high degree of laser stability. Typical duty cycle and fluence values are 0.4-0.5 and 18kJcm^{-2}, respectively which represents an effective compromise between grating strength and interferometric stability.

Prior to this thesis, fluence matching was achieved by adjusting the diffraction strength of the AOM. The AOM would be fed digital data determining the on/off firing positions, and an analogue signal to control the diffraction strength. However, this technique is slow as the AOM is continually fed analogue data along the grating length. Other problems included instability in the diffraction strength due to thermal fluctuations, and the voltage-diffraction strength response of the AOM being non-linear and containing hysteresis. Instead, the system now uses control of the translation speed to change the fluence. This avoids any impedance mismatch between waveguide and grating, and also reduces error in the grating strength profile. An example of impedance control is shown in Fig. 6.3. With the writing power normalized to unity for a channel waveguide, it can be seen that the average writing power is halved for a fully modulated beam during grating inscription. The translation speed would therefore need to be halved in order to avoid fluence mismatch.

The substrates used for DGW in this work were hydrogenated FHD samples and were hydrogen loaded for a minimum of 5 days at a pressure of 120bar. They exhibited photosensitivity that produced index changes of the order ×10^{-3}, after UV writing. This allows for the fabrication of buried channel waveguides and Bragg gratings using the DGW technique. The core thickness, as described earlier, is 5-7μm and the focussed laser spot is ~5μm. Hence this technique produces reasonably radially symmetric channel waveguides whose effective modal area is similar to that of standard telecomms fiber.

It should be noted that the hydrogen indiffusion is a reversible process. Once removed from the pressurized hydrogen environment, the hydrogen will imme-

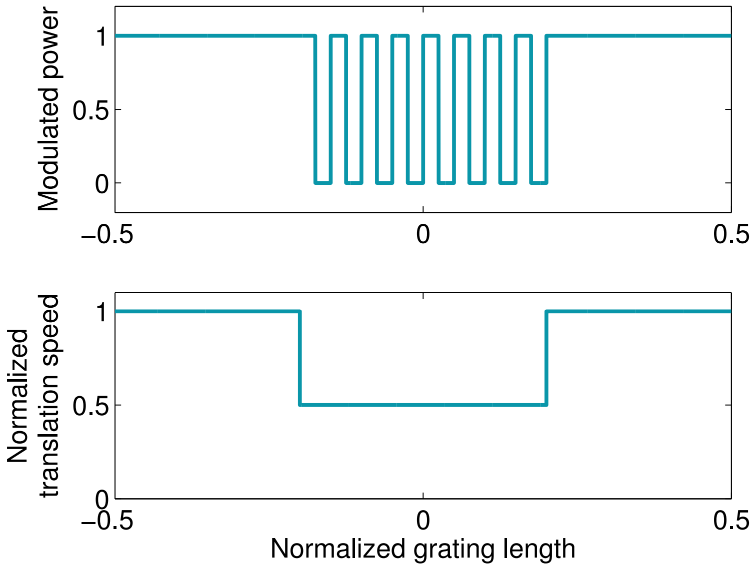

Figure 6.3: Control of UV writing speed avoids the problem of fluence mismatch between waveguide and grating.

diately begin to outdiffuse. This effect is reduced by immediately transferring samples to a liquid nitrogen environment until UV processing begins, as the rate of outdiffusion depends on temperature. For samples kept at moderately low temperatures of -33°C during writing[1], there was found to be no degradation in the strength of the waveguides during the duration of writing [2].

6.1.1 Grating Response

So far the discussion of DGW has involved only uniform Bragg gratings. However, with minor alterations to system parameters, Bragg gratings with different responses can be fabricated. In this thesis there are demonstrations of uniform, apodized, chirped and chirp-apodized gratings, all made with the same DGW system.

Fig. 6.4 shows a 1mm long uniform Bragg grating written with a duty cycle of 0.5 and a fluence of 15kJ/cm^{-2}, and a 5mm long Gaussian apodized grating with a duty cycle of 0.5 and fluence of 25kJ/cm^{-2}. By using a Gaussian envelope over the entire grating, the resultant spectral response is approximately Gaussian. The side lobes are suppressed by almost 20dB and only the central reflection peak remains above the noise floor. Apodization is achieved by utilizing the duty cycle

---

[1] Compared to the temperature of liquid nitrogen, -196°C

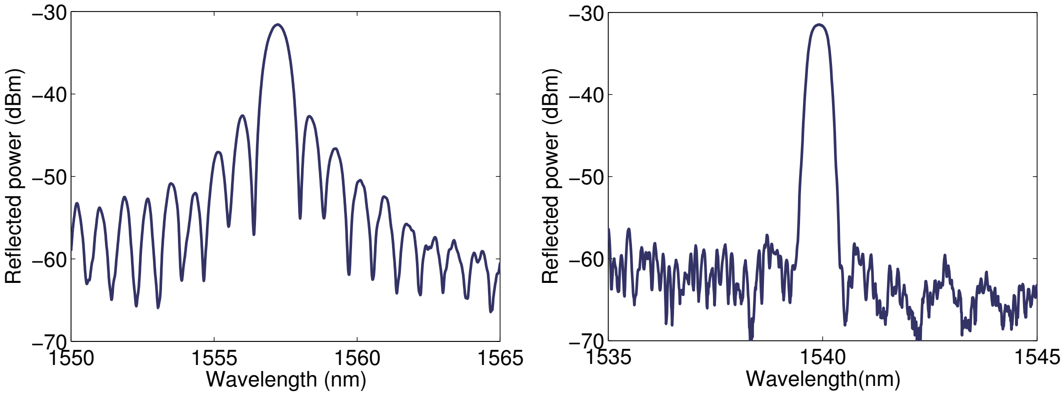

Figure 6.4: Uniform (unapodized) and apodized Bragg gratings fabricated with DGW. Uniform grating courtesy Helen Rogers.

parameter. By changing the duty cycle as a function of position, the effective strength of the grating changes as a function of position (analogous to pulse width modulation). However, this would cause the average refractive index to vary along the length. To compensate for this, the speed of translation is adjusted in tandem with the duty cycle, as shown in Fig. 6.5. Hence the writing speed is defined by:

$$\nu_{\text{grating}} = \nu_{\text{channel}} \delta \mathbb{A} \tag{6.1}$$

where ν_{grating} is the position dependent writing speed, ν_{channel} is the channel writing speed, δ is the duty cycle, and $\mathbb{A}$ is the profile of the apodization function.

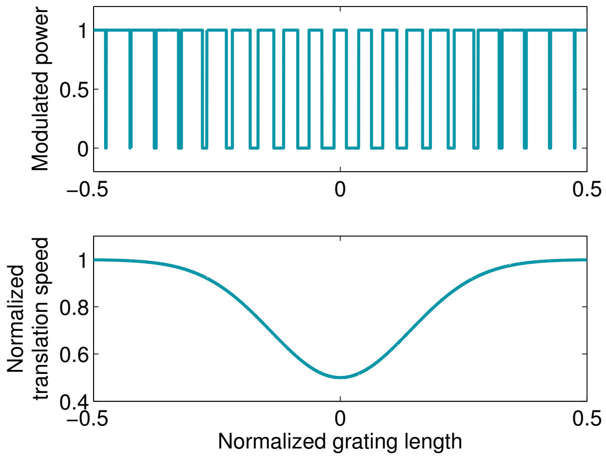

Figure 6.5: An example of duty cycle changing allowing the formation of an apodized Bragg grating. The translation speed is adjusted concurrently such that the total illuminated power (fluence) is the same at all times.

In order to fabricate chirped Bragg gratings, the period of the grating must change as a function of position. For linearly chirped gratings this is obviously a linear increase (or decrease) in the grating period. Therefore instead of producing an array of AOM firing positions with constant separation, the array is filled with firing positions whose separation linearly increases along the grating. A grating with linear chirp is written into the sample as the stages are translated.

Examples of four different grating types are shown in Fig. 6.6. These gratings were all written into the same sample under the same conditions. The gratings were 5mm long and written with a fluence of 25kJ/cm^{-2} and a minimum duty cycle of 0.5. The apodized gratings used a Gaussian apodization profile, and the chirped gratings used a positive linear chirp. The chirp rate was 6nm/cm. Gratings were written to examine their spectral shape only, and as such the grating spectra were not normalized.

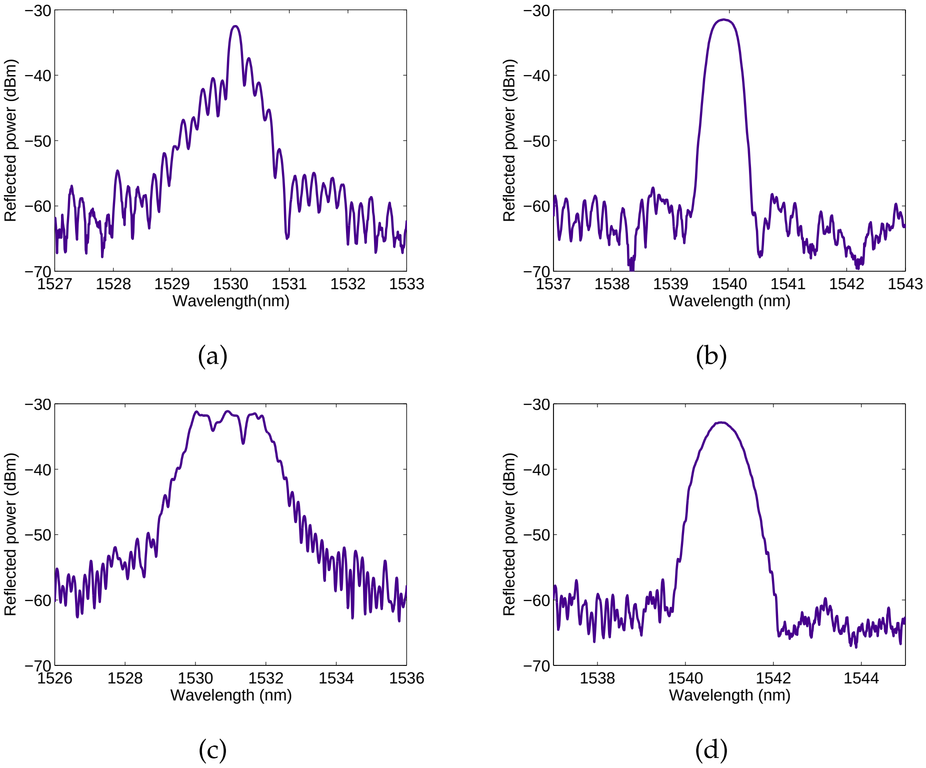

(a) (b) (c) (d)

Figure 6.6: Comparison of four grating types written under the same conditions: (a) uniform, (b) apodized, (c) chirped, (d) chirp-apodized.

Chirped gratings will still have the problem of spectral side lobes. Again, this can be overcome by using apodization. Shown in Fig. 6.7 is a chirped and a chirp-apodized grating. The chirped grating has significant ripple in the group delay spectrum and is therefore unsuitable for applications such as dispersion compensation, which will be described in Chapter 9. The effect of apodizing the grating is that the group delay becomes much more linear with respect to wavelength. It is therefore more suited for use in dispersion compensating devices where control of the group delay as a function of wavelength is critical.

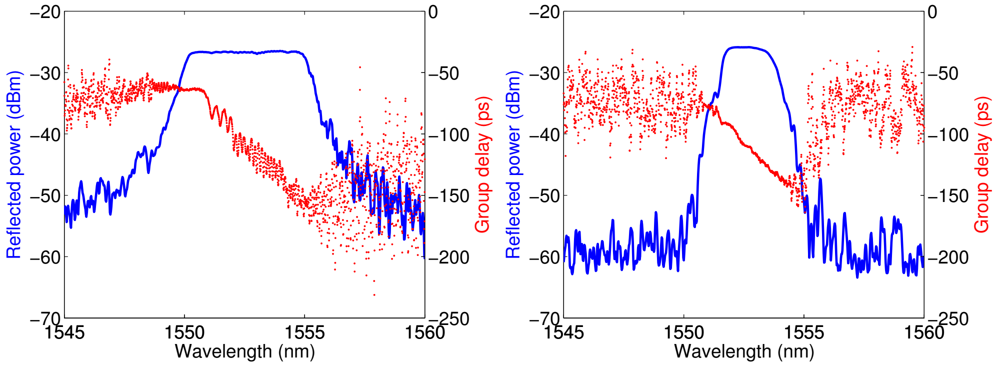

Figure 6.7: Chirped and chirp-apodized gratings with group delay spectra

6.2 Liquid Crystal Cells

Now that the process of fabricating buried channel waveguides and Bragg gratings has been described, the processes used to fabricate liquid crystal cells will now be presented.

The typical LC cell used in this thesis consists of one standard glass substrate and an ITO-coated glass substrate. Both are treated with a non-ionic homeotropic surfactant (Merck LiquiCoat ZLI-3334 0.2% solution in ethanol) to provide homeotropic alignment at both surfaces. Surfactant is applied to the substrates and baked to drive off the solvent. The surfactant molecules, in essence soap-like molecules, contain a hydrophilic, often polar, head and a hydrophobic tail [3]. The hydrophilic head binds to the glass and the hydrophobic tail extends out normal to the surface.

The tail of the surfactant molecules is what produces the desired alignment. Alignment arises from steric interactions between LC molecules and the surfactant molecules and the alignment quality is dependent on the surface density of the surfactant. If the surfactant density at the surface is too low, there are insufficient steric interactions to cause favourable alignment in the direction

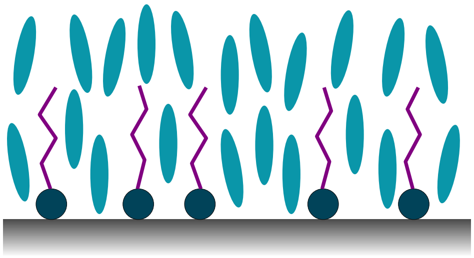

Figure 6.8: Substrate coated with correct density of surfactant molecules for homeotropic alignment

normal to the surface. Conversely, if the surfactant density is too high the LC molecules cannot penetrate into space between surfactant molecules, and again random orientation is produced. Where the surface density of surfactant molecules is such that the distance between them is of the order of the LC molecular length, homeotropic alignment is obtained.

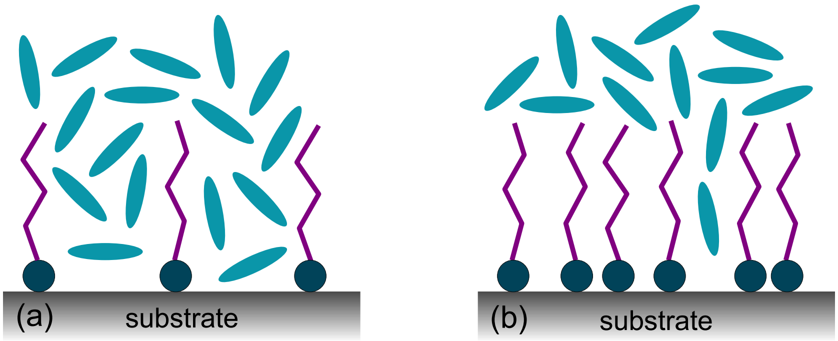

Figure 6.9: Substrate coated with incorrect concentrations of surfactant molecules for homeotropic alignment

Cells requiring planar alignment utilize a solution consisting of polyimide (PI) in the solvent 1-methyl-2-pyrrolidinone, in a ratio of 1:10. Samples are spun coated with the solution which is then baked to remove any remaining solvent. Coated samples are then rubbed using a velvet roller, creating unidirectional, micron-sized grooves.

The next step in fabricating an LC cell is patterning of the ITO electrodes. This was originally performed using a spark erosion technique whereby a metal stylus tip was connected to a voltage supply while the ITO was held at ground potential. The stylus was translated across, and in contact with, the ITO. The electric field at the surface of the substrate caused the ITO to erode, leaving a strip of exposed glass as the stylus is translated. However, the resultant electrode quality was poor. During the work performed in this thesis the author developed a photolithographic technique, as shown in Fig. 6.10.

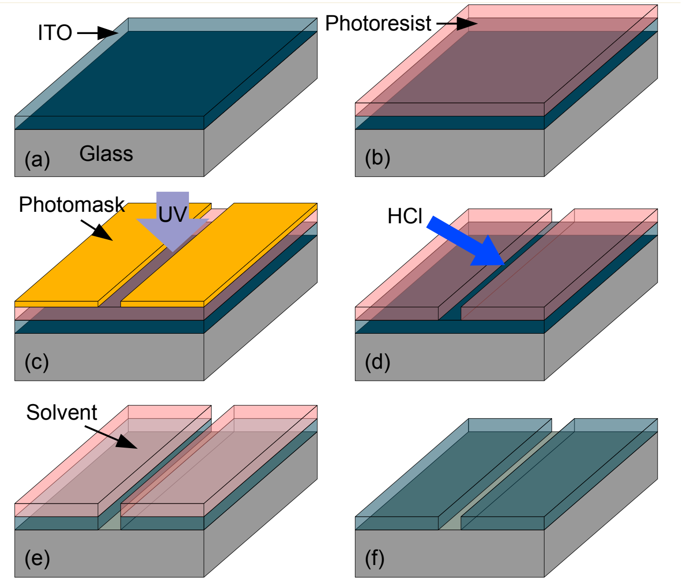

Figure 6.10: Photolithographic process for fabricating electrodes in ITO coated glass

The ITO is spin-coated with a positive photoresist (a), Microposit S1813, which becomes soluble in a weakly basic solution when exposed. The developer used in this work was Microposit MF-319. The mask designed for this thesis contained simple strip electrodes and periodically patterned electrodes. Taking the strip electrode as an example, the UV-exposed strip is base-soluble and washes away with developer (b, c). This exposes a thin region of ITO which is dissolved away using concentrated hydrochloric acid (d). Now two isolated electrodes have been formed, the remaining resist is washed off with solvent (e). The distance between the electrodes ranged from ~20-50μm, depending on the mask pattern used (f). Once the electrodes have been defined the surfactant can be added to the surface.

Fig. 6.11 shows the difference between the spark erosion and photolithographic techniques used to create parallel ITO strip electrodes for use in LC tuning cells. The surface profile data was collected using a KLA Tencor P-16 surface profiler. Both produce an electrode width of 40-50μm with a depth of 20-40nm, depending on the thickness of ITO on the substrate. However, the spark erosion technique produces unwanted artifacts which can be detrimental to LC tuning. Spark erosion produces debris on either side of the eroded region, likely due

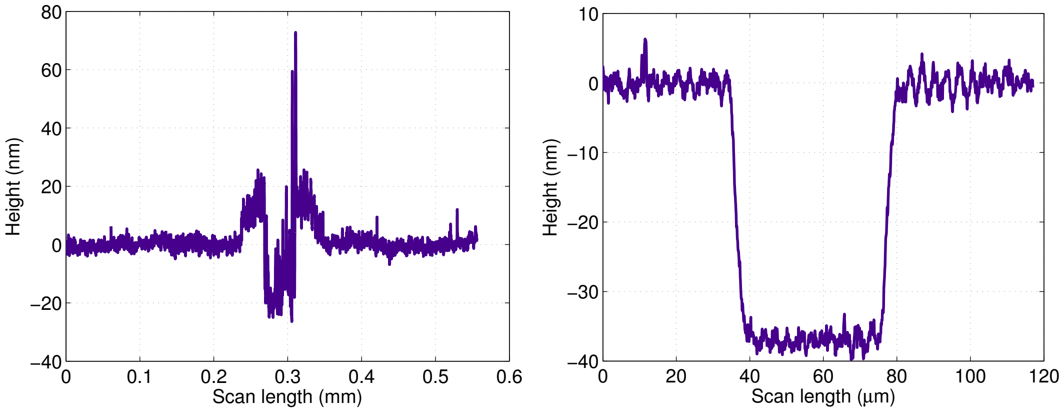

Figure 6.11: Comparison of two electrode fabrication techniques, left: spark erosion, right: photolithography

to ITO melting and solidifying beside the trench due to heat from the spark. More importantly, the roughness of the etched region for the photolithographic technique is lower, and is indeed limited by the noise floor of the surface profiler. This is beneficial for LC surfactant alignment as surface features will govern the average director orientation.

Once the substrates have been processed and treated they must be combined to form a cell. They must also be separated by a sufficient distance to allow the LC molecules to rotate. This is achieved by using glass micro-rods suspended in UV-curable glue, in this case Norland Optical Adhesive NOA 61. Rods used in these devices are typically 7μm in diameter, creating a cell with a thickness of 7μm. The glue-rod suspension is applied to the substrates, which are then pushed together with sufficient force to ensure a mono-disperse layer of glass rods. The glue is then cured via UV exposure.

The cell is then sealed around three edges with epoxy, leaving one edge open. This is to allow for infiltration of the cell with LC. The cell is placed in a vacuum chamber which is evacuated to remove air from the cell. LC is then applied to the open edge and drawn in via capillary action. The vacuum is released and the open edge of the cell is also sealed with epoxy. Electrodes are added to an exposed region of ITO by either indium solder or silver-loaded epoxy. These devices are used to interrogate the LC molecular behaviour in a confined geometry under the influence of an external applied electric field.

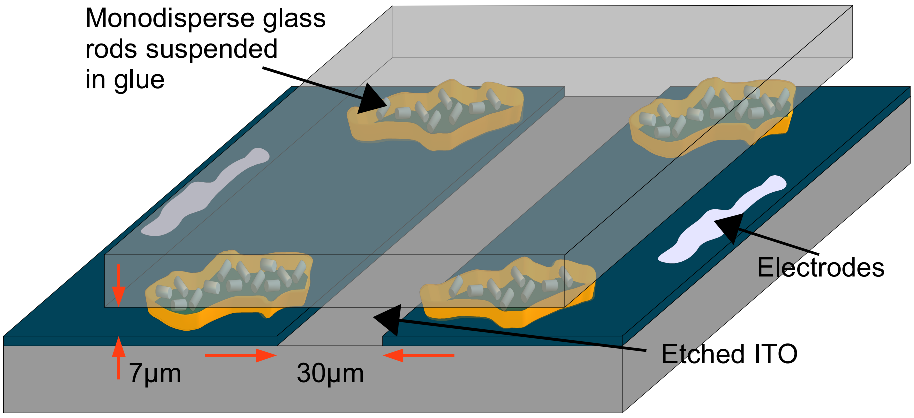

Figure 6.12: Cell substrates bonded together with UV-curable glue containing 7μm glass spacers

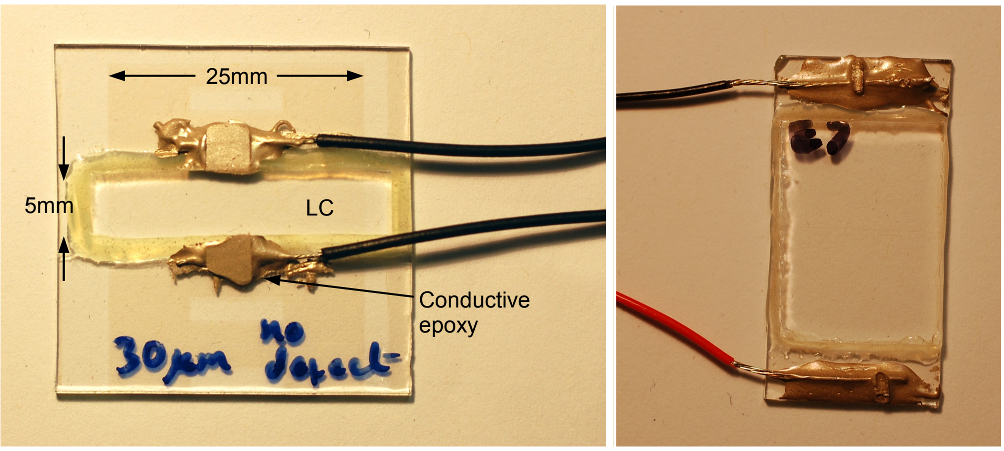

Figure 6.13: An LC cell with a 30μm wide straight strip electrode and a cell with 50μm wide electrode

6.2.1 Tunable Bragg Gratings

LC tunable Bragg gratings are fabricated in a similar fashion to standard transparent interrogation cells. However, there is added complexity due to aligning the strip electrodes with the channel waveguide. Misalignment of the waveguide axis and the electrode axis results in reduced tuning response [4]. Instead of fabricating a completely sealed cell, the sample containing the waveguide is housed between two glass substrates, one of which contains the ITO electrodes. This is to allow movement of the sample under the ITO electrodes for alignment purposes. Fig. 6.14 shows the cross-section of a LC tunable Bragg grating device. The sample containing the channel waveguide and Bragg grating is etched using a HF (hydrofluoric) acid solution. The sample is masked with UV-curable glue,

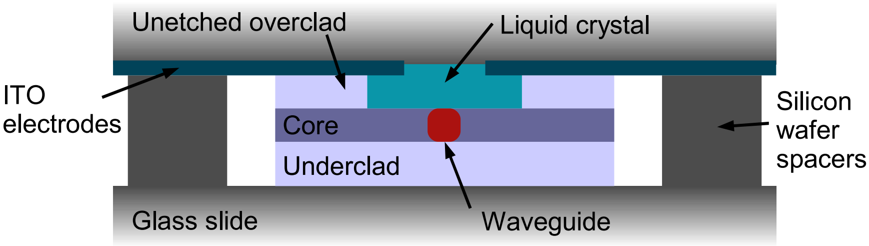

Figure 6.14: LC tunable planar Bragg grating device

Dymax OP-54, to protect the sample around the waveguide. Samples were initially masked with polyamide tape, however work performed in this thesis showed that using UV-curable glue provided a better mask. Tape masks required a distance of 1mm or more to produce the required etch depth, whereas glue masks allow for a greater etch depth with only ~200µm lateral displacement. The glue mask also provided a smoother etch wall, as can be seen from the surface features on the etched wall of the tape-masked sample in Fig. 6.15. The etched surface roughness is greater for the glue mask as borosilicate used for the glue mask experiment is softer than FHD silica due to more impurities.

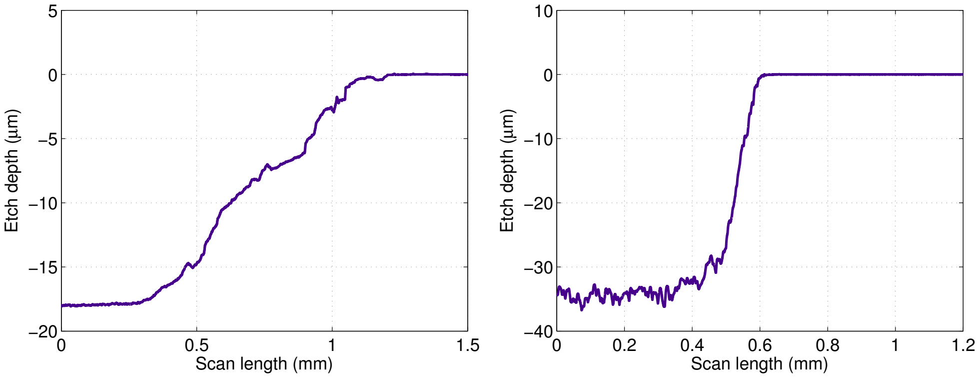

Figure 6.15: Comparison of two masking techniques for HF acid etching, left: tape mask, right: glue mask. Data taken using a surface profiler.

The glue mask process is a modification of standard lithographic processes. Silicone rubber is cut to the required size and shape and then pushed onto the area of the sample to be etched. Glue is applied around the rubber and cured to produce the mask. The rubber is removed leaving an exposed region. The sample is now ready for cleanroom processing. It is immersed in an HF acid solution for up to two hours, depending on the required etch depth. The solutions used were either etchall® dip'n etch, or a weak (~5%) HF acid solution. Unmasked regions are exposed to HF solution and are etched down to the core layer, exposing the

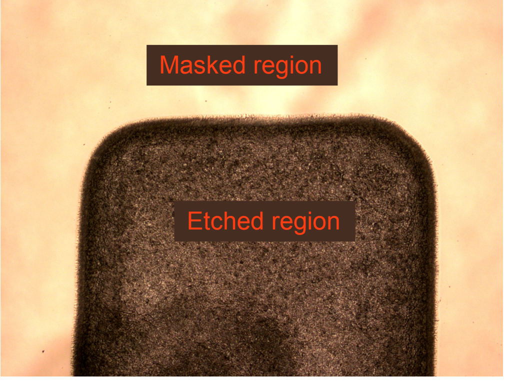

Figure 6.16: A borosilicate glass slide etched with HF using a glue mask

grating and therefore allowing effective index modification. During the etching, the sample is monitored using an optical characterization setup, as shown in Fig. 6.17. This includes a broadband light source, a circulator, an optical spectrum analyzer (OSA) and a computer for data acquisition. The charaterization setup will be described in section 6.3.

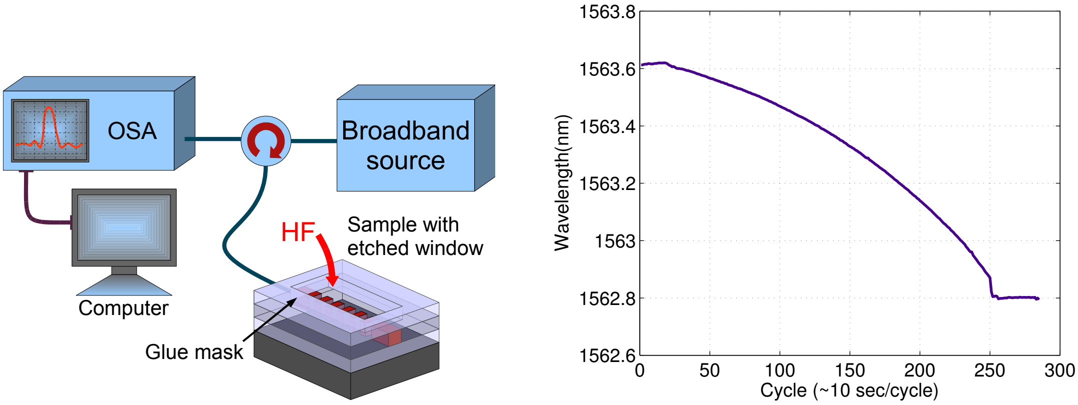

Figure 6.17: Left: standard setup for optical device characterization, right: wavelength tuning during etching

As the HF solution has a lower refractive index than the overclad, the effective index seen by light propagating in the waveguide and grating decreases. This is due to the overclad being etched away, which therefore becomes thinner and the HF solution is in closer proximity to the core layer. This is seen as a wavelength shift towards shorter wavelengths in the grating spectrum, as shown in Fig. 6.17. A wavelength shift of 0.8-1.2nm correlates to an etch within a few µm of the core, depending on the composition of the sample. The drop in wavelength at the end of the etch is due to the sample being removed from the HF solution and placed into a water bath to quench the reaction. The temperature of the water bath is lower than the etch solution, hence the wavelength reduces abruptly.

The Bragg gratings written in the samples are now exposed and can be influenced more readily by external perturbations. The most common of which in this thesis are the LC cladding layers used as adaptive overlayers for effective index tuning. Physical effects arising from LC cladding layers will be discussed in Chapter 7. The surfaces are then treated with the homeotropic surfactant, the cell is assembled and the LC is applied under vacuum.

6.3 Device Characterization

Once the Bragg grating devices are fabricated, they are examined using an optical characterization system as described for etching. An AFC BBS 1550 A-TS amplified spontaneous emission source, (ASE), provides broadband IR light over the telecomms C-band (1525-1565nm) for use with the UV-written Bragg gratings designed for these wavelengths. The light is then fed into a circulator whose next port connects to the grating and the final port connects to an ANDO AQ6317B Optical Spectrum Analyzer (OSA). The OSA acquires and displays data of the gratings spectral response which can be connected to a computer for data acquisition. For transmission measurements no circulator is required as the light is transmitted through the waveguide and observed at the output with the OSA.

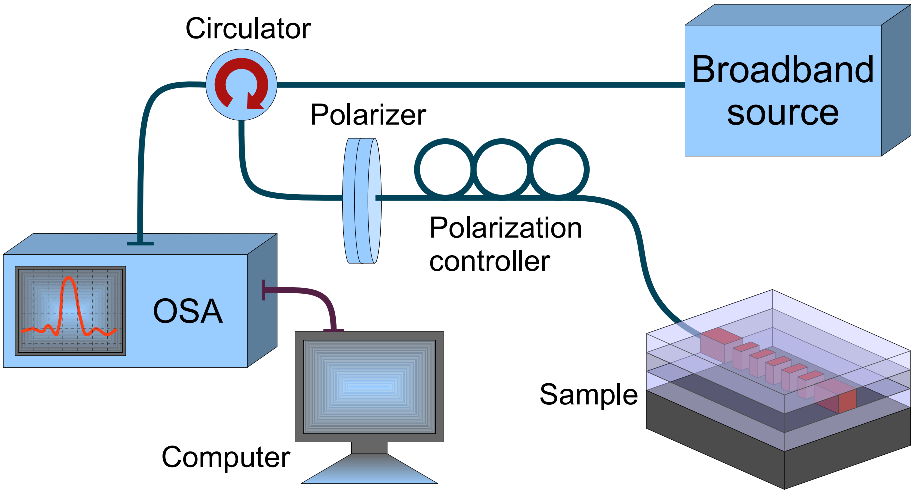

Figure 6.18: Standard setup for optical characterization including polarization control

Although the ASE source is spectrum flattened, it does exhibit spectral features within its useable bandwidth. The spectrum of the broadband source is shown in Fig. 6.19. In order to normalize grating spectra, the ASE spectrum is taken by disconnecting the sample from the circulator, leaving the fiber unconnected, and recording the ~4% Fresnel reflected spectrum with the OSA. The spectrum can then be used to normalize the background power for Bragg gratings. Fresnel reflected background spectra are also useful for exposing poor optical connections, or contaminated connectors. For a standard characterization setup, the resultant background power will remain approximately constant unless an optical connection is misaligned or contaminated. Thus the background spectrum provides a useful indicator of the setup condition.

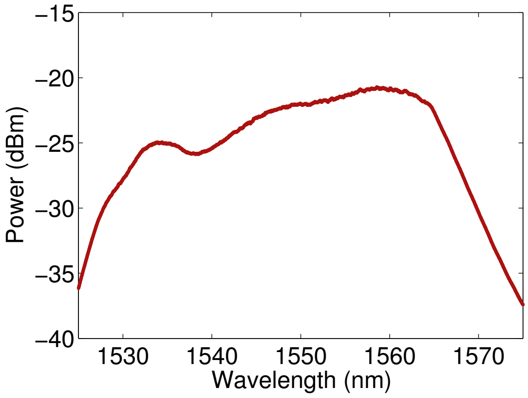

Figure 6.19: Spectrum from the broadband source.

Data acquisition is performed by a purpose made program written in the LabView™ environment which records the optical power as a function of wavelength. As the optical power spectra for Bragg gratings often have Gaussian profiles, a Gaussian fitting algorithm is utilized to extract extra data from the spectra. Using a Gaussian fitting algorithm allows the grating height, width and centre wavelength to be extracted in real-time. Thus the raw data and fitting parameters can be saved for future analysis.

For devices requiring a more robust package, the bare optical fiber connection to the sample can be replaced with a packaged fiber pigtail. Here a single mode optical fiber is housed in a V-groove between a silicon base and a silica capping layer, shown in Fig. 6.20. The planar end facet of the pigtail allows easy adhesion to a planar sample using Dymax OP-4-20641 UV-curable glue for a permanent fiber connection. In the case of polarization sensitive devices, the pigtail uses polarization maintaining fiber.

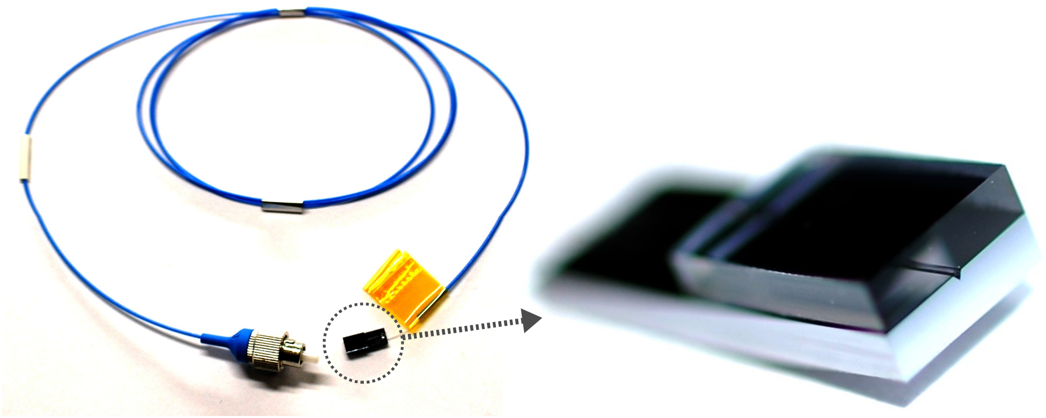

Figure 6.20: (Left) Fiber pigtail with polarization maintaining fiber, (right) fiber sandwiched between silica cap and silicon base containing a V-groove.

For polarization sensitive devices the characterization system can be modified to provide polarization control. A polarization maintaining (PM) polarizer can be used between the circulator and sample. This ensures the power entering the sample is in one of the two principle polarization modes, TE or TM, assuming a PM pigtail is also used. This is because the principal axis of the fiber pigtail is aligned with the pigtail housing. The other method is to use a combination of polarizer and polarization controller, as shown in Fig. 6.18. Using a controller allows for any arbitrary polarization state to be launched into the device. However, a PM polarizer provides a more convenient method of launching plane polarized light parallel to a principle axis without the need for extra alignment equipment.

In addition to the periodic reflection from the grating itself, unwanted Fresnel reflections can occur from the end facet of the sample. Fresnel reflections can be avoided by stopping the written waveguide before it reaches the end of the sample. However, this method does not allow transmission data to be taken, nor does it allow for observation of the output mode with an IR camera as a launch alignment aid. Instead, waveguides and gratings are written at an 8° angle, similar to angled physical contact connectors for fiber, such that Fresnel reflections from the end facet are eliminated. This is achieved by simply rotating the substrate by the chosen angle prior to UV writing. The result is that most reflected light is reflected back into the cladding rather than the core, such that it cannot interfere with the reflected grating spectrum.

6.4 Summary

Following on from the Direct UV Writing technique described previously, a more advanced Direct Grating Writing technique has been described. DGW allows for simultaneous definition of buried channel waveguides and Bragg grating structures. A description of the DGW system has been given, including all important software and hardware components and how they interact with each other. An explanation of the processes involved in producing advanced gratings, such as apodized and chirped gratings, was provided. Example spectra of such gratings were also given.

An overview of liquid crystal cell fabrication was also provided. Important parameters are the surface quality, the electrode uniformity, and the surface treatment. Using surface treatments such as homeotropic surfactants or rubbed polymer layers, the alignment of the LC can be controlled. The LC molecules can be further controlled by application of an electric field. This is achieved by using transparent ITO electrodes. Integrating the LC and electrodes with the UV-written planar Bragg gratings allows for tunable grating structures. Subsequently, the process of fabricating the tunable planar Bragg grating structures was presented. An explanation of the techniques used to optimize the etching process was also provided.

Finally, the standard device characterization setup was presented. Interrogation typically involves using broadband IR light sources emitting around 1550nm to illuminate a grating. The reflection spectrum is then analyzed with an OSA such that grating parameters, including tuning of the reflection wavelength, can be determined.

References

[1] G. D. Emmerson. *Novel Direct UV Written Devices.* PhD thesis, University Of Southampton, 2003.

[2] M. Svalgaard. “Effect of D2 outdiffusion on direct UV writing of optical waveguides”. *Electronics Letters*, 35(21):1840, 1999.

[3] I. Dierking. *Textures of liquid crystals*. Wiley, 2003.

[4] F. R. M. Adikan. *Direct UV-Written Waveguide Devices*. PhD thesis, University Of Southampton, 2007.

Chapter 7

The Behaviour of Liquid Crystals in Tunable Bragg Gratings

7.1 Introduction

It has been predicted that the current energy consumption of the internet stands at 2% of the total energy consumption of the planet, as of 2009 [1]. As data access rates increase, the percentage of power used in core networks, which involve routers and switches, is set to become as significant as the access network. Indeed, the energy bottlenecks of the Internet are the routers, not data access links [2]. Replacing power hungry server switches with more efficient devices is desirable due to cost, reliability and performance.

Also, as optical networks become more complex, rapidly increasing in size and data transfer rates, it is desirable to introduce reconfigurable network elements such that real-time modification of the network can be performed. Much research has been focussed on devices in integrated optical platforms, such as MEMS (micro-electro-mechanical systems) based switches [3] and Arrayed Waveguide Gratings (AWG) [4, 5]. Reconfigurable Optical Add-Drop Multiplexers (ROADM) used for channel add/drop functions in Wavelength Division Multiplexed (WDM) systems often employ wavelength resonant components such as ring resonators or Bragg gratings [6, 7].

In silica-based platforms it is common to use Bragg gratings as the resonant device. This is because silica ring resonators require large radii to reduce bend losses, and also Bragg gratings are simpler to fabricate. The most common methods for Bragg wavelength tuning in fiber gratings are thermal or stress tuning [8–10]. However, both of these methods have certain disadvantages when used with the silica-on-silicon platform. Firstly, silicon has a thermal conductivity value approximately 100 times greater than that of silica. As a result, any grating heating that permeates through the silica underclad to the silicon wafer will rapidly conduct along the wafer, reducing the heating effect. Secondly, as the silica-on-silicon devices are robust, the stresses required to tune the Bragg wavelength are greater than those required to tune a fiber grating. One method of tuning a planar Bragg grating is to use bend-induced strain, however this alters the spectral shape of the grating by inducing chirp [11].

An alternative to the tuning methods noted above is the electrically-tunable Bragg grating. As silica has no electro-optic coefficient,it is more common to use an electro-optic material in conjunction with the waveguide and grating. Tuning is achieved by modifying the evanescent field component of the guided mode. This in turn alters the effective refractive index of the waveguide, changing the Bragg reflection wavelength. One method of achieving effective index tuning is by using liquid crystals (LC) as the cladding material. LC's exhibit phases that have properties similar to those of uniaxial crystals, the important difference is that LC's are fluid. They have the ability to reorient under the influence of an external field and this allows exploitation of their birefringence.

Altough LC's have been integrated with optical systems since the 1970's, the concept of using LC's to tune Bragg gratings is relatively new. Sirleto et al [12] proposed the use of an LC overlayer to produce bistable switching devices or electrically tunable planar relief Bragg gratings. Sparrow demonstrated a small tuning range with LC tunable grating structures in 2005 [13]. More recently, Adikan et al have published work on tunable LC Bragg grating structures using the DGW technique combined with an electrically tunable LC overlay [14]. This thesis aims to further explore the performance of such devices and the underlying physical behavior.

7.2 Tunable Devices

The purpose of a tunable Bragg grating device is to modify the peak reflection wavelength of the grating. From the equation for the Bragg wavelength, $\lambda_B = 2n_{eff}\Lambda$, it can be seen that there are two means of changing the wavelength. However, since the grating period, Λ, is defined during fabrication the effective refractive index is the only parameter that can be modified. The effective refractive index is the index seen by a propagating mode in the core which is affected by all surrounding media within the mode field diameter. This is because the evanescent field component of the propagating mode extends transversely beyond the core.

Propagating light experiences a refractive index contribution from the LC which in these devices is Merck 18523. The acid etch exposes a region of the core and the grating such that the LC is in contact with the core. As the LC's used in this thesis behave like rotatable uniaxial crystals, they have an extraordinary axis which is defined as the average direction of the constituent molecules long axes, known as the director. The ordinary axis is any direction normal to the director. Light polarized along the director experiences a refractive index n_e whereas light polarized along an ordinary axis experiences a lower index n_o. Rotating the LC molecules relative to the polarization axis of the input light changes the refractive index experienced by the propagating light. Therefore the peak Bragg reflection wavelength changes. A diagram of the device is shown in Fig. 7.1.

Rotation is achieved by utilizing the LC's dielectric anisotropy. Nematic LC molecules are rod-like and they exhibit collective behaviour creating optical anisotropy. The dielectric anisotropy is caused by the polarizability anisotropy of the molecules, as explained in Chapter 4. The molecules contain induced electric dipoles and these dipoles are oriented along the molecular long axes. Therefore, as an electric field is applied to the cell the molecules rotate such that they align with the field lines which are defined by the geometry of the cell and the electrodes. Merck 18523 has positive dielectric anisotropy and therefore exhibits this behaviour.

Cells for Bragg grating tuning are fabricated such that the field-off state is defined by the homeotropic anchoring induced by the surfactant, Merck LiquiCoat ZLI-

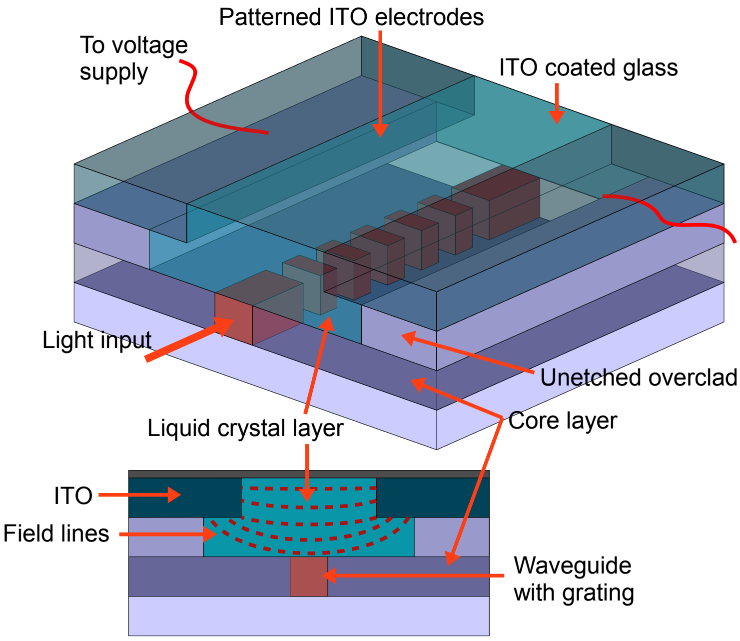

Figure 7.1: Diagram of an electrically tunable LC Bragg grating device

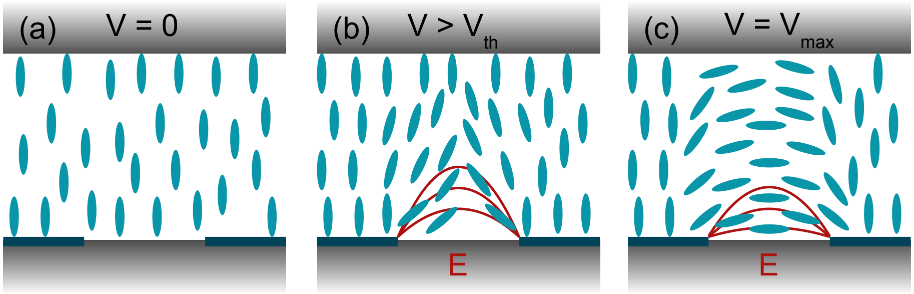

Figure 7.2: Expected LC molecular rotation under an applied field, (a) no field, (b) field large enough to overcome initial order, (c) molecular alignment under maximum applied field

3334. Surfactant is applied to both the etched wavguide and the etched ITO electrodes such that the LC is everywhere normal to both substrates. The electrodes are positioned so that the applied field is normal to the initial orientation, thus an increasing field causes increasing rotation towards the field lines.

Nematic LC Merck 18523 is chosen because it has a similar refractive index to that of silica, with n = 1.444 for undoped silica and n_o = 1.444 and n_e = 1.489 for NLC 18523, all at 1550nm. This is important for tuning purposes to ensure mode confinement of the propagating light. Shown in Fig. 7.3 is the effect of a relatively high index overlayer on the mode confinement. It can be seen that the mode is no longer symmetrical about the centre of the waveguide, and it is indeed pulled towards the higher index LC above the core layer. The yellow region displays how much of the mode is influenced by the LC. Linearly polarized light

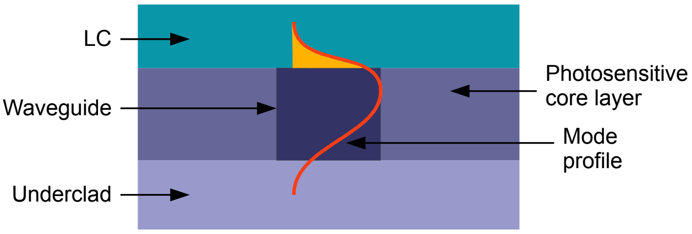

Figure 7.3: Gaussian beam propagation in a tuning device with an LC overclad

is launched into the waveguide below the LC cladding region. The evanescent field component of the propagating mode that extends into the LC experiences the electric field-induced refractive index change. This is turn produces a Bragg wavelength change. As the light extends into the LC, rotation of the director will cause the incident light to experience a varying refractive index. For a director axis rotating towards the axis of polarization, the light will experience increasing refractive index. Conversely, if the director rotates away from the polarization axis, the effective index decreases.

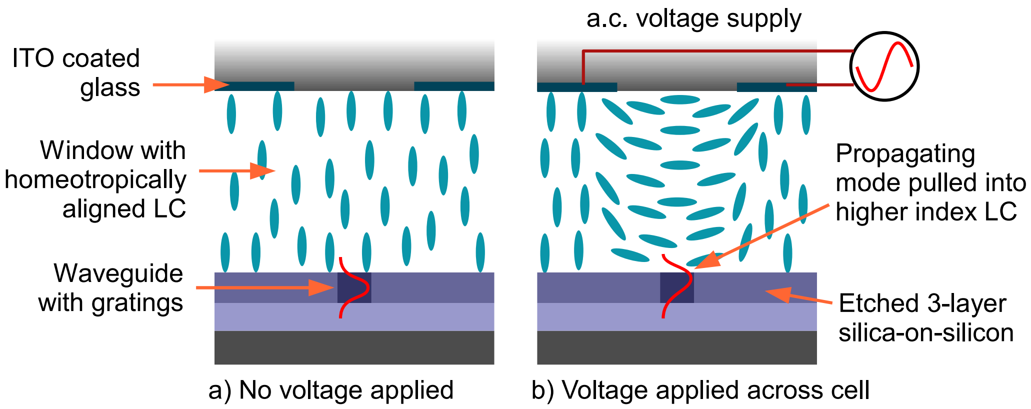

a) No voltage applied b) Voltage applied across cell

Figure 7.4: Tunable LC cell showing ideal molecular alignment

It is important to note that the mode will be increasingly pulled into the LC if the effective index for that polarization increases. At some point the guidance condition fails for the propagating light in the waveguide and the mode is lost if using an LC whose index is above that of the core. Reflection spectra rely on the forward propagating mode being converted into a backward propagating mode via the grating. Any part of the mode propagating in the LC layer cannot be converted into a backward propagating mode as it is no longer in the coupling region. This effect manifests itself as a reduction in reflection strength of grating structures.

7.2.1 Silica-on-Silicon Liquid Crystal Devices

In work performed by a previous student in the group, the Direct-UV-written silica-on-silicon tunable LC devices exhibited a Bragg wavelength shift of 932.7pm (corresponding to 114GHz at λ=1561.8nm for TE polarization) with 170Vpp applied across the LC cell [15]. The Bragg wavelength shift is the change in the centre wavelength of the grating's spectral response. The shift therefore defines the tuning range of the filter. However, it was observed that the wavelength shift was not a linear function of applied field, and indeed hysteresis was seen in the tuning curves. The tuning curves for these devices are shown in Fig. 7.5 with hysteresis clearly evident between points A and B. This behaviour was observed consistently with repeated measurements conducted over the course of several weeks. Insets (i) and (ii) show each part of the hysteresis curve separately. Inset (i) shows the tuning curve with increasing voltage whereas inset (ii) shows the curve with decreasing voltage. All measurements in the tuning curves for increasing voltage displayed two distinct points where the tuning gradient changes significantly. These points are circled in inset (i). The first

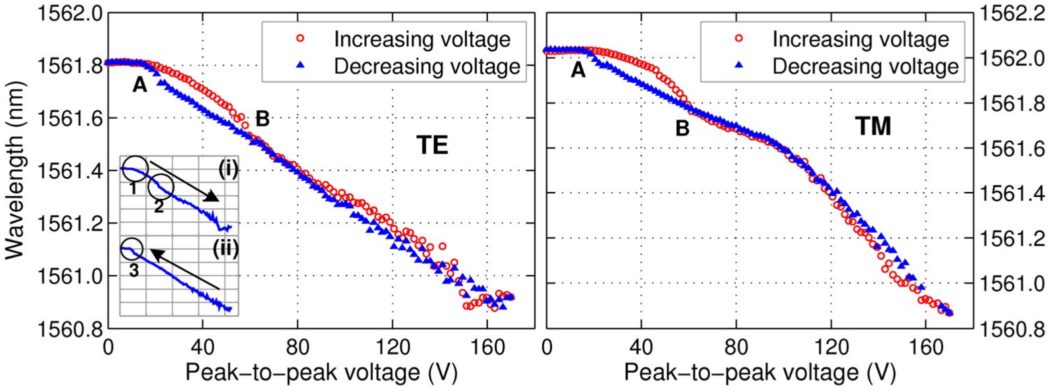

Figure 7.5: Absolute device tuning curves for both TM and TE polarised light showing hysteresis between points A and B [15]. The insets show the same curves for increasing (arrow pointing downwards) and decreasing (arrow pointing upwards) voltages. In inset (i), the circles numbered 1 and 2 show the two threshold points at ~22V and ~57V respectively. In inset (ii), the low voltage threshold at ~17V is circled and numbered 3.

lower threshold point (1) occurs at ~17Vpp, with increasing voltage, whereas the upper threshold point (2) occurs at ~57±10Vpp. The curve for decreasing voltage exhibits such a change at ~17Vpp (3).

The threshold points (1) and (3) were attributed to the Fréedericksz transition. At this voltage the LC begins to align with the applied field. Below this voltage the applied electric field is insufficient to overcome interactions of the LC with surfaces and elastic forces. However, threshold point (2) was attributed to the possible multi-domain structure of LC's in confined geometries and their interaction with applied fields, creating a disclination. It was hypothesized that the tuning behaviour between points A and B in Fig. 7.5 was the result of a disclination line forming (A) and subsequently disappearing (B). The disclination would not reappear until the applied voltage was again reduced to the lower voltage threshold. The result is the hysteresis loop shown in the tuning data.

Provided now is the authors own work on investigating the hysteresis behaviour.

7.3 Exploring Anomalous LC Behaviour

It would be expected that the tuning curve would be a simple function of applied voltage, from the Fréedericksz transition up until maximum molecular realignment. However, due to the complex behaviour exhibited in these results further analysis was required. As such, experiments were performed in order to discover the reason for the anomalous behaviour. This involved fabricating transparent LC cells for use in transmission microscopy experiments. Polarized transmission microscopy provides a convenient tool for analyzing LC behaviour as LC cells are highly polarization sensitive and exhibit behaviour reminiscent of waveplates. *In situ* measurements of LC dynamics in a tuning cell proved impractical due to the device construction and difficulty in the ability to perform reflection microscopy.

The LC cells were fabricated with attributes similar to those in the tunable Bragg grating device. The electrode separation, cell thickness and surface treatments were similar for both devices. The key difference is that LC cells are transparent allowing easier device interrogation. Cells were filled with LC 18523, as with tuning cells, to observe any physical behaviour that could be causing the hysteresis seen in previous devices.

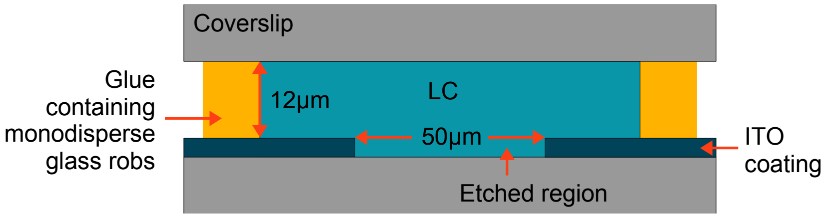

Figure 7.6: Standard transmissive cell for LC interrogation.

Polarized light from a white light source illuminated a transmissive cell, shown in Fig. 7.6, and a camera recorded the images through crossed polarizers in a microscope system. LC outside of the electrode region can not rotate and this region will therefore remain dark due to the crossed polarizers. However, LC in the electrode region can rotate and therefore will allow transmission of light as the polarization vector is rotated. The electrode axis is aligned at 45^o to both polarizer and analyzer to allow maximum image contrast. Maximum transmission is achieved when the input polarized light is rotated through 90^o by the LC.

At first there is no transmission even with applied voltage as the electric field is insufficient to overcome the elastic energy keeping the LC aligned hometropically. Once the field strength is sufficient to overcome the Fréedericksz transition, the LC begins to rotate towards the field lines, producing areas of increasing transmission. However, it can be seen that between the electrodes, running coaxially along them, is a long and dark region. This is otherwise known as a wall. As the wall maintains the initial homeotropic alignment it provides no rotation of the polarization vector and thus always appears dark in cross-polarized microscopy.

Shown in Fig. 7.7 are still frames taken from a video of a cell during tuning. The applied voltage is ramped up at a rate of 2.5V/sec until the maximum of 100V. It is then held for 30 seconds to ensure the wall is completely transformed before returning to the initial voltage with the same ramp rate. The wall is formed from the Fréedericksz transition at 25V, it is "pinched": the wall becomes thinner as it is increasingly restricted to the weak field region. At 100V the elastic forces in the LC can no longer maintain the wall and the director pushes through the

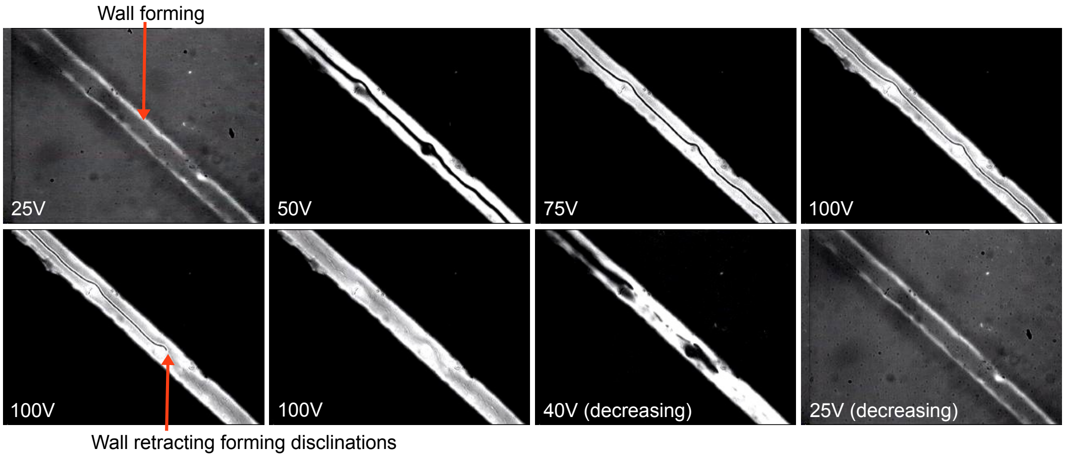

Figure 7.7: Splay-bend wall forming above the Fréedericksz transition and then disappearing in a homeotropically aligned LC cell.

wall aligning itself with the field. The wall does not reform until the voltage is decreased to approximately 40V. This hysteresis is reminiscent of the behaviour seen in LC tunable Bragg grating devices (Fig. 7.5) and the critical voltage values correlate with values seen in such devices.

In this cell geometry the wall is caused by LC rotating towards the centre from both electrode edges. As the rotation exhibits mirror symmetry, there are two regions of LC both attempting to rotate parallel to the field lines. Both regions hinder each others rotation at the centre, the result being a region which resists field-induced reorientation and forms a wall. This wall is stable so long as the field is kept below a threshold that causes reorientation at a nucleation site. Point defects in the cell, which can be caused by poorly aligned LC or contaminants, provide nucleation sites from which the LC can begin to fully align with the applied field. Such defects provide a perturbation in the director field and thus make it easier for the field to influence LC molecular reorientation at that location. The result is a front which separates realigned LC from unaligned LC. This front propagates along the cell parallel to the electrode axis.

To test whether the hysteresis behaviour was a property of the LC 18523 specifically or of nematic LC's in general, another nematic LC was tested. Further polarized transmission microscopy experiments were performed with nematic LC (NLC) Merck 6815, which has a slightly higher refractive index but similar birefringence[1]. Fig. 7.8 shows that LC 6815 produces very similar behaviour

---

[1] $\Delta n = 0.049$ for 18523, $\Delta n = 0.052$ for 6815, both at 589nm.

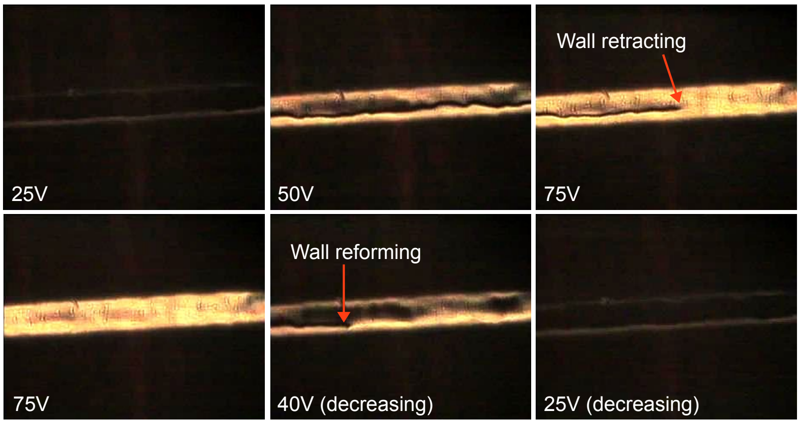

Figure 7.8: Splay-bend wall forming a disclination pair in Merck NLC 6815

to that of 18523 and thus implies the splay-bend wall dynamics are common to nematic LC's in the confined geometry considered here. The discrepancy in the initial wall retraction voltage is likely to be caused by slightly different surface treatments, causing a different anchoring strength and director field continuity. Both cells had homeotropic surface treatments that involved coating the samples with surfactant solution. Changes in the concentration of the solution could give rise to the surface effects described in Chapter 6, where the surface density of surfactant molecules determines the bulk alignment quality. This would change the required voltage for nucleation of a disclination pair at a point along the wall.

7.4 Temperature Effects

It was suggested that tuning in previous samples may have been a combination of the thermo-optic effect, due to Ohmic heating, and LC molecular realignment in the sample [16]. To ensure the tuning behaviour was purely a result of LC reorientation, experiments were undertaken to identify any thermal tuning behaviour using cells shown in Fig. 7.9. The three-layer silica-on-silicon samples used for these devices have small but noticeable thermo-optic coefficients. They are typically 8-12pm/°C as found in similar samples [13].

Cells containing UV written samples were mounted onto a thermo-electric (Peltier) module and covered with foam for thermal insulation. In this case the samples were not etched, to avoid LC tuning of the gratings and ensure all tuning was thermal. A thermocouple was attached to the Peltier and read by a

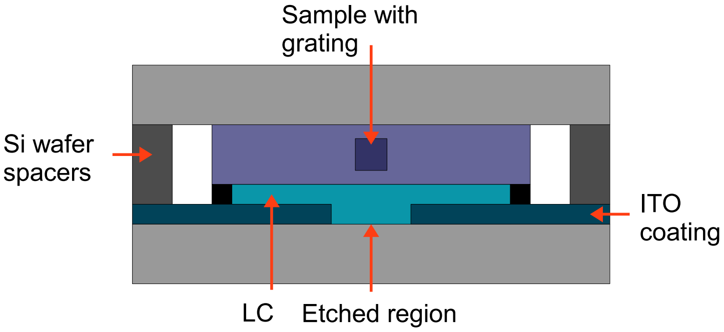

Figure 7.9: Diagram of cell for temperature measurements

multimeter connected to a computer. The Peltier was attached to a voltage supply for control of temperature. Broadband light form an ASE source was launched into the waveguides and the reflection spectrum was recorded with an Optical Spectrum Analyzer. Fig. 7.10 (left) illustrates the thermal stability of the devices under ambient conditions, showing less than 10pm thermal drift during the 1 hour experiment. Fig. 7.10 (right) demonstrates thermal tuning by varying the temperature of the unetched sample, showing a shift of 17-20pm/°C.

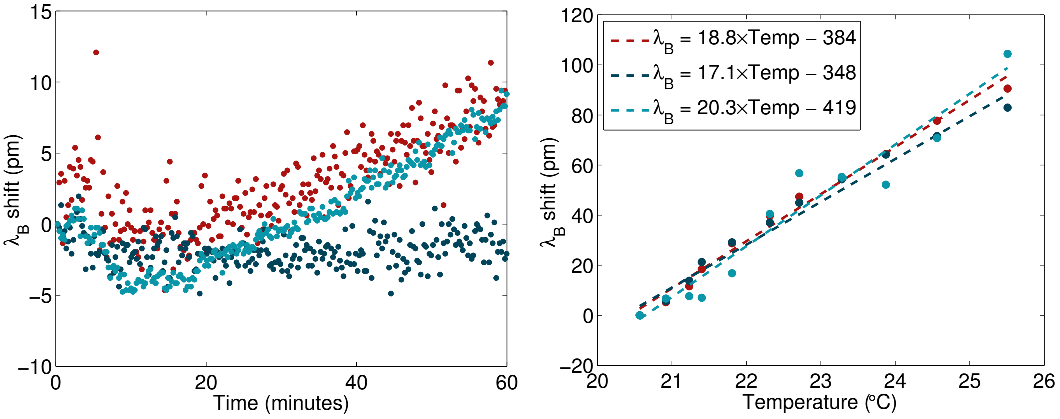

Figure 7.10: Left: Centre Bragg wavelength drift under ambient conditions for three gratings, right: wavelength shift with controlled temperature. The three data sets are produced from the three gratings present in the sample. This is the authors own work, but has been published previously in [15].

Next, a voltage of 150Vpp was applied across the electrodes for extended periods to test for any Ohmic heating. Fig. 7.11 shows the Bragg wavelength shift for a grating in the sample. It is apparent that little or no Ohmic heating was present, and here the drift of ~5pm can be attributed to change of ambient conditions, corresponding to ~0.5°C. This demonstrates that the measured peak

Bragg reflection wavelength shift in previous devices (932pm) is completely voltage driven.

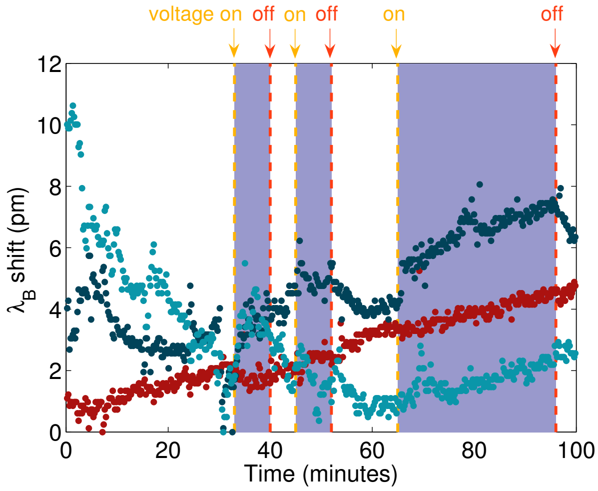

Figure 7.11: Effects of applying a voltage to LC cell for various durations and at various intervals. Three different gratings in the sample are shown. This is the author's own work, but has been published previously in [15].

7.5 High Resolution Microscopy

During data acquisition for hysteresis measurements some videos displayed traces of anomalous LC alignment behaviour. These anomalies were often too difficult to resolve, however some images did display evidence of residual perturbations in regions where the wall retracted. Using post-processing to enhance images of wall retraction, this perturbation can be seen in Fig. 7.12. The data was taken from the same cell as Fig. 7.7.

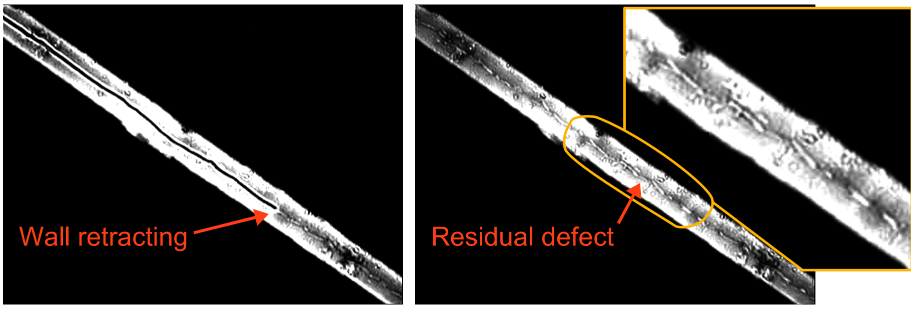

Figure 7.12: Enhanced images of a perturbation in the director field after the splay-bend wall has been removed at high voltages.

As data taken from the microscope was insufficient to explore fine detail during tuning, a purpose-built polarized transmission microscopy system was built, as shown in Fig. 7.13. The microscope constructed during this thesis was designed so it could incorporate a high-resolution camera, multiple light sources and the ability to both translate and rotate the device in the image plane. Light sources included narrow-band (~20nm) visible light emitting diodes (LED) and a white light source. Laser light was not used as its narrow linewidth produced interference fringes and thus impeded image analysis.

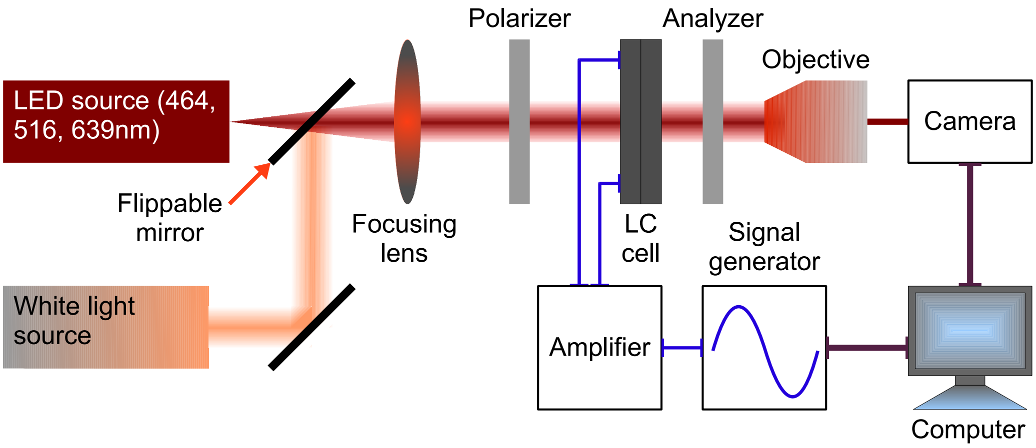

Figure 7.13: Polarized transmission microscopy setup for LC cell analysis

The LC used for tuning devices, Merck 18523, is a proprietary mixture and as such contains unknown components. Such components may be the cause the hysteresis behaviour instead of, or in addition to, the liquid crystalline component. Therefore a pure LC compound, 4n'-pentyl-cyanobiphenyl (5CB), was also used to determine if the multi-component nature of the 18523 mixture was contributing to the anomalous behaviour, or if it was exclusively the liquid crystalline component. 5CB was chosen for its similar properties to that of 18523. Both are nematics and stable at room temperature, both have positive dielectric anisotropy and are transmissive in the visible region.

For a homeotropically aligned cell viewed between crossed polarizers and aligned at 45° to both polarizer axes the total birefringence is zero. All incident light experiences the ordinary refractive index ($n_\perp$) as the polarization is perpendicular to the molecular long axes. However, when field-induced reorientation causes the long axes to rotate into the plane of polarization, light can be transmitted. The wavelength and intensity of the transmitted light depends on the total retardation of the LC cell as a function of position, as discussed in Chapter 4. Retardation is given by:

$$R = \Delta n(\lambda)d \tag{7.1}$$

where $\Delta n(\lambda)$ is the birefringence and d is the thickness of the cell. Remember that the equation for relative transmission is:

$$T(\lambda) = \sin^2\left(\frac{\pi\Delta n(\lambda)d}{\lambda}\right) = \sin^2\left(\frac{\pi R(\lambda)}{\lambda}\right) \tag{7.2}$$

so the transmitted wavelengths will be a function of the retardation and the illumination wavelength. The thickness of the cell, d, is fixed, however the effective birefringence is controlled by the applied field. Increasing rotation of the LC towards the field lines exposes more of the total birefringence. For a 7μm thick cell, the retardation can vary from 0 to 1.2μm for red (639nm) light. Hence LC cells are analogous to variable waveplates.

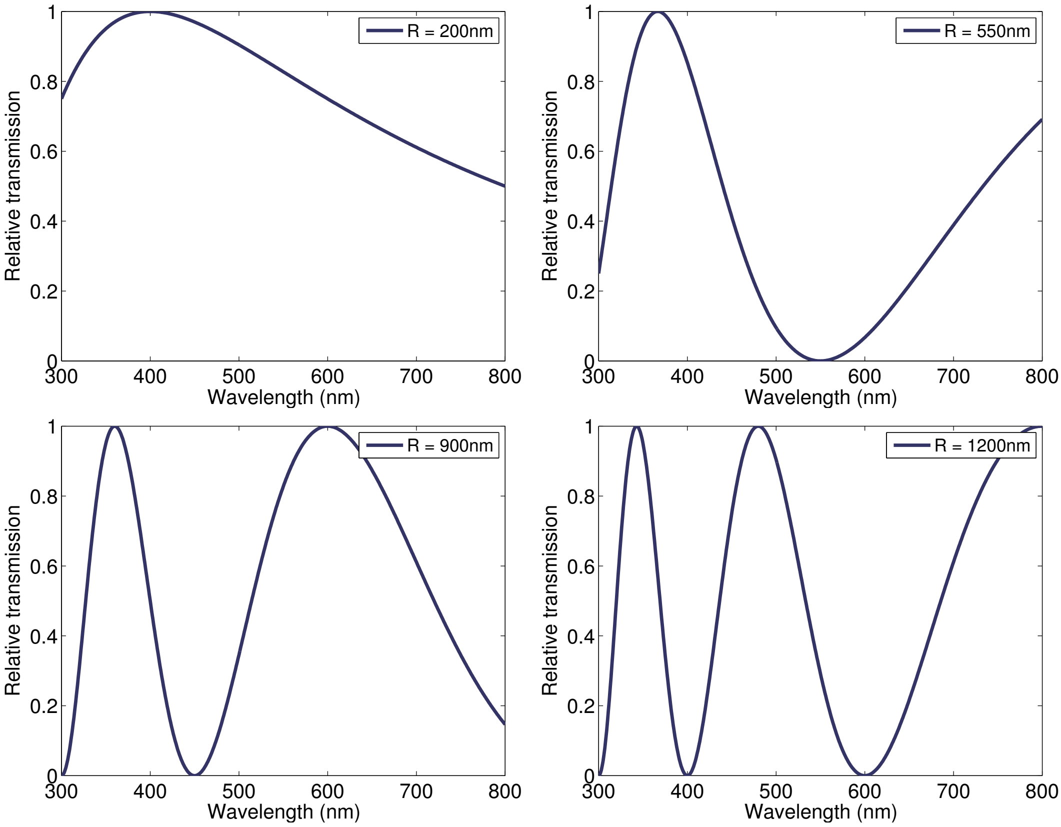

Figure 7.14: Light transmission as a function of wavelength for linearly polarized light incident on a LC cell with various retardations.

With no retardation there is no rotation of the polarization vector and thus the cell appears dark. For small retardations Eqn.7.2 has no minima in the visible and thus the whole visible spectrum is transmitted in varying proportions. The result is transmission of white or off-white light. As the retardation approaches 400nm the first transmission minimum is in the blue (~400nm) and the transmitted colour becomes yellow then red. At 550nm the minimum is in the green, such that red and violet are transmitted producing magenta. The cycle from magenta to red is termed an order. Each order will produce less vivid colours as more transmission windows open, mixing more colours. The calculated transmission characteristics of an LC cell with various retardations are shown in Fig. 7.14. A colour cycle for a cell illuminated with white light is shown in Fig. 7.15.

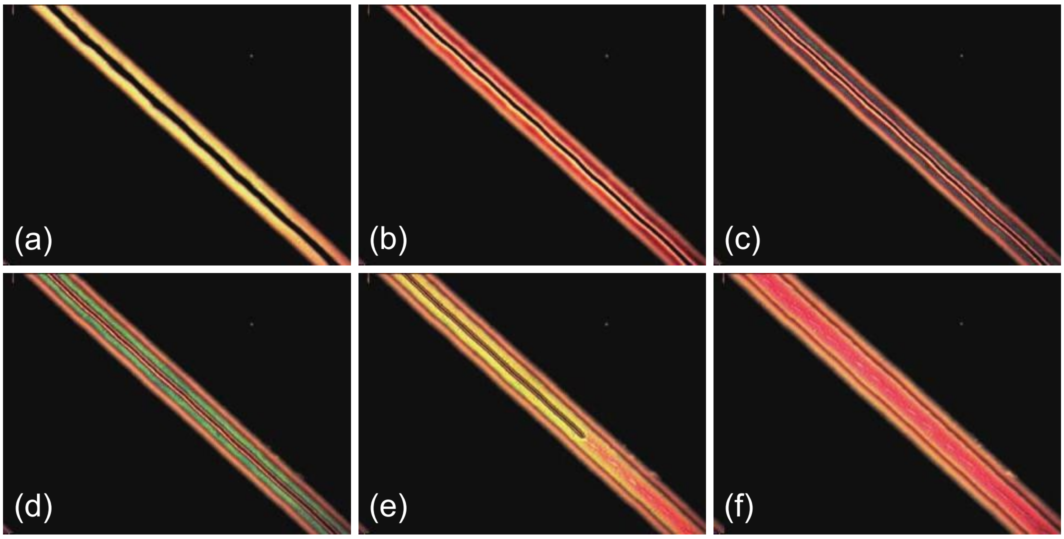

Figure 7.15: Colour cycling in a homeotropically aligned nematic LC cell with increasing applied voltage. Low voltage rotation causes off-white/yellow transmission (a), moving to red at higher voltages (b). As the incandescent source has little or no light below 500nm the blue cannot be resolved (c), however green light is seen (d). The colour cycles through to yellow (e) where the wall retracts along the electrode axes leaving a magenta hue (f).

7.5.1 The Pincement Transition

Further interrogation of the behaviour shown in Fig. 7.12 was performed with the high resolution cross-polarized microscopy setup. Fig. 7.16 shows a splay-bend wall retracting upwards leaving behind two line defects, or disclinations. This process has been called "pincement" [17, 18]. Pincement is the structural transition from a Fréedericksz wall into a pair of ±1/2 disclination lines under the influence of an applied field [19]. Increasing the applied field increases the elastic energy of the wall. When the wall energy reaches the nucleation energy of the disclination pair, the wall collapses and the pincement transition can occur.

The continuity of the director field around the wall is shown by the colour cycling. At the edges of the electrodes the colour cycling is similar to that in Fig. 7.15, however the cycles are more compressed due to the higher field strength. Beside the wall, the colour cycling reverses and the colours change sharply due to the rapidly varying director at the wall interfaces. The director in the disclination is discontinuous rather than rapidly varying and as such a more diffuse white/magenta region is produced from scattering off the disclination.

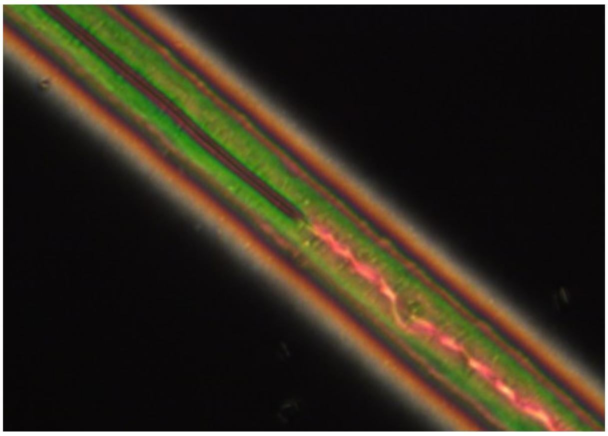

Figure 7.16: Splay-bend wall retracting upwards leaving behind a disclination pair.

Once the LC is fully aligned with the field, the wall is transformed into a disclination pair along the full length of the electrodes, as shown in Fig. 7.17. A pair of disclinations are formed to ensure conservation of topological charge. Disclinations are in essence filaments of unaligned LC, which behave like the LC in isotropic phase. As they are discontinuities in the director field, they cause perturbations in the LC which can be seen with high-resolution microscopy. The core of a disclination defect can be as small as tens of nm, however the perturbation caused by the defect can be much larger.

As disclination pairs are line defects they are energetically costly. Disclination pairs require relatively large field strengths to produce, and moderate field strengths to maintain. Disclination pairs can recombine to reform walls once the

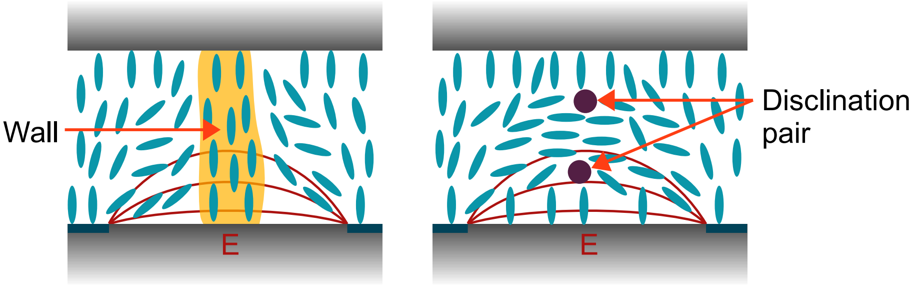

Figure 7.17: Splay-bend wall forming a disclination pair

applied field strength is sufficiently low to favour the transition. The transition from stable disclination to propagating front requires a nucleation site, therefore the triggering field strength is arbitrary. However, as cells are fabricated using a standard procedure, this field strength is often predictable. From repeated measurements it has been observed that new cells tend to have higher threshold voltages than older cells. This would correlate with the requirement for the transition to have a defect to nucleate from as older cells tend to acquire more defects over time. Defects can be due to mobilized fragments of glue used to seal the cell, or agglomerations of surfactant molecules and LC molecules.

Fig. 7.18 shows the pincement transition in a cell illuminated with 516nm narrowband light with polarizer and analyzer at 45° to the electrode axis. The wall is retracting from left to right while being transformed into a disclination pair. The transition occured at 32V with increasing applied field and was stable at the maximum voltage of the amplifier (~150V). Only when reducing the voltage to 18V would the wall reform. This behaviour is comparable to that seen in LC tunable Bragg grating devices in Section 7.2.1.

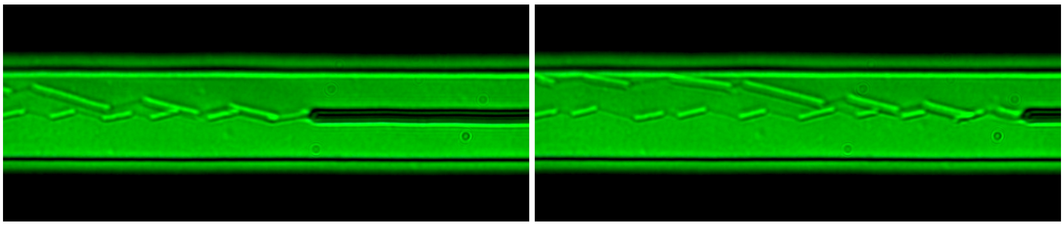

Figure 7.18: The pincement transition. A splay-bend wall, moving from left to right, is being transformed into a disclination pair.

The best indicator that this transition is indeed pincement would be observing the disclinations at different depths. As they should be in different planes, it should be possible to focus on each independently. Indeed in Fig. 7.18 it appears that while the central disclination is in focus, the other that has been displaced to the top electrode is out of focus. This observation would suggest that they exist at different depths in the cell. Considering the cell thickness is ~7µm, it is estimated from the focal adjustment that the disclinations are separated by a depth of 5-6µm.

In order to achieve controlled separation of the disclinations, periodically patterened ITO electrodes were fabricated using a photolithographic technique. Whereas previous electrodes had the central region completely etched away, these electrodes had periodic diamond structures that remained unetched. Although the structures only had a surface relief of 20-30nm, it was sufficient to perturb the disclination path sufficiently such that the upper disclination propagated over the diamond unaltered, whereas the lower disclination was redirected by the surface feature. This behaviour is shown in Fig. 7.19 where the upper disclination propagates over the ITO structure. The other disclination that is in close proximity to the ITO substrate is redirected by the diamond defect and propagates around it.

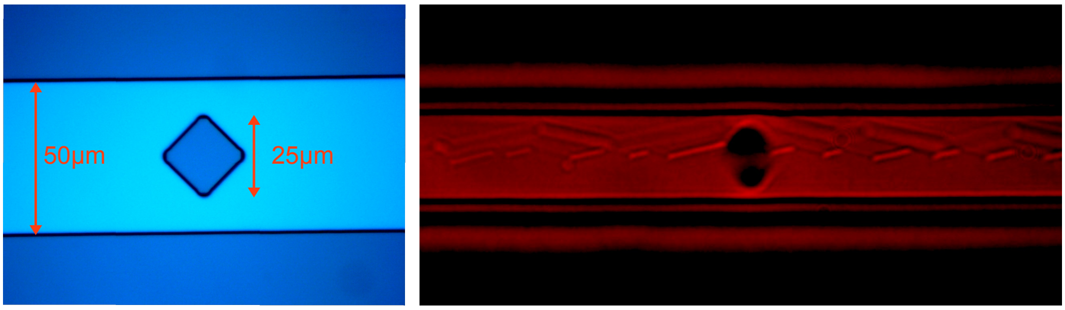

Figure 7.19: (left) Image of the ITO electrode structure. Dark regions contain ITO, light regions contain no ITO. (Right) Image through crossed polarizers of a cell with two disclinations clearly evident at different depths.

The following conclusions can be drawn from the experiments performed above:

- The hysteresis behaviour previously attributed to a single disclination line was, in fact, a Fréedericksz (or splay-bend) wall being produced at moderate field strengths, and transformed into a pair of ±1/2 disclinations at high applied field. This transition is known as pincement. The disclination pair is stable below the voltage at which it was formed. It transforms back into a wall at a lower voltage, producing a hysteresis loop.

- The pincement transition was verified by using periodically patterened ITO electrodes. Patterning forced the two disclinations to propagate at different depths in the cell, which proved that there were two unique line defects.
- Threshold point (3) in Fig. 7.5 does not correlate simply to the Fréedericksz transition. Around point (3) the tuning curve exhibits two gradients. The high-field gradient is due to the hysteresis where the disclination pair is still supported. The second, lower field, gradient is the intermediate configuration where the disclination pair has been transformed back into a Fréedericksz wall, but the field is sufficiently strong to produce molecular reorientation.
- The hysteresis behaviour is not unique to LC 18523, and has been observed in other multi-component and single component LC’s.
- By using a pure liquid crystalline compound, 5CB, it was verified that the hysteresis behaviour is common to nematic LC’s in the tuning cell geometry.
- The tuning response is a result of LC molecular reorientation in an applied field, and has little or no contribution from Ohmic heating.

7.5.2 Origin of the Zig-Zag Disclination

During the high-resolution microscopy experiments performed to uncover the origin of the tuning hysteresis, the author observed an unexpected LC configuration after the pincement transition. There was a consistent disclination configuration common to all of the cells fabricated in this thesis. Instead of the disclinations aligning themselves parallel to the electrode axes, the disclinations propagated along the cell with an oscillatory pattern. The experiments performed in this section aimed to uncover the physical causes of this behaviour.

It has been noted that the disclination is not completely co-axial with the electrodes as would be expected from this geometry. There is a zig-zag configuration which propagates perpendicular to the applied electric field. Shown in Fig. 7.20 is one of the fully formed disclinations which exhibits a zig-zag configuration. The origin of the zig-zag in these samples is not completely understood. It is possible that the wall is not a pure splay-bend deformation and may also contain some component of twist deformation [20]. The twist is possible in two directions normal to the electrode plane, either into or out of the page. However, this zigzag configuration is related to the splay-bend wall and not the disclinations.

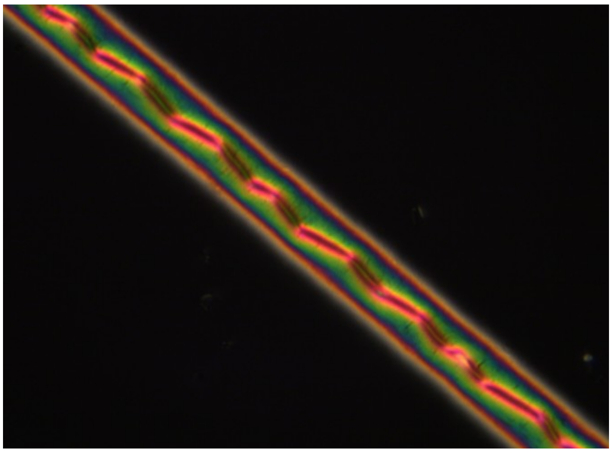

Figure 7.20: Image focussing on one disclination forming a zig-zag pattern

The mechanism that causes the zig-zag configuration is related to the disclinations [21], rather than the wall. It is suspected that the director becomes co-axial with the disclination near to the core [22]. Further from the core the director is determined by a combination of the surface anchoring and the applied field direction. The director field lines are shown in Fig. 7.21 for two different director configurations. Experimental examples are given in Fig. 7.22. It can be seen that a perfectly straight disclination would result in a tighter bend angle near the core than a zig-zag disclination. The zig-zag configuration is less energetically costly because there is less bend deformation in this configuration as $\theta_1 < \theta_2$. When the disclination approaches the edges of the electrode region, the elastic energy becomes too large and a point defect is formed causing the disclination to redirect towards the centre. This process is repeated forming the zig-zag shape.

Further interrogation showed that the director field varied more rapidly at each vertex of the zig-zag disclination than along each zig or zag. This is shown by a more rapid spatially varying colour cycle. It is expected that each vertex contains a point defect of the type shown in Chapter 4 [21]. The point defects alternate in topological charge from -1 to +1 in order to conserve total charge, which must be zero as there are no defects before the disclinations are produced. This is analogous to an effect seen in confined 2-dimensional geometries, such as LC-

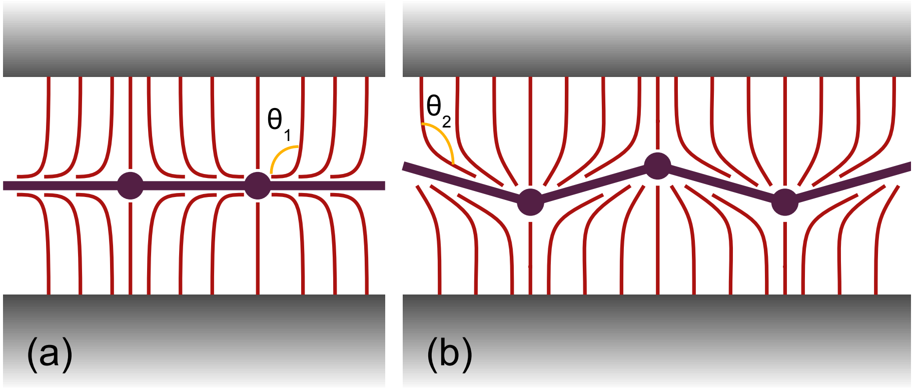

Figure 7.21: (a) Director field configuration for a straight disclination. The tighter bend angle requires more energy. (b) Director field configuration for a zig-zag disclination.

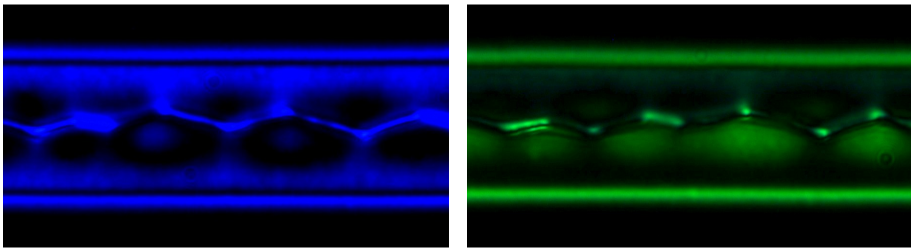

Figure 7.22: Examples of the director field distribution shown in Fig. 7.21(b). Both images are taken from a cell with 18V applied for 464nm light (left) and 516nm light (right).

filled capillaries, when the LC is aligned homeotropically at the surface. The possible configurations in a cylindrical geometry are shown in Fig. 7.23.

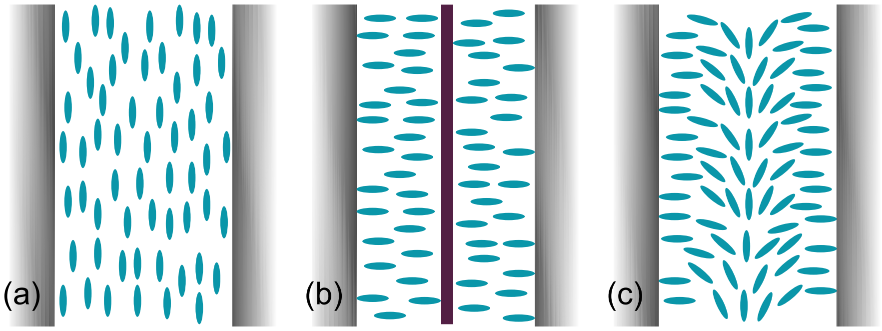

Figure 7.23: Possible configurations in a cylindrical geometry: (a) planar, (b) radial with +1 disclination, (c) escaped radial.

The molecular alignment for a homeotropically aligned LC in a capillary is shown in Fig. 7.25. In the center there is a disclination of strength +1. However line defects of integer strength are not stable and this line readily collapses along its

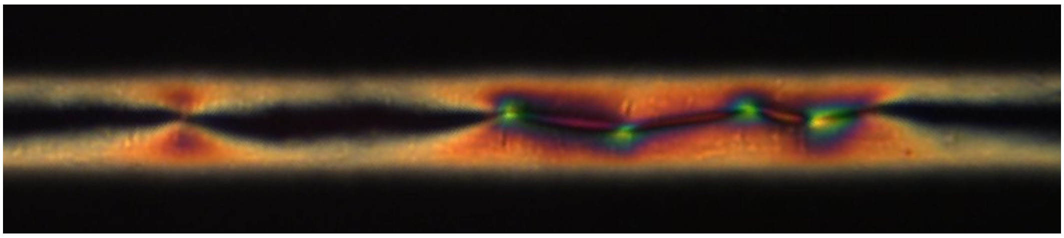

Figure 7.24: Pincement transition seen with white light. Transition regions appear pinched where the wall transforms into a pair disclination. The rapidly varying colours around the zig-zag vertices are indicative of point defects at each vertex.

length into pairs of point defects. This allows the director to align axially into a more stable configuation in a process known as "escape in the third dimension". If no point defects are present this process produces the standard escaped radial configuration, containing no director field discontinuities [23]. Half-integer disclinations, such as those in the pincement transition, are topologically stable and as such cannot be transformed into arrays of point defects.

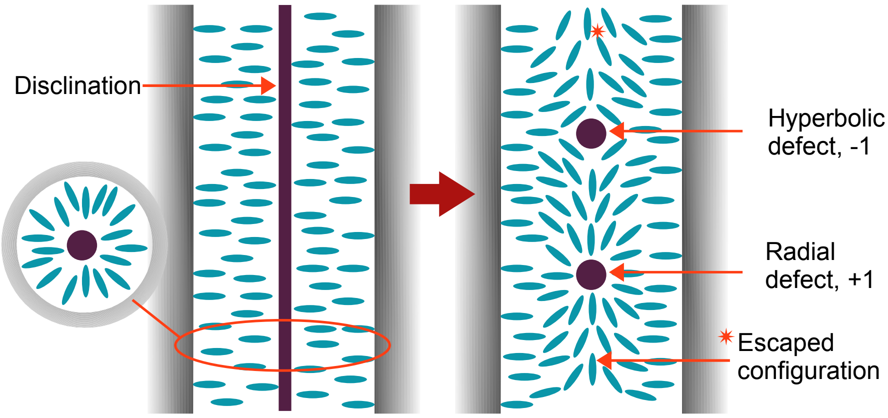

Figure 7.25: The initial radial configuration with a +1 disclination at the centre is unstable to escape in the third dimension. The result is pairs of +1, -1 point defects and either side the escaped configuration.

7.5.2.1 Distribution of Point Defects along the Zigzag

The pair defects must form sufficiently far apart to avoid being annihilated, which would leave behind a continuous +1 disclination [24]. For two defects of opposite charge separated by a distance L, the minimum interaction distance is of order $L = w$, where w is the width of the container [25]. This has been observed in LC cells during voltage application where two vertices will occasionally "snap" together and annihilate if they become too close. It is also apparent from the results taken in this thesis that the interaction distance is voltage related. Stronger applied fields allow oppositely charged defect pairs to exist in closer proximity than in low field regimes. Further work was performed in order to discover the cause of this behaviour.

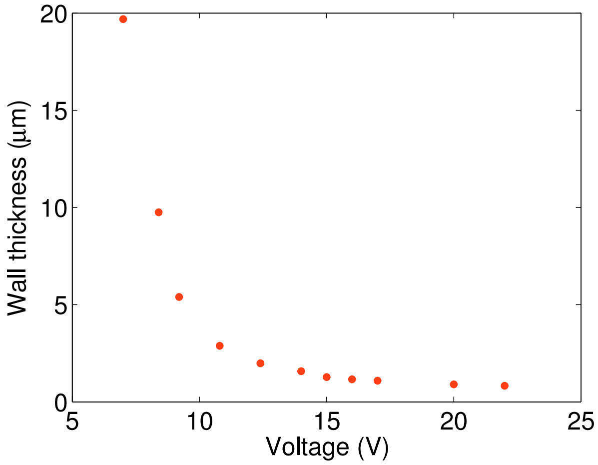

Figure 7.26: Thickness of the Fréedericksz wall as a function of applied voltage.

In confined geometries, metastable states consisting of periodic repetitions of the hyperbolic and radial defects can be observed. However, the dependence on the applied voltage of the distance between oppositely charged point defects along a disclination is yet to be discovered. It is known that the thickness of a Fréedericksz wall as a function of applied field follows an inverse power law [17]. This has been seen in LC cells fabricated in this thesis, as illustrated in Fig. 7.26. It has been found that the mean separation of oppositely charged point defects along the disclination as a function of voltage also follows an inverse power law. The reason for this is not fully understood. However, it has been found that the elastic energy associated with an array of point defects has a maximum with respect to defect spacing [26].

The relationship between elastic energy and distance between the periodic defects is of the form shown in Fig. 7.27. For separations below d_{max}, the defects will attract and annihilate. For separations larger than d_{max}, the defects will slowly move apart forming a metastable equilibrium state. It is suspected that an increasing applied field shifts the curve, and therefore the maximum, left towards shorter inter-defect distances. The field restricts the width of where the disclination, and therefore point defects, can be supported which causes

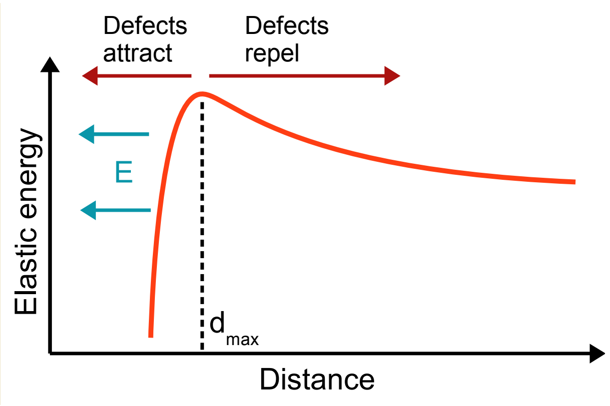

Figure 7.27: Elastic energy of the LC as a function of distance between two point defects of opposite charge.

a more rapidly varying director field. The width is the same as displayed in Fig. 7.26, but is only valid for the decreasing voltage regime when the disclinations are supported. This implies the elastic energy increases for the same defect separation and therefore the minimum repulsion distance becomes shorter. The result is that closely spaced, oppositely charged point defects will no longer annihilate as the applied field has stabilized the system for smaller defect separations.

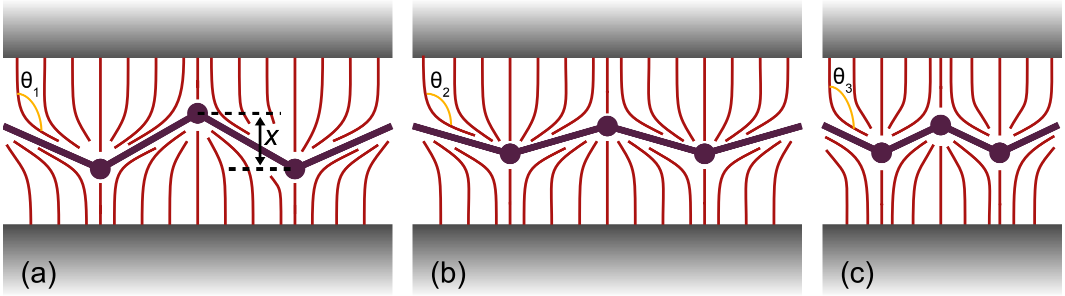

Figure 7.28: When the applied field reduces the width, x, where the disclination can exist, the elastic energy can be reduced by moving the vertices closer together. The angle θ_3 becomes larger than θ_2 when the vertices, and therefore point defects, move closer together resulting in a weaker bend deformation.

For a zigzag disclination at low fields, the maximum transverse distance, x, it can occupy is large. Therefore θ_1 is large and the elastic energy is kept low. As the field increases, L must decrease as the LC is aligning with the field from both sides of the cell. This forces θ_2 to decrease which increases the elastic energy in the system. One method of relaxing the system is to bring the point defects closer together, increasing θ_3 and reducing the tension in the director field.

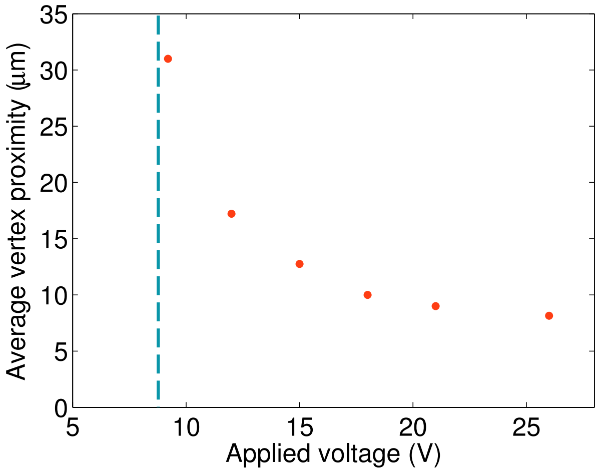

Figure 7.29: Average distance between adjacent zigzag vertices, or point defects of opposite topological charge. The blue line illustrates the threshold voltage below which disclinations are not supported.

Displayed in Fig. 7.29 is the average distance between adjacent zigzag vertices. The dotted line illustrates the threshold voltage below which disclinations cannot be supported. It can be seen that the average distance between point defects for weak fields is 31μm, which is similar to the electrode spacing of 30μm. As the field strength increases, point defects of opposite topological charge can coexist in closer proximity, the mean separation reducing to ~8μm at 26V. The separation distance is approximately constant for higher voltages. Fig. 7.30 displays images of the cell at 9.2V and 26V, showing the difference in separation of the point defects. The bottom disclination has its zigzag pitch reduced by the periodic ITO defects along the bottom substrate. The electric field distribution is also different as the disclination in focus is further from the electrodes. In the 9.2V image, the disclinations are overlaid and appear as a single line defect.

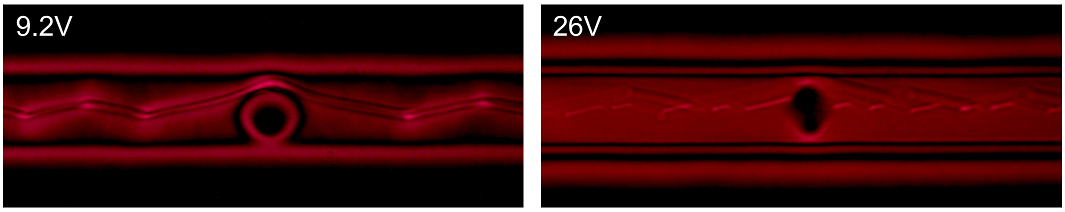

Figure 7.30: Images of disclinations from the same LC cell at 9.2V (left) and 26V (right).

7.6 Summary

This chapter has introduced the concept of LC-tunable planar Bragg gratings, utilizing the evanescent field component of a propagating mode to modify the effective refractive index of the grating. Previous devices exhibited hysteresis in their tuning curves which was found to be caused by a process known as *pincement*. This involves the transition from a splay-bend wall, where two equivalent tilted configurations are separated by an unperturbed region, to a pair of disclinations of opposite half-integer strength.

The disclinations exhibited a peculiar zigzag configuration which was found to be due to the director aligning axially with the disclination lines when approaching them. Perfectly straight disclinations would produce a more energetically costly bend deformation, therefore the line becomes kinked to reduce the bend in the director field. The width of the zigzag region was found to be voltage dependent.

At each vertex of the zigzag disclination point defects of alternating integer topological charge are produced. This configuration is analogous to the pairs of alternating charge defects found in the escaped geometry of homeotropically aligned capillaries. A theory has been proposed to explain the distribution of these point defects as a function of the applied voltage. It is suspected that the elastic energy in the director field can be reduced if the periodicity in the zigzag disclination is increased. This is a consequence of the applied field reducing the width of the region where the disclination can be maintained.

References

[1] B. Sanso and H. Mellah. "On reliability, performance and Internet power consumption". *2009 7th International Workshop on Design of Reliable Communication Networks*, pages 259–264, October 2009.

[2] J. Baliga, K. Hinton, and R. S. Tucker. "Energy Consumption of the Internet". *COIN-ACOFT 2007 - Joint International Conference on the Optical Internet and the 32nd Australian Conference on Optical Fibre Technology*, (June):1–3, June 2007.

[3] J. E. Ford, V. A. Aksyuk, D. J. Bishop, and J. A. Walker. "Wavelength Add-Drop Switching Using Tilting Micromirrors". *Journal of Lightwave Technology*, 17(5):904–911, May 1999.

[4] H. Takahashi, S. Suzuki, K. Kato, and I. Nishi. "Arrayed-Waveguide Grating for Wavelength Division Multi/Demultiplexer with Nanometre Resolution". *Electronics Letters*, 26(2):87, January 1990.

[5] I. P. Kaminow. "Optical Integrated Circuits: A Personal Perspective". *Journal of Lightwave Technology*, 26(9):994–1004, May 2008.

[6] G. Bourdon, G. Alibert, A. Beguin, B. Bellman, and E. Guiot. "Ultralow Loss Ring Resonators Using 3.5% Index-Contrast Ge-Doped Silica Waveguides". *IEEE Photonics Technology Letters*, 15(5):709–711, May 2003.

[7] C. R. Giles. "Lightwave Applications of Fiber Bragg Gratings". *Journal of Lightwave Technology*, 15(8):1391–1404, 1997.

[8] H. G. Limberger, N. H. Ky, D. M. Costantini, and R. P. Salath. "Efficient Miniature Fiber-Optic Tunable Filter Based on Intracore Bragg Grating and Electrically Resistive Coating". *Technology*, 10(3):361–363, 1998.

[9] S. Y. Set, B. Dabarsyah, C. S. Goh, K. Katoh, Y. Takushima, K. Kikuchi, Y. Okabe, and N. Takeda. "A widely tunable fiber Bragg grating with a wavelength tunability over 40 nm". *OFC 2001. Optical Fiber Communication Conference and Exhibit. Technical Digest Postconference Edition (IEEE Cat. 01CH37171)*, (1):MC4/1–MC4/3, 2000.

[10] A. Iocco, H. G. Limberger, R. P. Salathe, L. A. Everall, K. E. Chisholm, J. A. R. Williams, and I. Bennion. "Bragg Grating Fast Tunable Filter for Wavelength Division Multiplexing". *Journal of Lightwave Technology*, 17(7):1217–1221, July 1999.

[11] C. Holmes. *Direct UV Written Planar Devices for Sensing and Telecommunication Applications*. PhD thesis, University Of Southampton, 2009.

[12] L. Sirleto, G. Coppola, G. Breglio, G. Abbate, G. C. Righini, and J. M. Oton. "Electro-optical Switch and Continuously Tunable Filter based on a Bragg Grating in a Planar Waveguide with a Liquid Crystal Overlayer". *Optical Engineering*, 41(11):2890, 2002.

[13] I. J. G. Sparrow. *Development and Applications of UV Written Waveguides*. PhD thesis, University Of Southampton, 2005.

[14] F. R. Mahamd Adikan, J. C. Gates, A. Dyadyusha, H. E. Major, C. B. E. Gawith, I. J. G. Sparrow, G. D. Emmerson, M. Kaczmarek, and P. G. R. Smith. "Demonstration of 100 GHz electrically tunable liquid-crystal Bragg gratings for application in dynamic optical networks". *Optics Letters*, 32(11):1542–1544, 2007.

[15] F. R. M. Adikan. *Direct UV-Written Waveguide Devices*. PhD thesis, University Of Southampton, 2007.

[16] F. R. Mahamd Adikan, J. C. Gates, A. Dyadyusha, H. E. Major, C. B. E. Gawith, I. J. G. Sparrow, G. D. Emmerson, M. Kaczmarek, and P. G. R. Smith. "Demonstration of 100 GHz electrically tunable liquid-crystal Bragg gratings for application in dynamic optical networks". *Optics Letters*, 32(11):1542, 2007.

[17] P. G. de Gennes. *The Physics of Liquid Crystals*. Oxford University Press, 1995.

[18] A. de Lózar, W. Schöpf, I. Rehberg, D. Svenšek, and L. Kramer. "Transformation from walls to disclination lines: Statics and dynamics of the pincement transition". *Physical Review E*, 72(5):051713, 1–11, 2005.

[19] A. Rey. "Defect controlled dynamics of nematic liquids". *Liquid Crystals*, 7(3):315–334, 1990.

[20] C. Chevallard, M. Clerc, P. Coullet, and J. M. Gilli. "Interface dynamics in liquid crystals". *The European Physical Journal E*, 1(2-3):179–188, 2000.

[21] Y. Galerne and L. Liébert. "Zigzag Disclinations in Biaxial Nematic Liquid Crystals". *Physical Review Letters*, 55(22):2449–2451, November 1985.

[22] M. Mihailovic and P. Oswald. "Zigzag disclination in uniaxial nematic phases: study in capillary tubes". *Journal de Physique*, 49(8):1467–1475, 1988.

[23] P. E. Cladis and M. Kléman. "Non-singular disclinations of strength S = + 1 in nematics", 1972.

[24] R. Repnik, L. Mathelitsch, M. Svetec, and S. Kralj. "Physics of defects in nematic liquid crystals". *European Journal of Physics*, 24(4):481–492, July 2003.

[25] M. Kléman and O. D. Lavrentovich. "Topological point defects in nematic liquid crystals". *Philosophical Magazine*, 86(25-26):4117–4137, 2006.

[26] J. Ignés-Mullol, J. Baudry, and P. Oswald. "Formation and distribution of point defects on a disclination line near a free nematic interface". *Physical Review E*, 63(3):1–9, 2001.

Chapter 8

Grooved Tunable Bragg Grating Devices

8.1 Introduction

The devices introduced in Chapter 7 provided spectral tuning of over 100GHz in the telecommunications C-band. However, it was shown that the tuning response was not a linear function of the applied field. This anomalous behaviour was found in the work performed in this thesis to be the result of a liquid crystal (LC) transition known as pincement. The transition for increasing voltage occurs at a larger field strength than that for decreasing voltage, hence the cells exhibit hysteresis in their tuning curves.

In the transition region, the LC behaviour is transient, it is not stable and depends strongly on the applied field strength. This is undesirable for telecomms tuning devices as they require stability. Therefore in order to remove the transient behaviour the disclination dynamics must either be removed or restricted to regions away from the waveguide and grating region. Control of LC dynamics can be achieved by a new substrate geometry known as grooved substrates.

Tunable devices require access to the evanescent field component of the propagating mode. After UV writing the gratings, the top cladding layer is removed to expose the grating and allow access to the evanescent field. The cladding is removed by a time-consuming and undesirable hydrofluoric (HF) acid wet etch process. An alternative method of accessing the evanescent field is utilizing prestructured planar substrates. The substrates have vertical grooves machined into the silica layers prior to UV writing. Waveguides and gratings are subsequently written up to the side of the grooves. The change in geometry provides several benefits which can be found in [1]. Most importantly the grooved geometry removes the necessity for the HF acid etching process, reducing fabrication time and avoiding acid handling. The grooves can also be accessed from both sides, increasing device density, and the proximity to the groove and therefore the adaptive cladding can be carefully controlled.

8.2 Grooved Substrates for LC Tunable Devices

Grooved substrates use the same three-layer silica-on-silicon substrates fabricated via Flame Hydrolysis Deposition that have been used for the etched window LC tuning devices. Once the substrates are fabricated, grooves are added by a precision machining technique. This utilizes a standard wafer dicing process, however the blade used is much thinner (~50μm wide). Fig. 8.2 shows a typical sample that has been cut by a saw blade producing grooves approximately 35μm high and 75μm wide.

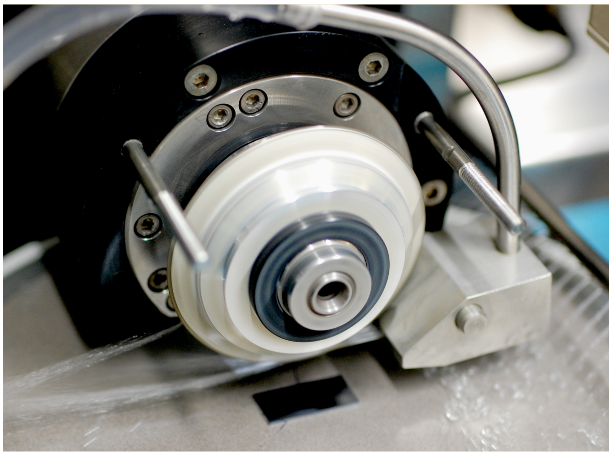

Figure 8.1: Dicing saw used for dicing wafers and cutting grooves into samples.

The substrates are then prepared for UV writing by hydrogen loading at 120bar for one week to increase UV photosensitivity. For grooved samples the waveguides are written up to within a few μm of the groove edge. This is achieved

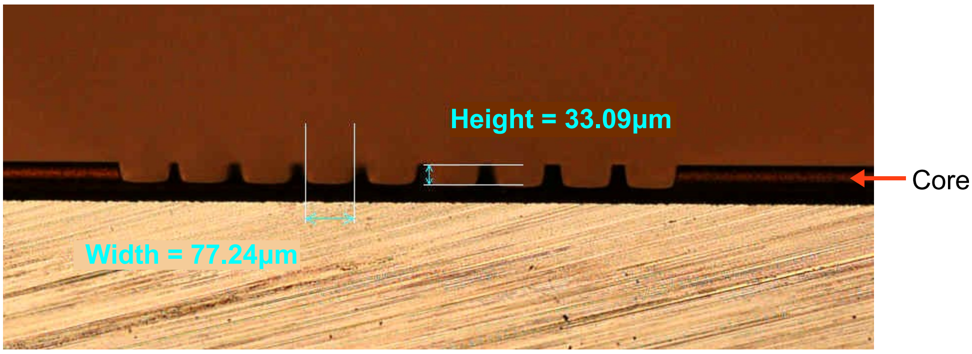

Figure 8.2: Three-layer silica-on-silicon sample with grooves cut using a dicing saw blade. The germanium-doped core layer is approximately half way down the groove edge.

by implementing an additional waveguide structure called an "s-bend". S-bends consist of two sinusoidal sections written consecutively to create an S shape. The radius of curvature for such a structure must be large enough to avoid too much bend loss. Therefore lateral displacements of 1-100μm are used over lengths of several mm. This also allows the waveguide input to be kept away from the groove which is beneficial for several reasons. Firstly, it allows reference gratings to be written away from the groove such that temperature tuning effects can be negated. Secondly, it allows for easier fabrication as pigtailing beside an LC filled groove is difficult. Finally, a waveguide written in close proximity to a groove along its length will experience additional waveguide losses due to scattering from the groove sidewall. Therefore the waveguide is only written near the groove where necessary.

In practise several s-bends are used in a single waveguide in order to approach the groove edge incrementally. This is necessary so that the waveguide and therefore the guided mode extends sufficiently into the groove region, but not so much that it is unnecessarily attenuated or poorly guided. Hence the initial s-bend usually contains a lateral displacement of ~100μm along a length of several mm, whereas subsequent s-bends are only a few μm wide. This allows the waveguide to gradually approach the groove.

Once the gratings have been written the device is assembled in a similar fashion to etched window devices. Both grooved sample and ITO are spin-coated with homeotropic surfactant, which is then baked to drive off any remaining solvent. The ITO is not patterned for these devices as the electric field is applied between

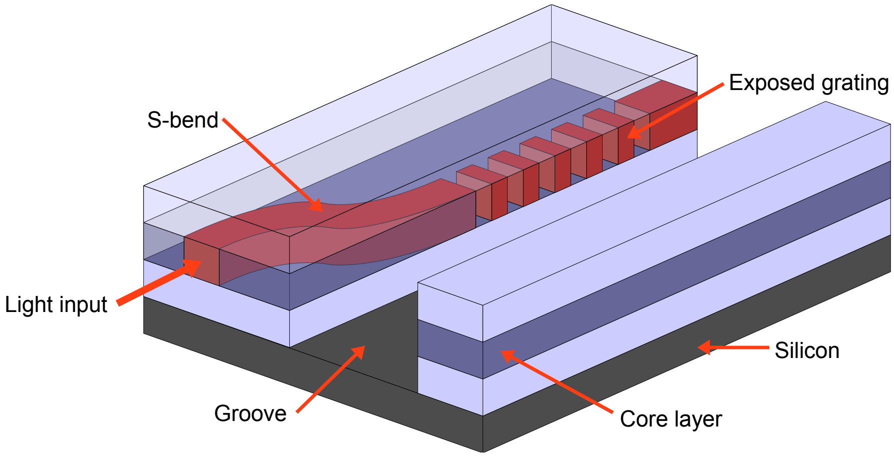

Figure 8.3: Three-layer silica-on-silicon substrate with groove machined into silica layers. An s-bend is used to approach the groove edge before the grating is written.

ITO coverslip and the silicon base of the sample. The sample is sealed on three sides with epoxy and LC is applied under vacuum to the grooves which fill via capillary action. The fourth side is sealed and electrodes are added to the ITO and a polished section of silicon for good electrical contact. A schematic of the device is shown in Fig. 8.4 along with a photograph of a working device.

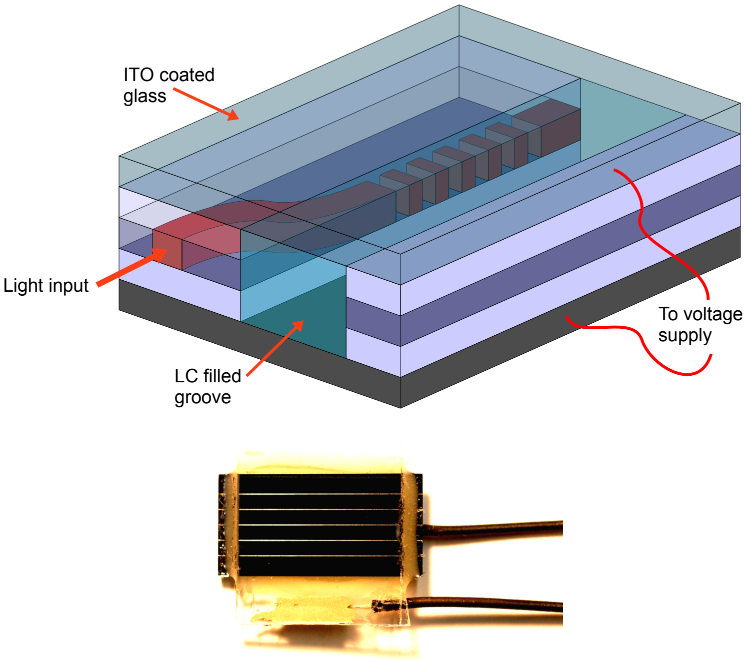

Figure 8.4: Top: LC tunable Bragg grating device in the groove geometry. Bottom: Photograph of a groove tuning cell.

8.3 Principle of Operation

Grooved tuning devices expose the waveguide and gratings from the side, rather than from above. Homeotropic surfactant aligns the LC normal to all four surfaces, and the electrodes are above and below the waveguide. The cells are shown in Fig. 8.5 and produce the same escaped configuration as seen in circular capillaries. The field is applied between the ITO coated coverslip and the silicon base of the samples producing vertical field lines.

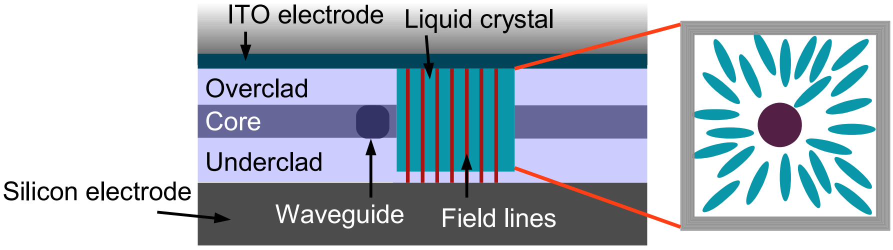

Figure 8.5: Grooved LC tuning cell using the silicon substrate base as an electrode. The same escaped radial configuration as seen in the last chapter is expected.

These devices employ the same principles of effective refractive index modification used in etched window tuning devices. The evanescent field of the propagating polarized optical mode experiences a refractive index that depends on the relative orientation of the LC molecules with respect to the polarization vector. In the field-off state, the LC is aligned normal to the side of the waveguide, and hence a TE mode will experience a higher effective index than a TM mode. As the field is increased, the LC rotates towards the vertical, and the effective indices experienced by orthogonally polarized modes reverses. Hence for increasing voltage a TE guided mode should experience a decreasing effective index, and the peak Bragg reflection wavelength should decrease with increasing applied voltage. The converse is true for TM guided modes.

However, the reorientation of the LC molecules in such a confined geometry is not trivial. It is expected that pair disclinations are formed and that the voltage tuning would be highly dependent on the locations of these defects. Shown in Fig. 8.6 is one potential director field distribution for a homeotropically aligned groove with a vertically applied electric field. It is possible that the +1 defect splits into two singular line defects of strength 1/2.

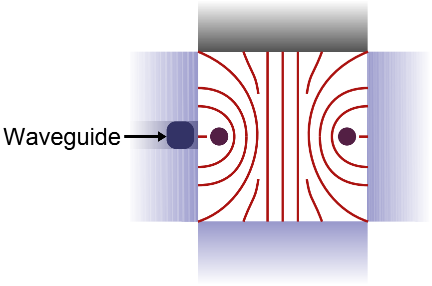

Figure 8.6: Potential director field distribution for a homeotropically aligned groove cell with electric field applied vertically.

This scenario would be problematic for LC tuned gratings as it can be seen that one of the pair defects is likely to be in close proximity to the waveguide and therefore the grating. This would produce unwanted tuning behaviour. As shown in Fig. 8.7, the tuning curves are not a linear function of applied voltage and contain additional features. These could be due to the disclination propagating towards the waveguide region, where it may become anchored. It is also possible that the disclination can propagate vertically along the groove sidewall until it finds an energetically favourable position, which may or may not reside in close proximity to the grating.

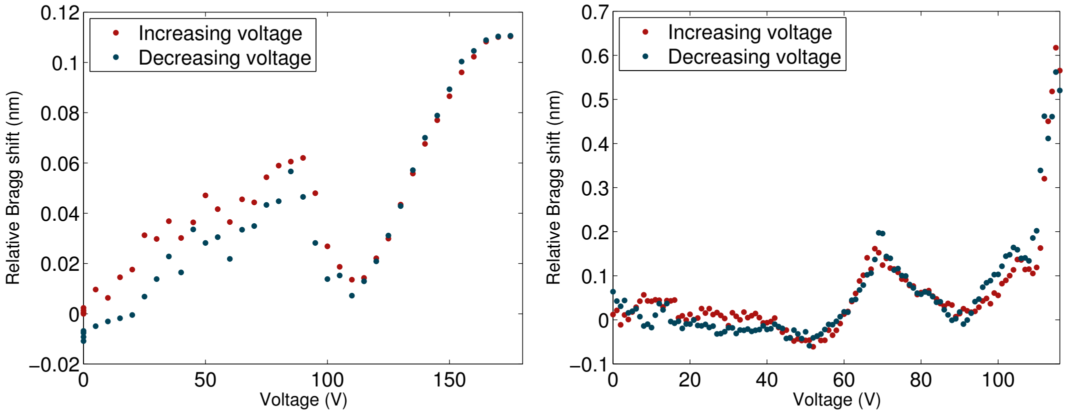

Figure 8.7: Tuning response of two different grooved cells with homeotropic alignment.

8.3.1 Hybrid Alignment Grooved Cells

In order to avoid unwanted tuning behaviour new devices were fabricated with hybrid surface alignment. The grooves were coated with homeotropic surfactant as before, however the ITO substrate was treated to provide planar alignment of the LC. This was achieved by spin coating a polyimide (PI) solution onto the ITO, which was the baked to drive off any remaining solvent. The PI coated ITO is then rubbed with a fine velvet roller in order to produce microscopic grooves in the polymer. The resultant LC alignment is shown in Fig. 8.8 where the result is one strength 1/2 disclination which is not situated near the waveguide.

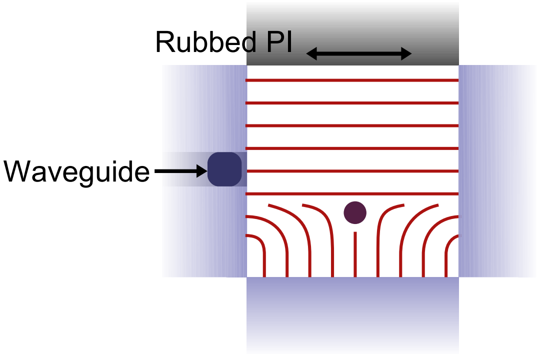

Figure 8.8: Director field distribution for a hybrid cell with planar alignment on the ITO substrate and homeotropic alignment on the three groove sidewalls.

Transparent grooved cells with the same hybrid alignment were fabricated to test for the presence of the disclination and to ensure the alignment was as expected. Cells were illuminated with white light in a transmission microscopy system. Shown in Fig. 8.9 are images of a hybrid aligned LC cell that exhibit the expected molecular alignment. The zig-zag disclination is clearly visible in the centre of the groove.

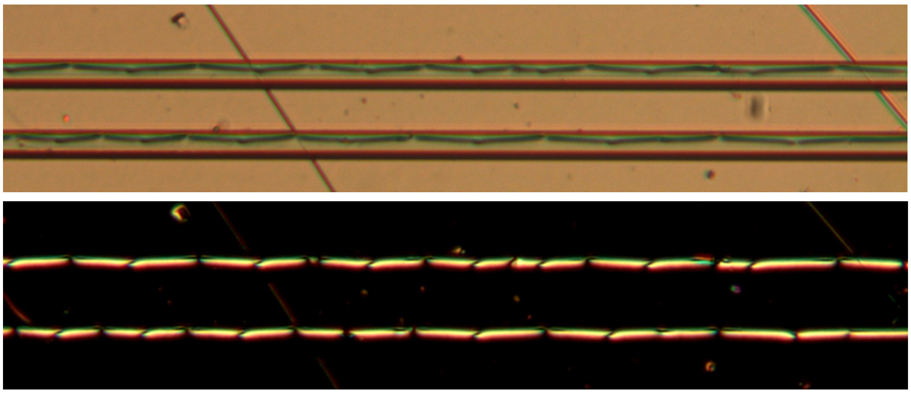

Figure 8.9: Images of hybrid aligned grooves filled with 5CB. (Top) Cell viewed through parallel polarizers, (bottom) cell viewed through crossed polarizers.

It was found that hybrid alignment was not guaranteed to produce the expected director configuration in the capillary. Indeed, the capillary can be seen to produce alternative disclination configurations, as shown in Fig. 8.10. Zigzag disclinations co-exist with straight disclinations, which can also become anchored to the groove edges. The zigzag configuration was reproducible upon optimization of the PI rubbing technique to produce the planar aligned surface, and optimization of the surfactant treatment.

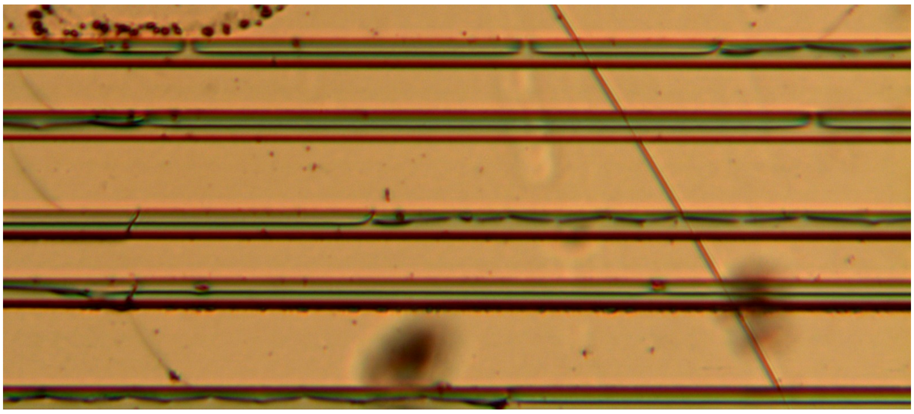

Figure 8.10: Image of hybrid aligned grooves filled with 5CB. Note the zigzag disclination can transform into a straight disclination which may become anchored at the groove edges. The anchoring is reminiscent of the behaviour seen in [2] and [3].

As the disclination is confined to the centre of the groove, it should not interfere significantly with the waveguide and grating. Therefore the tuning curves should be a more linear function of applied voltage. The tuning response shown in Fig. 8.11 is approximately linear until ~25V where the gradient becomes steeper and the fitting noise increases. This behaviour may be due to the strength of the reflection spectrum becoming weaker as the voltage increases. Notice there is no significant hysteresis, which is to be expected from this geometry. Hence the disclination has been successfully restricted to regions away from the grating.

The Bragg wavelength for all these samples is determined via a fitting algorithm used in the LabView™ computer programming environment. This uses a least-squares curve fitting process with a Gaussian fit profile to find spectral parameters of the grating response such as centre wavelength. Fig. 8.12 shows the evolution of the grating power and spectral position as a function of voltage. It can be seen that the peak position is shifting to shorter wavelengths, and also the peak height is diminishing. Reduced peak height is the cause of the gradient

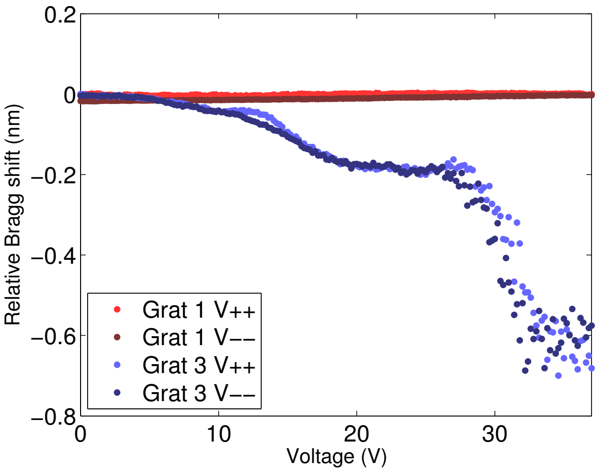

Figure 8.11: Tuning response of a grooved cell with hybrid alignment. Grating 1 is shown as a temperature reference and is not in close proximity to the LC region. Grating 3 supports a mode whose field profile extends into the LC region and thus is a tunable grating.

change in the tuning curves, another consequence is the increase in noise.

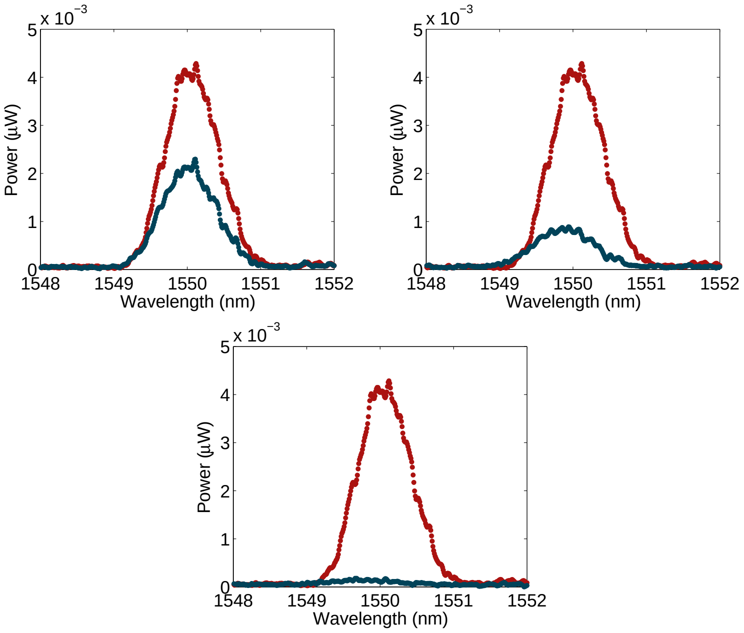

Figure 8.12: Grating spectra for grating 3 in Fig. 8.11. The red line is the untuned grating spectrum (0V), whereas the blue lines are the grating response at 10, 20 and 30V respectively.

8.3.2 Rapid Thermal Annealing of Grooved Samples

It was suspected that surface roughness may have caused unwanted spurious features in the device tuning curves. Roughness can be seen in Fig. 8.13 where the lower groove is considerably worse than the upper groove. Therefore a surface profiler was used to investigate the magnitude of the surface roughness. This apparatus is a stylus-based profiler operating in contact mode capable of performing area interrogation with numerical analysis.

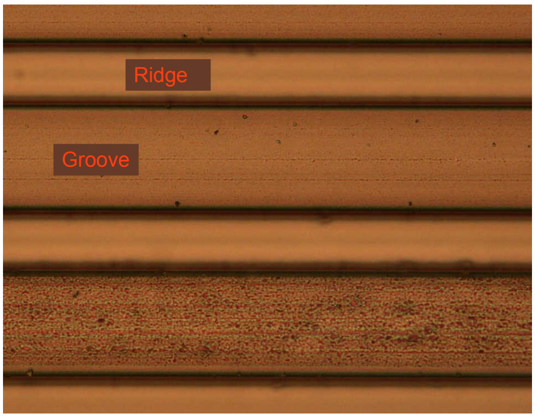

Figure 8.13: Top-down view of the grooves shown in Fig. 8.2. The upper groove has a relatively smooth surface whereas the lower groove exhibits far more surface roughness and would be problematic for LC alignment.

Using a wet etched sample as an example, two offcuts were taken from the same substrate. One offcut was unaltered, however the other was treated with a process known as Rapid Thermal Annealing (RTA) [4, 5]. This process exposes samples to elevated temperatures for brief periods and is often used for wafer annealing. In this thesis the RTA process is used to reduce roughness by removing surface artifacts. The temperature is ramped up to 1100°C and held for 7 seconds, which was determined experimentally to be the optimum duration.

Shown in Fig. 8.14 are surface profiler images of two three-layer silica-on-silicon offcuts taken from the same etched substrate. The first is not exposed to the RTA process, and exhibits a surface roughness value of 64.5nm. This is an arithmetic mean value of the roughness or $\mathrm{R_a}$ value, and is given by:

$$R_a = \frac{1}{n}\sum_{i=1}^{n}|y_i| \tag{8.1}$$

where y_i is the vertical distance from the mean line to the i^{th} data point. The second sample that is exposed to RTA exhibits a R_a value of 4.5nm. It can therefore be deduced that the RTA process significantly decreases the surface roughness and would therefore aid LC molecular surface alignment.

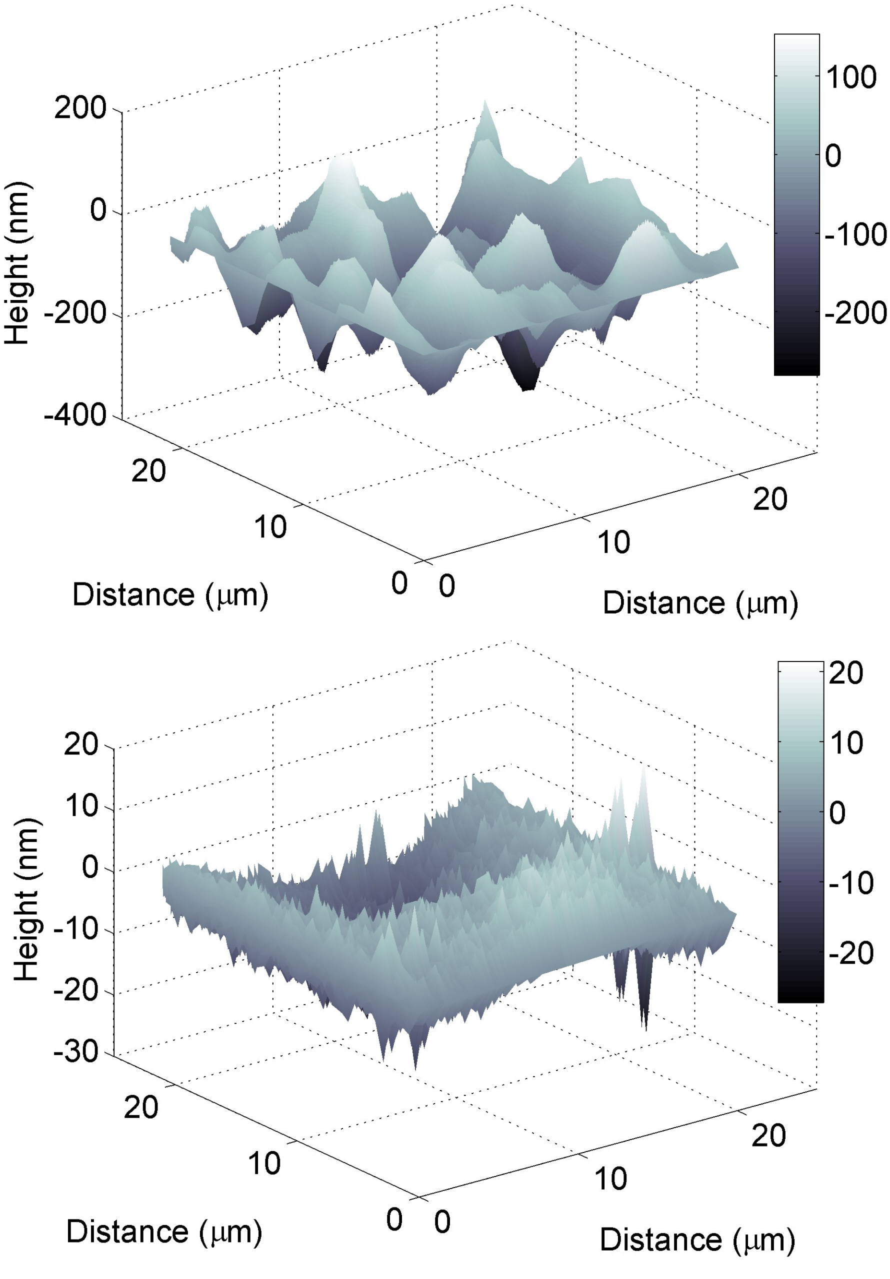

Figure 8.14: Area surface profile of an untreated sample (top) and an RTA treated sample (bottom). Notice the large variation in the height scaling between the two images.

Tuning curves for another hybrid aligned tuning cell are shown in Fig. 8.15. The silica-on-silicon grooved substrate used in this device was exposed to RTA treatment at 1100°C for 7 seconds. It can be seen that although the tuning is discontinuous around 25V the tuning curve is much smoother than in Fig. 8.11. The reduction of artifacts in the tuning curve can be associated with the smoother groove sidewalls from the RTA treatment. The discontinuity was expected to be due to a noisy spectrum causing a poor fit with the Gaussian fitting profile. However, on inspection it was seen that the discontinuity is a genuine physical effect. Spectra taken from the tuning curves at various voltages are shown in Fig. 8.16. It can be seen that the peak begins on the short wavelength side of the field-off position, before rapidly switching to the longer wavelength side. The peak wavelength then gradually reduces towards the initial value.

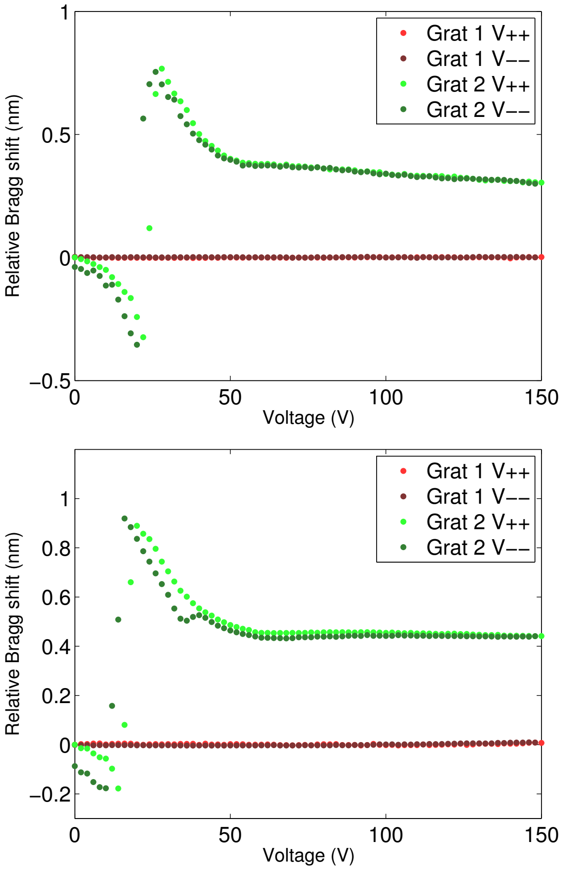

Figure 8.15: Tuning response of a grooved cell with hybrid alignment using TM polarised light. Grating 1 is shown as a temperature reference. Grating 2 exhibits discontinuous tuning behaviour possibly due to an anchored defect.

The origin of this behaviour is not fully understood. However, it is possible that a disclination line is pinned to the groove sidewall in the vicinity of the grating and then becomes mobile with increasing voltage [6]. LC molecules beside the sidewall may be kept in a homeotropic configuration by the defect until it detaches, the LC can then align with the field rapidly altering the effective

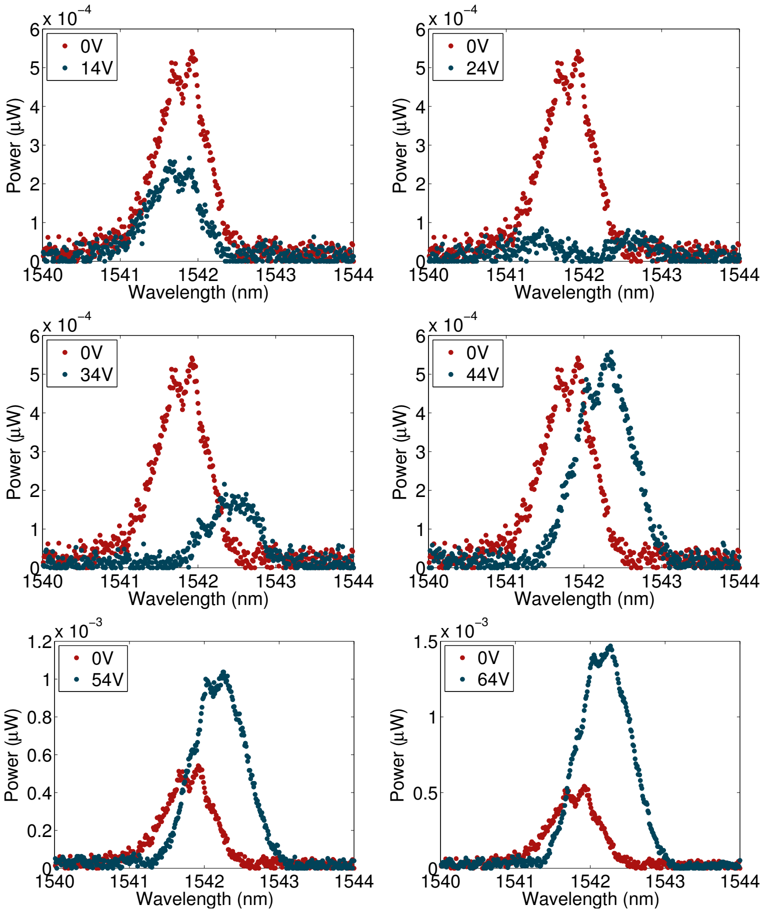

Figure 8.16: Grating spectra for grating 2 of Fig. 8.15 for increasing voltage. The grating peak starts on the shorter wavelength side of the field-off position and then transforms into an intermediate state with two small 'peaks' (24V). The peak then switches rapidly to the longer wavelength side before slowly moving back towards its initial position.

refractive index.

This behaviour could be used to form a switching device for telecommunications applications. In Dense Wavelength Division Multiplexed (DWDM) Systems, channels are often spaced by 100GHz, or even 40GHz. This corresponds to ~ 0.8nm spacing at 1550nm spectral position. Therefore this device has the potential to act as a switch between adjacent channels in a DWDM network system.

8.4 Summary

A new substrate geometry for LC tunable planar grating devices has been presented. These substrates include a dicing saw machined groove for side-access of the Bragg grating. The groove is subsequently filled with LC, and the electrodes are placed at the top and bottom of the substrate. Grooved tunable devices aimed to remove the hysteresis seen in previous top-access devices. Indeed, the resultant tuning curves for such devices exhibit no hysteresis as seen in previous samples, and the pincement transition is avoided.

Rapid thermal annealing of samples was used to remove surface roughness which can cause poor alignment quality. The resultant tuning curves had fewer spurious features, but did exhibit a discontinuous jump in the reflected wavelength. This was suspected to be due to surface pinning of defects around the grating region, causing a local modification of the effective index.

References

[1] J. C. Gates, C. H. Holmes, F. R. M. Adikan, C. B. E. Gawith, and P. G. R. Smith. “New geometry for planar UV written refractive index sensors”. In *Proceedings of SPIE*, volume 44, pages 65850O–65850O–8. SPIE, 2007.

[2] J. Ignés-Mullol, J. Baudry, L. Lejcek, and P. Oswald. “Formation of disclination lines near a free nematic interface”. *Physical Review E*, 59(1):568–577, January 1999.

[3] J. Ignés-Mullol, J. Baudry, and P. Oswald. “Formation and distribution of point defects on a disclination line near a free nematic interface”. *Physical Review E*, 63(3):1–9, 2001.

[4] A. T. Fiory. “Methods in Rapid Thermal Annealing”. In *Eighth International Conference on Advanced Thermal Processing of Semiconductors*, pages 15–25, 2000.

[5] J.-C. Zhou, D.-T. Luo, Y.-Z. Li, and Z. Liu. “Effect of sputtering pressure and rapid thermal annealing on optical properties of Ta2O5 thin films”. *Transactions of Nonferrous Metals Society of China*, 19(2):359–363, April 2009.

[6] J. Cheng. “Surface pinning of disclinations and the stability of bistable nematic storage displays”. *Journal of Applied Physics*, 52(2):724–727, 1981.

Chapter 9

Tunable Chirped Planar Bragg Gratings

9.1 Introduction

Where apodized and even uniform gratings have found a niche in filtering applications, chirped gratings are an invaluable tool for dispersion management and compensation applications [1,2]. Chirped gratings are those that contain a non-uniform period along their length. Therefore the Bragg reflection wavelength is spatially dependent and hence no longer constant. Chirp will therefore broaden the Bragg reflection spectrum because different wavelengths within the reflection band are effectively reflected from different positions along the grating. What is valuable about this behaviour is that light propagating through the grating will have different wavelength components reflected from different positions. The time taken to propagate to their reflection point and back again, the group delay, is therefore also wavelength dependent. If the group delay spectrum is carefully engineered it can be used to compensate for chromatic dispersion [3].

Chromatic dispersion is the wavelength dependence of the refractive index of a material. As such, if the refractive index changes, that implies the group velocity of light propagating in that medium also changes. Therefore the time taken for different wavelength components of the light to propagate through the medium is not constant. For instance, a pulse of light will consist of a finite spectrum of wavelengths defined by either the light source or the temporal windowing from the modulation. During propagation through tens or hundreds of kilometres of fiber, the pulse becomes temporally broadened due to dispersion.

In telecomms, the propagation medium is standard single-mode silica fibre, which has dispersion of 17ps/nm.km. This states that a pulse that is spectrally 1nm broad propagating over a length of 1km will be temporally broadened by 17ps. This may seem small, but for high bit-rate transmission systems this means adjacent temporal pulses will overlap such that data carried by those pulses is corrupted and ultimately lost. In a telecomms system operating at 10Gbps using a non-return-to-zero (NRZ) signal protocol with a 2dB power penalty, the maximum tolerable dispersion is 1800ps/nm [4]. This implies the distance limit for standard transmission fiber is around 105km before compensation is necessary.

As chromatic dispersion is a linear effect it can be compensated for by recompressing the pulse to regain the original data. Pulse compression requires a material, or device, with equal and opposite dispersion. Typically recompression of pulses is achieved by using a length of dispersion compensating fibre (DCF), which exhibits negative dispersion in the required wavelength range. However, DCF has issues with unmatched dispersion slopes when coupled with standard transmission fibre [5], resulting in residual dispersion which will be explained in section 9.2.1. DCF is also more susceptible to nonlinear effects[1] due to its smaller effective core area [4]. Another method used to combat the degrading effects of dispersion is electronic dispersion compensation (EDC) [6]. EDC uses a *transversal filter* to reshape pulses that have been temporally broadened due to dispersion [7,8]. The transversal filter will typically include multiple stages, each with a different delay and amplification. The filter reshapes the pulse to regain data integrity and reduce the bit-error-rate[2]. Pulse recompression can also be achieved by chirped Bragg gratings, which have tunable dispersion slopes and due to their short lengths are not susceptible to nonlinear processes.

This chapter demonstrates the concept of using standard PCB technology to

---

[1] For example self-phase modulation (SPM) is a nonlinear process that can degrade signal integrity. SPM is the modification of the phase of a propagating pulse due to its own intensity profile. Higher intensity regions of the pulse experience larger refractive indices (Kerr effect) and as such their phase becomes distorted and the pulse temporally broadens.

[2] Bit-error-rate is the ratio of incorrectly received bits to the total number of bits transmitted.

create arrays of heating elements from surface mount resistors. Such heating arrays can be used for tuning the reflection wavelength of planar Bragg gratings via the thermo-optic effect. Specifically, the work performed in this thesis demonstrates the ability to use PCB resistor arrays to modify the group delay slope of chirped gratings for the purpose of dispersion compensation.

9.2 Chirped Bragg Gratings

As explained in Chapter 3, chirp describes the increase or decrease in the grating period as a function of position. This chapter utilizes linearly chirped planar Bragg gratings, where the grating period monotonically increases (or decreases) as a function of position along the grating. The equation for the Bragg reflection wavelength is:

$$\lambda_B(z) = 2N_{eff}\Lambda(z) \tag{9.1}$$

where $\lambda_B(z)$ is the position dependent reflection wavelength, N_{eff} is the effective refractive index of the propagating mode, and $\Lambda(z)$ is the position dependent grating period. Linear chirp can be defined as:

$$\Lambda(z) = \Lambda_0 + \Lambda_1(z) \tag{9.2}$$

where Λ_0 is the starting period and Λ_1 is the linear change in the period along the grating. Chirp is given in nm/cm, which describes the spectral change in Bragg reflection wavelength per cm of grating length.

From Eqn.9.1 it can be seen that the reflection wavelength is not single-valued and spans a range of wavelengths dependent on the amount of chirp. Shown in Fig. 9.1 are spectra of linearly chirped Bragg gratings. As the chirp increases the reflection bandwidth increases accordingly.

9.2.1 Group Delay and Dispersion Compensation

In terms of dispersion management, the most important grating parameter is its group delay as a function of wavelength. Fig. 9.2 shows the group delay spectra of the gratings in Fig. 9.1 and the associated fitting. The important

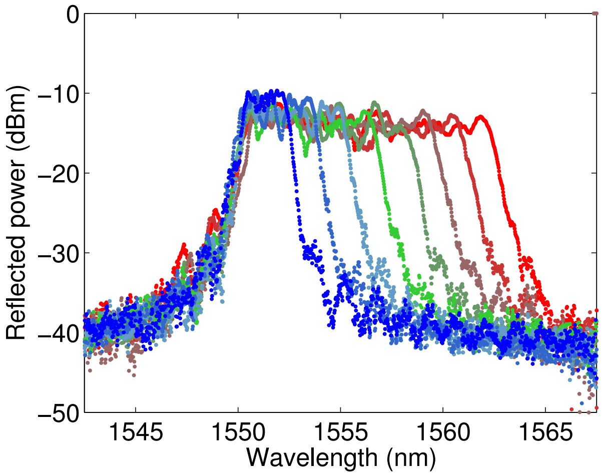

Figure 9.1: Reflection spectra of 9mm long linearly chirped Bragg gratings with chirp rates of 2.8 - 14.4nm/cm. Data courtesy of Helen Rogers.

property of the group delay spectrum in a chirped grating is the gradient. If the gradient is equal and opposite to that accumulated by the transmission fiber, the chromatic dispersion can be compensated and the pulse-broadening recompressed. The degree of compensation is limited by the grating length, as the amount a certain wavelength can be delayed is determined by the position from where it is reflected. Succinctly, $\tau(\lambda) = 2L_{\mathrm{resonance}}/\mathrm{v}_{\mathrm{group}}$, where $\tau(\lambda)$ is the group delay for a given wavelength, $L_{\mathrm{resonance}}$ is the distance along the grating for resonance at that wavelength, and $\mathrm{v}_{\mathrm{group}}$ is the group velocity. Therefore for fiber links where the accumulated dispersion is large, lengths of DCF are often used intermittently to cancel the acquired dispersion.

This poses a problem because the dispersion slope of the transmission fiber is often not matched to the dispersion compensating device, which leads to residual dispersion. If the dispersion slopes differ the compensation can only be matched to one wavelength, hence any other wavelengths will still acquire some residual dispersion. This effect is shown in Fig. 9.3 where only λ_1 is properly compensated, and all other wavelengths acquire residual delay. This is where planar chirped Bragg gratings can provide the level of spectral resolution required to compensate for mismatches in dispersion slopes. Each grating can address the residual dispersion on a per-channel basis, and as multiple Bragg gratings can be written on a single silica-on-silicon substrate, the resulting device can be compact, low cost and require little power.

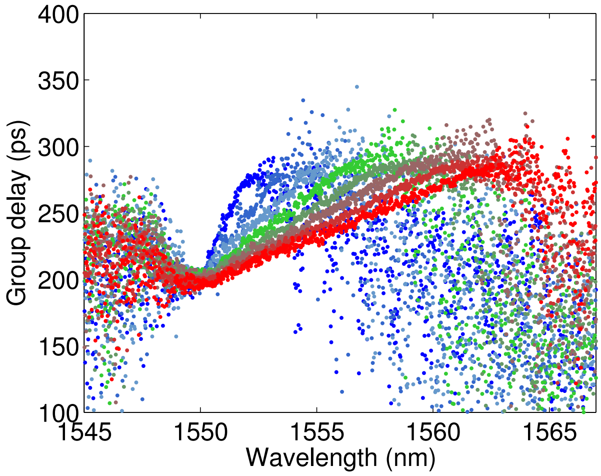

Figure 9.2: Group delay spectra of 9mm long linearly chirped Bragg gratings with group delay slopes of 7 to 39ps/nm. Data courtesy of Helen Rogers. Group delay data is taken using a network analyzer with the modulation phase shift technique (see section 9.3).

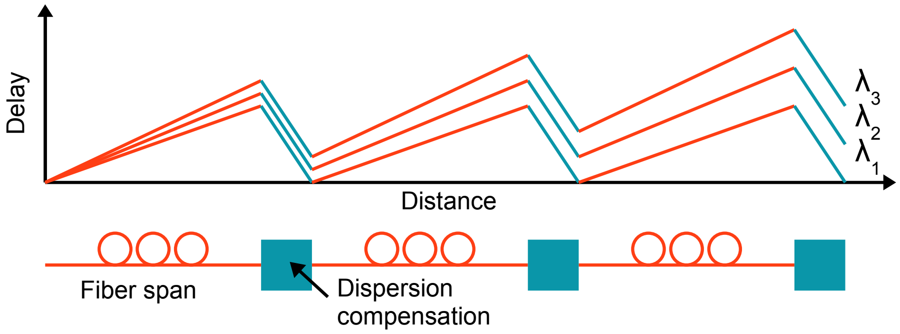

Figure 9.3: Dispersion compensating devices can only fully compensate one wavelength (or channel) if the slopes are not matched.

9.3 Planar Chirped Bragg Gratings

Chirped Bragg grating inscription in silica-on-silicon planar samples uses the same technique as the gratings described previously in this thesis. This involves the Direct Grating Writing (DGW) process to define both the input/output waveguides and the grating in one process. In order to chirp the grating the laser power modulation frequency is linearly adjusted whilst also linearly adjusting the speed of the translation stage to keep the effective index of the waveguide and grating equal. The spectrum of a 10mm long grating with 2.5nm/cm chirp is shown in Fig. 9.4. Solid lines show the theoretical spectrum obtained from a Matlab program script specifically designed for this thesis (see Appendix A). The program uses the coupled mode equations and performs Runge-Kutta 4th order numerical integration to determine parameters such as the reflectivity and group delay of the grating.

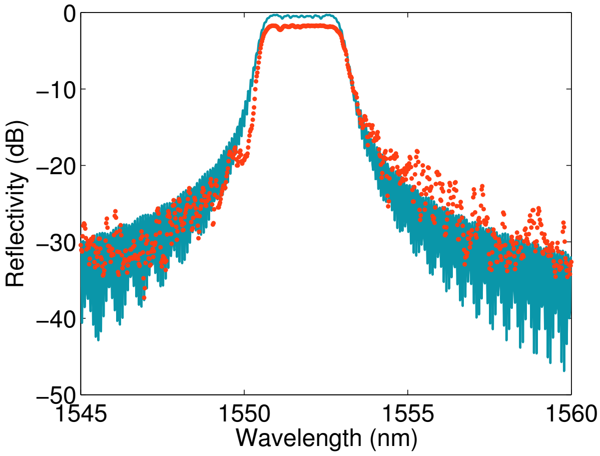

Figure 9.4: Reflection spectrum of a 10mm long, linearly chirped planar Bragg grating with 2.5nm/cm of chirp shown in orange. The simulated grating spectrum from the Matlab program is also shown in blue. The reduction in peak power compared to the simulation is due to coupling loss.

The grating in Fig. 9.4 exhibits a peak reflectivity of 66%. For dispersion management purposes, the group delay spectrum is also vital. For the above grating, the group delay spectrum, and simulated spectrum, are shown in Fig. 9.5. The spectra are in good agreement, confirming that DGW is a suitable technique for the manufacture of planar chirped Bragg grating structures. Group delay measurements are taken using a modulation phase-shift (MPS) technique described below.

Shown in Fig. 9.6 is a schematic of the characterization system used to obtain group delay measurements from the planar chirped gratings. Light from an Agilent 81600B tunable laser source, controlled by a computer running LabVIEW™, is sent into a lithium niobate electro-optic modulator (EOM), in this case a Lucent 2623-NA 10Gb/s intensity modulator. The modulation signal is provided by an Agilent 8753ES S-Parameter network analyzer (VNA). The modulated laser source is coupled into the sample and the reflected light is captured by a New Focus model 1611 IR 1GHz photoreceiver. The photoreceiver signal is then fed back into the VNA where the electrical power and phase are measured. The laser source is stepped in wavelength by computer control,

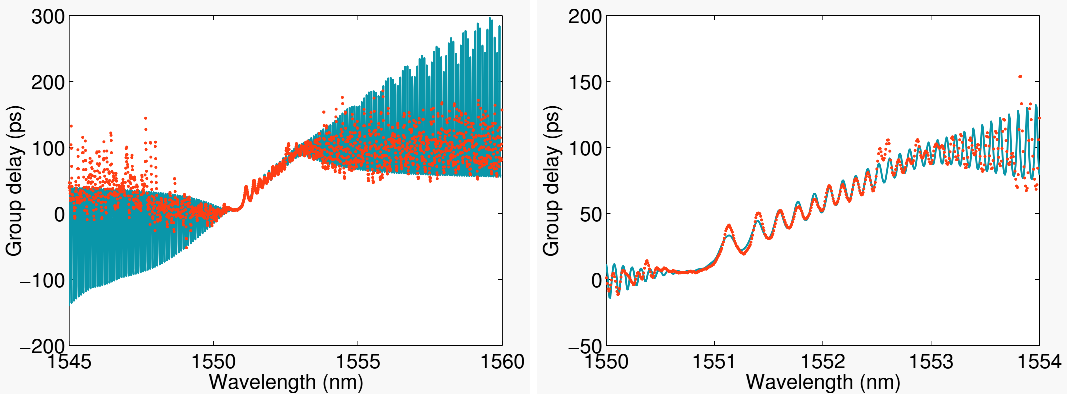

Figure 9.5: Group delay spectrum of a 10mm long, linearly chirped planar Bragg grating with 2.5nm/cm of chirp. On the right is a magnified image of the central region showing excellent agreement between the modelled (blue) and measured (orange) group delay. The group delay is ~40ps/nm and a distinct oscillatory component can be seen in the spectra.

providing a relative power and phase measurement at each wavelength.

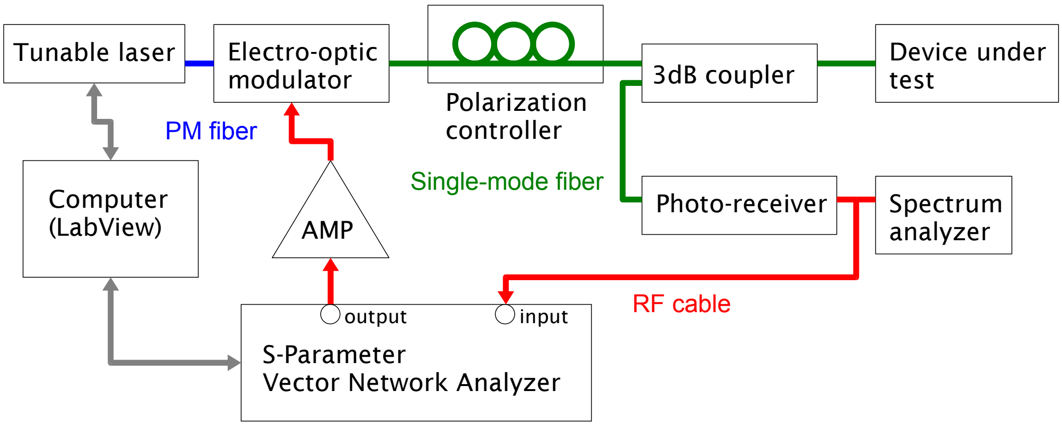

Figure 9.6: Characterization setup to test group delay of chirped gratings.

Because the optical signal is modulated (at 1GHz), the resultant spectrum contains sidebands around the laser wavelength (1550nm ± 8pm). MPS uses both the source wavelength and the sidebands to determine the relative phase shift produced by the grating. The photoreceiver converts the reflected optical signal into an R.F. electrical signal and sends it to the VNA. Due to the dispersive nature of the chirped grating, there is a difference in optical path length for different illumination wavelengths. Different path lengths manifest themselves as a change in phase at the photoreceiver, which in turn provides the group delay of the device. The measured phase of the modulated light is related to the group delay by [9]:

$$\Delta\tau = \frac{\phi_{\lambda 1} - \phi_{\lambda 2}}{2\pi f_{mod}} \tag{9.3}$$

Here $\phi_{\lambda 1,2}$ are the electrical phases of two adjacent interrogation wavelengths and f_{mod} is the modulation frequency. As the system cannot measure the phase of the signal directly, the system uses the sideband beating with the source wavelength to create a beat frequency. The phase of the beat signal can then be measured.

The group delay spectra are not completely linear in the reflection band as they contain an oscillatory component. This is known as group delay ripple (GDR) and is common to chirped gratings [10]. The ripple is caused by interference between the broadband reflection from the front of the grating and the position dependent reflection inside the grating itself. The interference oscillates between being constructive and destructive as the wavelength is scanned. For wavelengths near the launch end of the grating, in this case the short wavelength end, the beat frequency is low as the difference in path length is relatively short. As the path length difference increases, the beat frequency increases. This is analogous to a Fabry-Perot (F-P) resonator with linearly varying thickness [11]. The process is shown in Fig. 9.7. Incoming broadband light (a) has a small broadband reflection from the front of the grating (b) if the waveguide and grating are not impedance matched. Each wavelength in the reflection band is reflected from a different point along the grating (c), and this light will interfere with the broadband reflection (b). As the free spectral range of an etalon is given by:

$$\Delta\lambda = \frac{\lambda_0^2}{2nL\cos\theta + \lambda_0} \approx \frac{\lambda_0^2}{2nL\cos\theta} \tag{9.4}$$

the periodicity is proportional to $1/L$. As such, as the wavelength and therefore the distance into the grating increases, the frequency of the GDR increases. Since the delay time for light reflected from a grating is [12]:

$$\tau = \frac{d\theta}{d\omega} = -\frac{\lambda^2}{2\pi c}\frac{d\phi}{d\lambda} \tag{9.5}$$

the interference causes a modulation in $d\phi/d\lambda$, where ϕ is the phase of the reflected light, creating ripple. Deviations in the ripple can be due to the broadband reflection from the back of the grating (d) interfering with the grating reflection, causing additional periodicity.

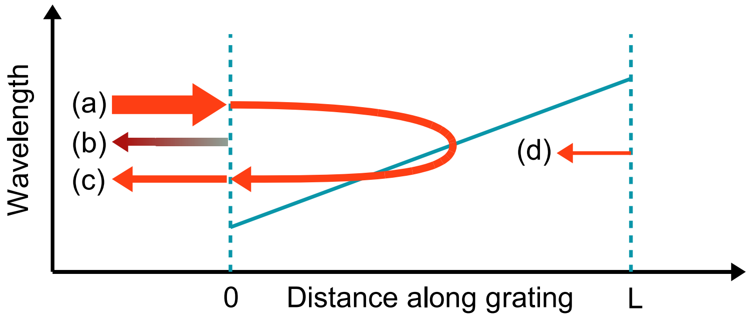

Figure 9.7: Diagram of the group delay ripple effect in a chirped grating.

9.3.1 Chirp-Apodized Gratings

The GDR is problematic for dispersion management applications as it causes highly wavelength-dependent group delay fluctuations. It has been shown that the ripple is caused by broadband reflections from the ends of the grating causing F-P resonances. Previously, a process known as apodization was used to reduce the side-lobes in the uniform gratings reflection spectrum. Similarly, apodization can be used to reduce the GDR by replacing the sharp impedance mismatch between waveguide and grating with a smoothly varying function, such as Gaussian apodization. This has the effect of reducing the F-P resonances and thus reducing the ripple. The reflection spectrum of a Gaussian apodized, linearly chirped grating is shown in Fig. 9.8. The peak reflectivity has dropped to 43% due to the apodization.

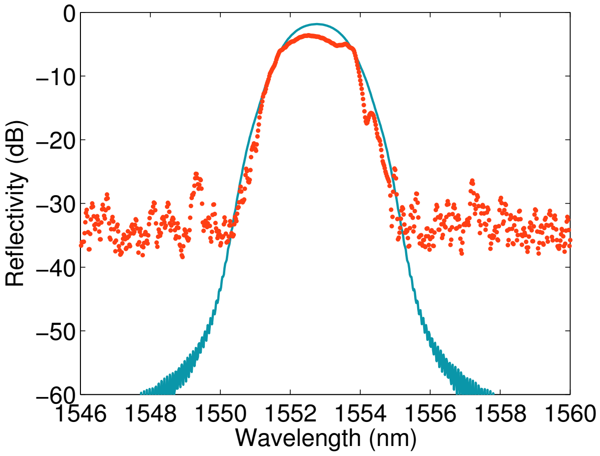

Figure 9.8: Reflection spectrum of a 10mm long, linearly chirped, Gaussian apodized planar Bragg grating with 5nm/cm of chirp.

It would be expected that the successfully chirp-apodized grating would have reduced GDR, and indeed this is the case as shown in Fig. 9.9. The group delay is a linear function of wavelength within the reflection band, with a moderate slope of 17ps/nm. However, this is a limitation of the substrate size and it is why these devices focus on residual dispersion compensation rather than long-haul dispersion compensation.

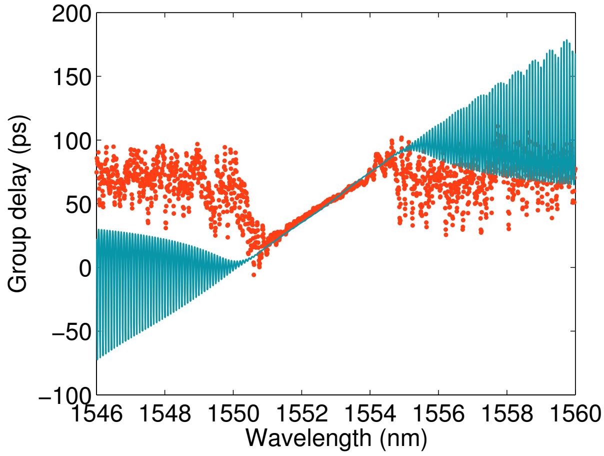

Figure 9.9: Group delay spectrum of a 10mm long, linearly chirped, Gaussian apodized planar Bragg grating with 5nm/cm of chirp.

9.3.2 Tuning Chirp-Apodized Gratings

The group delay slope of chirped gratings is constant as it is defined by the amount of chirp. However, by tuning the grating period as a function of position, the chirp can be adjusted. This can be achieved by thermally tuning the grating if a thermal gradient can be maintained along its length. Periodic heating elements have been used to exploit the thermo-optic effect in silica-based glasses [13–15]. In the case of silica-on-silicon samples, the thermo-optic coefficient is ~10pm/°C.

Integrated heating elements often require photolithographic processes and are therefore costly. The work in this thesis uses standard printed circuit board (PCB) technology with a mm-scale resistor array to achieve a thermal gradient across the grating. Fig. 9.10 shows an array of 10 resistors of dimension 1mm×0.5mm, with a pitch of 1mm. The 10 single in-line pins are attached to removable ribbon cable and are addressable individually. This module is designed to fit over the grating region of a UV-written sample. The sample used for tuning measurements is shown in Fig. 9.11, which includes a fiber pigtail attached via

UV-curable glue. The channel waveguides that contain the chirped gratings can be seen in the sample, and the resistor array is aligned parallel to the waveguides. In this device, the gratings were 6mm long such that up to 6 resistors would be available for thermal tuning.

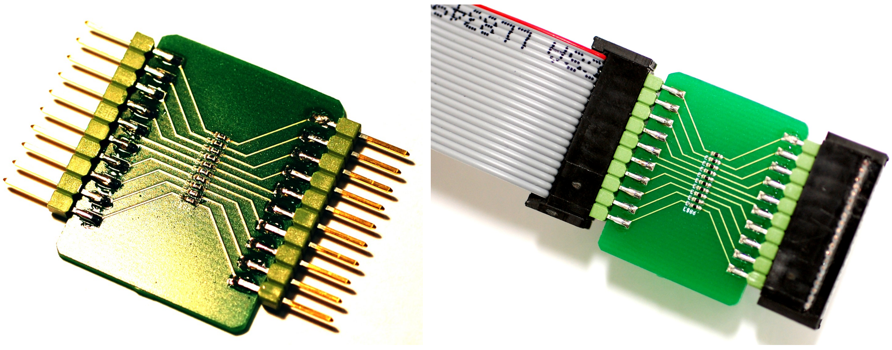

Figure 9.10: Resistor array for tuning of a DGW chirped planar Bragg grating.

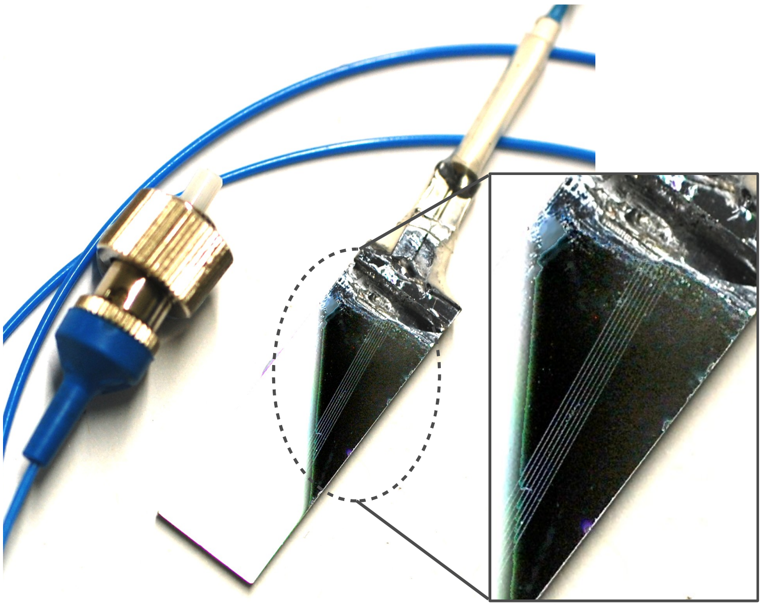

Figure 9.11: Pigtailed UV-written sample on a planar substrate. The waveguides can be seen in the sample.

The tuning calibration curves for the resistors are shown in Fig. 9.12. Thermal tuning of over 70°C is achievable with voltages of as little as 3.5V. It was also found that the temperature gradient between adjacent resistors (spaced 1mm apart) was between 40 and 50°C, implying that gratings could be thermally tunable by up to 500pm/mm. Once the resistors are aligned with the waveguide containing the gratings, and placed in contact with the sample, tuning data could be acquired. Fig. 9.13 demonstrates the range of thermal tuning available when heating all resistors to the defined temperatures. The total tuning was 0.56nm over 37°C, giving a thermal tunability of 15pm/°C. As the heating was uniform there was no appreciable change in group delay slope. Inconsistencies in the thermal spacing of the spectra are due to the difficulty in applying a thermocouple in close proximity to the grating when covered by the resistor array.

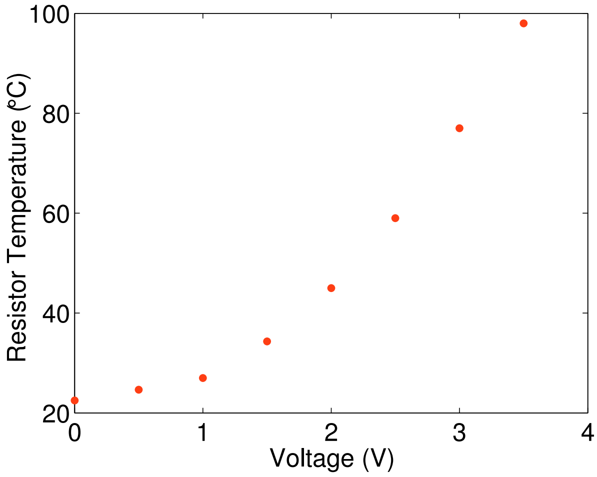

Figure 9.12: Temperature calibration curve of the resistors used for thermal tuning.

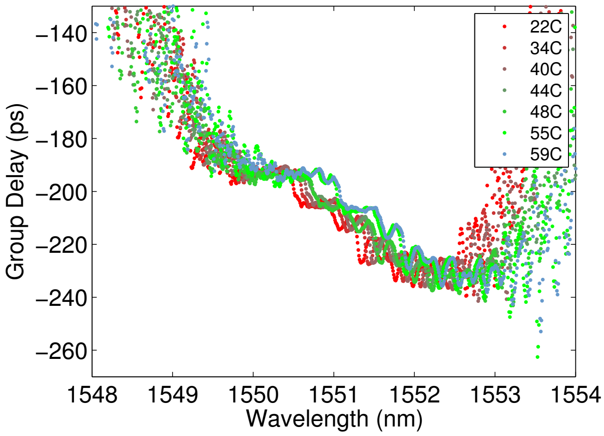

Figure 9.13: Group delay spectra of chirped grating under thermal tuning. In this case the grating was not apodized.

In order to modify the group delay slope, a Peltier thermoelectric module was used to cool the bottom surface of the sample below ambient temperature (22°C). Cooling of the sample is used in an attempt to negate the bulk heating caused by the silicon substrate base conducting heat along the length of the grating. As silicon has a thermal conductivity over 100 times larger than that of silica, any heat that reaches the silicon base will propagate along the length of the sample. This will reduce the maximum available thermal gradient and thus reduce the available tunability of the chirp and hence the group delay slope. The resistors were applied to the silica side of the sample and addressed individually resulting in localised heating of the grating.

In Fig. 9.14, the resistors were addressed sequentially from the front of the grating. As the grating contained a positive linear chirp, the period increases from front to back. Therefore by heating the front, the chirp should decrease as the difference in period reduces. As the chirp gradient is lower, light of a particular wavelength will have to travel further into the grating before being reflected. Hence it will experience more delay than with the unheated sample, the result being an increase in the group delay slope. As more resistors are addressed, the thermal gradient decreases, hence the chirp gradient increases. The result is a reduction in the group delay slope.

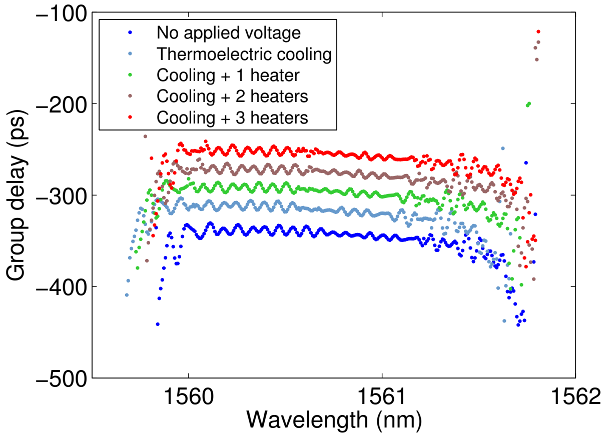

Figure 9.14: Group delay spectra of a chirp-apodized grating under thermal tuning using a thermoelectric module to cool the silicon base. The spectra are offset for clarity.

Although the maximum change in gradient is modest, at around 4 ps/nm, the principle of thermally tuned planar chirped Bragg gratings using simple PCB-based thermal arrays has been demonstrated. They are low power devices, with each active resistive element consuming less than 0.5W of power. Devices used to compensate residual chromatic dispersion after long fiber links often require

Thermal tuning	Group delay slope (ps/nm)
None	-12.92
Cooling only	-16.45
Cooling + 1 resistor	-14.07
Cooling + 2 resistors	-13.18
Cooling + 3 resistors	-12.35

Table 9.1: Least squares fit of group delay slope from a chirp-apodized grating utilizing various heating elements.

group delay slopes of -20 to 20ps/nm, on a per-channel basis. Therefore if the thermal gradient could be increased these chirped gratings could be used to address residual dispersion in telecommunications systems for individual channels. Due to the nature of the planar geometry, many such tunable gratings could be made on a single substrate, potentially allowing for an entire telecommunications band to be compensated with a single device.

9.3.2.1 Limitations of Thermally Tuned Chirped Gratings

The limitation with this geometry is due to the thermal conductivity of the silicon which hinders the maximum achievable thermal gradient inside the silica layer. Silica has a thermal conductivity of ~1.4W/mK (Watts per metre-Kelvin) compared to silicon with ~150W/mK. Using Fourier's Law for heat conduction:

$$q_x = -k\frac{\mathrm{dT}}{\mathrm{dx}} \tag{9.6}$$

where q_x is the heat flux, in W/m^2, k is the thermal conductivity, and $\frac{\mathrm{dT}}{\mathrm{dx}}$ is the thermal gradient, the maximum achievable gradient is 0.58°C/µm. Assuming a silica layer of 50µm, the maximum thermal difference from the top of the silica to the silicon is 30°C. However, the waveguide is 25µm below the surface, therefore the grating can be at most 15°C above the temperature of the silicon. This is assuming the resistor element is heated to 90°C where it requires 0.4W of electrical power. The silicon will rise to 60°C, with the grating at 75°C. As the silicon is a good thermal conductor, it conducts heat laterally along the waveguide and it is assumed that the silicon under the grating 1mm away is of a similar temperature. Therefore 25µm above this the grating will be at 45°C.

This implies the maximum thermal gradient along the grating is 30°C/mm, as illustrated in Fig. 9.15.

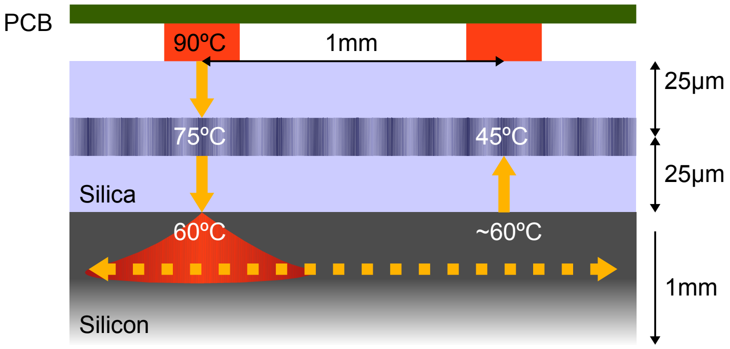

Figure 9.15: Thermal transport in a thermally tuned planar Bragg grating sample. Resistors are shown in orange.

However, this does not take into account the thermal conductivity of the PCB housing the resistors. It was found that heating a resistor to 90°C would cause adjacent resistors to rise to 45°C with the heater array uncovered. Thus the calculated thermal conductivity for the PCB array is ~18W/mK, over ten times that of silica. Hence the PCB will cause a loss of thermal gradient for tuning purposes. Also, if the air between the PCB and sample is heated, the maximum gradient across the silica reduces further. This is likely to be the cause of the small tuning response seen in these devices.

One method of addressing this problem is reducing the contact area of the heating elements. The resistors currently have a contact area of 0.5mm^2, but it may be possible to replace them with nickel-chromium (nichrome) based heating elements, which can be less than 0.1mm wide. Reducing the contact area by a factor of 5 would increase the maximum achievable gradient to over 70°C over a distance of 25μm. This would allow for greater gradients and thus greater changes in the group delay slope. NiChrome heaters would not require a covering PCB and thus more of the maximum thermal gradient could be realised. As 70°C/mm along the grating corresponds to 700pm/mm tuning, a grating with 5nm/cm (500pm/mm) of chirp could have its group delay slope doubled or flattened depending on the gradient direction. This would allow a broader tuning range in planar chirped gratings.

9.4 The Concept of Liquid Crystal Tunable Chirped Gratings

Another method of modifying the chirp gradient would be to spatially modify the effective refractive index of the grating by using a liquid crystal (LC) as an adaptive overlayer. If the orientation of the LC could be modified continuously along the length of the grating, then the effective index can also be modified along its length. In theory this would not only allow the chirp rate to be modified, it would also allow a uniform grating to acquire chirp purely through the action of LC reorientation.

The conceptual design of an LC-tunable chirped planar Bragg grating is illustrated in Fig. 9.16. An electrode made from deposited metal or ITO is used as a common potential, while a linearly resistive strip comprises the other electrode. As the resistance increases along the length, the field between the strip and electrode decreases. Thus the reorientation of the LC molecules also reduces with the local field strength. For a cell with planar and axial alignment, the high field regions will reorient and become transverse to the grating axis (a). Where the field is too low to overcome the Fréedericksz transition, the alignment is governed by the surface treatment, in this case planar (b). By addressing the resistive strip from both ends, the gradient and the direction of the effective index modulation can potentially be controlled.

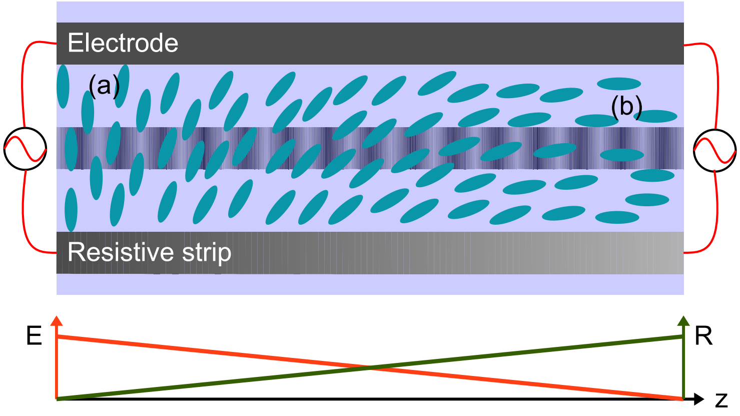

Figure 9.16: Concept of an LC-tunable chirped grating.

A TE mode launched into the waveguide in the scenario of Fig. 9.16 will experience decreasing refractive index when propagating from left to right.

Hence a chirped grating with linearly increasing chirp will have its total chirp reduced, increasing the group delay slope. Conversely if the voltage is increased from right to left, the chirp will be amplified and the group delay slope reduced. However, a TM mode will see no effective index modification and as such a limitation of this device would be high polarization sensitivity. Due to the added complexity of the design, and time constraints, the LC tunable chirped grating concept was not completed during this work.

9.5 Summary

This chapter presented work on developing and fabricating UV-written planar chirped and chirp-apodized Bragg gratings in the three-layer silica-on-silicon platform. Devices fabricated in this thesis used linearly chirped gratings in order to exploit their linear group delay response. The gratings are apodized in order to remove the group delay ripple inherent in unapodized chirped gratings.

Using a resistor array as a series of heating elements fabricated with standard PCB technology, the group delay gradient in a chirped grating was tuned by 4ps/nm. The limitations in the tuning range arise from the thermal conductivity of the silicon substrate and the PCB containing the heater array. The thermal gradient could be improved by using NiChrome heating elements which have a smaller contact area with the sample.

References

[1] K. O. Hill, F. Bilodeau, B. Malo, T. Kitagawa, S. Thériault, D. C. Johnson, J. Albert, and K. Takiguchi. “Chirped in-fiber Bragg gratings for compensation of optical-fiber dispersion”. *Optics Letters*, 19(17):1314, 1994.

[2] D. Pastor, J. Capmany, D. Ortega, V. Tatay, and J. Marti. “Design of Apodized Linearly Chirped Fiber Gratings for Dispersion Compensation”. *Journal of Lightwave Technology*, 14(11):2581–2588, 1996.

[3] J. Kwon, S. Kim, S. Roh, and B. Lee. “Tunable Dispersion Slope Compensator Using a Chirped Fiber Bragg Grating Tuned by a Fan-Shaped Thin Metallic

Heat Channel". *IEEE Photonics Technology Letters*, 18(1):118–120, January 2006.

[4] B. Chomycz. *Planning Fiber Optics Networks*. McGraw-Hill Professional, 2009.

[5] A. E. Willner. "Chromatic Dispersion and Polarization-Mode Dispersion". *America*, (March):16–21, 2002.

[6] H. Azgomi. "Enabling Enterprise 10 Gigabit Ethernet Deployment with Long Reach Multimode Optics", 2007.

[7] A. Borjak, P. P. Monteiro, J. J. O'Reilly, and I. Darwazeh. "High-speed generalized distributed-amplifier-based transversal-filter topology for optical communication systems". *IEEE Transactions on Microwave Theory and Techniques*, 45(8):1453–1457, 1997.

[8] P. M. R. S. Moreira, I. Z. Darwazeh, and J. J. O'Reilly. "Distributed amplifier signal shaping strategy for multigigabit digital optical transmission". *Electronics Letters*, 29(8):655, 1993.

[9] R. Hui and M. O'Sullivan. *Fiber Optic Measurement Techniques*. Academic Press, 2008.

[10] R. Kashyap. *Fiber Bragg Gratings*. Academic Press, USA, 1999.

[11] Z. Tan, Y. Liu, T. Ning, and S. Jian. "The generation of group delay ripple of chirped fiber gratings". *Chinese Optics Letters*, 2(1):18–20, 2004.

[12] T. Erdogan. "Fiber grating spectra". *Journal of Lightwave Technology*, 15(8):1277–1294, 1997.

[13] Z. Chen, C. Lu, J. H. Ng, X. Yang, and T. H. Cheng. "Tunable chirped fiber Bragg gratings by a distributed heater". *Optical Engineering*, 40(7):1156, 2001.

[14] N. Q. Ngo, D. Liu, S. C. Tjin, X. Dong, and P. Shum. "Thermally switchable and discretely tunable comb filter with a linearly chirped fiber Bragg grating.". *Optics letters*, 30(22):2994–6, November 2005.

[15] I. Petermann, S. Helmfrid, O. Gunnarsson, and L. Kjellberg. "Tunable and programmable optical bandpass filter". *Journal of Optics A: Pure and Applied Optics*, 9(11):1057–1061, November 2007.

Chapter 10

Liquid Crystal Waveguides

10.1 Introduction

Previous chapters have used liquid crystals (LC) exclusively as an adaptive overlayer or cladding for the silica-based waveguide. They have been employed to modify the effective refractive index of the guided mode in the silica waveguide. However, there is potential for the LC itself to be used as the guiding medium. If the guided mode is confined within the adaptive optofluid, rather than the silica or other passive material, a much greater component of the mode can be modified. The devices therefore do not rely on evanescent field modification, rather modification of the core itself. This is the premise behind LC waveguides and many optofluidic devices [1,2].

The concept of LC waveguides has been investigated by d'Alessandro et al [3]. Here the LC waveguides were fabricated on silicon substrates using silica-coated V-groove configurations. This chapter will present experiments based on employing LC waveguides in groove geometries fabricated with the dicing saw technique described previously. The LC will be housed in silica-based cladding materials to ensure modal confinement. Waveguides will require suitable surface treatment in order to ensure correct molecular alignment. Alignment is critical in LC-based devices, especially where the LC is the guiding medium itself, as LC waveguides are known to have large scattering losses [4,5]. In this thesis, it has been shown that the scattering loss can be reduced considerably by utilizing the LC in the isotropic phase, however this eliminates the benefit of having an easily reconfigurable birefringent optical material. Therefore much work was performed in order to fabricate LC waveguides that operate in the nematic phase.

In this work, devices were initially fabricated using ready-made substrates in the form of hollow-core fibers. These fibers contained small diameter cores that could be easily infiltrated with LC compounds. Subsequent devices focussed on employing machined grooved substrates to contain the LC. Planar substrates provide a more suitable geometry for field-induced realignment and device manufacture.

10.2 Liquid Crystal Filled Fibers

Before fabricating planar LC waveguide devices the suitability of LC's as a guiding medium was assessed using hollow optical fibers specially fabricated at the ORC. These fibers consisted of a hollow core of approximately 5μm diameter with a ~185μm diameter cladding. Shown in Fig. 10.1 is a microscope image of a cleaved fiber end. Sections of fiber approximately 6cm long were filled with LC via capillary action. They were left for several hours to ensure complete infiltration of the LC. Molecular alignment was then interrogated using the same transmission microscopy setup for analyzing LC cells, as shown in Chapter 4. The fiber was placed between crossed polarizers aligned parallel and perpendicular to the fiber axis. It was then illuminated with narrow-band LED light, and images were captured with a high-resolution camera.

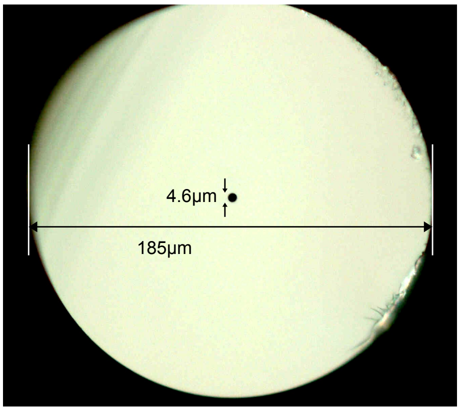

Figure 10.1: Microscope image of a cleaved end of a hollow fiber.

Shown in Fig. 10.2 is an image of the LC Merck NLC-7023 taken through crossed polarizers, which is a low refractive index nematic LC with similar properties to LC 18523. It can be seen that the alignment in the hollow fiber core is random which implies the LC is not forming the escaped (Fig. 10.5) configuration but rather forming micro-crystalline domains. This would cause excessive scattering loss and thus an alignment layer was required. LC alignment was achieved by filling a section of fiber with homeotropic surfactant, Merck LiquiCoat ZLI-3334, via capillary action, and then baking it at 200°C for several hours to remove any remaining solvent. The resulting capillary alignment can be seen in Fig. 10.3.

Figure 10.2: Image of a hollow core fiber filled with nematic LC 7023 taken through crossed polarizers using 464nm light.

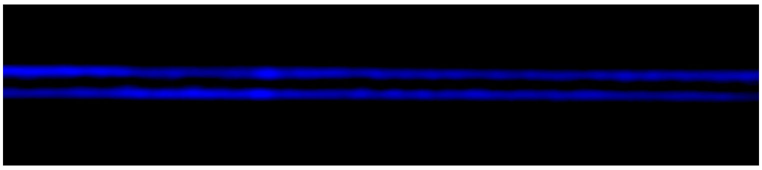

Figure 10.3: Image of a hollow core fiber filled with nematic LC 7023 taken through crossed polarizers using 464nm light. The fiber is treated with homeotropic surfactant prior to LC infiltration.

In order to achieve modal confinement the refractive index of the LC must be higher than the surrounding cladding. As the LC waveguide is likely to have considerable scattering losses, it is desirable to have a well guided mode. This can be achieved by ensuring the core refractive index is much higher than the surrounding cladding. Therefore a previously used LC (5CB) was tested for suitability in the hollow fiber capillary. Sections of hollow fiber were surfactant treated and filled with 5CB, and then interrogated with the transmission microscopy setup. Fig. 10.4 shows the alignment of 5CB in the hollow fiber.

The polarizers are perpendicular and parallel to the fiber axis, therefore LC aligned parallel to these directions will not cause rotation of the polarization vector. Light propagating in these regions will be extinguished by the analyzer

Figure 10.4: Image of a hollow core fiber filled with nematic LC 5CB. The polarizers orientations are shown in the inset denoted P.

and appear dark. Therefore the circumference and the centre of the core appear dark as the alignment is homeotropic and axial respectively. This behaviour is indicative of the escaped axial configuration as shown in Fig. 10.5.

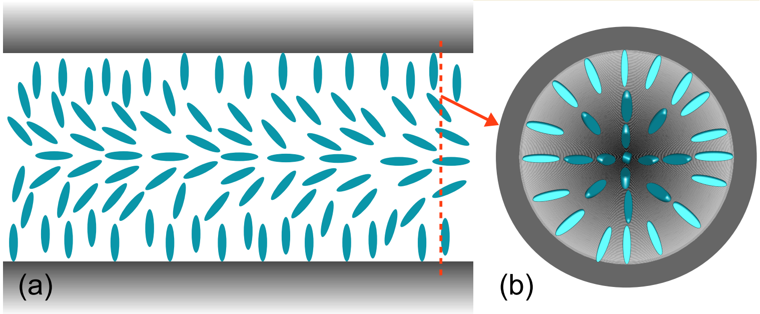

Figure 10.5: The escaped geometry in a circular capillary. (a) Cross-section in the plane parallel to the capillary axis, (b) cross-section in the plane perpendicular to the capillary axis. Note that although this is often called a disclination, it is non-singular, i.e. the director field is continuous everywhere and there is no central axial discontinuity.

10.2.1 LC Filled Fibers as Waveguides

Now that the LC is aligned in the fiber core, it is possible to guide light in the LC region itself. Using a simple fiber launch setup the output of the fiber can be imaged. The setup is shown in Fig. 10.6 where either an IR source or a HeNe laser is launched into the fiber core. Transmitted light is focussed with an objective and the resulting image is recorded with a camera. Examples are shown in Fig. 10.7 where it can be seen that the LC core is transmitting in the centre of the fiber.

Taking images from the fiber output for visible light is more difficult due to the wavelength dependent scattering of light caused by the LC. Although scattering loss is present for IR wavelengths, it is less severe as in nematics the scattering

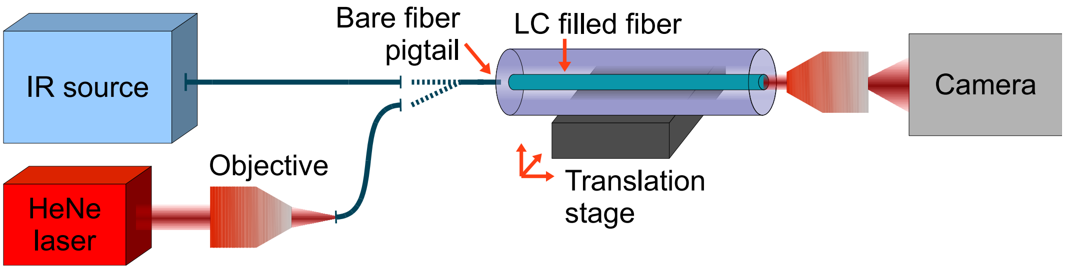

Figure 10.6: Characterization setup for LC filled fibers. Either a fiber coupled IR source or a HeNe laser is launched into the fiber core using a bare standard single mode fiber. The sample is translated to align the core with the fiber. Images are taken with an IR camera or a high-resolution visible camera.

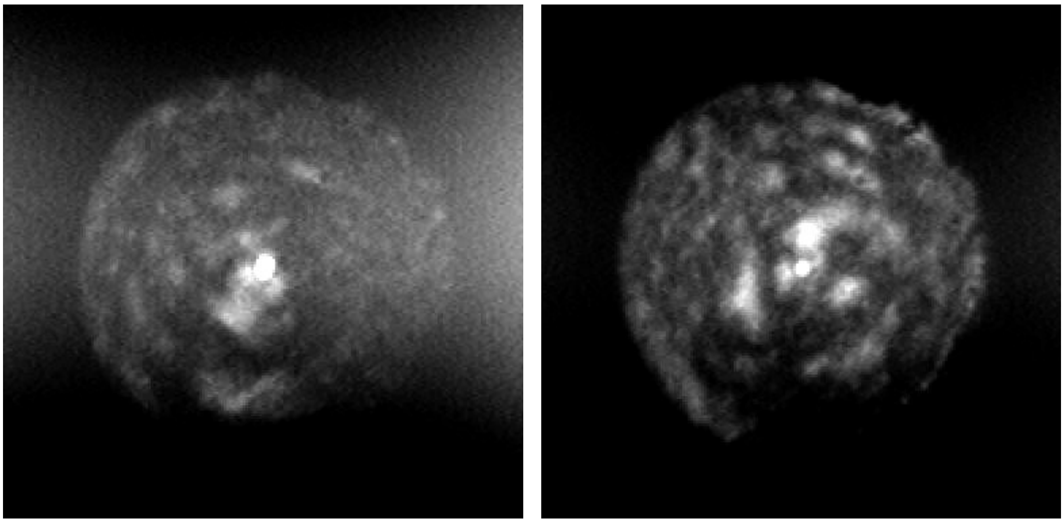

Figure 10.7: Images of core-guided light from the output facet of the LC filled fiber at 1300nm (left) and 1550nm (right). The diffuse circle is the fiber cladding being illuminated by scattered light. In the centre of the cladding is a small bright circular region is the hollow core of the fiber, filled with LC, that is guiding light.

scales as λ^{-4} [6]. This is due to Rayleigh scattering from two sources [7]. Firstly, small fluctuations in the local density and temperature will cause changes in the magnitude of $n_\perp$ and $n_\parallel$. Secondly, fluctuations in the director, **n**, cause micro-crystalline domains which scatter light. The domains are related to the nematic correlation length[1], which is the shortest characteristic length scale over which spatial fluctuations in **n** can exist. The second effect is therefore the more dominant in unaligned or poorly aligned LC cells. However, both will be present

---

[1] The nematic correlation length is typically ten times the molecular length, 5-10nm. It is due to the elastic forces in the LC restricting molecular reorientation and preventing the LC deforming appreciably over short length scales [7,8].

in the waveguides.

To overcome this problem, the entire length of filled fiber was heated via a thermoelectric (Peltier) module above its nematic-isotropic phase transition. For 5CB this occurs at 35°C. Isotropic phase LC favours light guidance because scattering in the isotropic phase is up to six orders of magnitude lower than in the nematic phase [9]. Therefore the transmission of visible light in the LC waveguide should be considerably improved. This is evident in the images shown in Fig. 10.8. The first image illustrates the output facet of the hollow fiber by launching light into the cladding rather than the core. The second image shows the output for light launched into the core but with the LC in the nematic phase. The scattering loss is sufficient to prohibit any light reaching the end of the 6cm section of fiber in the core, and the majority of the light is scattered into the cladding. The final image shows the ouput when the fiber is heated to 40°C. The LC in the core is in the isotropic phase and is guiding visible light successfully.

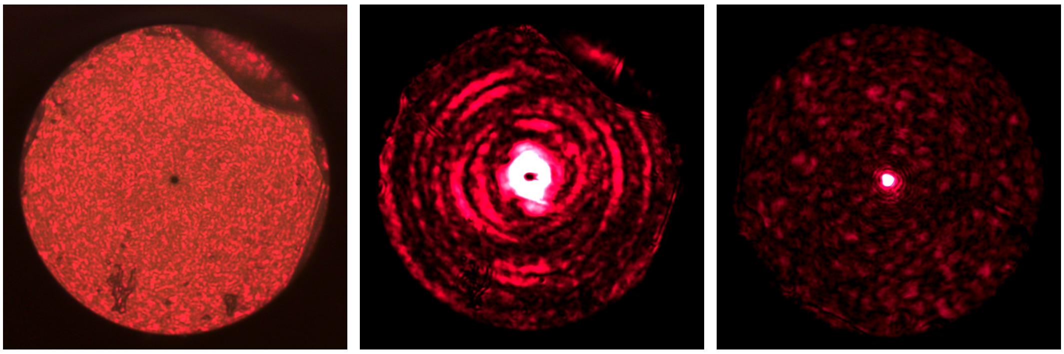

Figure 10.8: (Left) Illustration of the output facet of the fiber using cladding guided HeNe light. (Middle) Output of LC filled fiber below nematic-isotropic phase transition. (Right) Output of LC filled fiber in the isotropic phase. Images have been adjusted for clarity.

10.3 Liquid Crystal Planar Waveguides

Using the same concept of light guidance in a LC core fiber, experiments were performed to test the suitability of LC waveguides in the planar geometry. The devices were first fabricated using substrates similar to those used in Chapter 8. Silica-on-silicon substrates with dicing saw cut grooves were combined with standard unmodified silica-on-silicon samples to produce a hollow groove as an optofluidic channel. Shown in Fig. 10.9 is an image of the substrates used to create the LC waveguide channel. The grooves were initially fabricated by an external company, CIP Technologies, and were not optimized for quality of finish, unlike the in-house dicing system used in section 10.3.1. The groove is ~80µm wide and ~20µm deep which is much larger than the hollow fiber core and hence these grooves will produce highly multi-mode waveguides. However, these grooved substrates are suitable to prove the concept of planar LC waveguides.

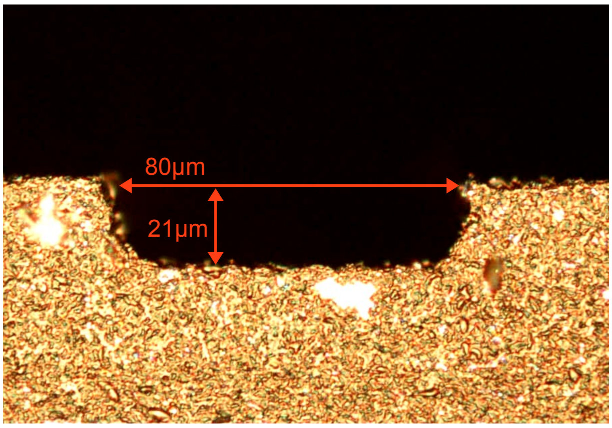

Figure 10.9: Groove cut into a silica-on-silicon sample using a dicing saw.

Both the grooved and non-grooved substrates are pre-treated with an alignment layer. It was expected that the micro-grooves produced by the dicing saw would be of the correct density and dimension to provide planar alignment of the LC. However, it was found that the micro-grooves did not provide any alignment of the LC and the resultant filled groove contained microcrystalline domains of arbitrary orientation. Thus it was necessary to treat the substrates in order to promote a liquid crystalline ordered phase.

Instead of using a surfactant to produce homeotropic alignment, a layer of polyimide (PI) is used to create planar alignment. PI solution is spin-coated onto both substrates and then baked to remove the solvent. The substrates are then rubbed in one direction with a velvet roller to produce a preferential alignment direction which is parallel to the waveguide axis[2]. This results in a planar LC alignment which is parallel with the groove axis.

---

[2] Although the resultant alignment is indeed axial and planar, there is a degree of pre-tilt at the surfaces such that the LC is angled ~5° from the waveguide axis. This is due to long alkyl side-chains of the PI being tilted in the same direction as the rubbing direction [10, 11].

Images of planar LC waveguides were taken using a similar setup to that shown in Fig. 10.6. Additional components such as polarizers and polarization maintaining fiber pigtails were used for polarization sensitive measurements. An image of the complete device is shown in Fig. 10.10 where the HeNe laser light is guided in a ridge between two grooves rather than the LC-filled groove. These two neighbouring grooves did not provide light confinement due to poor surface and therefore bulk alignment. However, other grooves were successful in forming LC waveguiding devices. One such example is illustrated in Fig. 10.11 where the launch has been optimized and the LC becomes the guiding medium.

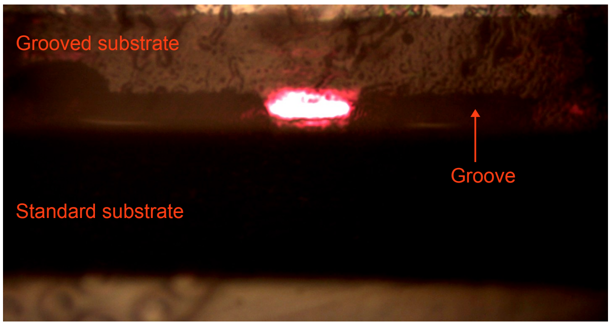

Figure 10.10: Light guided in the ridge between two LC-filled waveguides.

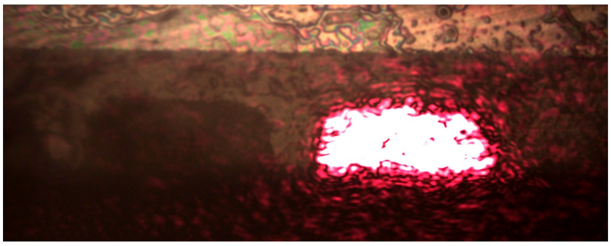

Figure 10.11: Image of two LC-filled grooves. The input launch is aligned with the right-hand groove.

10.3.1 LC Waveguides in Silica

Previous grooved samples using the silica-on-silicon substrates had grooves formed from dicing blades that were not optimized for quality of finish. They also possessed a larger cross-sectional area than required. Utilizing the same grooved waveguide geometry as before, new grooved devices were fabricated in pure silica substrates with smaller cross-sectional area. The grooves were machined with an in-house dicing saw system typically used for wafer processing in the semiconductor industry. Examples of the cut silica substrates are shown in Fig. 10.12 displaying both an end facet and the quality of the groove surface. The groove thickness is limited by the blade thickness, as thinner blades may yield when cutting pure silica. The accuracy of the cut depth is limited by the resolution of the sample stage in the dicing saw system.

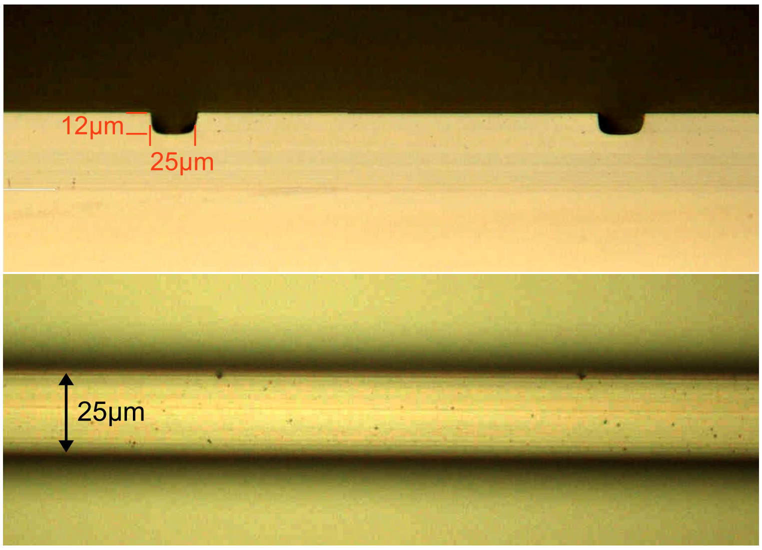

Figure 10.12: (Top) Image of two dicing saw cut grooves. (Bottom) Image of the cut surface.

The surface profiler was used to determine the extent of the surface roughness in dicing saw cut grooves. Shown in Fig. 10.13 is an area scan of the cut groove surface. The finish was of a good quality, exhibiting an R_a value of ~2.5nm. This implies that the surface is suitable for LC molecular alignment layers such as rubbed PI.

Again both the grooved and non-grooved pure silica substrates were PI coated and rubbed along the groove axis. In order to investigate the alignment quality the transparent silica cells were analyzed with the transmission microscopy system. This was not possible with the previous silica-on-silicon devices. Fig. 10.14 shows the LC-filled groove in a cross-polarized microscopy system both with and without the analyzer. The LC is well aligned with no discernable regions of alternative alignment. By contrast an image of a poorly aligned planar groove cell is shown in Fig. 10.15. Various domains can be seen within the groove region, indicating the PI rubbed surface treatment was not successful.

Using the launch setup of Fig. 10.6 transmission images of the LC waveguide

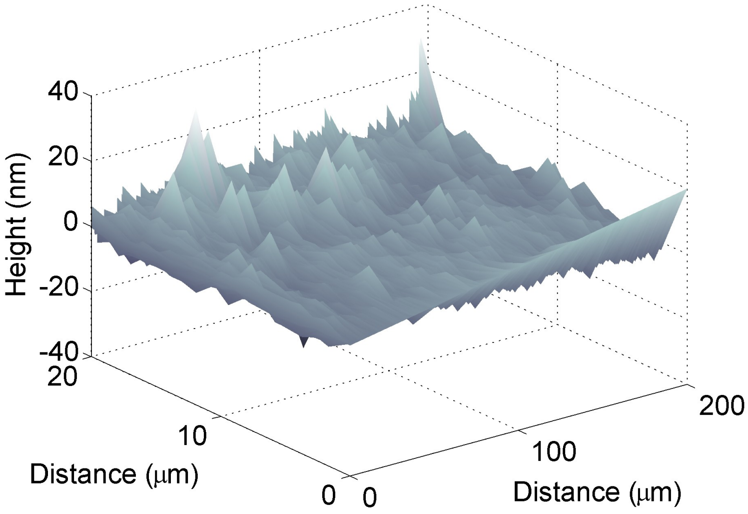

Figure 10.13: Surface area scan of a groove cut with the in-house dicing saw.

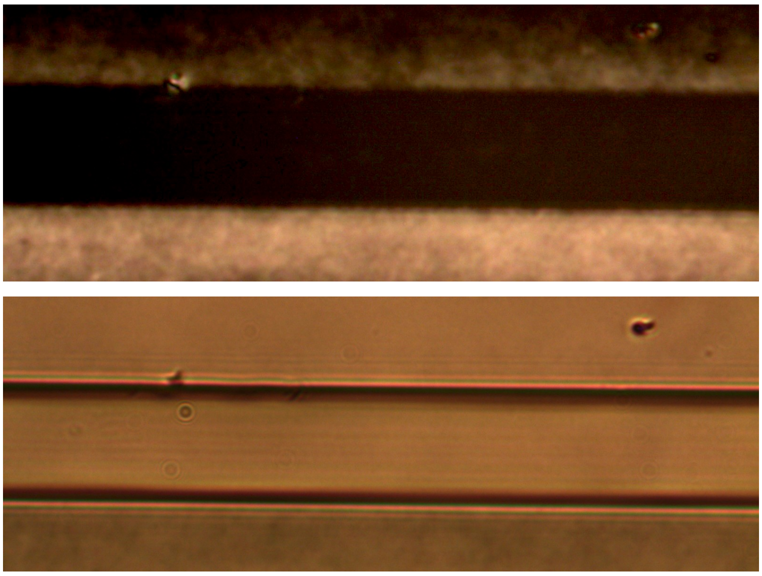

Figure 10.14: Cross-polarized microscopy images of an LC-filled planar aligned silica groove. (Top) Polarizer and analyzer aligned at 45° to groove axis, (bottom) analyzer removed to show alignment quality.

were obtained. HeNe laser light was fiber-coupled into the LC waveguide, as shown in Fig. 10.16, and the resulting transmitted light was recorded. Initial data was taken with the sample heated above the 5CB N-I phase transition temperature for easier alignment. As can be seen in Fig. 10.17 the LC in the isotropic phase supports light confinement in the groove.

The heating was then removed and the cell left to settle in the nematic phase before more measurements were taken. Fig. 10.18 shows two output intensity patterns for the unheated LC waveguide using 633nm laser light. To the right

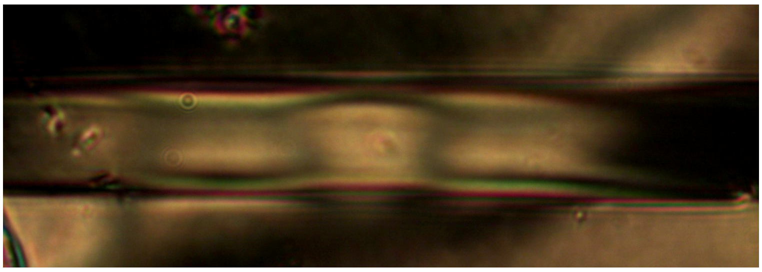

Figure 10.15: Cross-polarized microscopy image of an LC-filled silica groove with poor alignment. Both domain structures and defect regions can be seen in the image.

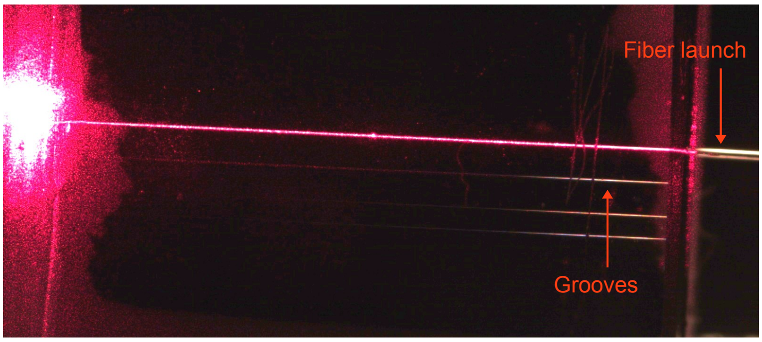

Figure 10.16: Image from above of a fiber pigtail launch into an LC filled groove heated above the N-I phase transition. The waveguide output can be seen at the far left of the picture. Total device length is ~12.5mm.

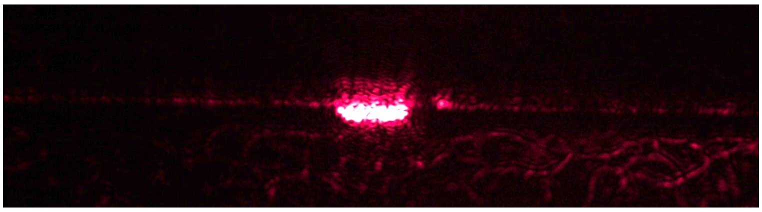

Figure 10.17: Image from the output facet of an LC waveguide filled with 5CB. The sample is heated to ~40°C to ensure the isotropic phase is present.

of Fig. 10.18 are examples of single mode intensity patterns calculated with the FIMMWAVE mode solver software for the same waveguide parameters. In reality the LC waveguide will support many tens of modes and as such the modelling is used only as a visual comparison. Fig. 10.19 shows transmitted light for the unheated LC waveguide using a 1550nm source. It can be seen that the waveguide successfully guides light even in the planar aligned nematic phase. This implies the surface treatment was successful and the dicing saw cut groove surface was of a sufficient quality to promote molecular alignment. Hence scattering losses were reduced sufficiently to allow modes to propagate the full

12.5mm length of the device.

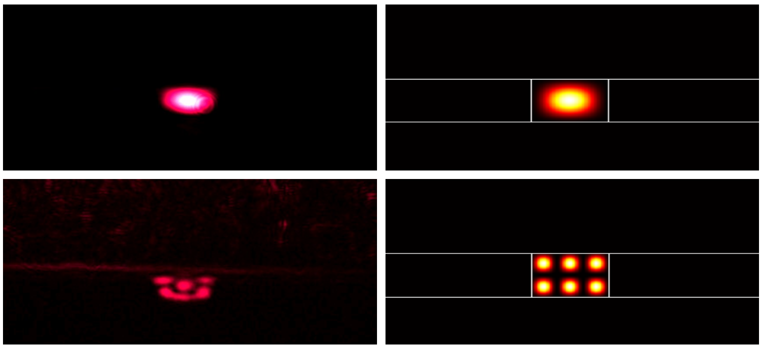

Figure 10.18: (Left) Two output modes successfully guided in the unheated LC waveguide device. (Right) Fimmwave modelling of two supported modes. The core is 25µm wide, 12µm high and has an index of 1.53. The cladding has an index of 1.457.

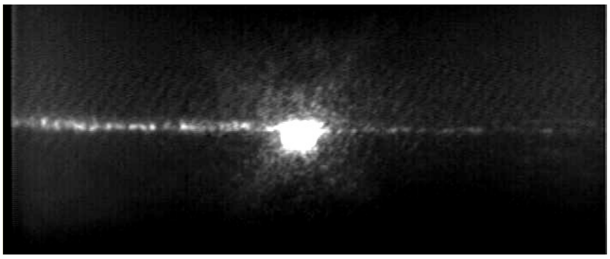

Figure 10.19: Light successfully guided in the LC waveguide at 1550nm.

10.3.2 Scattering Events in LC Waveguides

Using a transparent LC waveguide device allows properties other than just LC molecular alignment to be interrogated. One such effect seen in these devices is scattering from phase transition regions. This effect is similar to the phenomenon of critical opalescence [12]. Critical opalescence is an optical effect often associated with vapour-liquid transitions at the critical point of a substance. As vapour and liquid differ in density they scatter light. When density fluctuations are over length scales comparable to the wavelength of light, the scattering becomes strong. However, for a substance such as water, the critical point is at 374°C and 22MPa making it non-trivial to observe. However, liquid crystal phase transitions can be observed under easily obtainable conditions. The transition between the nematic and isotropic phase of 5CB, for example, only requires that the substance be heated to 35°C. Therefore it should be possible to observe a critical opalescence-like event in an LC waveguide.

Using a modified optical launch setup, such as that shown in Fig. 10.20, images of scattering events could be taken. Photodetectors were used to observe changes in transmitted power and also scattering events caused by phase transitions. Camera images were also taken from above the waveguide. Using a Peltier heating element to raise the temperature of the sample, the N-I phase transition temperature can be reached. Although the sample was heated uniformly along its length, there was sufficient horizontal thermal gradient to form isotropic and nematic domains simultaneously.

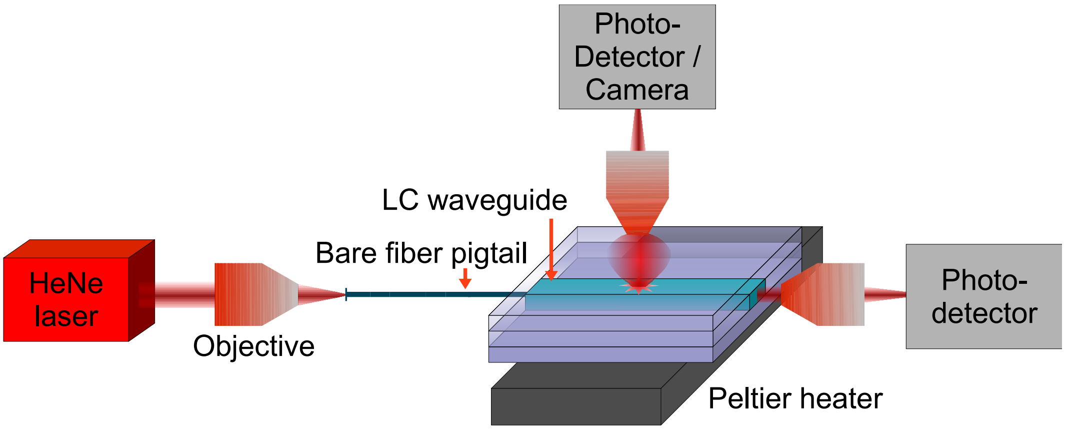

Figure 10.20: Launch setup for interrogation of scattering events in LC-filled silica waveguides.

Shown in Fig. 10.21 is a scattering event in an LC waveguide. The strong scattering occurs from a front separating isotropic LC at the top and nematic LC at the bottom in Fig. 10.21(a). The front is moving towards the bottom of the image in unison with the thermal gradient. Fig. 10.21(b) shows a region of nematic LC confined between two isotropic regions. The diffuse scattering section is due to isotropic droplets forming in the nematic ordered phase. This has been seen in previous homeotropically aligned tuning cells, an example of which is shown in Fig. 10.22, where the cell is being heated from the bottom left. The isotropic phase is moving upwards and to the right and it can be seen that there is a strong scattering region in the centre. Fig. 10.21(c) exhibits a confined nematic region but without diffuse scattering.

The photodetector data is shown in Fig. 10.23. The red data is the voltage

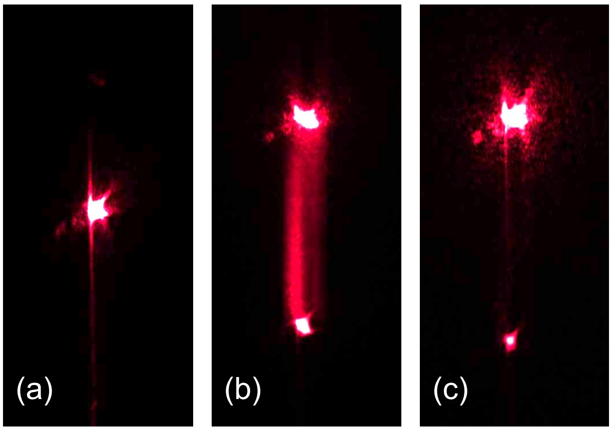

Figure 10.21: (a) Scattering event at the boundary between isotropic and nematic phase 5CB. (b) Region between two phase fronts causes diffuse scattering along the waveguide. (c) Similar bound nematic region but without diffuse scattering.

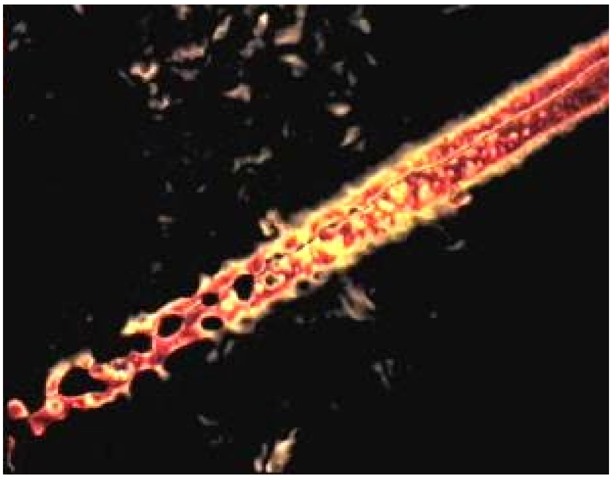

Figure 10.22: Homeotropically aligned nematic LC being heated from the bottom left region. The isotropic phase is propagating towards the top right, producing strong scattering in the centre where the isoptropic droplets have similar dimensions to the wavelength of visible light.

recorded from the photodetector positioned above the waveguide. Spikes are caused by a phase front and its associated scattering propagating through the focal position of the objective. Strong scattering produces a large photodetector signal. The green data is taken from the photodiode at the output of the LC waveguide and is scaled to fit the axes. It can be seen that the transmission reduces when the waveguide starts to contain isotropic regions which scatter light. If the waveguide was completely isotropic, however, the transmitted power should increase. Purple data shows the temperature recorded by a thermocouple attached to the centre of the Peltier underneath the sample. The sample is heated above 35°C to ensure some of the LC is in the isotropic phase.

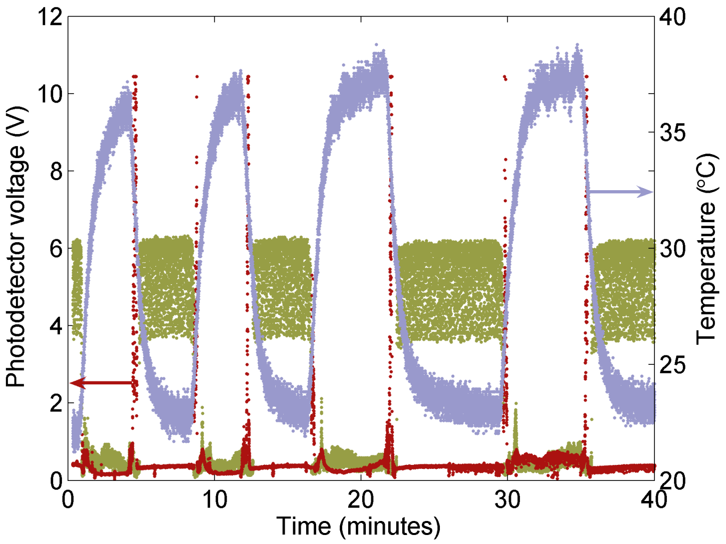

Figure 10.23: Photodetector data of scattering events. Red trace: voltage recorded from the photodetector positioned vertically above the waveguide. Green trace: voltage recorded from the photodetector positioned at the output of the waveguide. Purple trace: temperature recorded by a thermocouple attached to the Peltier module underneath the sample. Note that the spikes in the red trace indicate scattering at the transition temperature.

Following from the data given in Fig. 10.23, Fig. 10.24 shows photodetector data taken from the output of an LC waveguide. The orange line, initially in the nematic phase, shows how the transmission increases when the LC is heated to the isotropic phase, and disappears when the heating is removed. This is because heating of the sample caused misalignment of the fiber launch. The purple line shows the LC waveguide initially in the nematic phase. The transmitted power increases as the heating pushes the LC into the isotropic phase. Once the heating is removed, the sample slowly realigns due to the surface treatment and eventually regains its nematic-phase transmission characteristics.

10.3.3 Waveguide Loss Measurements

Experiments were performed in order to characterize the waveguide loss in planar LC waveguides. It has been previously noted that LC waveguides are intrinsically lossy unless exceptionally good alignment is achieved. Linear losses

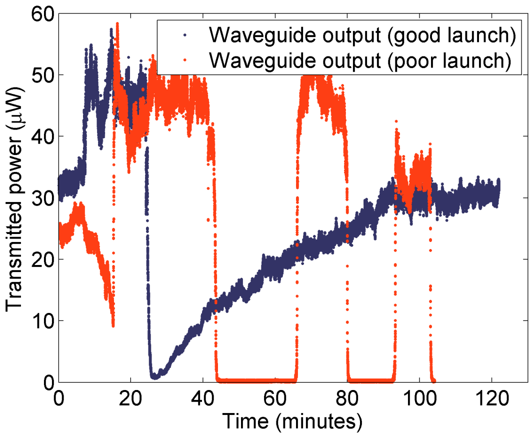

Figure 10.24: Transmitted power through a LC waveguide during N-I phase transitions. The photodetector is placed at the output of the waveguide and the transmitted HeNe laser light is measured. The orange line is the output from the waveguide with a slightly misaligned launch, hence no power is transmitted when the heating is removed, but transmission increases in the isotropic phase. The purple line shows the output with the LC initially in the nematic phase. The transmission increases when the LC is heated to the isotropic phase, and falls rapidly when the heating is removed. The waveguide gradually regains its original nematic transmission characteristics.

of 15-30dB/cm are common for these type of devices [4–6]. Hence for the 12.5mm long samples used in this work the loss should be easily observable.

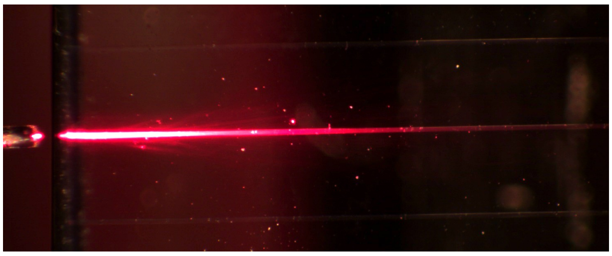

Figure 10.25: Fiber launch into a waveguide containing 5CB in the nematic phase at 25°C. Note the significant loss as the light propagates along the waveguide. The launch fiber can be seen on the left of the image.

The optical power loss as a function of distance along the waveguide was interrogated with a characerization setup similar to that in Fig. 10.20. However, the vertical photodiode was replaced with a linear response camera such that the scattered light intensity could be recorded along the waveguide. An image of the light propagating through the LC waveguide is shown in Fig. 10.26. The intensity values from the waveguide region of the image were extracted using a Matlab program. A least squares fitting function was then fitted to the resulting data. The graph of the raw data and fitting is shown in Fig. 10.27. Note that the bright dot on the far left of the image is light leakage from the end of the launch fiber and is not part of the LC waveguide. An exponential least squares fit produced a loss value of ~33dB/cm, which is common in devices of this type.

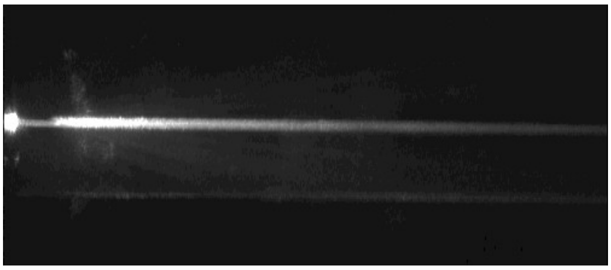

Figure 10.26: Contrast adjusted image of light propagation in an LC waveguide. The image was taken with a linear response camera.

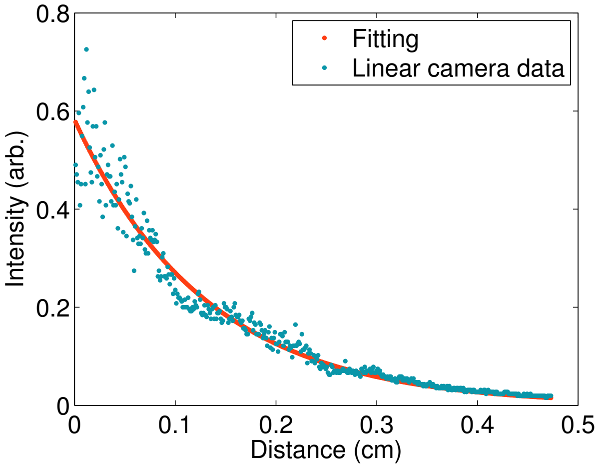

Figure 10.27: Loss measurement based on raw data taken from a linear camera image of the LC waveguide from above. A least squares curve fitting algorithm was used to fit to the data, and the best fit corresponds to 33dB/cm. The LC was in the nematic phase at 25°C.

10.3.4 NA Measurements

The NA or numerical aperture of a waveguide is a dimensionless parameter that characterizers the range of angles over which the waveguide can accept or emit light. In order to extract NA measurements from the waveguide, the same linear camera was used, but now at the end facet of the waveguide. Images were taken at increasing distances from the initial focal position of the waveguide output in order to analyze the spatial evolution of the light exiting the waveguide. By keeping the distance between the focussing objective and the camera constant, a three-dimensional map of the light exiting the waveguide could be acquired. The power distribution in both the horizontal and vertical directions was extracted by averaging over the total number of horizontal and vertical slices respectively. A Gaussian fitting function was then applied to the resulting distributions. The full width at half maximum was then taken to determine the spread of light exiting the waveguide.

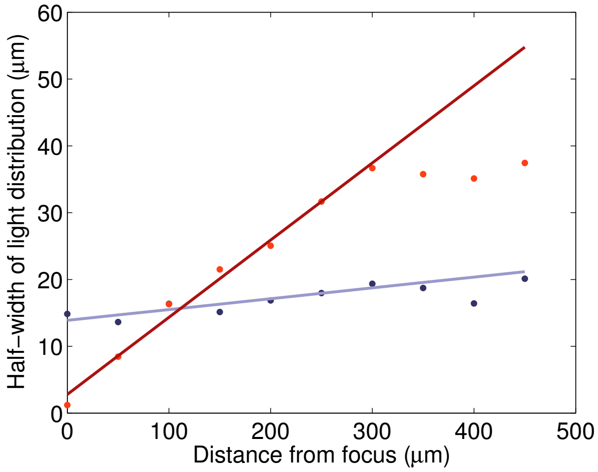

Figure 10.28: Half-width of the light distribution exiting the LC waveguide as a function of position from the focus. The linear fitting was fitted to the first 7 points only as the image quality beyond 300µm was insufficient to form accurate measurements.

From the data shown in Fig. 10.28 the values for the NA were 0.12 in the vertical direction and 0.016 in the horizontal direction. The distance between focussing objective and camera was kept constant, while the distance of that ensemble was moved away from the focus in incremental steps. Plotted here is the half-width of the light distribution as a function of distance from the focal plane. Data beyond 300µm was not used as the resulting images were not of sufficient quality for the Gaussian fitting algorithm to fit. This is due to the limited dynamic range of the linear camera. Using the equation:

$$\mathrm{NA} = \sqrt{n_1^2 - n_2^2} = \sqrt{n_{LC}^2 - n_{silica}^2} \tag{10.1}$$

to calculate the NA results in a value for the LC waveguide of ~0.47(3). There is a significant difference between calculated and acquired values. Firstly, it is known that the loss in the waveguide is approximately 30dB/cm, or 3dB/mm. This implies that the total optical power in the waveguide drops by approximately half for each mm traversed due to scattering. This also implies that the remaining light is unscattered and obeys Snells' law at the LC-silica boundary.

If all the light was to undergo total internal reflection (TIR) at the LC-silica boundary then the NA would be limited by the NA of the launch fiber, which in this case is ~0.12 for SM600 fiber. This is because the cone of angles the fiber can fill with light is limited by its NA, and as such no light past that angle is guided in the waveguide. The value for the fiber matches the value for the LC waveguide, implying that to some extent this behaviour is indeed occurring.

Furthermore, any light that is scattered below the critical angle of the waveguide will remain guided. As the scattered light is produced at random angles, it will not preserve the original TIR angle defined by the input fiber. It can therefore exit the LC waveguide at any angle up to that defined by its NA, 0.47. However the NA of the focussing objective is only 0.4, therefore any light exiting the waveguide above this value is not collected. Despite the difficulty in obtaining an accurate NA measurement, both the TIR and scattered light intensity patterns can be seen in a cross-section of the output light, as displayed in Fig. 10.29.

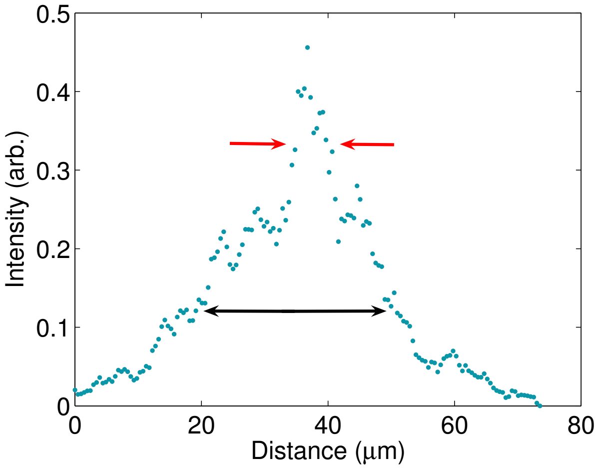

Figure 10.29: Intensity distribution of light exiting the waveguide in the horizontal direction.

---

[3] This is assuming the LC is planar aligned and as such the light only experiences n_o of the LC, which for 5CB is 1.53 (at 633nm). Silica has an index of ~1.457 at 633nm.

As the fitting is dominated by the peak due to the unscattered, guided light the NA value is dominated by the NA of the input fiber pigtail. The result is similar values for the LC waveguide and the fiber waveguide. However, this does not explain the disparity in the horizontal and vertical measurements for the NA, which is the subject of further discussion.

10.4 Summary

Table10.1 summarises the experiments performed on LC waveguides and the results achieved during this work.

Experiment	**Achievement/Result**
LC filled fibres	Hollow fibers of several cm successfully filled with nematic LC in escaped radial configuration. Guided both visible and IR light in isotropic phase.
LC planar waveguides	Precision machined grooves in silica-on-si substrates filled with LC successfully guided visible light.
LC waveguides in silica	Grooves fabricated in-house in silica substrates successfully guided light in both isotropic and nematic phases in both visible and IR regimes.
Scattering events	Critical opalescence-like scattering events successfully observed in transparent silica planar grooved substrates filled with LC.
LC waveguide loss	The loss in nematic phase planar LC waveguides filled with 5CB was found to be 33dB/cm.

Table 10.1: Summary of achievements from experiments performed with LC waveguides.

This chapter introduced the concept of using liquid crystals in confined geometries as a waveguiding medium. Initial experiments were undertaken to test the validity of using a nematic LC, 5CB, as the core guiding medium in a hollow fiber capillary. Once homeotropic alignment of 5CB had been achieved inside the hollow fiber, the samples were then tested for light guidance at visible and near-IR wavelengths. In both cases it has been demonstrated that the LC-filled fiber guided light successfully. However, in order to achieve guidance the LC had to be heated above its N-I phase transition temperature, thus negating the benefit of using a liquid crystalline compound.

Subsequently, planar silica samples were patterned using the same in-house dicing saw technique described in Chapter 8. The grooves were filled with 5CB and the launch setup was used as before. The waveguides successfully guided 633nm and 1550nm light in both the isotropic and nematic phases, thus proving the concept of nematic LC waveguides over cm length scales. The waveguides exhibited loss of 33dB/cm, and it was found that the NA measurements of the LC waveguide were governed by the NA of the launch fiber and of the objective collecting the transmitted light.

Additionally, scattering events were observed in the waveguides. These events correspond to transitions between different LC phases. Here the boundaries between nematic and isotropic regions of LC waveguide produced scattering events that were observed. Data was taken to exhibit the difference in transmission properties of the waveguide when firstly the waveguide contains isotropic LC domains and secondly when the waveguide is fully isotropic.

References

[1] C. Monat, P. Domachuk, and B. J. Eggleton. “Integrated optofluidics: A new river of light”. *Nature Photonics*, 1(2):106–114, February 2007.

[2] D. Psaltis, S. R. Quake, and C. Yang. “Developing optofluidic technology through the fusion of microfluidics and optics.”. *Nature*, 442(7101):381–6, July 2006.

[3] A. D’Alessandro, B. D. Donisi, R. Beccherelli, and R. Asquini. “Nematic Liquid Crystal Optical Channel Waveguides on Silicon”. *IEEE Journal of Quantum Electronics*, 42(10):1084–1090, October 2006.

[4] J. R. Whinnery, C. Hu, and Y. S. Kwon. “Liquid-crystal waveguides for integrated optics”. *IEEE Journal of Quantum Electronics*, QE-13(4):262–267, 1977.

[5] C. Hu and J. R. Whinnery. “Losses of a nematic liquid-crystal optical waveguide”. *Journal of the Optical Society of America*, 64(11):1424, November 1974.

[6] S. T. Wu and K. C. Lim. “Absorption and scattering measurements of nematic liquid crystals.”. *Applied optics*, 26(9):1722–7, May 1987.

[7] P. G. de Gennes. *The Physics of Liquid Crystals*. Oxford University Press, 1995.

[8] R. Repnik, L. Mathelitsch, M. Svetec, and S. Kralj. “Physics of defects in nematic liquid crystals”. *European Journal of Physics*, 24(4):481–492, July 2003.

[9] I.-C. Khoo. *Liquid Crystals*. Wiley, 2007.

[10] T. Sugiyama, S. Kuniyasu, D. Seo, H. Fukuro, and S. Kobayashi. “A Simple Model for Pretilted Nematic Liquid Crystal Medium and Its Torsional Surface Coupling Strength”. *Japanese Journal of Applied Physics*, 29(Part 1, No. 10):2045–2051, October 1990.

[11] D.-S. Seo, K. Araya, N. Yoshida, M. Nishikawa, and S. Kobayashi. “Effect of the Polymer Tilt Angle for Generation of Pretilt Angle in Nematic Liquid Crystal on Rubbed Polyimide Surfaces”. *Japanese Journal of Applied Physics*, 34(Part 2, No. 4B):L503–L506, April 1995.

[12] L. A. Zubkov and V. P. Romanov. “Critical opalescence”. *Soviet Physics Uspekhi*, 31(4):328–353, April 1988.

Chapter 11

Conclusions

The work performed in this PhD thesis can be summarised as follows:

- This thesis has analyzed the physical processes occurring liquid crystal (LC) tunable planar Bragg grating structures. It has determined the causes of the hysteresis tuning seen in the groups previous tunable devices.
- Several aspects of LC defect Physics and defect dynamics have been correlated due to this work.
- A new grooved geometry for LC tunable Bragg gratings was designed that successfully avoided the hysteresis in the device tuning curves.
- Planar chirped and chirp-apodized Bragg gratings have been shown to provide the possibility for dispersion management.
- The concept of LC-core planar waveguides has been demonstrated and have been shown to provide light guidance for visible and IR wavelengths.

11.1 Liquid Crystal Tunable Planar Bragg Gratings

The realignment processes occuring in the groups previous LC-tunable Bragg grating devices have been analyzed. New theories have been developed to explain the hysteresis seen in the device tuning curves. Prior to this thesis, the hysteresis behaviour was attributed to a single disclination (line defect) forming at low to moderate applied electric fields, and disappearing at high applied fields.

However it has been found that this behaviour was, in fact, a Freedericksz (or splay-bend) wall being produced at moderate field strengths, and transformed into a pair of ±1/2 disclinations at high applied field. This transition is known as pincement. The disclination pair is stable below the voltage at which it was formed. It transforms back into a wall at a lower voltage, producing a hysteresis loop.

The pincement transition was verified by using periodically patterened ITO electrodes. Patterning forced the two disclinations to propagate at different depths in the cell, which proved that there were two unique line defects. It was also discovered that pincement and the associated hysteresis behaviour is not unique to LC 18523, and has been observed in other multi-component and single component LC's. By using a pure liquid crystalline compound, 5CB, it was verified that the hysteresis behaviour is common to nematic LC's in the tuning cell geometry. Finally, it was found that the tuning response is dominated by LC molecular reorientation in an applied field, and Ohmic heating has little or no contribution to the tuning.

Disclinations forming due to the pincement transition were found to have a characteristic zig-zag structure. This was due to the director aligning axially with the disclination lines and the director field relaxing the bend deformation in close proximity to the disclinations. At the vertex of each defect it is expected that there are point defects of opposite topological charge. A theory has been proposed to explain the distribution of these point defects as a function of the applied voltage. It is suspected that the elastic energy in the director field can be reduced if the periodicity in the zigzag disclination is increased. This is a consequence of the applied field reducing the width of the region where the disclination can be maintained.

11.2 Grooved Geometry Liquid Crystal Tunable Planar Bragg Gratings

A new geometry of tuning cell was fabricated in order to circumvent the hysteresis loop seen in the vertical-access LC tunable devices. The grooved geometry LC tunable devices permit side-access of the UV-written waveguide and gratings. These substrates include a dicing saw machined groove for side-access. The groove is subsequently filled with LC, and the electrodes are placed at the top and bottom of the substrate. Grooved tunable devices aimed to remove the hysteresis seen in previous top-access devices. Indeed, the resultant tuning curves for such devices exhibit no hysteresis as seen in previous samples, and the pincement transition is avoided.

Rapid thermal annealing of samples was used to remove surface roughness which can manifest itself as poor LC alignment. The resultant tuning curves had fewer spurious features, but did exhibit a discontinuous jump in the reflected wavelength. This was suspected to be due to surface pinning of defects around the grating region, causing a local modification of the effective index.

11.3 Planar Chirped Gratings

This chapter presented work on developing and fabricating UV-written planar chirped and chirp-apodized Bragg gratings in the three-layer silica-on-silicon platform. Devices fabricated in this thesis used linearly chirped gratings in order to exploit their linear group delay response. The gratings are apodized in order to remove the group delay ripple inherent in unapodized chirped gratings.

Using a resistor array as a series of heating elements fabricated with standard PCB technology, the group delay gradient in a chirped grating was tuned by 4ps/nm. The limitations in the tuning range arise from the thermal conductivity of the silicon substrate and the PCB containing the heater array. The thermal gradient could be improved by using NiChrome heating elements which have a smaller contact area with the sample.

11.4 Liquid Crystal Waveguides

This chapter introduced the concept of using liquid crystals in confined geometries as a waveguiding medium. Initial experiments were undertaken to test the validity of using a nematic LC, 5CB, as the core guiding medium in a hollow fiber capillary. Once homeotropic alignment of 5CB had been achieved inside the hollow fiber, the samples were then tested for light guidance at visible and near-IR wavelengths. In both cases it has been demonstrated that the LC-filled fiber guided light successfully. However, in order to achieve guidance the LC had to be heated above its N-I phase transition temperature, thus negating the benefit of using a liquid crystalline compound.

Planar silica samples were patterned using the in-house dicing saw technique. The grooves were filled with 5CB and light from a HeNe laser and a tunable IR laser was launched into the LC waveguide. The waveguides successfully guided 633nm and 1550nm light in both the isotropic and nematic phases, thus proving the concept of nematic LC waveguides over cm length scales. The waveguides exhibited loss of 33dB/cm, and it was found that the NA measurements of the LC waveguide were governed by the NA of the launch fiber and of the objective collecting the transmitted light.

Critical opalescence events were also observed in the waveguides. These events correspond to transitions between different LC phases. Here the boundaries between nematic and isotropic regions of LC waveguide produced scattering events that were observed. Data was taken to exhibit the difference in transmission properties of the waveguide when firstly the waveguide contains isotropic LC domains and secondly when the waveguide is fully isotropic.

11.5 Future Work

11.5.1 Tunable Planar Bragg Gratings

The main limitation with LC tunable planar Bragg gratings is the relatively high refractive index of the LC layer in relation to the UV-written core. As the extraordinary refractive index of the LC is above that of the waveguide, the full tuning range cannot be realised. The consequence of having a higher cladding index than core index is that the propagating mode is pulled out of the core into a region where mode coupling into a counter-propagating mode cannot occur. This is qualitatively shown in Fig. 11.1. There are two methods the author suggests to overcome this problem. Firstly, a lower refractive index liquid crystalline material could be used. Polymer-LC hybrid materials have the potential to obtain lower refractive indices as the polymer containing the LC can be made to possess a relatively low index [1,2].

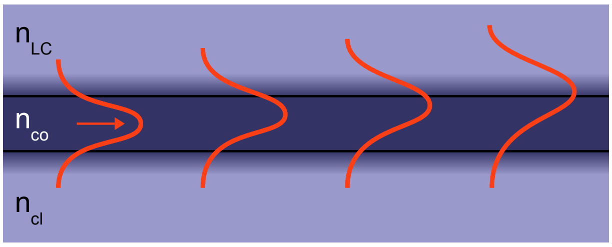

Figure 11.1: Single mode propagation in a LC clad UV written planar waveguide with $n_{LC} > n_{core}$. The mode is pulled out of the region where mode coupling can occur and as such the reflected power reduces considerably.

A common polymer-LC hybrid is the polymer dispersed liquid crystal (PDLC). PDLC's contain a mixture of monomer and LC which undergo phase separation when the monomer is polymerized. The result is spheres of LC suspended in a polymer matrix [3]. PDLC based materials usually match the ordinary refractive index of the LC to the polymer containing the LC such that the mixture can appear to have no impedance mismatch when suitably aligned [3]. However, for the purpose of a tunable Bragg grating, the scattering loss caused by an index mismatch between LC and polymer would not be as problematic as in this case the PDLC is not the guiding medium.

Polymer-LC hybrids can, however, be used as the guiding medium. The polymer-liquid crystal-polymer slice (POLICRYPS) layered systems have been used to create switchable diffraction gratings for visible and IR wavelengths [4]. The slices can be created by the process of polymerization-induced phase separation (PIPS) [5]. The polymerization is photo-induced, via UV radiation, such that layers of polymer are formed in areas of high intensity radiation, while the LC is forced into areas of low intensity radiation. The LC layers are electrically tunable, therefore the reflection wavelength of the grating can be tuned by application of a suitably oriented electric field. Using the groups Direct Grating Writing (DGW) system, the author of this thesis proposes the possibility of creating tailored POLICRYPS gratings on planar silica-on-si substrates. Using the DGW to define standard buried channel waveguides in the photosensitive silica, and gratings in the polymer-LC hybrid, an integrated tunable Bragg grating filter may be realised. An example device is shown in Fig. 11.2.

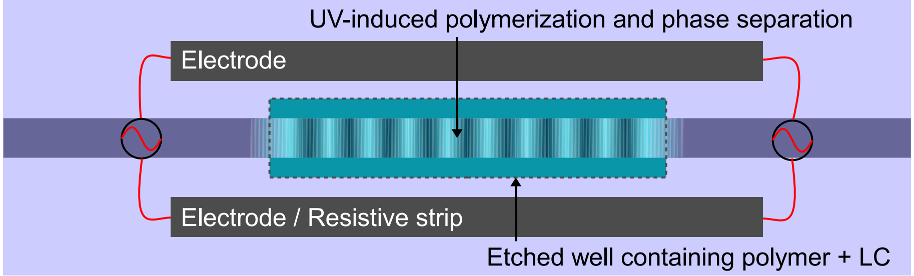

Figure 11.2: Silica-on-silicon sample with etched window containing monomer and LC. Buried channel waveguides written via Direct UV Writing. Grating written into polymer/LC mixture by UV-induced polymerization causing phase separation in the mixture. Regions where the UV intensity is high cause polymerization of the monomer, however regions of low UV intensity do not cause polymerization. The result is a Bragg grating with alternating regions of polymer and LC. The molecular orientation in the LC regions can be controlled by an applied electric field to create a tunable grating.

The second proposed method to overcome the problem of excessive cladding refractive index is increasing the refractive index of the substrate during fabrication. The Flame Hydrolysis Deposition process is suitable for tailoring layer properties during fabrication. By increasing the concentrations of phosphorus and germanium, the core layer refractive index can be increased. Adding more germanium would also increase the photosensitivity such that UV written channels will also have a relatively higher index, reducing the penalty for having a high index LC cladding layer. However, there are limitations to the maximum concentration of dopant that can be added to the glass before the layer quality becomes too poor for UV inscription [6].

11.5.2 LC Tunable Chirped Planar Bragg Gratings

Chapter 9 concluded with a possible extension of the work performed on thermally tuned planar chirped Bragg gratings. The author proposes that the chirped gratings can be tuned via an LC overlay. The concept of an LC tunable chirped planar Bragg grating is shown again in Fig. 11.3. The silica-on-silicon substrate contains UV-written buried channel waveguides and a linearly chirped Bragg grating. Remember that the effective refractive index of a mode propagating in the core and grating region is influenced by all surrounding media. Therefore the effective index can be modified by the relative orientation of the LC molecules with respect to the input polarization of light.

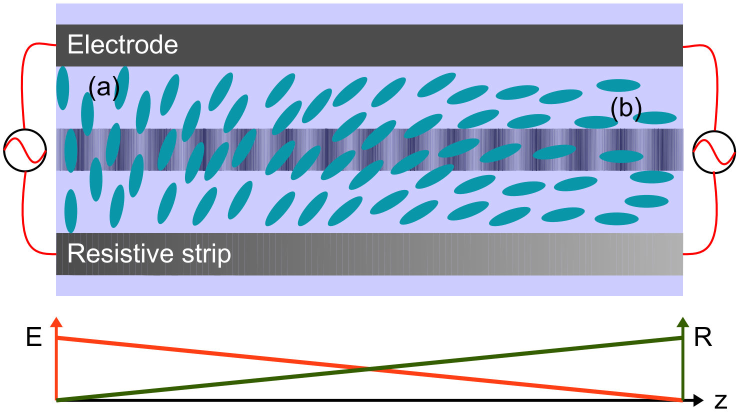

Figure 11.3: Concept of an LC-tunable chirped grating.

For the example given in Fig. 11.3, a TE polarized mode will experience a decreasing refractive index as it propagates from left to right. Hence the Bragg reflection wavelength would typically decrease with propagation distance. By adjusting the distribution of the applied voltage, the LC molecular reorientation, and hence the effective modal index, can be adjusted as a function of position, creating a reconfigurable chirped planar Bragg grating. The LC tunable grating device also allows for an increase or decrease in chirp rate of a pre-chirped grating. This may be preferable for devices that require lower power consumption, as the chirp would be present even in the field-off state.

The choice of LC materials is similar to that for standard tunable grating devices. A purely nematic phase LC compound could be used, or a polymer-stabilized mixture such as a PDLC could be incorporated above the exposed UV written grating. Another form of stabilized LC compound has also been investigated. Similar to PDLC, the gel-glass dispersed liquid crystal (GDLC) compound has the potential to house LC microdroplets in a silica glass matrix [7,8]. Potentially this could allow for easier integration into planar silica-based optical components.

References

[1] J. V. DeGroot, Jr. “Hybrid integration of silicone PDLC into a planar light circuit”. In *Proceedings of SPIE*, volume 5222, pages 163–170. SPIE, 2003.

[2] C.-H. Lee, J.-W. Song, and J.-H. Park. “Mode Analysis of a Tunable Side-Polished Optical Fiber Filter by a Polymer-Dispersed Liquid Crystal Based on Coupled-Mode Theory”. *Journal of the Korean Physical Society*, 51(1):383, 2007.

[3] P. C. Lallana, C. Vazquez, B. Vinouze, K. Heggarty, and D. S. Montero. “Multiplexer and Variable Optical Attenuator Based on PDLC for Polymer Optical Fiber Networks”. *Molecular Crystals and Liquid Crystals*, 502(908420906):130–142, May 2009.

[4] R. Asquini, A. D’Alessandro, C. Gizzi, P. Maltese, R. Caputo, C. Umeton, A. Veltri, and A. V. Sukhov. “Optical Characterization at Wavelengths of 632.8nm and 1549nm of Policryps Switchable Diffraction Gratings”. *Molecular Crystals and Liquid Crystals*, 398(1):223–233, June 2003.

[5] Y. J. Liu and X. W. Sun. “Holographic Polymer-Dispersed Liquid Crystals: Materials, Formation, and Applications”. *Advances in OptoElectronics*, 2008:1–53, 2008.

[6] S. P. Watts. *Flame hydrolysis deposition of photosensitive silicate layers suitable for the definition of waveguiding structures through direct ultraviolet writing*. PhD thesis, University Of Southampton, 2002.

[7] M. Zayat and D. Levy. “The performance of hybrid organic-active-inorganic GDLC electrooptical devices”. *Journal of Materials Chemistry*, 15(35-36):3769, 2005.

[8] D. Levy, A. N. A. Serrano, and J. M. Oton. “Electrooptical Properties of Gel-Glass Dispersed Liquid Crystals”. *Liquid Crystals*, 807:803–807, 1994.

Appendix A

Bragg Grating Simulation

A.1 Grating Model

```
clc; clear;

%% Define Runge-Kutta parameters
tol1 = 1e-8; % Defines the tolerance of each variable in the ode45
% function below. The smaller it is, the longer the computation
% takes, but the zeroes are much better defined.
options = odeset('RelTol',1e-6,'AbsTol',[tol1 tol1 tol1 tol1 tol1,...
    tol1]);

%% Define variables
Lambda = 535.827e-9; K = 2*pi/Lambda; neff = 1.448;
delta_l = 7.5e-12; % Wavelength resolution. Can rapidly increase
%computational time if too small!
lambda_min = 1.545e-6;
lambda_max = 1.560e-6;
lambda = (lambda_min:delta_l:lambda_max)'; % Wavelength range
gamma = (4*pi*neff./lambda) - K ; % Detuning
dneff = 0.0004; % Change in effective index
kappa = (pi*dneff)/(2*neff*Lambda);
n=length(gamma);
L = 0.5e-2; % Half grating length
chirp_amt = 2.5 ; % nm/cm
chirp = (chirp_amt*1e-7)*2*pi*neff / (2*neff*Lambda)^2; % Quadratic
% phase term in exponent
```

```
apod = L; % Apodization length = half grating length by default

%% Perform R-K on coupled mode equations
AA = zeros(1, n); BB = zeros(1, n); % Predefine array for speed
for ii = 1:n
[Z,Y] = ode45(@coupled,[L -L],[1 0 kappa gamma(ii) chirp apod,...
    chirp2 chirp3], options);
AA(ii)=Y(end,1);
BB(ii)=Y(end,2);
end

r = (BB./AA)'; rr=abs(r).^2;
rx = real(r); rx2 = rx(1:length(rx)-1);
ry = imag(r); ry2 = ry(1:length(ry)-1);
phase = -unwrap(2*angle(r));

v = 3e8/neff; t = 2*L/v; % Time taken for light to travel half way
%down the grating and back

%% Find FWHM, not robust
tdb = max(10*log10(rr))-3;
data = 10*log10(rr);
[val1,ind1] = min(abs(data(1:1:round(end/2))-tdb));
[val2,ind2] = min(abs(data(round(end/2):end)-tdb));
index2 = ind2 + round(length(data)/2);
FWHM = 1e9*(lambda(index2) - lambda(ind1));
fwhm = strcat(num2str(FWHM),'nm')

% Gaussian apodization, visualization only
z_increment = (2*L)/length(gamma);
z = (-L:z_increment:L-z_increment);
apod_prof = exp(-(z.^2/((apod/2.5)^2)));

%% Plotting
col1 = 'b';
subplot(2,3,1)
plot(lambda, rr, col1)
xlabel('Wavelength (m)')
ylabel('Reflectivity')
xlim([lambda_min lambda_max])
hold on
subplot(2,3,2)
```

```
plot(lambda, apod_prof, col1)
xlabel('Wavelength (m)')
ylabel('Apodization profile')
xlim([lambda_min lambda_max])
hold on
subplot(2,3,3)
plot(lambda, 10*log10(rr), col1)
xlabel('Wavelength (m)')
ylabel('Reflectivity (dB)')
xlim([lambda_min lambda_max])
hold on
subplot(2,3,4)
plot(lambda, phase, col1)
xlim([lambda_min lambda_max])
xlabel('Wavelength (m)')
ylabel('Phase (rads)')
hold on
subplot(2,3,5)
plot(lambda(1:end-1), 1e12*(-diff(phase)/delta_l),...
    .*(((lambda(1:end-1)).^2)/(4*pi*3e8))+t*1e12, col1)
xlim([lambda_min lambda_max])
title('Direct phase derivative')
xlabel('Wavelength (m)')
ylabel('Delay (ps)')
hold on
subplot(2,3,6)
plot(lambda(1:end-2), 1e12*diff((diff(phase)/delta_l),...
    .*(((lambda(1:end-1)).^2)/(4*pi*3e8))+t), col1)
xlim([lambda_min lambda_max])
title('Second derivative of phase')
xlabel('Wavelength (m)')
ylabel('Dispersion (ps/nm)')
hold on

%% Output graph as pdf
set(gcf, 'PaperUnits', 'centimeters');
set(gcf, 'PaperSize', [14 11]);
set(gcf, 'PaperPosition', [0.4 0.2 14 10.5]);
set(gcf, 'Units', 'centimeters');
set(gcf, 'Position', [4 4 18 15]);
export_fig 'filename' '-pdf';
```

A.2 Coupled Mode Equations

```matlab
function dy = coupled(z,y)
dy = zeros(6,1);     % a column vector

apod = 1; % To remove apodization use this

% Gaussian apodization
% apod = exp(-(z^2/((y(6)/2)^2)));

% Super-Gaussian apodization
% apod = exp(-(((z)^4)/((y(6))/2)^4));

% Raised cosine apodization
% apod = 0.5*(1 + cos((pi*z)/y(6)));

dy(1) = apod.*y(3) .*y(2) .*  exp(1i.*(y(4).*z + y(5).*(z.^2)));
dy(2) = apod.*y(3) .*y(1) .*  exp(-1i.*(y(4).*z + y(5).*(z.^2)));
```

Appendix B

Publication List

The journal and conference proceeding publications arisen from this work.

C. Sima, J. C. Gates, B. D. Snow, H. L. Rogers, C. Holmes, M. N. Zervas, P. G. R. Smith, 'Simple planar Bragg grating devices for photonic Hilbert transform', 3rd International Photonics and OptoElectronics Meetings (POEM 2010)/Optoelectronics Devices and Integration (OEDI), Wuhan, P.R.C., 3-5 Nov 2010.

C. Sima, J. C. Gates, B. D. Snow, H. L. Rogers, M. N. Zervas, P. G. R. Smith, 'Realisation of photonic Hilbert transformer with a simple planar Bragg grating', Photon 10, Southampton, 23-26 Aug 2010.

C. Sima, J. C. Gates, B. D. Snow, H. L. Rogers, M. N. Zervas, P. G. R. Smith, 'Realization of a planar Bragg grating for all-optical Hilbert transformer', ECIO 2010, Cambridge, 7-9 Apr 2010.

B. D. Snow, H. L. Rogers, C. Holmes, J. C. Gates, C. Sima, M. Kaczmarek, P. G. R. Smith, 'UV-written planar chirped Bragg gratings for use in dispersion management', ECIO 2010, Cambridge, 7-9 Apr 2010.

P. G. R. Smith, D. Kundys, J. C. Gates, C. Holmes, B. D. Snow, R. M. Parker, 'UV written waveguides for photonic quantum circuits', Quantum Photonics Workshop, Bristol, 17-18 Sep 2009 (Invited).

B. D. Snow, J. C. Gates, F. R. M. Adikan, C. B. E. Gawith, A. Dyadyusha, H. E. Major, D. O. Kundys, M. Kaczmarek, P. G. R. Smith, 'Liquid crystal based tunable WDM planar Bragg grating devices based on precision sawn groove substrates', CLEO/Europe-EQEC 2009, Munich, 14-19 Jun 2009.

J. C. Gates, D. O. Kundys, C. Holmes, B. D. Snow, R. M. Parker, H. E. Major, C. B. E. Gawith, P. G. R. Smith, 'Direct UV writing at the University of Southampton - substrates, structures and sensors', LAMP 2009, Kobe, 29 Jun - 2 Jul 2009.

B. D. Snow, F. R. M. Adikan, J. C. Gates, C. B. E. Gawith, A. Dyadyusha, H. E. Major, M. Kaczmarek, P. G. R. Smith, 'Direct optical observation of walls and disclination effects in active photonic devices', Molecular Crystals and Liquid Crystals, 502, pp.178-184, 2009.

P. G. R. Smith, C. B. E. Gawith, J. C. Gates, C. Holmes, B. D. Snow, F. R. M. Adikan, 'UV written planar Bragg grating sensors - geometries and applications', Photon '08, Edinburgh, 26-29 Aug 2008.

B. D. Snow, F. R. M. Adikan, J. C. Gates, C. B. E. Gawith, A. Dyadyusha, M. Kaczmarek, P. G. R. Smith, 'Direct optical observation of disclination effects in active photonic devices', LCP 2008, Cambridge, 21-23 July 2008.

B. D. Snow, F. R. M. Adikan, J. C. Gates, C. B. E. Gawith, A. Dyadyusha, H. E. Major, M. Kaczmarek, P. G. R. Smith, 'Controlling disclinations in liquid crystal planar Bragg gratings', CLEO/QELS 2008, San Jose, 4-9 May 2008.

J. C. Gates, C. Holmes, B. D. Snow, C. B. E. Gawith, P. G. R. Smith, 'UV written evanescent devices fabricated in micro-structured substrates for optofluidics', CLEO/QELS 2008, San Jose, 4-9 May 2008.

B. D. Snow, F. R. M. Adikan, J. C. Gates, C. B. E. Gawith, A. Dyadyusha, M. Kaczmarek, P. G. R. Smith, 'Line defects and temperature effects in liquid crystal tunable planar Bragg gratings', Optics Express, 15(25), pp.17129-17135, 2007.

P. G. R. Smith, C. B. E. Gawith, J. C. Gates, D. O. Kundys, M. F. R. Adikan, C. Holmes, H. E. Major, M. Garcia-Ramirez, B. D. Snow, 'UV written waveguide devices - Bragg gratings and applications in sensors', Conference on Advancement of Materials and Nanotechnology (ICAMN 2007), Langkawi, Malaysia, 29 May - 1 Jun 2007 (Invited).

B. D. Snow, F. R. M. Adikan, A. Dyadyusha, J. C. Gates, H. E. Major, C. B. E. Gawith, M. Kaczmarek, P. G. R. Smith, 'Towards high-speed liquid crystal electrically tunable planar Bragg gratings for integrated optical networks', 21st Annual Conference British Liquid Crystal Society (BLCS 2007), Sheffield, 28-30 Mar 2007.

F. R. M. Adikan, J. C. Gates, A. S. Webb, H. E. Major, C. Holmes, M. A. G. Ramirez, B. D. Snow, D. O. Kundys, C. B. E. Gawith, P. G. R. Smith, 'Recent developments in direct-UV-written planar waveguides, gratings, sensors and substrates', ECIO 2007, Copenhagen, 25-27 Apr 2007.

F. R. M. Adikan, J. C. Gates, B. D. Snow, A. Dyadyusha, H. E. Major, C. B. E. Gawith, M. Kaczmarek, P. G. R. Smith, '100 GHz electrically tunable planar Bragg gratings via liquid crystal overlay', CLEO-Europe/IQEC 2007, Munich, 17-22 Jun 2007.